NASA Contractor Report 159019

NASA-CR-159019

Modern Digital Flight Control System Design for VTOL Aircraft

John R. Broussard
Paul W. Berry
Robert F. Stengel

THE ANALYTIC SCIENCES CORPORATION
Reading, Mass. 01867

CONTRACT NAS1-14358
MARCH 1979

National Aeronautics and
Space Administration

Langley Research Center
Hampton, Virginia 23665
AC 804 827-3966

FOREWORD

The investigation described in this report was performed by TASC during the period from March 17, 1976 to November 1, 1977 under Contract No. NAS1-14385 for the National Aeronautics and Space Administration. The Navigation and Guidance Research Branch of the Flight Instrumentation Division sponsored this work as a contribution to the VTOL Approach and Landing Technology (VALT) Program. Dr. David R. Downing Served as Technical Monitor for this contract.

The study was directed by Dr. Sol W. Gully and by Dr. Robert F. Stengel. Engineering investigation was conducted by Mr. John R. Broussard and Mr. Paul W. Berry, who were assisted in computer program development by Mr. Michael R. Burns. Dr. Michael Athans, Professor of Electrical Engineering at the Massachusetts Institute of Technology, served as technical consultant. Dr. Michael G. Safonov, who was a graduate student at MIT, participated in the developments in Appendix B.

ABSTRACT

Methods for and results from the design and evaluation of a digital flight control system (DFCS) for a CH-47B helicopter are presented. The DFCS employs proportional-integral control logic to provide rapid, precise response to automatic or manual guidance commands while following conventional or spiral-descent approach paths. It contains attitude- and velocity-command modes, and it adapts to varying flight conditions through gain scheduling. Extensive use is made of linear systems analysis techniques -- the DFCS is designed using linear-optimal estimation and control theory, and the effects of gain scheduling are assessed by examination of closed-loop eigenvalues and time responses. Simulation evaluation of the DFCS permits direct comparison of alternative navigation, guidance, and control philosophies, confirms the practical merits of the DFCS design approach, and demonstrates techniques which will aid the development of future guidance and control systems.

TABLE OF CONTENTS

TABLE OF CONTENTS (Continued)

LIST OF FIGURES

LIST OF FIGURES (Continued)

LIST OF FIGURES (Continued)

LIST OF FIGURES (Continued)

LIST OF TABLES

LIST OF TABLES (Continued)

LIST OF SYMBOLS

VARIABLE	DESCRIPTION
A	Gain matrix in PIF control law Constant in quadratic equation in MLS transformation
a	Scalar constant in guidance equation Regression constant Acceleration Azimuth in MLS measurement vector
$\underline{a}$	Inertial acceleration at the center of gravity expressed in body axes
B	Gain matrix in PIF control law Constant in quadratic equation in MLS transformation
$\underline{b}$	Accelerometer bias vector expressed in body axis
C	Constant in quadratic equation in MLS transformation Spiral guidance gain Gain matrix in PIF control law Gain matrix in PI control law
c	Scalar constant in guidance equation Scalar in Euler angle filter
D	Gain matrix in PIF control law Whitening gain matrix in Kalman filter
E	Feedforward gain matrix in PIF control law
e	2.71828...
F	Fundamental matrix (continuous-time system)
$\underline{f}$	Nonlinear functions for vehicle equations of motion

VARIABLE	DESCRIPTION
G	Control effect matrix (continuous-time system) Transfer function Disturbance effect matrix (continuous-time system)
H	Transformation matrix Observation matrix
H_E^l	Transformation matrix from the earth-relative frame to the local-level body frame $H_E^l = \begin{bmatrix} \cos\psi & \sin\psi & 0 \\ -\sin\psi & \cos\psi & 0 \\ 0 & 0 & 1 \end{bmatrix}$
H_E^G	Transformation matrix from the earth-relative frame to the local-level guidance frame $H_E^G = \begin{bmatrix} \cos\xi & \sin\xi & 0 \\ -\sin\xi & \cos\xi & 0 \\ 0 & 0 & 1 \end{bmatrix}$
h	Nonlinear transformation matrix Nonlinear observation matrix
I	Identity matrix
J	Scalar cost function (or functional)
K	Gain matrix in Kalman filter Scalar gains in guidance equation
L	Nonlinear function of disturbances
L_B	Transformation from Euler rates to body angular rates
ℓ	Dimension of observation vector
M	Cross weighting matrix between states and controls
m	Dimension of control vector Meters

VARIABLE	DESCRIPTION
n	Scalar constant in guidance equation Dimension of state vector
P	State covariance matrix
p	Pressure Roll rate
Q	State weighting matrix
$\bar{q}$	Dynamic pressure
q	Pitch rate
R	Control weighting matrix Range from vehicle cg to DME equipment Range from vehicle cg to earth relative axes origin in the MLS measurement vector
R_{CT}	Radius of turn
r	Yaw rate Range from vehicle cg to elevation equipment
s	Laplace operator (continuous-time system) Seconds
T	Matrix partition
t	Time
U	Matrix partition
u	Vehicle body x-axis earth relative velocity component
$\underline{u}$	Control vector
V	Velocity Matrix partition
V_H	Horizontal velocity
v	Vehicle body y-axis earth relative velocity component

VARIABLE	DESCRIPTION
$\underline{v}$	Control rate vector Velocity vector Observation noise vector
W	Disturbance covariance matrix Matrix partition Wind component
w	Vehicle body z-axis earth relative velocity component Markov model state
$\underline{w}$	Disturbance vector Wind vector
X	State covariance matrix
x	Axial position
$\underline{x}$	State vector Position vector Eigenvector
y	Lateral position
$\underline{y}$	Observation vector Guidance command vector
z	Normal position Laplace operator (discrete time)
$\underline{z}$	Measurement vector

VARIABLES (GREEK)

α	Angle of attack
β	Sideslip angle
Γ	Control effect matrix (discrete-time system)
γ	Vertical flight path angle (positive in a climb)
δ	Control displacement Impulse function

VARIABLE (GREEK)	DESCRIPTION
ε	Elevation in MLS measurement vector Drift error
ζ	Damping ratio
η	Specific heat ratio of air
θ	Pitch attitude angle
λ	Eigenvalue
$\underline{\mu}$	Trim setting vector
$\underline{\nu}_E$	Euler angle vector
Ξ	Discrete process noise covariance matrix
ξ	Integration vector variable in PIF Horizontal flight path angle
Σ	Summation
σ	Standard deviation
τ	Time constant Integration dummy variable
Υ	Discrete observation noise covariance matrix
Φ	State transition matrix (discrete-time fundamental matrix)
ρ	Correlation coefficient Free stream air density
ϕ	Roll attitude angle
χ	Discrete process noise covariance matrix
ψ	Yaw attitude angle
ω_B^E	Body angular rate vector
ω_n	Natural frequency

SUBSCRIPTS	DESCRIPTION
A	Air relative
a	Azimuth/DME equipment
B	Differential collective Body axis
b	Bias
C	Gang collective
c	Command value
d	Desired value
E	Earth-relative axis
go	Measured from final value (as t_{go} = time to go)
H	Horizontal
i	Element index for vectors and matrices
j	Element index for vectors and matrices
k	Sampling instant index
m	Measured value
N	Nominal value
o	Nominal value
p	Roll rate Linearized command observation matrix
q	Pitch rate
R	Differential lateral cyclic
r	Yaw rate
S	Gang lateral cyclic
s	Static pressure
T	Total value Total pressure

SUBSCRIPTS	DESCRIPTION
u	x-axis velocity
v	y-axis velocity
w	Wind z-axis velocity
x	Horizontal perpendicular to y and z
y	Horizontal perpendicular to x and z
z	Vertical perpendicular to x and y
θ	Pitch attitude angle
ε	Elevation equipment
ϕ	Roll attitude angle
ψ	Yaw attitude angle

SUPERSCRIPTS	
j	Transfer function numerator index
T	Transpose of matrix
-1	Inverse of matrix
*	Steady state Trim

PUNCTUATION	
$(\dot{})$	Derivative of quantity with respect to time
$(\underline{\ })$	Vector quantity
$(\bar{})$	Augmented quantity Mean value
$\partial(\ )/\partial(\ )$	Partial derivative of one variable with respect to another

PUNCTUATION	DESCRIPTION
$\Delta(\ )$	Perturbation variable
$(\ )^*$	Reference, nominal, optimal or trim value
$(\hat{\ })$	Estimated quantity
$E(\ )$	Expected value of variable
$\mathrm{cov}(\ )$	Covariance of variable
∞	Infinity
$\int$	Integral
$(\sim)$	Matrix equivalent to vector cross product, Specifically, if $\underline{x}$ is the three-dimensional vector $\underline{x} = \begin{bmatrix} x \\ y \\ z \end{bmatrix}$, then $\tilde{x} = \begin{bmatrix} 0 & -z & y \\ z & 0 & -x \\ -y & x & 0 \end{bmatrix}$ and the cross product of $\underline{x}$ and $\underline{f}$ is equal to the product of the matrix $\tilde{x}$ and the vector $\underline{f}$, $\underline{x} \times \underline{f} = \tilde{x}\underline{f}$

ACRONYM	CORRESPONDING PHRASE
AD	Air Data
BA	Barometric Altimeter
CF	Complementary Filter
CL	Closed Loop
CR	Cross Range
cg	Center of gravity
DFCS	Digital Flight Control System
DME	Distance Measuring Equipment
DR	Down Range

ACRONYM	CORRESPONDING PHRASE
ECF	Extended Complementary Filter
EKF	Extended Kalman Filter
ER	Enroute
fpm	Feet per minute
IAS	Indicated Air Speed
IVSI	Instantaneous Vertical Speed Indicator
kt	Knot
LAT	Lateral
LON	Longitudinal
LTV	Linear Time Varying
ln	Natural Logarithm
MAX	Maximum
MLS	Microwave Landing System
NASA	National Aeronautics and Space Administration
MGC	Navigation Guidance and Control
PI	Proportional Integral
PIF	Proportional Integral Filter
PSD	Power Spectral Density
QTV	Quadratic with Time
rad	Radians
SL	Sea Level
sec	Seconds
TAGS	Tactical Aircraft Guidance System
TAS	True Airspeed

ACRONYM	CORRESPONDING PHRASE
TRI	Multilateration
VALT	VTOL Approach and Landing Technology
VTOL	Vertical Takeoff and Landing

1. INTRODUCTION

1.1 BACKGROUND

Vertical Take-Off and Landing (VTOL) Aircraft are able to operate from small landing areas and in the vicinity of natural and man-made obstacles which would prevent the operatons of conventional aircraft. This capability can be used only if navigational information is adequate to identify safe and efficient flight paths, if guidance strategies can keep the vehicle on its intended path, and if control laws stabilize the vehicle and provide satisfactory response to guidance commands throughout the flight envelope. To perform these functions in all weather and with aircraft whose unaugmented flying qualities may be marginal (due to turbulence, low airspeed, steep flight paths, and/or configuration design), some degree of automatic control is required. Fully integrated navigation, guidance, and control can ease the air crew's workload, allowing more time to conduct the executive functions of mission management which are crucial to efficiency, safety, and on-time performance.

Digital systems employing adaptive concepts can be of great value in achieving the improvements in VTOL flight controls that are necessary for future operations. Digital logic facilitates many features which are desirable in advanced control systems -- e.g., branching, mode switching, gain changing, multi-loop closures, integration, multiplication, and division -- and digital control laws are readily interfaced with navigation and guidance logic. Flexibility for design, testing, and service modification is unmatched by a comparable analog system, which is fixed once its components

and circuit connections are defined. The control system's ability to adapt to dynamic variations is particularly important for VTOL aircraft, which may undergo configurational changes as well as large flight-condition variation during hover/cruise transitions.

The purpose of this investigation is to further improve the gain-scheduled digital controllers and estimators developed by TASC under a previous contract (Ref. 1), and to evaluate these digital controllers and estimators in a realistic helicopter simulation. The output of this contract consists of controller and estimator structures and gains for use in the NASA VTOL Approach and Landing Technology (VALT) aircraft test flights.

Significant features of the VTOL digital control design process, which are addressed in Ref. 1 and this report includes:

- Unified design of multi-input/multi-output command-response systems
- Design of discrete-time controllers to continuous-time specifications
- Selection of digital sampling interval
- Design for rate-and displacement-limited actuators
- Explicit adaptation to flight condition and vehicle configuration
- Links between classical response criteria and modern design techniques
- Implementable filters designed using Kalman filter techniques and blending diverse sensor outputs.

- Direct evaluation of control system response on time-varying flight paths.

The following sections of this chapter review the project structure, provide an overview of results, and outline the organization of this report.

1.2 PROJECT STRUCTURE

The VTOL Approach and Landing Technology (VALT) Program of the National Aeronautics and Space Administration is developing a technology base for the navigation, guidance, control, display and flight management requirements of VTOL short-haul transportation systems in the 1980's time period. This program requires the development of a navigation, guidance, and control (NGC) system that permits automatic flight along complex four-dimensional (space and time) mission profiles from takeoff to landing under all weather conditions. Flight tests will be conducted at the NASA Wallops Flight Center using a CH-47B Research Aircraft, as shown in Fig. 1.2-1. This helicopter will contain standard air data sensors and gyroscopic instruments for control system measurements. Control logic will be executed in a digital flight computer, and control commands will be transmitted to the helicopter's mechanical control linkages by hydraulic actuators.

The VALT Research Aircraft, a tandem-rotor medium transport helicopter, provides a good baseline for NGC demonstration and evaluation. Its size is representative of future passenger-carrying VTOL aircraft, and its climb and descent performance is adequate for terminal-area operational studies.

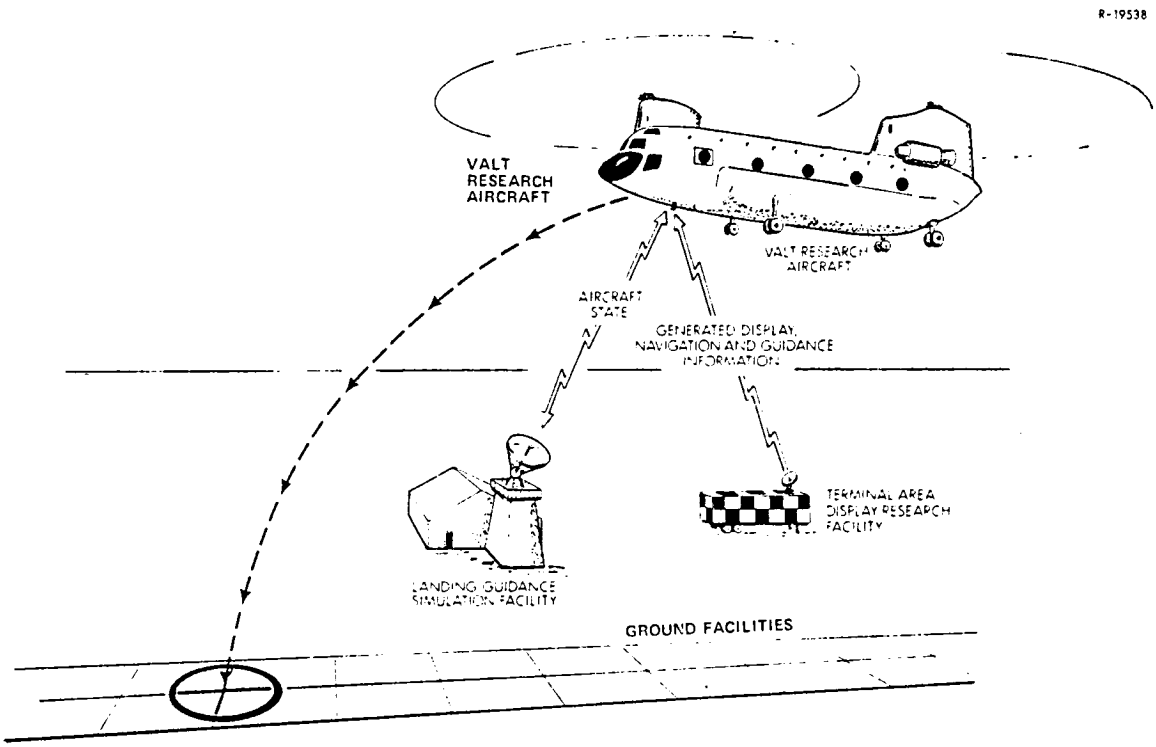

Figure 1.2-1 VALT Integrated Flight Test Facilities

Prior use of this aircraft in the United States Army's Tactical Aircraft Guidance System (TAGS) program provides flight test results for comparison and flight-rated equipment for application to this NASA research.

The present investigation contributes to VALT Program objectives and has been organized to provide both theoretical and practical results to aid the design of fully automatic VTOL navigation, guidance, and control systems. In the course of this work, new techniques have been developed for the design of digital set-point regulators, and a powerful method for explicit adaptation of control gains to predictable variations in system dynamics has been demonstrated. The latter is an extension of conventional gain scheduling techniques which does not require (but is aided by) prior knowledge of the

parameter sensitivity of the system to be controlled. By using optimal control theory, system stability margins are assured from the outset, and attention can be centered on command response and disturbance rejection. Sampling intervals of the digital system can be chosen on the basis of system performance, and the dynamic structure of the discrete-time control laws including integral feedback paths, provides the flexibility to compensate for computation delays. Consideration of rate and displacement limits of control actuators in the design process leads to low control gains, which in turn reduce control sensitivity to aircraft parameter variations and system nonlinearities.

This project extends the work described in Ref. 1 in the following areas:

- Control Law Improvement
- State Estimator Improvement
- Guidance Law Implementation
- Evaluation Tool Development
- System Evaluation.

These elements are summarized briefly. The control laws are improved because they now are implemented in incremental form. This eliminates the need for complex and error-prone trim state and control calculations. Response is improved by optimal feedforward command. These improvements are discussed in Refs. 2 and 3. The state estimators are completely revised, with the new versions based on discrete-time Kalman filter techniques. Wind and selected sensor errors are estimated to improve the quality of the state estimates. The implementation of velocity and spiral guidance laws is examined, and

all laws are placed in a common framework. A new computerized evaluation tool, described in Ref. 4, is developed and it is used to perform a series of system evaluation runs, which are discussed in Ref. 5 and this report.

1.3 OVERVIEW OF RESULTS

The development of the control laws demonstrates that modern control theory provides a unified, easily understood basis for practical control system design once the necessary design tools are developed. A principal advantage of the design approach is that the necessary control structure is visable at an early stage of the design process. All state control paths are determined, allowing the designer to evaluate the relative importance of each. Adjustable design parameters are provided which have a direct and predictable effect on system response. The resulting control laws provide precise and efficient command response for VTOL aircraft.

The filter designs developed in this work utilize digital Kalman filter techniques to derive angular and translational complementary filters. These filters are straightforward in implementation, yet complete in their use of all available instrumentation. They are analogous to low-pass and complementary filters of the type extensively used in conventonal aircraft systems. The system evaluation results indicate that the filters effectively combine sensor information to create state estimates for controller use.

Examination of the cartesian position and spiral guidance laws has shown that either can be used as the VALT guidance law. Either velocity or attitude command vectors can be formed as control command, and specific spiral guidance results are shown.

The helicopter simulation developed in this work is described in Ref. 4 and is used to generate the simulation results presented in this report. The simulation incorporates a realistic flight computer executive structure, along with complete helicopter, sensor and actuator models.

1.4 ORGANIZATION OF THE REPORT

Each of the next three chapters is directed to a specific phase of the control system design and evaluation. Chapter 2 presents the foundations of helicopter control system design and provides an overview of the various parts of the digital flight control system. Chapter 3 details the control system design procedure, and discusses the design model, as well as the controller and estimator design procedures. The guidance structures are presented in forms suitable for implementation with the controllers developed in this report. Chapter 4 evaluates the performance of the digital flight control system by using the evaluation program constructed for this purpose. The controller designs are compared, and the state estimation time histories are illustrated. The performance of the complete digital flight control system in the presence of sensor noise, actuator and rotor dynamics and wind disturbances is examined. An example of a spiral descent entry is used to illustrate guidance control interaction. Chapter 5 summarizes the major conclusions of this project, and suggests areas where further work is necessary to solidify preliminary results.

2. CONTROL SYSTEM OVERVIEW

The control system design presented in this report is an advanced digital flight control system (DFCS) which stabilizes the vehicle at all flight conditions while accommodating guidance commands from a trajectory generator. The DFCS is composed of a digital proportional-integral control law which accepts commands from an automatic guidance law and processes vehicle state information from digital filters for stability. A block diagram of the DFCS is shown in Fig. 2-1.

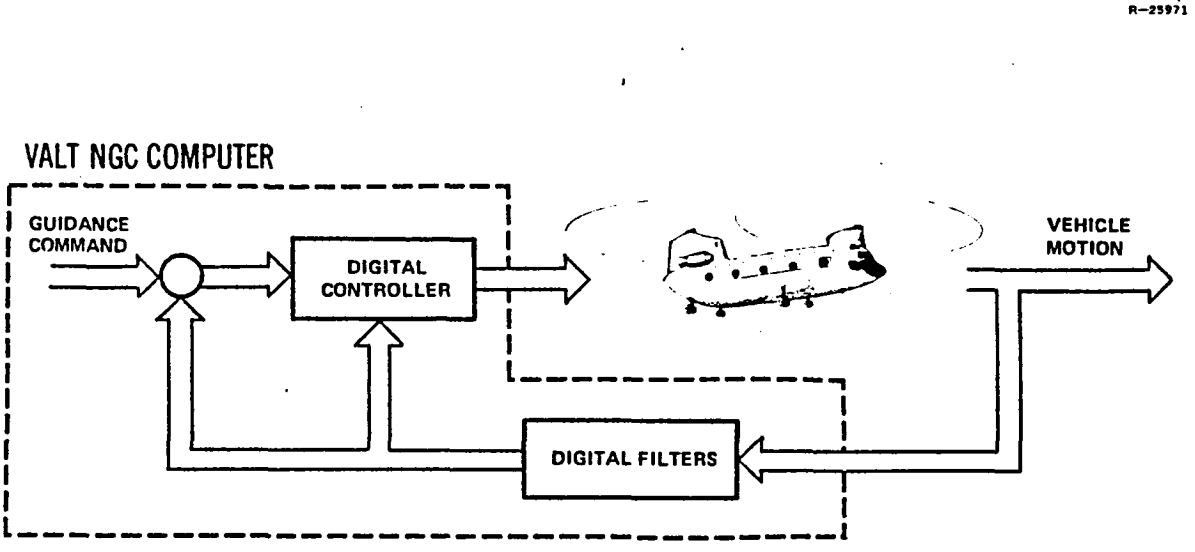

Figure 2-1 VALT Digital Flight Control System

2.1 VEHICLE, STATE AND CONTROL CHARACTERISTICS

The VALT Research Aircraft shown in Fig. 2.1-1 is a medium transport vehicle (CH-47B helicopter) which carries payloads up to 4000 kg (8800 lb) (approximately 30 passengers) at its normal operating weight of 15,000 kg (33,000 lb). It operates at indicated airspeeds up to 82 m/s (160 kt). Lateral and aft velocities are limited to 18 m/s (35 kt) and 15 m/s (-30 kt), respectively; normal cruise speed is 72 m/s (140 kt). Maximum service ceiling is 4270 m (14,000 ft).

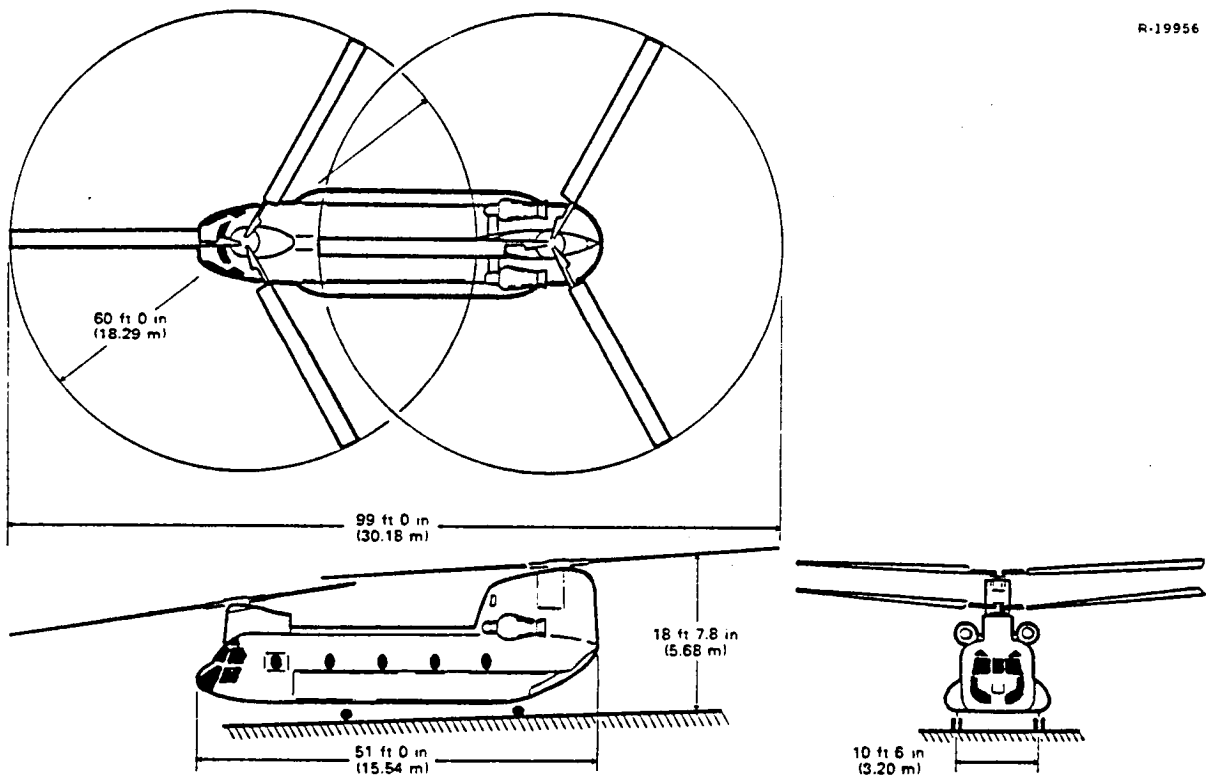

Figure 2.1-1 Basic Features of the VALT Research Aircraft

Neglecting disturbance inputs, the nonlinear equations which govern vehicle motion can be described by the vector differential equation

$$\dot{\underline{x}}(t) = \underline{f}[\underline{x}(t), \underline{u}(t)] \qquad (2.1\text{-}1)$$

For the rigid-body control problem assumed in DFCS design, the state vector contains 3 components each of translational rate, angular rate, and attitude,

$$\underline{x}^T = \left[u, v, w, p, q, r, \phi, \theta, \psi\right] \qquad (2.1\text{-}2)$$

The states (u, v, w) are body-axis velocites, (p, q, r) are body-axis rotational rates, and (ϕ, θ, ψ) are Euler angles of the body axes with respect to an Earth-relative frame. The control vector includes differential collective, gang collective, gang cyclic and differential cyclic rotor deflections:

$$\underline{u}^T = \left[\delta_B, \delta_C, \delta_S, \delta_R\right] \qquad (2.1\text{-}3)$$

These four primary control variables provide control moments about all three axes, as well as vertical force. Horizontal forces are obtained by tilting the entire vehicle to provide a component of rotor lift in the desired direction.

The total state and control can be divided into nominal and perturbation components,

$$\underline{x}(t) = \underline{x}_o(t) + \Delta\underline{x}(t) \qquad (2.1\text{-}4)$$

$$\underline{u}(t) = \underline{u}_o(t) + \Delta\underline{u}(t) \qquad (2.1\text{-}5)$$

leading to a first-order Taylor series expansion of Eq. 2.1-1:

$$\dot{\underline{x}}_o(t) = \underline{f}\left[\underline{x}_o(t), \underline{u}_o(t)\right] \qquad (2.1\text{-}6)$$

$$\Delta\dot{\underline{x}}(t) = F(t)\Delta\underline{x}(t) + G(t)\Delta\underline{u}(t) \qquad (2.1\text{-}7)$$

where

$$F(t) = \frac{\partial}{\partial\underline{x}}\,\underline{f}\left[\underline{x}_o(t), \underline{u}_o(t)\right] \qquad (2.1\text{-}8)$$

$$G(t) = \frac{\partial}{\partial\underline{u}}\,\underline{f}\left[\underline{x}_o(t), \underline{u}_o(t)\right] \qquad (2.1\text{-}9)$$

F(t) and G(t) are slowly varying functions of time and actually are explicit functions of the flight condition rather than time. Specifying the perturbation matrices F and G at specific points in the flight envelope rather than along a specific flight profile allows for control laws based on linear-time-invariant models of the aircraft,

$$\Delta\dot{\underline{x}}(t) = F\Delta\underline{x}(t) + G\Delta\underline{u}(t) \qquad (2.1\text{-}10)$$

Equation 2.1-10 leads to the design formalism used in the DFCS construction. The control law is designed at a finite number of points in the flight envelope; regression analysis is then used to schedule the control law gains. Storing control gains as functions of flight variables enables the control law to be used for any flight trajectory, provided the flight points used in the design are sufficiently representative of expected operating conditions. Examining control law performance with the scheduled gains is an important part of the control law evaluation.

Since the control law is designed using perturbation variables, it would seem that the nominals, $\underline{u}_o(t)$ and $\underline{x}_o(t)$ would be involved in the implemented control logic. Techniques for incorporating the nominals follow the same line of reasoning as the control gains (Ref. 1), i.e., scheduling nominals with flight conditions. An alternative to calculating the nominals is to exploit the relationship between nominals and perturbation system steady state in the construction of the digital control law algorithm. This results in a control law which does not use nominals and is based on the incremental form (Refs. 6 and 7). Testing the behavior of the incremental form in time-varying simulation and in flight is an important system evaluation.

2.2 CONTROL LAWS

Two different types of control laws are used in the design: the proportional integral (PI) controller and the proportional integral filter (PIF) controller. Both control laws are designed using modern control theory. The PI controller has a more common structure employing direct feedback of state and command error integrator information to the vehicle actuators. The PIF controller uses a more complicated structure with a digital filter interfacing between state and integrator feedback and vehicle actuators. The compensator attempts to improve high frequency noise suppression without compromising control design specifications (Ref. 8). Comparisons of the VALT DFCS performance under the two control laws will indicate whether the increased control complexity of the PIF is warranted.

PI and PIF controllers both have the Type 1 or integral property. The Type 1 property insures that as long as the system is stable, the control laws will force the vehicle

to track constant guidance commands with zero steady state error. New digital proportional-integral relationships were derived because adequate theoretical results using optimal control could not be found in the open literature. These results are reported in Appendix B.

PI and PIF both weight the control rate in their quadratic cost functions. The control rate restraint is believed to manifest itself as modest control gain magnitudes, i.e., increasing the control rate weighting decreases the gain magnitudes. Optimal control requires full state feedback to all controls, however, we have investigated eliminating feedback paths with "small" gains. Evaluating the effect of zeroed gains occurs concurrently with the gain scheduling evaluation. Zeroing gains is considered a part of the gain scheduling procedure.

2.3 GUIDANCE LAWS

Two automatic guidance laws are used to evaluate the DFCS in simulation; a velocity guidance law designed in Ref. 9 and a spiral guidance law designed in Ref. 10. The velocity guidance law forms nominal and perturbation vehicle position and velocity in earth-relative axes and constructs three commands consisting of downrange, crossrange and vertical velocities. The spiral guidance law forms vehicle nominal and perturbation true airspeed, crossrange position, yaw angle and time and constructs three commands; roll angle, longitudinal specific force, and vertical velocity.

The PI and PIF control laws require four commands because there are four available controls, hence, yaw angle is added to the two guidance law command sets which are sent to the control law. Wind estimates, when available, are used

to adjust the yaw angle command so that the projection of the body x-axis lies along the air-relative velocity vector.

2.4 COMMAND MODES AND DESIGN CRITERIA

The assumed command input to the PI and PIF control laws do not conform exactly to the time varying commands issued from the guidance laws. Appropriate logic is used to correctly interface the guidance law and the control law. The control design assumes commands, $\underline{y}_d$, are either attitude commands or velocity commands. For the attitude command, 3 Euler angles and vertical velocity are specified, i.e.:

$$\underline{y}_d^T = \left[\phi, \theta, \psi, V_z\right] \qquad (2.4\text{-}1)$$

For the velocity command, yaw angle and the translational velocity components (expressed in an earth-relative frame oriented with the initial yaw angle at zero) are dictated, or:

$$\underline{y}_d^T = \left[V_x, V_y, V_z, \psi\right] \qquad (2.4\text{-}2)$$

The criteria used in the controller design process is to individually step each of the commands and require that the system response to the commanded variable fall within an admissible transient response envelope. The key design bounds are on rise time, overshoot, and settling time. The design specifications for the velocity system are

- V_z Command:

  Rise time criterion: Amplitude >90% of the final value within 2 sec

Overshoot criterion: Overshoot <5% of the final value for $0<V_x<10$ kt

Overshoot <20% of the final value for $V_x>40$ kt

- V_x, V_y Commands:

Rise time criterion: Amplitude >80% of the final value within 5 sec

Overshoot criterion: Overshoot $<(4+.4V_x)$% of the final value for $0<V_x<40$ kt

Overshoot <20% of the final value for $V_x>40$ kt

- ψ Command:

Rise time criterion: Amplitude >90% of the final value within 1.8 sec

Overshoot criterion: Overshoot <15% of the final value

Settling time criterion: Amplitude within 5% of the final value in 5 sec or less

No settling times are specified for the velocity commands. For the attitude command system the specifications are:

- Angle Commands: θ, ϕ, ψ

Rise time criterion: Amplitude >90% of the final value within 1.5 sec

Overshoot criterion: Overshoot <15% of the final value

Settling time criterion:	Amplitude within 5% of the final value in 5 sec or less

- V_z Command: Same as the velocity system

An important concept investigated during the DFCS design is: Does the step response criteria provide sufficient information for specifying or defining the desired optimal control cost function weighting elements?

Although closed-loop pole locations are not specified, the pole locations are computed and are used to aid in the choice of cost function weighting matrices. Mapping discrete-time poles into the left-half complex plane enable MIL-F-83300 (Ref. 11) to be used as a guide. Design specification parameters used include damping ratio, frequency and the inverse of a real root (time constant).

2.5 STATE ESTIMATORS

The control laws and the guidance laws require estimates of the nine rigid body states and three components of aircraft position. In addition, any estimate of the slowly varying atmospheric wind greatly aids gain scheduling and guidance law performance. The use of the aircraft perturbation system in Eq. 2.1-10 as an internal model (or bank of internal models) in the design of the estimators was rejected early because it was too complex.

The approach taken is to combine the sensors that measure states in each of the three groups (velocity and position, angular position and angular rates) and design estimators for each group. The internal model states for each estimator are simple random walks, markovs, and integrations

driven by white noise. Kalman filter theory is used to design the estimator gains which, in some cases, are scheduled with flight condition. The estimators are designed separately from the control and guidance laws (Ref. 12).

An important consideration in estimator design is the degree of complexity required in the state estimators, as well as the number of sensors required. Two approaches to the velocity filters design are pursued, one being more complex that the other. In addition, two types of ground-based landing aids are used in the velocity filter design with one landing aid providing more information in order to provide comparative results.

2.6 TRIM AND STEADY STATE

Control laws are possible in incremental form because of the relationship between the nonlinear aircraft model quasi-static trim and the linear aircraft model's steady state. That is, for a constant command,

$$\underline{y}_{d_o} = h(\underline{x}_o) \tag{2.6-1}$$

the aircraft is in quasi-static trim if, given $\underline{y}_{d_o}$, there is a $\underline{u}_o$ which satisfies Eq. 2.6-1 and

$$0 = \underline{f}(\underline{x}_o, \underline{u}_o) \tag{2.6-2}$$

Techniques for finding $\underline{u}_o$ are discussed in Ref. 13. For a linear system, steady state is given by

$$0 = F\Delta\underline{x}^* + G\Delta\underline{u}^* \tag{2.6-3}$$

$$\Delta\underline{y}_d = H_p\Delta\underline{x}^* \tag{2.6-4}$$

and the $\Delta\underline{u}^*$ which satisfies Eqs. 2.6-3 and 2.6-4 can be found from

$$\begin{bmatrix} F & G \\ H_p & 0 \end{bmatrix} \begin{bmatrix} \Delta\underline{x}^* \\ \Delta\underline{u}^* \end{bmatrix} = \begin{bmatrix} 0 \\ I \end{bmatrix} \Delta\underline{y}_d \qquad (2.6\text{-}5)$$

The matrix H_p is the linearized version of h in Eq. 2.6-1 and for small increments in $\underline{y}_d$, H_p satisfies,

$$\underline{y}_d = \underline{y}_d + \Delta\underline{y}_d \cong \underline{h}(\underline{x}_o) + H_p \Delta\underline{x}^* \qquad (2.6\text{-}6)$$

Defining the inverse of the composite matrix,

$$\begin{bmatrix} F & G \\ H_p & 0 \end{bmatrix}^{-1} = \begin{bmatrix} S_{11} & S_{12} \\ S_{21} & S_{22} \end{bmatrix} \qquad (2.6\text{-}7)$$

$\Delta\underline{x}^*$ and $\Delta\underline{u}^*$ can be found from

$$\Delta\underline{x}^* = S_{12}\, \Delta\underline{y}_d \qquad (2.6\text{-}8)$$

$$\Delta\underline{u}^* = S_{22}\, \Delta\underline{y}_d \qquad (2.6\text{-}9)$$

The inverse existing in Eq. 2.6-7 is a sufficient requirement for constructing a proportional-integral controller and indicates why the commands and controls should be equal. Using Eqs. 2.6-8 and 2.6-9, the linearization produces

$$\underline{x}^* \cong \underline{x}_o + \Delta\underline{x}^* = \underline{x}_o + S_{12}\, \Delta\underline{y}_d \qquad (2.6\text{-}10)$$

$$\underline{u}^* \cong \underline{u}_o + \Delta\underline{u}^* = \underline{u}_o + S_{22}\, \Delta\underline{y}_d \qquad (2.6\text{-}11)$$

for small changes in the command.

We will now demonstrate how Eqs. 2.6-10 and 2.6-11 can be used to eliminate the use of trim in a perturbation control law using the incremental form.

The incremental form for the simple perturbation regulator

$$\Delta \underline{u}_k = K\Delta \underline{x}_k \tag{2.6-12}$$

is obtained by subtracting $\Delta \underline{u}_{k-1}$ from $\Delta \underline{u}_k$,

$$\Delta \underline{u}_k = \Delta \underline{u}_{k-1} + K(\Delta \underline{x}_k - \Delta \underline{x}_{k-1}) \tag{2.6-13}$$

Rewriting Eq. 2.6-13 using trim and total values we have

$$\underline{u}_k = \underline{u}_{k-1} + K(\underline{x}_k - \underline{x}_{k-1}) + (\underline{u}_{o_k} - \underline{u}_{o_{k-1}}) - K(\underline{x}_{o_k} - \underline{x}_{o_{k-1}}) \tag{2.6-14}$$

Using Eqs. 2.6-10 and 2.6-11, Eq. 2.6-14 reduces to the regulator incremental form,

$$\underline{u}_k = \underline{u}_{k-1} + K(\underline{x}_k - \underline{x}_{k-1}) + (S_{22} - KS_{12})(\underline{y}_{d_k} - \underline{y}_{d_{k-1}}) \tag{2.6-15}$$

The regulator incremental form does not use the trim value, whereas the regulator position form does, i.e.,

$$\underline{u}_k = \underline{u}_{o_k} + K(\underline{x}_k - \underline{x}_{o_k}) \tag{2.6-16}$$

Unfortunately, the regulator incremental form "loses its place" and proper tracking of y_{d_k} is not guaranteed. Integral compensation eliminates this drift problem in PI and PIF as discussed in Section B.4.

2.7 CONTROL SYSTEM DESIGN AND EVALUATION PROGRAMS

Three computer programs are used in the DFCS design and evaluation: DIGADAPT, SCHED and TVHIS. The programs DIGADAPT and SCHED were originally documented in Ref. 14 but have been updated. DIGADAPT is used to design the constant gain PI and PIF control laws at a flight point and to perform closed-loop eigenvaues/eigenvectors and step response simulations using perfect measurements. The Kalman filter gains are also found with DIGADAPT. SCHED performs the gain regressions using standard IBM regression analysis subroutines. TVHIS simulates guidance, control and estimators using time-varying perturbation dynamics (Eq. 2.1-7) along either of two stored trajectories; the spiral descent and the approach trajectory. Any of the options previously discussed can be chosen and combined in TVHIS for a simulation evaluation along either of the trajectories.

3. DIGITAL FLIGHT CONTROL SYSTEM DESIGN

The synthesis of a digital flight control system (DFCS) for the VALT Research Aircraft is presented in this chapter. The system is designed to augment aircraft stability throughout the maneuvering envelope and to provide precise response either to pilot or to automatic guidance commands. The DFCS design employs new techniques in discrete Kalman filter construction and discrete proportional-integral command system formulation.

By and large, current control design practice treats each aircraft axis separately in preliminary design, using "prior art" to define control structures and "tuning" the system (including the addition of selected nonlinearities and crossfeeds) during a program of exhaustive testing. The DFCS design takes the opposite approach, by first defining the gain-scheduled, coupled-control structure which is required to satisfy step response design criteria throughout the aircraft's maneuvering envelope and then using the testing phase to simplify the controller as appropriate. The advantage of this approach is that control system requirements are visible at an early stage of system development. Testing is required in either approach; however, the VALT DFCS design relies less on the designer's intuition and more on quantitative measures of system performance.

The chapter starts with design models, sensors and flight conditions for the control and filter designs. The sampling interval is identified and the filter designs are presented. The velocity filter has six different forms

depending on filter complexity and the type of landing aid employed. The chapter continues with the presentation of the proportional integral (PI) and proportional-integral-filter (PIF) control law designs. PIF is designed for both types of automatic guidance (attitude and velocity) while the secondary control law, PI, is designed for attitude only. The methodology used for gain scheduling is outlined and the automatic guidance algorithms are detailed. The chapter concludes with an overview of the recommended flight computer software for onboard implementation.

3.1 DESIGN MODELS OF THE AIRCRAFT

The design model of the helicopter for the attitude-command and velocity-command primary (PIF) control laws is represented by the linear-time-invariant differential equation

$$\begin{bmatrix} \Delta\dot{\underline{x}}(t) \\ \Delta\dot{\underline{u}}(t) \\ \Delta\dot{\underline{\xi}}(t) \end{bmatrix} = \begin{bmatrix} F & G & 0 \\ 0 & 0 & 0 \\ H_p & 0 & 0 \end{bmatrix} \begin{bmatrix} \Delta\underline{x}(t) \\ \Delta\underline{u}(t) \\ \Delta\underline{\xi}(t) \end{bmatrix} + \begin{bmatrix} 0 \\ I \\ 0 \end{bmatrix} \Delta\underline{v}(t) + \begin{bmatrix} 0 \\ 0 \\ I \end{bmatrix} \Delta\underline{y}_d(t) \tag{3.1-1}$$

where $\Delta()$ indicates a perturbation variable. Equation 3.1-1 is obtained by local linearization of the helicopter's nonlinear model (Ref. 1). The state, control, and command perturbations ($\Delta\underline{x}$, $\Delta\underline{u}$, and $\Delta\underline{y}_d$) correspond to the previous total-value definitions, $\Delta\underline{\xi}$, represents "command integrator states" to be added in the control system, and $\Delta\underline{v}$ is the control rate. The helicopter's kinematics, stability derivatives, and inertial effects are contained in the (9×9) matrix F and the control derivatives are contained in the (9×4) matrix G, as in Ref. 13. In symmetric flight, F and G contain aerodynamic

coupling but otherwise partition into the conventional longitudinal and lateral-directional equation sets. In turning flight, F and G also contain certain turn-induced coupling terms.

The design model of the helicopter for the secondary control law (PI) is similar to Eq. 3.1-1, except that the command integrator state vector is removed, i.e.,

$$\begin{bmatrix} \Delta\dot{\underline{x}}(t) \\ \Delta\dot{\underline{u}}(t) \end{bmatrix} = \begin{bmatrix} F & G \\ 0 & 0 \end{bmatrix} \begin{bmatrix} \Delta\underline{x}(t) \\ \Delta\underline{u}(t) \end{bmatrix} + \begin{bmatrix} 0 \\ I \end{bmatrix} \Delta\underline{v}(t) \qquad (3.1\text{-}2)$$

The Type 1 command property is obtained with this model even though an explicit integration of command error is not incorporated in the design aircraft model. The conditions for a digital control law to have the Type 1 property are given in Appendix B.

A distinction is made between the design model of the helicopter described here and the "truth model" used for control system evaluation. The design model portrays the rigid-body states for feedback information. The "truth model" augments the design model with details of the state estimators, rotors, actuators, and sensors. If there is an unacceptable disparity between results obtained from the two models, the design model must be augmented accordingly; that has not proved necessary here, as will be demonstrated in Chapter 4.

The (4×9) matrix H_p in Eq. 3.1-1 transforms the perturbation state vector to command-vector coordinates. For the velocity-command law, the transformed total command state is

$$\underline{y} = \begin{bmatrix} V_x \\ V_y \\ V_z \\ \psi \end{bmatrix} = \left[\begin{array}{c|c|c} H_B^E & 0 & 0 \\ (3\times3) & (3\times3) & (3\times3) \\ \hline 0 & 0 & 001 \\ (1\times3) & (1\times3) & \end{array}\right] \begin{bmatrix} u \\ v \\ w \\ p \\ q \\ r \\ \phi \\ \theta \\ \psi \end{bmatrix} = h(\underline{x}) \qquad (3.1\text{-}3)$$

where H_B^E is the body-to-earth relative Euler angle transformation shown in Appendix A. Since H_B^E varies with the Euler angles, the perturbation velocity transformations must include this sensitivity to $(\Delta\phi, \Delta\theta, \Delta\psi)$:

$$\Delta\underline{y} = H_P \Delta\underline{x}$$

$$= \left[\begin{array}{c|c|c} H_B^E & 0 & -H_B^E \tilde{v}_B L_B \\ \hline 0 & 0 & 001 \end{array}\right] \Delta\underline{x} \qquad (3.1\text{-}4)$$

where $\tilde{v}_B$ is the cross-product equivalent matrix of the body-axis velocities (no wind),

$$\tilde{v}_B = \begin{bmatrix} 0 & -w & v \\ w & 0 & -u \\ -v & u & 0 \end{bmatrix} \qquad (3.1\text{-}5)$$

and L_B transforms Euler angle perturbations to body-axis coordinates (see Eq. 3.3-16). It is important to include $H_B^E \tilde{v}_B L_B$ in H_P, as the angle perturbations have a significant effect on the earth-relative velocity perturbations; velocity-command controllers which neglect this term will experience difficulties when implemented on the actual helicopter.

The total command state for the attitude-command law is

$$\underline{y} = \begin{bmatrix} \phi \\ \theta \\ \psi \\ V_z \end{bmatrix} = \left[\begin{array}{c|c|c} 0 & 0 & 0 \\ (3\times3) & (3\times3) & (3\times3) \\ \hline H_B^E & 0 & 0 \\ (1\times3) & (1\times3) & (1\times3) \end{array}\right] \begin{bmatrix} u \\ v \\ w \\ p \\ q \\ r \\ \phi \\ \theta \\ \psi \end{bmatrix} \qquad (3.1\text{-}6)$$

where the last row in H_B^E is used. The perturbation attitude H_p includes the same sensitivity to the Euler angles with V_z as the velocity command system,

$$\Delta\underline{y} = \left[\begin{array}{c|c|c} 0 & 0 & I \\ (3\times3) & (3\times3) & (3\times3) \\ \hline H_B^E & 0 & -H_B^E\tilde{v}_B L_B \\ (1\times3) & (1\times3) & (1\times3) \end{array}\right] \Delta\underline{x} \qquad (3.1\text{-}7)$$

The design models given by Eqs. 3.1-1 and 3.1-2 are linear and time-invariant, but the dynamics of the helicopter change a great deal during the course of a typical flight; therefore, it is necessary to specify F, G, and H_p at enough flight conditions to characterize the helicopter's flight envelope. A constant-coefficient control law is computed at each condition, and the resulting control gains are scheduled (with flight conditions) for on-board implementation. In the current case, the helicopter model has been defined at 28

flight conditions representing the following range of flight variables:

Forward airspeed: 0 to 82 m/s (160 kt)

Climb rate: 2.5 to -5.1 m/s (+500 to -1000 fpm)

Turn rate: 0 to ± 0.1 rad/sec

Working points for control system design are shown in Fig. 3.1-1; they are clustered in the vicinity of level flight and the spiral descent approach maneuver.

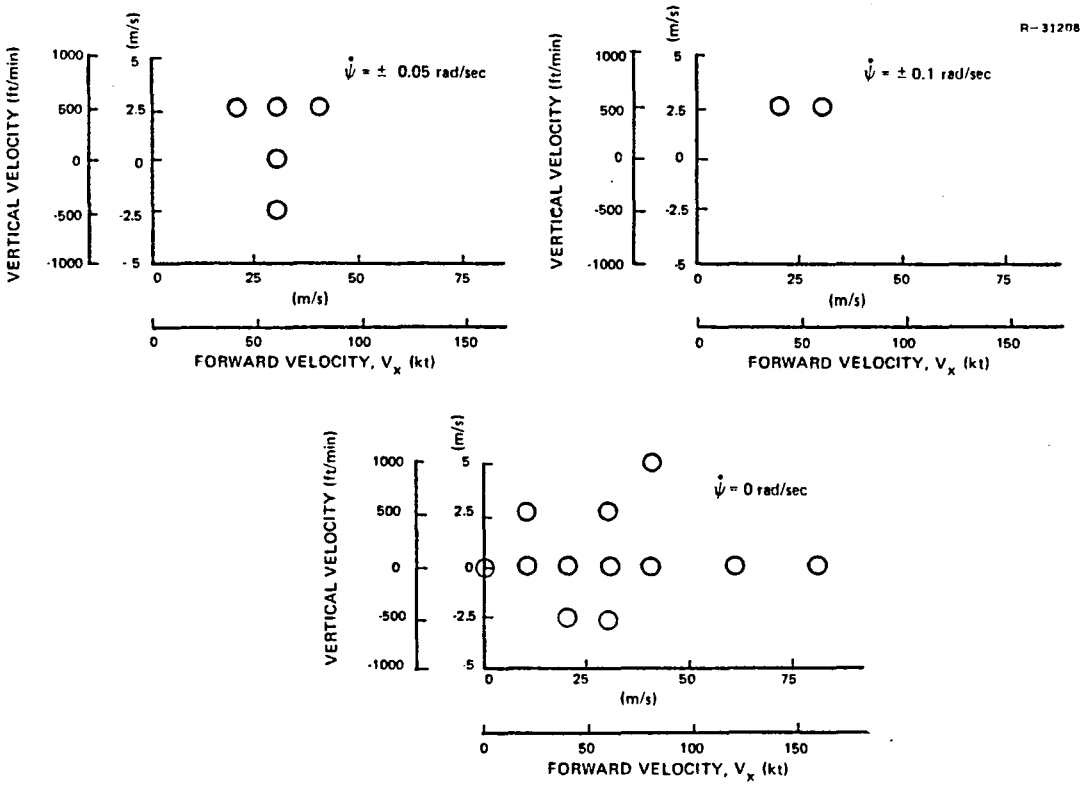

Figure 3.1-1 Design Points for Control System Design

The control system is to operate digitally, hence a control and measurement sampling interval must be specified. To minimize computational burden, it is desirable for the control sampling interval to be as long as possible; however, between control commands, the helicopter is running "open-loop", i.e., errors between the desired and actual states of the craft (Eq. 3.1-1) can build up. This suggests a criterion for selecting the sampling inverval: choose the interval so that error buildup is limited to acceptable values under "worst case" conditions (Ref. 15).

For the VALT DFCS, the "worst case" (from an error propagation viewpoint) is hover in heavy turbulence, and the error buildup is assumed to be described by propagating the covariance of the perturbation state error, X (Ref. 16).* For turbulence with an rms value of 6 m/s (20 fps) and a correlation time of 1 sec, an error buildup interval of 0.16 sec was found to be allowable at hover. The bounds for the acceptable values are taken to be 0.5 deg for angles, 5 deg/sec for angular rates, and 2 fps for translational velocities. Lateral velocity reached its bounding value at hover. The low-pass filter in the PIF control law delays feedback information by one sampling interval; hence two intervals could occur before the controller opposes error buildup, suggesting a sampling interval of 0.08 sec (or a sampling rate of about 12 frames per sec). The VALT computer is being programmed for frame rates that are multiples of 10. Consequently, a control sampling interval of 0.1 sec has been chosen for the VALT DFCS.

*The state covariance is defined as the expected value of the products of states, i.e., $X = E(\Delta\underline{x}\Delta\underline{x}^T)$; and it is propagated using the differential equation, $\dot{X} = FX+XF^T+W$, where W is the disturbance covariance matrix.

The spiral descent is one of two reference trajectories used in the DFCS design, the other being the approach trajectory. Both are composed primarily of straight lines and circular arcs in the horizontal plane and use a constant-heading decelerating descent in the final trajectory segment.

The approach trajectory is shown in Fig. 3.1-2. The airspeed and altitude throughout most of the trajectory is 33.5 m/s (65 kt) and 152.4 m (500 ft), respectively. The final portion of the trajectory involves a ($\dot{\gamma}>0$) decelerating descent that exhibits desirable characteristics from the pilot's viewpoint, as discussed in Refs. 17 and 18. The constant speed descent is designed so that the decelerating descent can commence at 76.3 m (250 ft) altitude, 784 m (1800 ft) south of the landing point. The speed and descent rate to be followed are taken from Refs. 17 and 18 and are

$$\dot{x}_E = k\, e^{-(x/c)^n} \qquad (3.1\text{-}8)$$

$$\dot{z}_E = a\left(1-\sqrt{b/(x+b)}\right)\dot{x}_E \qquad (3.1\text{-}9)$$

where k = 59.3 m/s (194.4 fps), c = 250.0 m (821.0 ft), n = -0.455, a = 0.149, and b = 116.0 m (381.0 ft).

The spiral descent trajectory is composed primarily of a steady turn during a constant vertical velocity descent. This maneuver is designed to allow descent in a geographically limited area. Figure 3.1-3 depicts the horizontal plane trajectory of the spiral descent. The horizontal speed is 31 m/s (60 kt) and the descent rate is 2.54 m/s (500 fps). The last segment, starting at z = -76.3m (250 ft), uses the same descent trajectory shown in Eqs. 3.1-8 and 3.1-9.

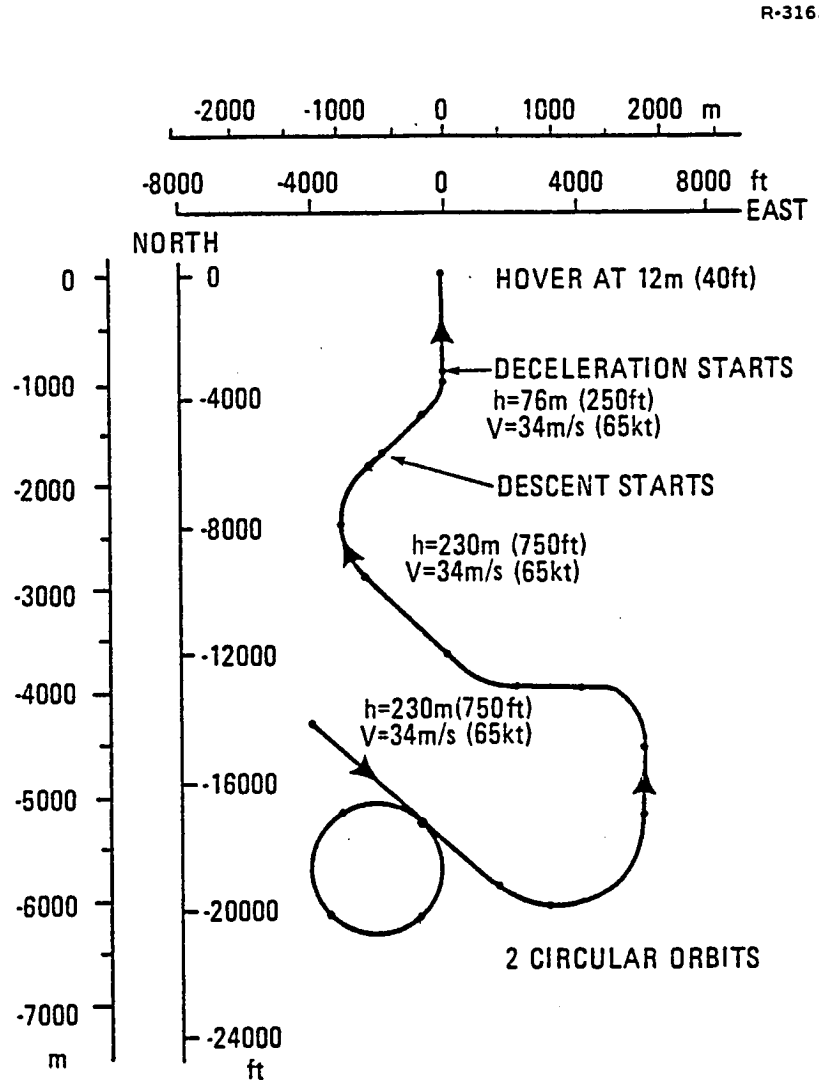

Figure 3.1-2 Approach Trajectory in the Horizontal Plane

The touchdown point of each trajectory is at the origin of the earth-fixed reference frame used in the DFCS design model. The x, y, and z axes are oriented along the north, east, and down directions, respectively. The touchdown locations depend on the type of navigational equipment used and are shown in Figs. 3.2-1 and 3.2-3. The earth-fixed frame is assumed to be stationary in inertial space on a flat non-rotating earth.

Three other reference frames are important in the aircraft design model; they are the body-fixed, the local-level-guidance, and the local-level-body reference frames. The body-fixed reference frame is the coordinate system of the nine rigid-body vehicle states. The body-axes system has its origin at the body center of gravity (cg), with the x-axis forward, the y-axis to the right and the z-axis down. The x-z body axis plane is chosen to be the body plane of symmetry. The earth-fixed frame is rotated into the body frame by the Euler angles yaw (ψ), pitch (θ) and roll (ϕ) using the transformation matrix H_E^B.

The two other reference frames used in DFCS design are encountered in guidance implementation. Both have origins at the vehicle cg and are local-level frames (i.e., their x-y planes are parallel to the earth-fixed frame). The local-level-guidance reference frame has the x-axes yawed relative to the earth-fixed frame by the helicopter ground relative heading angle. The local-level-body reference frame is yawed by the commanded helicopter body yaw angle. If the helicopter yaw angle is commanded to match the ground relative heading angle, the two local-level frames are the same.

The velocities and positions encountered in the approach trajectory are used to determine the design points for the velocity filters. The two terminal area velocity filter design points are shown in Tables 3.1-1 and 3.1-2. A third velocity filter which does not use position information from the ground uses the design points shown in Table 3.1-3.

The design models for the filters in the DFCS use total values for the helicopter states. The design model dynamics are discrete versions of the random walk process,

$$\dot{x}(t) = w(t) \qquad (3.1\text{-}10)$$

and the first-order Markov process,

$$\frac{1}{\tau}\,\dot{x}(t) = x(t) + w(t) \qquad (3.1\text{-}11)$$

where w(t) is white Gaussian noise and τ is the associated time constant. Integrations of the processes are also used as states in the filter design models.

TABLE 3.1-1
VELOCITY-POSITION DESIGN POINTS FOR THE MICROWAVE LANDING SYSTEM FILTER DESIGN

x_E (m)	y_E (m)	z_E (m)	V_x (m/s)	V_y (m/s)	V_z (m/s)
18532.0	0	229.0	33.5	0	0
13900.0	0	457.0	61.0	0	0
9266.0	0	229.0	33.5	0	0
6949.0	0	914.0	45.7	0	5.06
4633.0	0	229.0	33.5	0	0
3475.0	0	457.0	61.0	0	0
2316.0	0	229.0	33.5	0	0
1158.0	0	169.0	33.5	0	2.54
762.0	0	137.0	33.5	0	2.54
610.0	0	125.0	29.0	0	2.54
457.0	0	113.0	23.5	0	2.54
244.0	0	84.1	16.2	0	2.54
122.0	0	49.7	10.5	0	2.54
30.5	0	23.8	2.62	0	2.54
15.2	0	15.2	1.31	0	0

TABLE 3.1-2

VELOCITY-POSITION DESIGN POINTS FOR THE MULTILATERATION LANDING SYSTEM FILTER DESIGN

x_E (m)	y_E (m)	z_E (m)	V_x (m/s)	V_y (m/s)	V_Z (m/s)
3706.0	0	229.0	33.5	0	0
2768.0	0	610.0	61.0	0	0
2316.0	0	229.0	33.5	0	0
1737.0	0	305.0	45.7	0	5.06
1158.0	0	169.0	33.5	0	2.54
914.0	0	149.0	33.5	0	2.54
762.0	0	137.0	33.5	0	2.54
610.0	0	125.0	29.0	0	2.54
457.0	0	113.0	23.5	0	2.54
305.0	0	102.0	18.3	0	2.54
244.0	0	84.1	16.2	0	2.54
122.0	0	49.7	10.5	0	2.54
30.5	0	23.8	2.62	0	2.54
15.2	0	15.2	1.31	0	0

TABLE 3.1-3

VELOCITY-POSITION DESIGN POINTS FOR THE ENROUTE FILTER DESIGN

x_E	y_E	z_E	V_x	V_y	V_z
18532.0	0	229.0	33.5	0	0
18532.0	0	305.0	76.2	0	0
18532.0	0	610.0	33.5	0	0
18532.0	0	914.0	33.5	0	5.06
18532.0	0	229.0	41.1	0	0
18532.0	0	229.0	51.5	0	0
18532.0	0	229.0	61.9	0	0
18532.0	0	457.0	41.1	0	2.54
18532.0	0	457.0	25.8	0	2.54
18532.0	0	274.0	71.9	0	2.54

Sensor bias and wind states are modeled in the filter designs as uncoupled first-order Markov processes. Standard deviations of the states and time constants used in the models are shown in Table 3.1-4. These parameters are obtained from Refs. 19 to 21. The difference between the wind models reflect the difference in coverage area of the landing aids. Multilateration will be available only within the last 3700 m before touchdown and should encounter wider wind variations during the time wind is estimated. A more detailed description of the sensors is presented in the next section.

TABLE 3.1-4
BIAS AND WIND FIRST-ORDER MARKOV MODELS

ESTIMATED STATE	TIME CONSTANT, τ SEC	STANDARD DEVIATION
Accelerometer Bias	100.0	0.8 ft/sec^2
Microwave Landing System Wind	30.0	2.29 m/sec
Multilateration Landing System Wind	30.0	9.14 m/sec

3.2 SENSORS AND ACTUATORS

The VALT Research Aircraft sensors are assumed to consist of three accelerometers, three angular rate gyros, one vertical gyro, one gyromagnetic compass, a barometric altimeter, a pitot tube measuring dynamic pressure, a ground-based microwave landing system (MLS) and a ground-based multilateration system (TRI). The sensors' dynamic models, locations with respect to the vehicle center of gravity, and measurement ranges are shown in Table 3.2-1.

TABLE 3.2-1

SENSORS FOR VALT RESEARCH AIRCRAFT FILTER SYSTEM DESIGN

SENSOR	DYNAMIC MODEL	LOCATION WITH RESPECT TO C.G. x(in) (m)	y(in) (m)	z(in) (m)	RANGE
Accelerometer (3)	$\frac{1}{0.005s+1} \approx 1$	10 (0.254)	0 (0)	-20 (-0.508)	±4.9 m/sec^2 (±0.5g)
Angular Rate Gyro (3)	$\frac{(100)^2}{s^2+2(0.65)(100)s+(100)^2}$	-110 (-2.8)	20 (0.508)	30 (0.762)	±28.6 deg/sec(±0.5 rad/sec)
Vertical Gyro:	1	-110 (2.8)	20 (0.508)	30 (0.762)	
Pitch					±30 deg (±0.52 rad)
Roll					±45 deg (±0.78 rad)
Gyromagnetic Compass	$\frac{(100)^2}{s^2+2(0.65)(100)s+(100)^2}$	Not Specified			0 to 360 deg (0 to 6.28 rad)
Barometric Altimeter	$\frac{1}{0.07s+1}$	Pressure Ports at 280 (7.11)	40 (1.016)	-10 (-0.254)	0 to 1524 m (0 to 5000 ft)
Calibrated Airspeed	$\frac{1}{0.025s+1}$	Aircraft Nose			25.74 m/sec to 103 m/sec (50 to 200 kt)
Microwave Landing System (MLS):	1	Does Not Apply			
Azimuth					±60 deg (±1.05 rad)
Elevation					0 to 20 deg (0 to 0.349 rad)
DME					18532 m (10 nm)
Multilateration Landing System	1	Does Not Apply			3710 m (2 nm)

The three accelerometers aid in determining the vehicle accelerations $\dot{u}$, $\dot{v}$, and $\dot{w}$. The relationship between the high bandwidth accelerometer outputs and the vehicle accelerations are derived in Appendix A. The three rate gyros measure the body angular rates, p, q, and r. A second-order gyro model is adequate for the average range of the gyro parameters.

The two-degree-of-freedom vertical gyro measures the sine and cosine of the body Euler angles, θ and ϕ. It is slaved to the apparent vertical using electrolytic (bubble) levels for sensing gravity. When the roll angle exceeds 9 deg, the erection mechanism cuts off, and the gyro is free to drift at a randomly varying rate. The heading Euler angle, ψ, is obtained from a gyro magnetic compass set. The gyro magnetic compass is a directional gyro slaved to the earth's magnetic field with a magnetic sensor. The gyro can also be operated in the free mode for high latitude operations, which are not considered here.

Indicated airspeed (IAS) obtained from measuring dynamic pressure with a pitot tube gives an approximate measurement of total body air-relative velocity. IAS is available only above 25.74 m/s (50 kt), as rotor downdraft and low dynamic pressure disrupt the measurement at lower speeds. In compressible subsonic flow, the total pressure, p_T, is (Ref. 22) represented by

$$p_T = p_s \left[1 + \left(\frac{\eta-1}{\eta}\right) \left(\frac{\rho}{2p_s}\right) TAS^2\right]^{\frac{\eta}{\eta-1}} \qquad (3.2\text{-}1)$$

where η is the specific heat ratio of air (=1.4), TAS is the true air-relative velocity of the vehicle, ρ, is the free-stream air density, and p_s is static pressure. At low speeds and low altitudes Eq. 3.2-1 reduces to

$$\bar{q} = p_T - p_s = \rho_{SL} \frac{IAS^2}{2} \qquad (3.2\text{-}2)$$

where $\bar{q}$ is the dynamic pressure and ρ_{SL} is the air density at sea level. The velocity in Eq. 3.2-2 is,

$$IAS = \sqrt{\frac{2\bar{q}}{\rho_{SL}}} \tag{3.2-3}$$

where IAS is indicated airspeed. Various corrections can be applied to Eq. 3.2-3, such as static defect and known instrument errors, to produce calibrated airspeed (CAS). The static defect is the difference between the pressure on the aircraft's skin and the free-stream pressure at a particular location; it depends on speed, angle of attack, and altitude. For the low-velocity, low-altitude operations of the VALT Research Aircraft, Eq. 3.2-3 is considered to be an adequate measure of true airspeed. If significant air density variations are expected, however, Eq. 3.2-3 should be modified appropriately.

Position information about the aircraft is available from a barometric altimeter, a multilateration system, and a MLS. A diagram of the proposed MLS geometry is shown in Fig. 3.2-1. The MLS provides range from the Distance Measuring Equipment (DME) and azimuth from equipment located at the rear of the runway, while elevation is measured with equipment near the beginning of the runway. The positions of the equipment and vehicle with respect to the origin at touchdown point are given by

$$\underline{R}_a^T = (x_a, y_a, z_a) \tag{3.2-4}$$

$$\underline{R}_\varepsilon^T = (x_\varepsilon, y_\varepsilon, z_\varepsilon) \tag{3.2-5}$$

$$\underline{x}_E^T = (x_E, y_E, z_E) \tag{3.2-6}$$

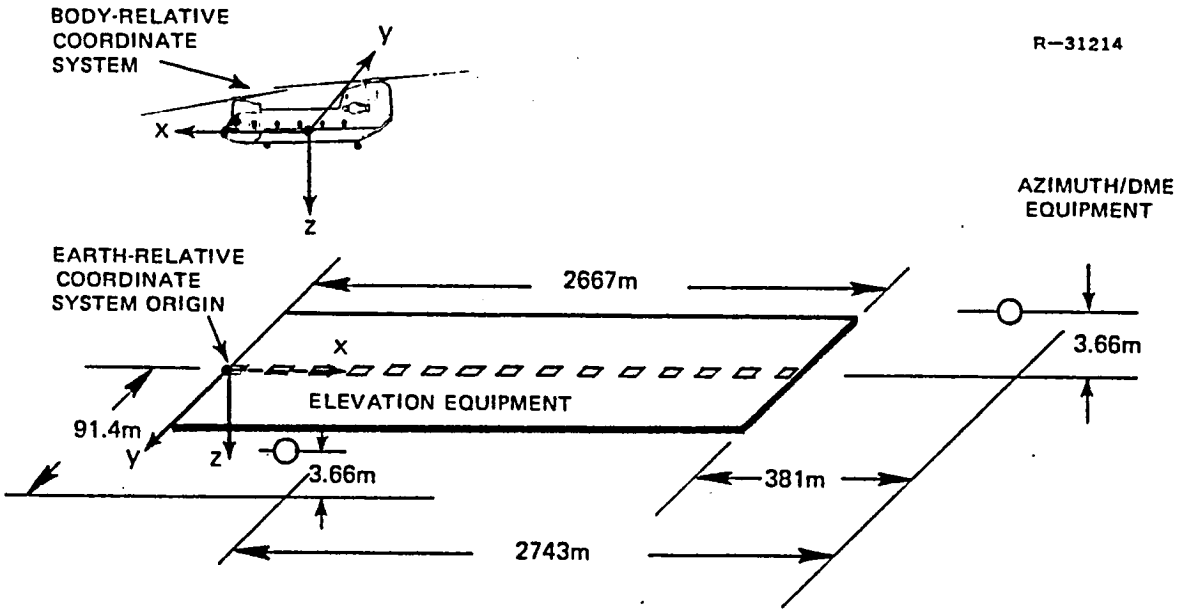

Figure 3.2-1 Coordinate System for Simulated MLS

The relationships between the MLS conical coordinate system measurements, illustrated in Fig. 3.2-2, and vehicle position is given in Table 3.2-2.

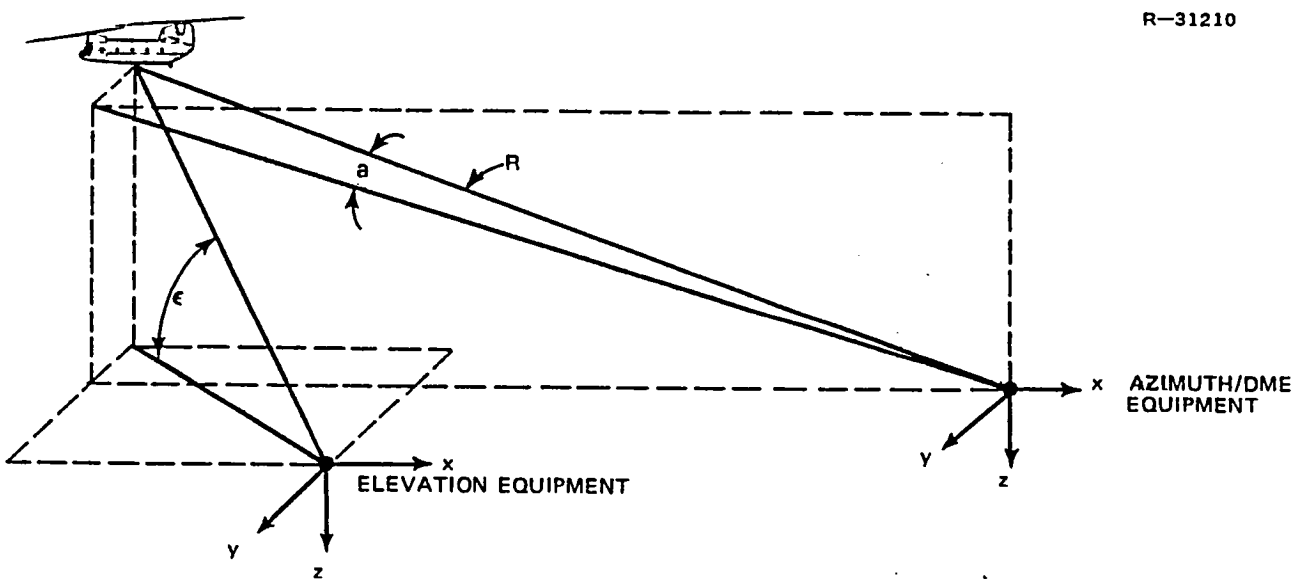

Figure 3.2-2 MLS Conical Coordinate System

TABLE 3.2-2
MLS TRANSFORMATION EQUATIONS

Range	$R = \left((x_E - x_a)^2 + (y_E - y_a)^2 + (z_E - z_a)^2 \right)^{\frac{1}{2}}$
Azimuth	$a = \sin^{-1} \left[\frac{(y_E - y_a)}{R} \right]$
Elevation	$\varepsilon = \tan^{-1} \left[\frac{-(z_E - z_\varepsilon)}{(x_E - x_\varepsilon)^2 + (y_E - y_\varepsilon)^{2\,\frac{1}{2}}} \right]$
Cross Track	$y_E = y_a + R \sin a$
Along Track	$x_E = x_\varepsilon + \frac{(-B) \pm \left[B^2 - 4AC \right]^{\frac{1}{2}}}{2A}$
Vertical	$z_E = z_\varepsilon - \tan \varepsilon \left[(x_E - x_\varepsilon)^2 + (y_E - y_\varepsilon)^2 \right]^{\frac{1}{2}}$
	$A = 1 + \tan^2 \varepsilon$
	$B = 2(x_\varepsilon - x_a)$
	$C = (y_E - y_a)^2 + (x_a - x_\varepsilon)^2 - R^2 + (y_E - y_\varepsilon)^2 \tan^2 \varepsilon$

The MLS has significant range but does not have full 360 deg coverage. To provide highly accurate position and velocity measurements with full coverage during approach and landing, a RF multilateration system is being developed. The system uses an angle-modulated ranging signal to provide both

range and range rate measurements between an aircraft transponder and multiple ground stations. Range and range rate measurements are converted to cartesian coordinate measurements and the coordinate and coordinate rate information is transmitted via an integral data link to the aircraft. The multilateration system considered here employs one transmitter and four receivers at the locations shown in Fig. 3.2-3.

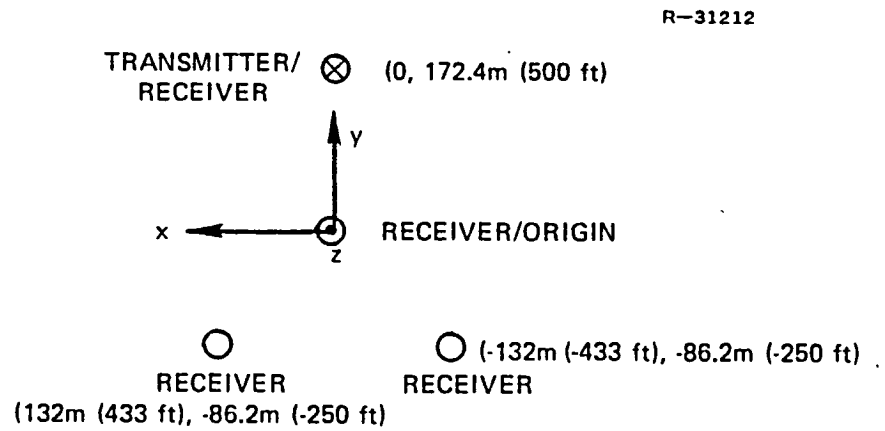

Figure 3.2-3 Multilateration System Receiver Locations

Sensor errors are assumed to be composed of three types; a zero-mean, uncorrelated Gaussian measurement noise, a bias error, and a scale factor error. More extensive models of sensor errors exist but are not included here for simplicity, since they are felt to be second order for this application. Specifying simple models and standard deviations for error sources to be used in a simplified Kalman filter is difficult (Ref. 16). Other difficulties encountered include the discrepancy between bench test results from manufacturers and in-flight testing (Ref. 23). The sensor error models used here should be considered design aids and are not presumed to be exact sensor descriptions.

The measurement noise standard deviations assumed for the sensors are given in Table 3.2-3, the bias standard deviations are given in Table 3.2-4, and the scale factor standard deviations are given in Table 3.2-5. Sensor error model parameter information are obtained from NASA Langley (Ref. 24).

TABLE 3.2-3

MEASUREMENT NOISE CHARACTERISTICS OF THE VALT RESEARCH AIRCRAFT SENSORS

SENSOR	STANDARD DEVIATION*
Angular Rate Gyro	0.167 deg/sec
Attitude Gyro	0.167 deg
Heading Gyro	1.0 deg
Accelerometer	0.61 m/s^2 (2.0 fps^2)
Calibrated Airspeed	0.515 m/s (1.69 fps)
Sideslip	0.5 deg
Barometric Altimeter	7.62 m (25 ft)
MLS Azimuth	$\frac{0.0847}{\left(\frac{R_a}{1852} + 9.396\right)} + \frac{0.0095}{1852} R_a$ deg
MLS Elevation	$\frac{0.0153}{\left(\frac{R_\varepsilon}{1852} + 1.694\right)} + \frac{0.0053}{1852} R_a$ deg
MLS Range	4.88 m (16 ft)
TRI x_E	$(0.274 + 2.61(10^{-3})\ R_r)$m
TRI y_E	$(0.579 + 2.61(10^{-3})\ R_r)$m
TRI z_E	$(0.128\ R_r - 19.56)$ m for $R_r \geq 171$ m; 2.33 m for $R_r < 171$ m
TRI V_x	$(1.66(10^{-4})\ R_r + 0.0305)$ m/s
TRI V_y	$(1.66(10^{-4})\ R_r + 0.0305)$ m/s
TRI V_z	$(3.85(10^{-2})\ R_r - 3.93)$ m/s for $R_r > 114$ m; 0.46 m/s for $R_r \leq 114$ m

*R_a is the range to the azimuth equipment. R_ε is the range to the elevation equipment. R_r is the range to the center multilateration receiver.

TABLE 3.2-4

BIAS CHARACTERISTICS OF THE
VALT RESEARCH AIRCRAFT SENSORS

SENSOR	STANDARD DEVIATION
Angular Rate Gyro	0.3 deg/sec
Attitude Gyro	0.333 (10^{-2}) deg/sec
Heading Gyro	0.764 (10^{-2}) deg/sec
Accelerometer	0.244 m/s^2 (0.8 fps^2)
Calibrated Airspeed	0.152 m/s (0.5 fps)
Sideslip	unknown
Barometric Altimeter	30.48 m (100 ft)
MLS Azimuth	0.012 deg
MLS Elevation	0.011 deg
MLS Range	4.88 m (16 ft)
TRI x_E	-
TRI y_E	- estimated on ground
TRI z_E	-
TRI V_x	-
TRI V_y	-
TRI V_z	-

Other sensor references reviewed for error model consistency are the Space Shuttle navigation system (Ref. 25), the J-Tec velocity sensor (Ref. 26), the multilateration system (Ref. 27), the VALT Research Aircraft (Ref. 28), and a report on helicopter instrument errors (Ref. 29).

A schematic of the different actuators which interface the VALT NGC system and the cockpit controls, with the rotor blade incidence, is shown in Fig. 3.2-4. Pilot commands enter the mechanical system through the lower-boost hydraulic

TABLE 3.2-5

SCALE FACTOR CHARACTERISTICS OF THE VALT RESEARCH AIRCRAFT SENSORS

SENSOR	STANDARD DEVIATION
Angular Rate Gyro	0.02
Attitude Gyro	-
Heading Gyro	-
Accelerometer	0.00025
Calibrated Airspeed	0.005
Sideslip	unknown
Barometric Altimeter	0.03
MLS Azimuth	-
MLS Elevation	-
MLS Range	-
TRI x_E	-
TRI y_E	-
TRI z_E	-
TRI V_x	-
TRI V_y	-
TRI V_z	-

actuators, which are physically located near the cockpit. VALT computer commands drive the same actuators used in the TAGS (Ref. 30), and the TAGS actuator outputs drive the lower-boost actuators. Operational SAS inputs are in series with the lower-boost outputs. The combined signals are mixed before commanding the upper-boost actuators that drive the two rotor swash plates which control blade incidence. There is a SAS cancelling system which is activated when the VALT computer commands are operational.

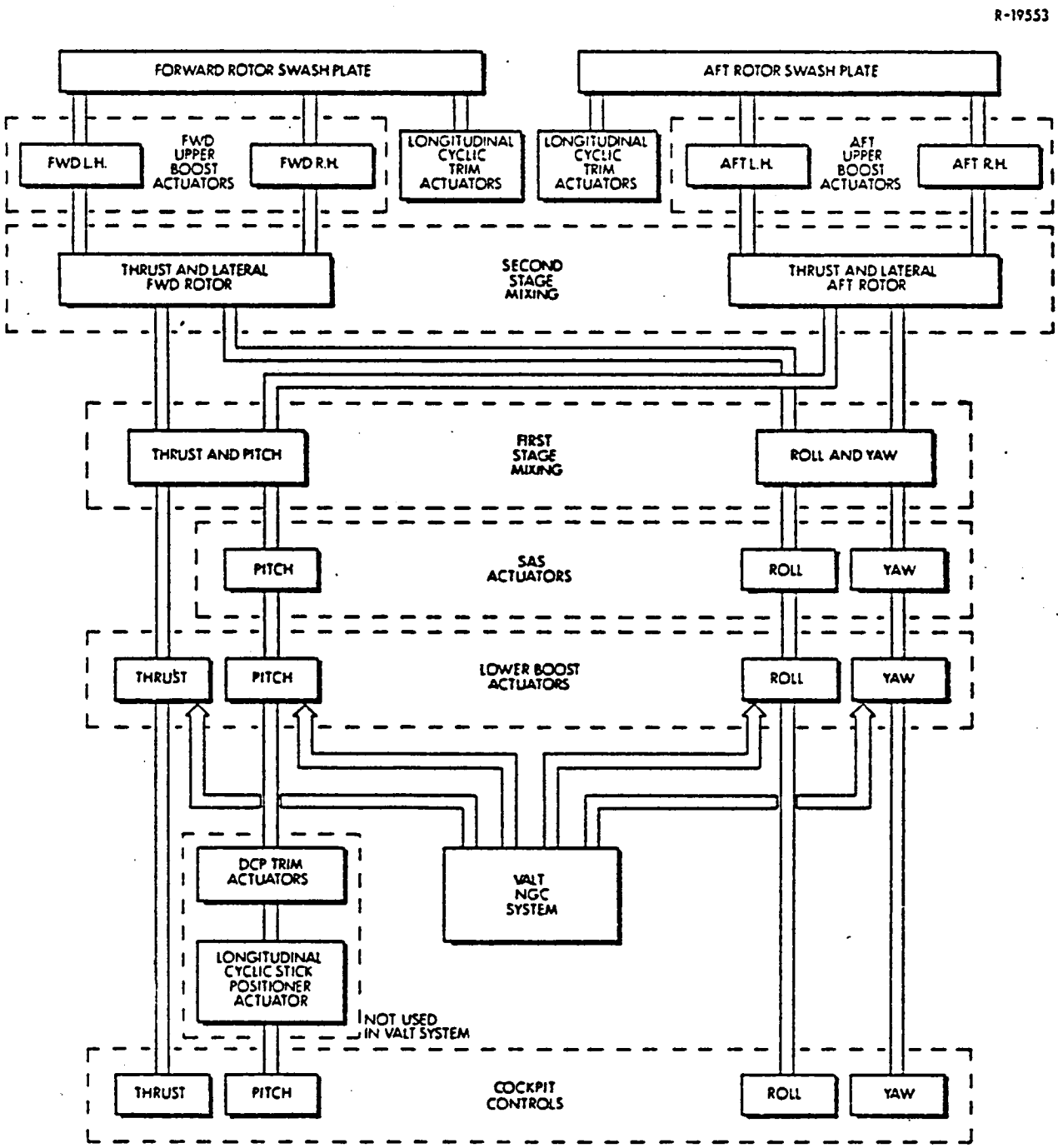

Figure 3.2-4 Elements of the VALT Research Aircraft Control System

The mathematical models used for the actuators are shown in Fig. 3.2-5. Each TAGS actuator has a time constant of 0.0125 sec and a rate limit of ± 3 in/sec. The gang collective actuator, δ_C, is position limited to +4.0 in while the other controls have displacement limits of ± 2.0 in. Rotor dynamic response is modeled as a second-order system with a natural frequency of 24 rad/sec and a damping ratio of 0.6.

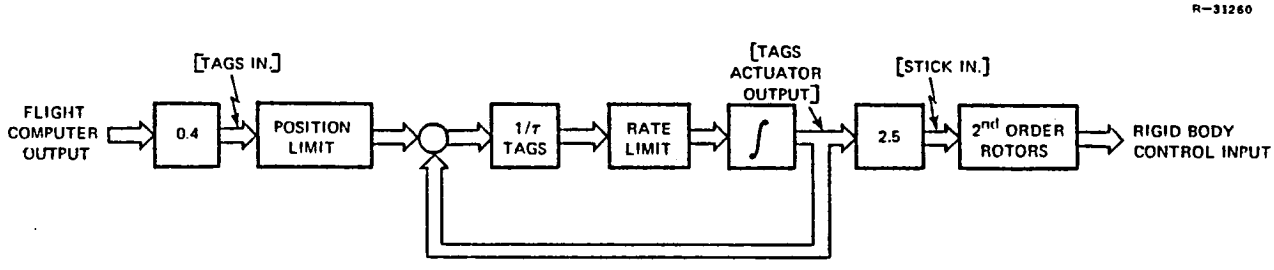

Figure 3.2-5 VALT Research Aircraft Actuator Model

3.3 STATE ESTIMATORS

This section presents the state estimator algorithms that combine different sensors to estimate vehicle angular rate (p, q, r), vehicle angular position (ϕ, θ, ψ), vehicle velocity (u, v, w), and vehicle position (x_E, y_E, z_E). The states p, q, r, ϕ, θ, ψ, u, v, w are required for feedback in the control laws; ϕ, θ, ψ, V_z and V_x, V_y, V_z, ψ are required to construct the command error and x_E, y_E, z_E are used by guidance to correct for position errors.

Optimal estimates of the states could be obtained using a full-state Kalman filter (Ref. 16); however, such a filter is overly complex for this application. If all states and some state rates are measured, and if the measurement noise is less than the "process noise" (consisting of random

inputs and system uncertainties), the Kalman filter can effectively decouple into a bank of reduced-order Kalman filters. These conditions are satisfied in the VALT Research Aircraft (Ref. 1). The reduced-order Kalman filters can be designed by partitioning and decoupling the system model into random walk processes, markov processes and integrations of these process states. The resulting filters are found to be analogous to low-pass and complementary filters, both of which are used extensively in conventional aircraft systems.

By applying the partitioning procedure described in the next section, three uncoupled filters result; the angular rate filter, the angular position filter and the velocity-position filters. Each of these are described in the following sections.

3.3.1 Filter Partitioning

Partitioning is desirable for simplicity of design and computation. Partitioned filters are derived by modeling the dynamics of each state variable that is not a pure integration of other state variables as a random-walk or markov process driven by disturbance noise which, in some cases, has special correlation with the measurement noise. If an aircraft state and all its derivatives are available at a point in time, then the future value of the state for small intervals can be written using the Taylor series expansion as

$$\underline{x}_{k+1} = \underline{x}_k + \Delta t \dot{\underline{x}}_k + \frac{\Delta t^2}{2} \ddot{\underline{x}}_k + \ldots + L(\underline{w}_k) \qquad (3.3\text{-}1)$$

where $L(\underline{w}_k)$ is the nonlinear forcing function of the disturbances. If the derivatives of high order terms are sufficiently small, they can be combined with $L(\underline{w}_k)$ into a redefined

"process noise" input, $\underline{w}'_k$, which is assumed to be Gaussian white noise. Using the new process noise for the twelve rigid body states of the helicopter, we have,

$$\underline{x}_{E_{k+1}} = \underline{x}_{E_k} + \Delta t \left[H^E_{B_k} \underline{v}_{B_k} \right] + \frac{\Delta t^2}{2} \left[H^E_{B_k} \dot{\underline{v}}_{B_k} + H^E_{B_k} \tilde{\omega}^E_{B_k} \underline{v}_{B_k} \right] + \frac{\Delta t^3}{6} w'_{x_k} \tag{3.3-2}$$

$$\underline{v}_{B_{k+1}} = \underline{v}_{B_k} + \Delta t \, \dot{\underline{v}}_{B_k} + \frac{\Delta t^2}{2} \underline{w}'_{v_k} \tag{3.3-3}$$

$$\underline{v}_{E_{k+1}} = \underline{v}_{E_k} + \Delta t \, L_B^{-1} \, \underline{\omega}^E_{B_k} + \frac{\Delta t^2}{2} \underline{w}'_{v_k} \tag{3.3-4}$$

$$\underline{\omega}^E_{B_{k+1}} = \underline{\omega}^E_{B_k} + \Delta t \underline{w}'_{\omega_k} \tag{3.3-5}$$

The (3×1) vectors $\underline{x}_E$ and $\underline{v}_B$ are vehicle position and velocity shown in Eqs. 3.2-6 and A-39, respectively, while $\underline{v}_E$ is the (3×1) vector containing the Euler angles (ϕ, θ, ψ) and $\underline{\omega}^E_B$ is the (3×1) vector for the body angular rates (p, q, r). The transformation matrix from body angular rates to Euler rates, L_B^{-1}, is defined in Eq. 3.3-16 while the body to earth relative transformation matrix, H^E_B, is defined in Eq. A-42.

The derivatives of the states retained are influenced by the available sensors for the vehicle. Equations 3.3-2 to 3.3-5 will be the propagation equation in the filters. To specify the models for design, however, derivatives are again included in the process noise, but cause some elements in the new process noise, $\underline{w}''_k$, and some elements in the observation noise, $\underline{v}_k$, to be correlated, i.e.,

$$\underline{x}_{k+1} = \underline{x}_k + \underline{w}''_k \tag{3.3-6}$$

$$\underline{z}_k = H\underline{x}_k + \underline{v}_k \tag{3.3-7}$$

$$E\left\{\underline{w}''_k \ \underline{v}_k^T\right\} = \Xi \tag{3.3-8}$$

Similar reasoning can be used with the rigid-body perturbation dynamics and the state transition matrix in partitioning the filter model, as shown in Ref. 2. Equations 3.3-6 to 3.3-8 are, of course, simplifications; greater detail on filter design and filter gain construction is given in Appendix A.

3.3.2 Angular Rate Filters and Aliasing

The three angular rate filters have similar derivations, hence, only the roll rate filter is derived in this section. The roll rate dynamic model for filter design discussed in the previous section is,

$$p_{k+1} = p_k + \Delta t w_k \tag{3.3-9}$$

with the roll rate gyro observations,

$$p_{m_k} = p_k + v_k \tag{3.3-10}$$

where, in this case, w_k and v_k are not correlated. Using results in Appendix A.2, the steady-state Kalman filter for the angular rate random walk model becomes

$$\hat{p}_k(+) = \hat{p}_k(-) + K\left[p_{m_k} - \hat{p}_k(-)\right] \tag{3.3-11}$$

$$\hat{p}_{k+1}(-) = \hat{p}_k(+) \tag{3.3-12}$$

where

$$K = \frac{2}{1 + \left(1 + \frac{4\Upsilon_p}{\Delta t^2 \chi_p}\right)^{\frac{1}{2}}} \qquad (3.3\text{-}13)$$

Since the process noise represents an incremental roll rate, it can be related to roll acceleration by dividing by the sample period. The process noise covariance, χ_p, is chosen by assuming the maximum roll acceleration which is typically encountered in flight is a $2\sigma_w$ value. Using the rate gyro measurement noise covariance in Table 3.2-3 for Υ_p, the angular rate filter gains are constant and shown in Table D-21.

The high bandwidth of the angular rate filters (which primarily provide smoothing of the rate gyro signals) is common in aircraft control applications where, in many cases, only analog prefilters are used (Ref. 30). (Analog filters are not permitted in the VALT DFCS design.) The purpose of the analog prefilter is to suppress high frequency noise, and reduce aliasing errors, prior to sampling the measurements at the primary control sampling rate. Aliasing errors occur when high frequency noise is folded to low frequencies because of sampling.

The sampling interval of the TAGS controller was changed from 20 frames per second to 18.5 frames per second and this reduced aliasing errors caused by rotor vibration picked up by body mounted rate sensors. The 3-per-rev and 6-per-rev rotor vibration noise power peaks are evident in the measured Power Spectral Density (PSD) of the pitch rate sensor shown in Fig. 3.3-1. This figure is taken from Ref. 31 which analyzed the CH-46C (a smaller, lighter aircraft than the VALT Research Aircraft). The 10 to 12 Hz power spike could be particularly troublesome for a sampling rate of 10 Hz. This

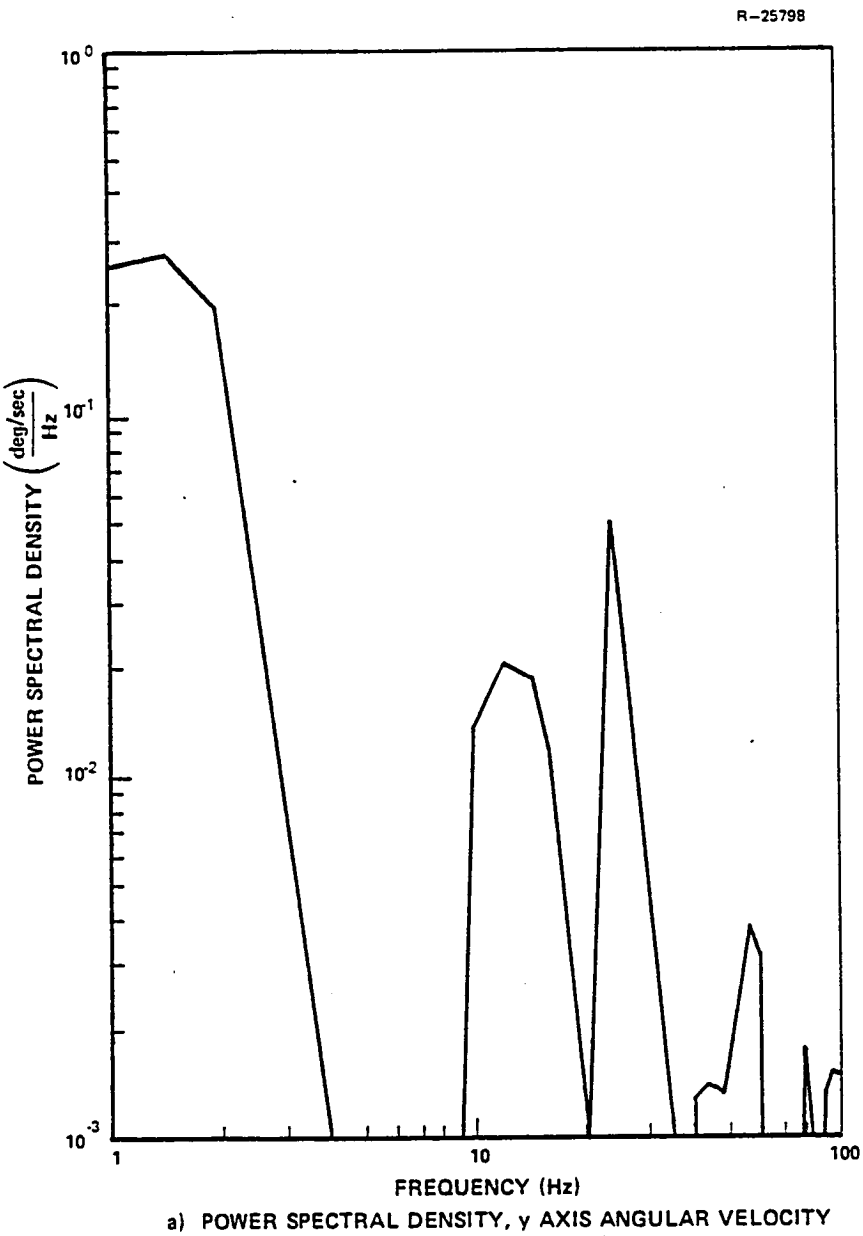

Figure 3.3-1 Power Spectral Density for the CH-46C Helicopter y-axis Angular Velocity Measurement

problem exists for the other rate gyros and for the accelerometers. Correcting for aliasing errors in the VALT DFCS is not considered part of the DFCS design but is recognized as a potential problem for which many solutions are possible.

3.3.3 Angular Position Filters

The angular position filter is a Kalman filter in which the system dynamics are represented by a scalar random walk with correlated observation and process noise. The resulting algorithm is called a complementary filter and is derived in Section A.3. The roll angle filter is discussed as an example in this section.

The angular position filters complement vertical and heading gyro signals with rate gyro signals to estimate the Euler angles and are of the form

$$\hat{\phi}_k(+) = \hat{\phi}_k(-) + cK\left[\phi_{m_k} - \hat{\phi}_k(-)\right] \tag{3.3-14}$$

$$\hat{\phi}_{k+1}(-) = \hat{\phi}_k(+) + D\,\dot{\phi}_k \tag{3.3-15}$$

The body-referenced rate estimates are transformed to earth-relative coordinates for incorporation in the angular position filters using the equation

$$\begin{bmatrix} \hat{\dot{\phi}}_{k-1} \\ \hat{\dot{\theta}}_{k-1} \\ \hat{\dot{\psi}}_{k-1} \end{bmatrix} = \begin{bmatrix} 1 & \sin\hat{\phi}_{k-1}(+)\tan\hat{\theta}_{k-1}(+) & \cos\hat{\phi}_{k-1}(+)\tan\hat{\theta}_{k-1}(+) \\ 0 & \cos\hat{\phi}_{k-1}(+) & -\sin\hat{\phi}_{k-1}(+) \\ 0 & \sin\hat{\phi}_{k-1}(+)\sec\hat{\theta}_{k-1}(+) & \cos\hat{\phi}_{k-1}(+)\sec\hat{\theta}_{k-1}(+) \end{bmatrix} \begin{bmatrix} \hat{p}_{k-1}(+) \\ \hat{q}_{k-1}(+) \\ \hat{r}_{k-1}(+) \end{bmatrix} \tag{3.3-16}$$

The constant c in Eq. 3.4-14 reflects the decreasing value of the attitude measurement (θ and ϕ only) when the attitude gyro erection mechanism cuts off. When the gyro drifts, the measurement is assumed to be

$$\phi_m(t) = \phi(t) + \varepsilon t + v(t) \tag{3.3-17}$$

where εt is the gyro drift which is absent when the gyro is slaved.

The process noise covariance for the angular position filters is chosen by assuming the maximum angular rate typically encountered in flight is a $2\sigma_w$ value. The angular position filter gains are computed using Eqs. A-34 and A-35 and are listed in Table D-22. The angular rate observation noise covariance in Table D-22 is the root-sum-square of the observation noise, bias, and scale factor at a nominal angular rate of change of 20 deg/sec. The attenuation factor, c, is scheduled by fitting a function to

$$c = K_k/K \tag{3.3-18}$$

where K_k is the decreasing Kalman filter angular position gain resulting from the measurement noise covariance

$$\Upsilon_{\phi_k} = \Upsilon_\phi + \left[(0.00333)\Delta tk\right]^2 \tag{3.3-19}$$

The resulting curve for c is described by

$$c \approx \frac{1}{1 + (0.0166)\Delta tk} \tag{3.3-20}$$

where k is the number of computation frames since the erection mechanism has cut out. The ψ filter does not require c. The

gain, D, approaches Δt as τ_ϕ increases and is not changed in implementation from the value in Table D-22 during the short time the gyro drifts.

3.3.4 Velocity Position Filters

The velocity position filters for estimating the VALT Research Aircraft's earth-relative velocity and position are divided into three different filters, each designed using two different approaches. The three filters are a result of the different measurements that are available along the route. For true airspeed greater than 25.7 m/s (50 kt), TAS and side slip measurements are available. Barometric altimeter, BA, and accelerometer, $\underline{a}_m$, measurements are always available. The estimator which combines TAS, β, BA, and $\underline{a}_m$ measurements is the Enroute (ER) filter because it operates outside the range of the landing aids. When the landing aid, MLS, is available, it is combined with TAS, β, BA, and $\underline{a}_m$ and results in the second or MLS filter. Finally, when multilateration position and velocity measurements are available, they are combined with TAS, β, BA, and $\underline{a}_m$ to produce the third or TRI filter.

The two approaches to ER, MLS and TRI filter designs are the simple constant gain, complementary filter (CF) version and the more complex, time varying, scheduled gain, extended complementary filter (ECF) version. In the CF approach, all sensor measurements are transformed to a common coordinate system and the results presented in Appendix A.3 are used to produce the filter algorithms. TAS and sideslip are not used in the TRI and MLS complementary filter approaches. In the ECF approach, sensor measurements are processed in convenient coordinates and states are estimated in coordinates natural for feedback control implementation. TAS and sideslip measurements are employed in all ECF designs, which permits wind estimation.

The CF version of each velocity-position filter is considered important because of its simplicity and ease of implementation. A similar continuous-time CF design has successfully been employed in the VALT Research Aircraft (Ref. 28), and the MLS-CF is scheduled to be flight tested. The ECF version of each filter is also potentially desirable because the estimates are more accurate. TVHIS is programmed with the ECF filters, and flight testing of the ECF approach could occur at a later date.

Complementary Filter Designs - The ER-CF operates beyond the range of the VALT landing navigation aids (range > 18.5 km (10nm)) and within the range of the air-data sensors (TAS > 25.7 m/s (50 kt)). Using a first-order random walk model for body x-axis air-relative velocity, u_A, and a first-order markov model for accelerometer bias, we obtain

$$\begin{bmatrix} u_{A_{k+1}} \\ \dot{b}_{u_{k+1}} \end{bmatrix} = \begin{bmatrix} 1 & 0 \\ 0 & e^{-\Delta t/\tau_{\dot{b}_u}} \end{bmatrix} \begin{bmatrix} u_{A_k} \\ \dot{b}_{u_k} \end{bmatrix} + \begin{bmatrix} \Delta t w_{u_k} \\ \Delta t w_{b_k} \end{bmatrix} \qquad (3.3\text{-}21)$$

$$\underline{z}_k = \begin{bmatrix} TAS_{m_k} \\ \dot{u}_{m_k} \end{bmatrix} \cong \begin{bmatrix} 1 & 0 \\ 0 & 1 \end{bmatrix} \begin{bmatrix} u_{A_k} \\ \dot{b}_{u_k} \end{bmatrix} + \begin{bmatrix} v_{u_k} \\ w_{u_k} + v_{u_k} \end{bmatrix}$$

where $\dot{u}_m$ is obtained from the accelerometer output as shown in Eq. 3.3-33. The Kalman filter with correlated process and observation noise (see Appendix A) uses the following equations for estimating u_A and $\dot{b}_u$.

$$\begin{bmatrix} \hat{u}_{A_k}(+) \\ \hat{b}_{\dot{u}_k}(+) \end{bmatrix} = \begin{bmatrix} \hat{u}_{A_k}(-) \\ \hat{b}_{\dot{u}_k}(-) \end{bmatrix} + \begin{bmatrix} K_{uu} & K_{u\dot{u}} \\ K_{bu} & K_{b\dot{u}} \end{bmatrix} \begin{bmatrix} TAS-\hat{u}_{A_k}(-) \\ \dot{u}_{m_k}-\hat{b}_{\dot{u}_k}(-) \end{bmatrix} \qquad (3.3\text{-}22)$$

$$\begin{bmatrix} \hat{u}_{A_{K+1}}(-) \\ \hat{b}_{\dot{u}_{k+1}}(-) \end{bmatrix} = \begin{bmatrix} 1 & 0 \\ 0 & e^{-\Delta t/\tau_{\dot{u}_b}} \end{bmatrix} \begin{bmatrix} \hat{u}_{A_k}(+) \\ \hat{b}_{\dot{u}_k}(+) \end{bmatrix} + \begin{bmatrix} D_{u\dot{u}} \\ 0 \end{bmatrix} \begin{bmatrix} \dot{u}_{m_k}-\hat{b}_{\dot{u}_k}(+) \end{bmatrix} \qquad (3.3\text{-}23)$$

Values for covariances, filter gains and system parameters are shown in Table D-23. The first row in Table D-23 contains the primary design; $K_{u\dot{u}}$ and $K_{b\dot{u}}$ may be neglected in the filter implementations.

The body y-axis air-relative velocity filter is virtually identical to Eqs. 3.3-22 and 3.3-23 and the second row in Table D-23 is used for the primary design gain values. Sideslip and lateral acceleration measurements are used in the filter where

$$v_{A_m} = \sqrt{\hat{u}(+)^2 + \hat{w}(+)^2}\,\tan\beta_m \qquad (3.3\text{-}24)$$

In the filter, v_A, $\dot{v}_m$, v_{A_m}, and $b_{\dot{v}}$ replace u_A, $\dot{u}_m$, TAS, and $b_{\dot{u}}$, respectively.

The ER-CF vertical velocity filter estimates altitude as well as body-axis vertical velocity and accelerometer bias.

The difference between earth and body-relative z-axes velocity is neglected. The model for the dynamics is represented by

$$\begin{bmatrix} z_{E_{k+1}} \\ w_{k+1} \\ b_{\dot{w}_{k+1}} \end{bmatrix} = \begin{bmatrix} 1 & \Delta t & 0 \\ 0 & 1 & 0 \\ 0 & 0 & e^{-\Delta t/\tau_{\dot{w}_b}} \end{bmatrix} \begin{bmatrix} z_{E_k} \\ w_k \\ b_{\dot{w}_k} \end{bmatrix} + \begin{bmatrix} \frac{\Delta t^2}{2} w_{\dot{w}_k} \\ \Delta t w_{\dot{w}_k} \\ w_{b_k} \end{bmatrix} \tag{3.3-25}$$

$$\begin{bmatrix} z_{E_{m_k}} \\ \dot{w}_{m_k} \end{bmatrix} = \begin{bmatrix} 1 & 0 & 0 \\ 0 & 0 & 1 \end{bmatrix} \begin{bmatrix} z_{E_k} \\ w_k \\ b_{\dot{w}_k} \end{bmatrix} + \begin{bmatrix} v_{z_k} \\ w_{\dot{w}_k} + v_{\dot{w}_k} \end{bmatrix} \tag{3.3-26}$$

The 3rd-order filter consists of the update equation

$$\begin{bmatrix} \hat{z}_{E_k}(+) \\ \hat{w}_k(+) \\ \hat{b}_{\dot{w}_k}(+) \end{bmatrix} = \begin{bmatrix} \hat{z}_{E_k}(-) \\ \hat{w}_k(-) \\ \hat{b}_{\dot{w}_k}(-) \end{bmatrix} + \begin{bmatrix} K_{zz} & K_{z\dot{w}} \\ K_{wz} & K_{w\dot{w}} \\ K_{bz} & K_{b\dot{w}} \end{bmatrix} \begin{bmatrix} z_{m_k} - \hat{z}_{E_k}(-) \\ \dot{w}_{m_k} - \hat{b}_{\dot{w}_k}(-) \end{bmatrix} \tag{3.3-27}$$

and the propagation equation

$$\begin{bmatrix} \hat{z}_{E_{k+1}}(-) \\ \hat{w}_{k+1}(-) \\ \hat{b}_{\dot{w}_{k+1}}(-) \end{bmatrix} = \begin{bmatrix} 1 & \Delta t & 0 \\ 0 & 1 & 0 \\ 0 & 0 & e^{-\Delta t/\tau_{\dot{w}_b}} \end{bmatrix} \begin{bmatrix} \hat{z}_{E_k}(+) \\ \hat{w}_k(+) \\ \hat{b}_{\dot{w}_k}(+) \end{bmatrix} + \begin{bmatrix} D_{z\dot{w}} \\ D_{w\dot{w}} \\ 0 \end{bmatrix} \left[\dot{w}_{m_k} - \hat{b}_{\dot{w}_k}(+) \right] \tag{3.3-28}$$

The filter provides weighted rectangular integration of the accelerometer signal ($D_{w\dot{w}} \tilde{\sim} \Delta t$, $D_{z\dot{w}} \tilde{\sim} \Delta t^2/2$) and corrects integration drift with the barometric altimeter. The bias state accumulates position error and corrects the accelerometer signal. The covariances and gains for the w-filter are shown in the first row of Table D-24. The second and third rows in Table D-24 show the variation in the filter gains that should occur if the noise covariances are different from those assumed here.

The MLS-CF uses the same dynamic model and observations as the ER-CF w-filter, except that all filter states are in earth-relative axes, and earth-relative velocity and position are estimated. The implementable update and propagate versions of the filter are,

$$\begin{bmatrix} \hat{\underline{x}}_{E_k}(+) \\ \hat{\underline{v}}_{E_k}(+) \\ \hat{\underline{b}}_{B_k}(+) \end{bmatrix} = \begin{bmatrix} \hat{\underline{x}}_{E_k}(-) \\ \hat{\underline{v}}_{E_k}(-) \\ \hat{\underline{b}}_{B_k}(-) \end{bmatrix} + \begin{bmatrix} K_{xx} \\ K_{vx} \\ H^B_{E_k}(-)K_{b_k} \end{bmatrix} \left[\underline{x}_{E_{m_k}} - \hat{\underline{x}}_{E_k}(-) \right] \tag{3.3-29}$$

$$\begin{bmatrix} \hat{\underline{x}}_{E_{k+1}}(-) \\ \hat{\underline{v}}_{E_{k+1}}(-) \\ \hat{\underline{b}}_{B_{k+1}}(-) \end{bmatrix} = \begin{bmatrix} I & \Delta t I & 0 \\ 0 & I & 0 \\ 0 & 0 & e^{-\Delta t/\tau b_B} \end{bmatrix} \begin{bmatrix} \hat{\underline{x}}_{E_k}(+) \\ \hat{\underline{v}}_{E_k}(+) \\ \hat{\underline{b}}_{B_k}(+) \end{bmatrix} + \begin{bmatrix} D_{x\dot{v}} \\ D_{v\dot{v}} \\ 0 \end{bmatrix} \left[H^E_{B_k}(+) \left[\underline{a}_{m_k} - \hat{\underline{b}}_{B_k}(+) \right] \right] \tag{3.3-30}$$

The accelerometer bias is actually estimated in body axis coordinates as shown by multiplying the bias update equation with $H^B_{E_k}(-)$. The MLS-CF update and propagation gains are diagonal and constant; their values are shown in Table D-25.

The TRI-CF has the same structure as MLS-CF except for the addition of earth-relative velocity measurements. The implementable update equation for the TRI filter is

$$\begin{bmatrix} \hat{\underline{x}}_{E_k}(+) \\ \hat{\underline{v}}_{E_k}(+) \\ \hat{\underline{b}}_{B_k}(+) \end{bmatrix} = \begin{bmatrix} \hat{\underline{x}}_{E_k}(-) \\ \hat{\underline{v}}_{E_k}(-) \\ \hat{\underline{b}}_{B_k}(-) \end{bmatrix} \begin{bmatrix} K_{xx} & K_{xv} \\ K_{vx} & K_{vv} \\ H^E_{B_k}(-)K_{bx} & H^E_{B_k}(-)K_{bv} \end{bmatrix} \begin{bmatrix} \underline{x}_{E_{m_k}} - \hat{\underline{x}}_{E_k}(-) \\ \underline{v}_{E_{m_k}} - \hat{\underline{v}}_{E_k}(-) \end{bmatrix} \tag{3.3-31}$$

The propagation equation is the same as Eq. 3.3-30. The diagonal update and propagate gains for the TRI-CF is shown in Table D-25.

The variable, $\underline{a}_m$, in MLS-CF and TRI-CF is the vehicle inertial acceleration measurement expressed in body axis. The measurement is obtained from the accelerometer output, $\underline{a}_o$, after the gravity, g, and off cg location, $\Delta\underline{x}_B$, corrections are made. The corrections are implemented for the MLS-CF and TRI-CF as

$$\underline{a}_{m_k} = \underline{a}_{o_k} - \hat{\tilde{\underline{\omega}}}^E_{B_k}(+)\,\hat{\tilde{\underline{\omega}}}^E_{B_k}(+)\,\Delta\underline{x}_B + H^B_{E_k}(+) \begin{bmatrix} o \\ o \\ g \end{bmatrix} \tag{3.3-32}$$

and is discussed in Appendix A. The variable, $\underline{a}_m$, must also be corrected for coriolis acceleration, i.e.

$$\begin{bmatrix} \dot{u}_m \\ \dot{v}_m \\ \dot{w}_m \end{bmatrix}_k = \underline{a}_{m_k} - \hat{\tilde{\underline{\omega}}}^E_{B_k}(+)\,\hat{\underline{v}}_{B_k}(+) \tag{3.3-33}$$

for implementation in the ER-CF. The approximation

$$\hat{\underline{v}}_{B_k}(+) \cong \begin{bmatrix} \hat{u}_{A_k}(+) \\ \hat{v}_{A_k}(+) \\ \hat{w}_k(+) \end{bmatrix} \tag{3.3-34}$$

must be made in Eq. 3.3-33.

The CF approach to the velocity-position filters does not attempt to combine air-data with earth-relative position measurements. In order to do this, wind states must be introduced into the filter and estimated as shown in the following paragraphs.

Extended Complementary Filter Designs - The ECF combines all available velocity and position sensors into a unified implementable algorithm. The ECF approach allows the measurements to have a nonlinear relation with the system states which can in turn satisfy a nonlinear differential equation. The model for the resulting nonlinear stochastic system takes the form,

$$\dot{\underline{x}}(t) = \underline{f}\left[\underline{x}(t),\ t\right] + G(t)\ \underline{w}(t) \tag{3.3-35}$$

$$\underline{z}_k = \underline{h}_k\left[\underline{x}(t_k)\right] + \underline{v}_k,\ k=1,\ 2,\ \ldots \tag{3.3-36}$$

where $\underline{f}$ and $\underline{h}_k$ are nonlinear differentiable functions of the state vector, $\underline{x}$. $\underline{w}(t)$ and $\underline{v}_k$ are assumed to be zero mean, gaussian white noise processes. In the previous section, measurement noise is assumed to be white and Gaussian as a simplification, but the measurement noises used in the previous CF designs, in most instances, are nonlinear functions of $\underline{v}_k$ in Eq. 3.3-36.

The ECF algorithm for $\underline{x}(t)$ is obtained by linearizing the nonlinear functions $\underline{f}$ and $\underline{h}_k$ about a reference trajectory, applying conventional linear estimation theory, and then choosing the reference trajectory to be the current best estimate of the state, $\hat{\underline{x}}(t)$. The result is an extended Kalman filter (EKF) which is discussed in Section A.4. Further simplifications are made in the filter so that the filter gains can be scheduled, instead of computed with the filter covariance equations. The simplifications reduce the EKF to the extended complementary filter (ECF), which is discussed in Section A-5 using the MLS filter as an example.

The MLS-ECF combines TAS, sideslip, MLS range, azimuth, elevation, the barometric altimeter, and the accelerometers to estimate range, azimuth, elevation, $\underline{x}_{MLS}$, wind in earth-axes $\underline{w}_E$, vehicle earth-relative velocity in body axes $\underline{v}_B$, and accelerometer bias in body axes $\underline{b}_B$. From these estimates, earth-relative position ($\underline{x}_E$), earth-relative velocity in earth axes ($\underline{v}_E$), air-relative velocity in body axes ($\underline{v}_A$), and air-data states (TAS and β), are constructed. The detailed derivation of the MLS-ECF is presented in Section A-5. The final implementable version is

$$\begin{bmatrix} \hat{\underline{x}}^{(+)}_{MLS} \\ \hat{\underline{w}}_E(+) \\ \hat{\underline{v}}_B(+) \\ \hat{\underline{b}}_B(+) \end{bmatrix}_k = \begin{bmatrix} \hat{\underline{x}}^{(-)}_{MLS} \\ \hat{\underline{w}}_E(-) \\ \hat{\underline{v}}_B(-) \\ \hat{\underline{b}}_B(-) \end{bmatrix}_k + \left[\begin{array}{c|c|c} {}^{MLS}H(-)KMLS1 & KMLS2 & {}^{MLS}_{E}aH(-)^{E}_{B}H(-)^{B}_{A}KMLS3 \\ {}^{E}_{(3\times1)} & & {}^{E}_{B}bH(-)^{B}_{A}KMLS6 \\ a\ KMLS4 & {}^{E}_{B}aH(-)KMLS5 & {}^{B}_{A}aH(-)KMLS9 \\ {}^{B}_{E}H(-)KMLS7 & {}^{MLS}_{E}H(-)KMLS8 & {}^{B}_{A}aH(-)KMLS12 \\ {}^{B}_{E}H(-)KMLS10 & {}^{B}_{E}H(-)KMLS11 & \\ {}^{E}_{(3\times1)} & {}^{MLS}_{E} & \end{array}\right]_k \left[\begin{array}{c} z_{E_m} - \hat{z}_E(-) \\ \hline \underline{x}_{MLS_m} - \hat{\underline{x}}_{MLS}(-) \\ \hline TAS_m - \hat{TAS}(-) \\ \\ \beta_m - \hat{\beta}(-) \end{array}\right]_k \quad (3.3\text{-}37)$$

$$\begin{bmatrix} \hat{\underline{x}}_{MLS}(-) \\ \hat{\underline{w}}_E(-) \\ \hat{\underline{v}}_B(-) \\ \hat{\underline{b}}_B(-) \end{bmatrix}_{k+1} = \begin{bmatrix} I & 0 & \Delta t H^{MLS}_E(+) H^E_B(+) & 0 \\ 0 & \Phi_w & 0 & 0 \\ 0 & 0 & I & 0 \\ 0 & 0 & 0 & \Phi_b \end{bmatrix}_k \begin{bmatrix} \hat{\underline{x}}_{MLS}(+) \\ \hat{\underline{w}}_E(+) \\ \hat{\underline{v}}_B(+) \\ \hat{\underline{b}}_B(+) \end{bmatrix}_k + \begin{bmatrix} DMLS1 H^{MLS}_E(+) H^E_B(+) \left[\underline{a}_m - \hat{\underline{b}}_B(+) \right] \\ 0 \\ DMLS2 \left[\underline{a}_m - \tilde{\underline{\omega}}^E_B(+) \hat{\underline{v}}_B(+) - \hat{\underline{b}}_B(+) \right] \\ 0 \end{bmatrix}_k \quad (3.3\text{-}38)$$

The MLS-ECF is obtained by designing steady-state EKFs at the flight conditions shown in Table 3.1-1, factoring the transformation matrices, H^{MLS}_E, H^E_B, H^B_A (shown in Eqs. A-43, A-42, and A-62, respectively) from the EKF gains and scheduling the remaining <u>significant</u> gains. The MLS-ECF regression coefficients for the gains KMLS1-to-KMLS12, DMLS1 and DMLS2 are shown in Table D-13. The steady-state EKF designs at each flight condition assume the angles, angular rates and wind states are zero. In order to factor out the (3×3) transformation matrices, measurements that do not exist (x_{E_m}, y_{E_m}, and angle of attack, α), or are no longer valid (TAS and β^m below 25.7 m/s (50kt)), are used in the design process. After the significant gains are scheduled, x_{E_m}, y_{E_m}, and α are removed from the filter design and the scalars a^m and b are introduced as shown in Eq. 3.3-37.

The scalar parameters a and b are used to fade in and out the air-data measurements and wind estimates. Below TAS = 25.7 m/s (50 kt), a and b are zero and the wind states decay to zero in the propagate equation. When the aircraft air-data sensor outputs become valid, b is switched to unity for a short time (5 sec or more), to obtain an adequate initial

wind estimate, and then a switches to unity for the full filter computation. When the aircraft air-data sensors become invalid, a and b switch from unity to zero.

Components of the wind states (the largest component occuring in w_z) are not observable (because of the lack of an angle of attack sensor) but are detectable. If sideslip is also unavailable, the three wind states would still be retained in the filter, but larger components of the wind states would become unobservable. In a spiral maneuver without β and α, TAS would alternately sense the x and y components of wind, producing adequate horizontal estimates of a slowly varying wind provided Φ_w in Eq. 3.3-39 causes the wind estimate to decay slowly. The time constant used to obtain Φ_w is 30 seconds, as shown in Table 3.1-4.

The TRI-ECF uses the same approach as the MLS-ECF, except that the position measurements are in cartesian earth-relative axes and earth-relative velocity measurements are available. The implementable version of the TRI-ECF is

$$\begin{bmatrix} \hat{\underline{x}}_E(+) \\ \hat{\underline{w}}_E(+) \\ \hat{\underline{v}}_B(+) \\ \hat{\underline{b}}_B(+) \end{bmatrix}_k = \begin{bmatrix} \hat{\underline{x}}_E(-) \\ \hat{\underline{w}}_E(-) \\ \hat{\underline{v}}_B(-) \\ \hat{\underline{b}}_B(-) \end{bmatrix}_k + \left[\begin{array}{c|c|c} \text{KTRI1} & \text{KTRI2} & {}^{E}_{B}H(-){}^{B}_{A}H(-)\text{KTRI3} \\ \hline \text{aKTRI4} & \text{aKTRI5} & {}^{E}_{B}H(-){}^{B}_{A}H(-)\text{KTRI6} \\ \hline {}^{B}_{E}H(-)\text{KTRI7} & {}^{B}_{E}H(-)\text{KTRI8} & {}^{B}_{A}H(-)\text{KTRI9} \\ \hline {}^{B}_{E}H(-)\text{KTRI10} & {}^{B}_{E}H(-)\text{KTRI11} & {}^{B}_{A}H(-)\text{KTRI12} \end{array}\right]_k \left[\begin{array}{l} \underline{x}_{E_m} - \hat{\underline{x}}_E(-) \\ \hline \underline{v}_{E_m} - \hat{\underline{v}}_E(-) \\ \hline TAS_m - \hat{TAS}(-) \\ \\ \beta_m - \hat{\beta}(-) \end{array}\right]_k$$

(3.3-39)

$$\begin{bmatrix} \hat{\underline{x}}_E(-) \\ \hat{\underline{w}}_E(-) \\ \hat{\underline{v}}_B(-) \\ \hat{\underline{b}}_B(-) \end{bmatrix}_{k+1} = \begin{bmatrix} I & 0 & \Delta t \overset{E}{H}_B(+) & 0 \\ 0 & \Phi_w & 0 & 0 \\ 0 & 0 & I & 0 \\ 0 & 0 & 0 & \Phi_b \end{bmatrix}_k \begin{bmatrix} \hat{\underline{x}}_E(+) \\ \hat{\underline{w}}_E(+) \\ \hat{\underline{v}}_B(+) \\ \hat{\underline{b}}_B(+) \end{bmatrix}_k + \begin{bmatrix} DTRI1 \overset{E}{H}_B(+) \left[\underline{a}_m - \hat{\underline{b}}_B(+)\right] \\ 0 \\ DTRI2 \left[\underline{a}_m - \tilde{\underline{\omega}}_B(+) \hat{\underline{v}}_B(+) - \hat{\underline{b}}_B(+)\right] \\ 0 \end{bmatrix}_k$$

(3.3-40)

The regression coefficients for the filter gains are given in Table D-12.

The barometric altimeter measurement is optimally combined with the multilateration z-axis measurement before processing by the TRI-ECF,

$$z_{E_m} = \frac{\Upsilon_{z_{TRI}} \cdot z_{BA_m}}{\Upsilon_{z_{TRI}} + \Upsilon_{BA}} + \frac{\Upsilon_{BA} \cdot z_{TRI_m}}{\Upsilon_{z_{TRI}} + \Upsilon_{BA}} \qquad (3.3\text{-}41)$$

Υ is the root-sum-square of the various error sources in each position measurement,

$$\Upsilon_{BA} = \left[7.62^2 + 30.48^2 + (0.03 * \hat{z}_{E_k}(-))^2\right] m^2 \qquad (3.3\text{-}42)$$

$$\Upsilon_{z_{TRI}} = \begin{cases} \left[(0.128 * \hat{R}_{r_k}(-) - 19.56) m^2\right] & R_r \geq 171 \text{ m} \\ \left[2.29 \text{ m}^2\right] & R_r < 171 \text{ m} \end{cases} \qquad (3.3\text{-}43)$$

The ER-ECF is similar to the ER-CF except for the processing of TAS and sideslip. The implementable version of the ER-ECF is

$$\begin{bmatrix} z_E(+) \\ u_A(+) \\ v_A(+) \\ w(+) \\ \underline{b}_B(+) \end{bmatrix}_k = \begin{bmatrix} z_E(-) \\ u_A(-) \\ v_A(-) \\ w(-) \\ \underline{b}_B(-) \end{bmatrix}_k + \left[\begin{array}{c|c} \text{KER1} & \begin{matrix} E & B \\ H(-) & H(-)\text{KER2} \\ B & A \\ (1\times3) & (3\times2) \end{matrix} \\ \hline \begin{matrix} B \\ H(-)\text{KER3} \\ E \\ (3\times1) \end{matrix} & \begin{matrix} B \\ H(-)\text{KER4} \\ A \\ (3\times2) \end{matrix} \\ \hline \begin{matrix} B \\ H(-)\text{KER5} \\ E \\ (3\times1) \end{matrix} & \begin{matrix} B \\ H(-)\text{KER6} \\ A \\ (3\times2) \end{matrix} \end{array}\right]_k \begin{bmatrix} z_{E_m} - z_E(-) \\ \hline \text{TAS}_m - \text{TAS}(-) \\ \\ \beta_m - \hat{\beta}(-) \end{bmatrix}_k \qquad (3.3\text{-}44)$$

$$\begin{bmatrix} z_E(-) \\ u_A(-) \\ v_A(-) \\ w(-) \\ \underline{b}_B(-) \end{bmatrix}_{k+1} = \begin{bmatrix} 1 & \underset{(1\times3)}{\Delta t H_B^E(+)} & 0 \\ 0 & & \\ 0 & I & 0 \\ 0 & & \\ 0 & 0 & \Phi_b \end{bmatrix}_k \begin{bmatrix} z_E(+) \\ u_A(+) \\ v_A(+) \\ w(+) \\ \underline{b}_B(+) \end{bmatrix}_k + \begin{bmatrix} \underset{(1\times3)}{\text{DER1}H_B^E(+)}\left[\underline{a}_m - \underline{b}_B(+)\right] \\ \text{DER2}\left[\underline{a}_m - \underset{B}{\tilde{\omega}^E}(+)\begin{bmatrix} \hat{u}_A(+) \\ \hat{v}_A(+) \\ \hat{w}(+) \end{bmatrix} - \hat{\underline{b}}_B(+)\right] \\ 0 \end{bmatrix}_k \qquad (3.3\text{-}45)$$

The filter gain regressions are shown in Table D-11. The ER-ECF cannot provide earth-relative velocity and position in all three axes because of an assumed lack of external position measurements outside the terminal area.

3.4 CONTROL LAWS

The designs of the VALT digital control laws are presented in this section. The design employs full state feedback for stability and integral compensation for Type 1 response to vehicle guidance commands. The VALT digital control laws are obtained by augmenting the system dynamics with dynamic compensators, defining a continuous-time quadratic cost

function, and transforming both the cost function and the system to their discrete-time equivalents. The discrete cost functional is then minimized, resulting in a control algorithm suitable for digital implementation. In order to assure that no potentially significant cross-axis effects are overlooked, the control laws are developed assuming that longitudinal, lateral, and directional motions are coupled. For example, the helicopter's normal tendency is to pitch up when turning to the right and to pitch down when turning to the left. If the coupling is not significant it will be reflected in the control law gains, which partition accordingly.

Two different types of control laws, proportional-integral (PI) and proportional-integral-filter (PIF), and their respective designs are given in the next two sections. PIF is the primary control law for both attitude and velocity guidance. PI is employed as a theoretical alternative for comparative purposes (attitude guidance only).

3.4.1 PI Attitude Control Law

The proportional-integral (PI) control law is derived in Appendix B. The design objective is to find a digital feedback control law which smoothly transfers the system from one desired command vector to another while minimizing a quadratic cost function. The continuous-time cost function, which is employed to specify the discrete-time cost function weighting elements, is

$$J = \int_0^\infty \left\{ \left[\Delta \underline{x}^T(t) \Delta \underline{u}^T(t) \right] \begin{bmatrix} Q_1 & M \\ M & Q_2 \end{bmatrix} \begin{bmatrix} \Delta \underline{x}(t) \\ \Delta \underline{u}(t) \end{bmatrix} + \underline{v}^T(t) R \Delta \underline{v}(t) \right\} dt \qquad (3.4\text{-}1)$$

and the continuous-time design model is shown in Eq. 3.1-2. The discrete system model is

$$\begin{bmatrix} \Delta\underline{x} \\ \Delta\underline{u} \end{bmatrix}_{k+1} = \begin{bmatrix} \Phi & \Gamma \\ 0 & I \end{bmatrix} \begin{bmatrix} \Delta x \\ \Delta\underline{u} \end{bmatrix}_k + \begin{bmatrix} 0 \\ I \end{bmatrix} \Delta\underline{v}_k \qquad (3.4\text{-}2)$$

where the discrete transition matrix and control effect matrix are obtained from the continuous-time model as

$$\Phi = e^{F\Delta t} \qquad (3.4\text{-}3)$$

$$\Gamma = \int_0^{\Delta t} e^{Ft} dt G \qquad (3.4\text{-}4)$$

Although the exact discretized model of the plant shown in Eq. 3.1-2 is used to form the discrete cost function weighting matrices, the discrete system model, shown in Eq. 3.4-2, is used in the control design. The difference lies in the coupling term between the state and the control difference in the discrete control effect matrix, $[0\ I]^T$, shown in Eq. 3.4-2. PI controllers designed with nonzero coupling between the control difference command and the discrete system state are presented in Ref. 32. The coupling is of order Δt^2, as shown in Ref. 1, and can be neglected here as $\Delta t = 0.1$ sec.

The weighting matrices Q and R, in Eq. 3.4-1, are used as design parameters in specifying the control law gains. Q and R are chosen by forcing the closed-loop system to satisfy the step response criteria discussed in Section 2.2. Specifying Q and R, transforming to the discrete cost function matrices in Eq. B-18, and using results in Ref. 17, enables the discrete algebraic Riccati equation associated with the

optimal control problem to be solved. The solution to the Riccati equation is used to construct the controller gains. The controller gains are rearranged, as shown in Appendix B, to produce the PI control law which optimally transfers the system between steady-state conditions,

$$\underline{u}_k = \underline{u}_{k-1} - C_1(\underline{x}_k - \underline{x}_{k-1}) - \Delta t C_2(\underline{y}_{k-1} - \underline{y}_{d_k}) \qquad (3.4\text{-}5)$$

Figure 3.4-1 shows the incremental form of the PI controller, which accepts total guidance command and state inputs and issues total commands to the helicopter's actuators.

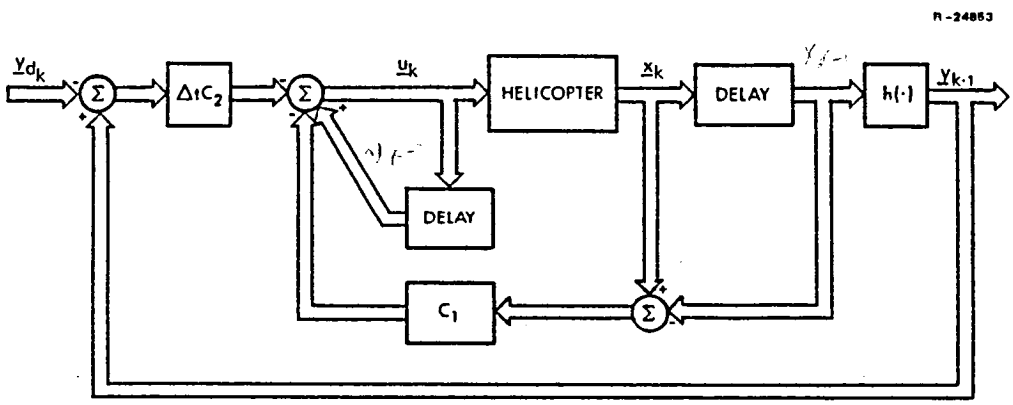

Figure 3.4-1 Proportional-Integral Control with Control-Difference Weighting in Incremental Form

Although the control law is designed with perturbation states and controls about the trim states, the incremental form does not require knowledge of the trim to be implemented. The state and command differences cancel out the trim state value and the control trim is retained in the

previous control actuator command. The control law can interface with a nonlinear model of the helicopter, the helicopter itself, or the linear-time-invariant model used for design in either the design, analysis or experimentation phase. The only difference is that H_p is used in the linear model and $h(\cdot)$ is used in the nonlinear model. In either case, the rectangular integration provided by Eq. 3.4-5 results in a Type 1 command response as discussed in Appendix B-2.

The diagonal elements of the weighting factors Q and R are chosen as the inverse of the maximum allowable mean-square values of the system states and control variables. Weighting of state displacements, state rates, control displacements, and command variables are expressed in the $(m+n)\times(m+n)$ symmetric matrix,

$$\begin{bmatrix} Q_1 & M \\ M^T & Q_2 \end{bmatrix} = \begin{bmatrix} 1/\Delta x_1^2 & & & 0 \\ & \ddots & & \\ & & 1/\Delta x_n^2 & \\ & & & 1/\Delta u_1^2 \\ 0 & & & & \ddots \\ & & & & & 1/\Delta u_m^2 \end{bmatrix}_{MAX} + \begin{bmatrix} F^T \\ G^T \end{bmatrix} \begin{bmatrix} 1/\Delta \dot{x}_1^2 & & 0 \\ & \ddots & \\ 0 & & 1/\Delta \dot{x}_n^2 \end{bmatrix}_{MAX} \begin{bmatrix} F & G \end{bmatrix} \tag{3.4-6}$$

and the control-rate weighting matrix is similarly expressed as

$$R = \begin{bmatrix} 1/\Delta \dot{u}_1^2 & & 0 \\ & \ddots & \\ 0 & & 1/\Delta \dot{u}_m^2 \end{bmatrix}_{MAX} \tag{3.4-7}$$

Once acceptable step responses are established for PI attitude control at several selected flight conditions, the values of Q and R are fixed, and control gains are generated for all 28 design flight conditions. The allowable mean-square values for PI are shown in Table 3.4-1. The resulting step response criteria at the 28 flight conditions are shown in Table 3.4-2. Of 336 separate requirements, only 6 are not precisely achieved for fixed Q and R. The six are minor yaw angle rise time infractions (1.6 instead of 1.5) and pitch angle difficulties at 10.2 m/s (20 kt), a transitory flight condition. Aside from step response, an additional effort is taken in the design to force the control gains to low values. The gains are kept small by weighting $\dot{u}$ in the cost function and by trying to match the most stringent step response requirement as precisely as possible, (which for PI-attitude is the rise time). Low gain values tend to keep sensitivity to sensor noise low, avoids limit cycles, and makes the control law tuned to the design point. Proper gain scheduling matches the control law with the aircraft flight condition as shown in Section 3.6.

The response criteria for PI attitude could easily be met at all flight conditions by adjusting Q and R at each flight condition as in Ref. 1. Aside from increasing the design effort and expense, changing Q and R at each flight condition could have an adverse effect on control gain variation, resulting in poor gain schedules. With the difficult flight conditions identified, it is possible to readjust the fixed Q and R to insure all response criteria are achieved. A complete redesign at all flight conditions would be necessary, however, and is not performed here because of the cost involved and also because exceeding a soft constraint by only 10% is not critical.

TABLE 3.4-1
DESIGN PARAMETERS FOR THE PI ATTITUDE CONTROL LAW

ALLOWABLE PERTURBATION	ATTITUDE COMMAND
Δu, m/s	-
Δv, m/s	-
Δw, m/s	1.83
Δp, deg/sec	10.0
Δq, deg/sec	20.0
Δr, deg/sec	8.0
$\Delta \phi$, deg/sec	3.10
$\Delta \theta$, deg	1.85
$\Delta \psi$, deg	2.0
$\Delta \dot{u}$, m/s^2	-
$\Delta \dot{v}$, m/s^2	-
$\Delta \dot{w}$, m/s^2	0.61
$\Delta \delta_B$, m	0.165
$\Delta \delta_C$, m	0.117
$\Delta \delta_S$, m	0.0889
$\Delta \delta_R$, m	0.106
$\Delta \dot{\delta}$(all)m/s	0.0508

TABLE 3.4-2
PI ATTITUDE STEP RESPONSE CHARACTERISTICS

FLIGHT CONDITION			PITCH ANGLE			ROLL ANGLE			YAW ANGLE			VERTICAL VELOCITY		
1	2	3	4	5	6	4	5	6	4	5	6	4	5	6
0	0 (0)	0 (0)	1.2	9.4	2.4	1.4	3.5	1.5	1.5	5.2	2.4	1.7	3.5	1.8
0	10.3 (20)	0 (0)	1.2	12.9	*	1.4	3.5	1.5	1.5	5.3	2.4	1.7	3.4	1.9
0	20.6 (40)	0 (0)	1.2	7.8	2.4	1.4	4.0	1.5	1.5	5.3	2.4	1.8	3.0	1.9
0	30.9 (60)	0 (0)	1.2	5.9	2.1	1.4	3.9	1.5	1.5	4.9	1.7	1.8	2.9	2.0
0	41.2 (80)	0 (0)	1.2	4.8	1.3	1.4	3.8	1.5	1.5	5.2	2.4	1.7	2.7	1.9
0	61.8 (120)	0 (0)	1.2	3.5	1.3	1.4	3.6	1.5	1.5	4.9	1.7	1.7	2.3	1.9
0	82.4 (160)	0 (0)	1.3	2.5	1.4	1.4	3.5	1.5	1.5	4.3	1.7	1.8	2.1	2.1
0	10.3 (20)	2.54 (500)	1.2	18	*	1.4	3.5	1.5	1.5	5.3	2.4	1.7	3.3	1.9
0	20.6 (40)	-2.54 (-500)	1.2	7.1	2.2	1.4	4.0	1.5	1.5	5.2	2.4	1.7	3.1	1.8
0	30.9 (60)	2.54 (500)	1.2	6.3	2.1	1.4	3.9	1.5	1.5	5.3	2.5	1.8	2.8	2.0
0	30.9 (60	-2.54 (-500)	1.2	5.6	2.0	1.4	3.9	1.5	1.5	5.2	2.4	1.7	2.9	1.9
0	41.2 (80)	5.08 (1000)	1.2	4.9	1.3	1.4	3.7	1.6	1.5	5.3	2.5	1.8	2.8	2.2
0.05	30.9 (60)	0 (0)	1.2	5.7	2.1	1.4	4.3	1.5	1.5	5.3	2.4	1.7	2.9	3.5
0.05	51.5 (100)	0 (0)	1.2	3.8	1.3	1.4	4.1	1.5	1.6	4.8	1.7	1.7	2.3	1.9
0.05	20.6 (40)	2.54 (500)	1.2	9.4	2.7	1.4	5.6	2.4	1.5	5.4	2.4	1.8	3.0	1.9
0.05	30.9 (60)	2.54 (500)	1.2	6.2	2.2	1.4	4.5	1.5	1.5	5.3	2.5	1.8	2.9	1.9
0.05	41.2 (80)	2.54 (500)	1.2	4.6	1.3	1.4	5.2	1.5	1.6	5.1	2.4	1.7	2.7	1.8
0.05	30.9 (60)	-2.54 (-500)	1.3	5.4	2.1	1.4	4.2	1.5	1.5	5.2	2.4	1.7	2.8	1.9
-0.05	30.9 (60)	0 (0)	1.2	5.7	2.1	1.4	4.3	1.5	1.5	5.1	2.4	1.7	2.8	1.9
-0.05	51.5 (100)	0 (0)	1.2	3.7	1.3	1.4	4.1	1.6	1.6	4.7	1.7	1.7	2.3	1.9
-0.05	20.6 (40)	2.54 (500)	1.2	9.6	2.7	1.4	5.3	2.3	1.5	5.2	2.4	1.8	3.0	1.9
-0.05	30.9 (60)	2.54 (500)	1.2	6.2	2.2	1.4	4.3	1.5	1.6	5.2	2.4	1.7	2.9	1.9
-0.05	41.2 (80)	2.54 (500)	1.2	4.5	1.3	1.4	4.2	1.5	1.6	5.1	2.4	1.7	2.6	1.9
-0.05	30.9 (60)	-2.54 (-500)	1.3	5.4	2.1	1.4	4.1	1.5	1.5	5.2	2.4	1.7	2.9	1.9
0.1	20.6 (40)	2.54 (500)	1.2	9.6	2.8	1.4	6.3	2.5	1.5	5.3	2.4	1.8	3.0	1.9
0.1	30.9 (60)	2.54 (500)	1.2	6.1	2.2	1.4	5.7	2.4	1.5	5.1	2.4	1.7	2.8	1.9
-0.1	20.6 (40)	2.54 (500)	1.2	10.3	3.1	1.4	5.8	2.4	1.5	5.4	2.4	1.8	3.0	1.9
-0.1	30.9 (60)	2.54 (500)	1.2	4.1	1.3	1.4	5.8	2.5	1.6	4.5	1.8	1.8	2.2	1.9

*Greater than 5 sec.
1) Turn Rate, rad/sec 2) Forward Velocity m/s (kt) 3) Vertical Velocity m/s (fpm)
4) Rise Time, sec 5) Over-Shoot, Percent. 6) Settling Time, sec

PI-attitude is used as an auxiliary to PIF attitude control for comparison purposes. PIF attitude and PIF velocity control designs are constructed in the next section.

3.4.2 PIF Attitude and PIF Velocity Control Laws

The proportional-integral-filter (PIF) control law design procedure is analogous to the procedure for PI. The main difference between PIF and PI is in the choice of the cost function. The continuous-time cost function which defines the discrete-time cost function weighting elements for PIF is,

(3.4-8)

where the discrete system model is written as

$$\begin{bmatrix} \Delta\underline{x} \\ \Delta\underline{u} \\ \Delta\underline{\xi} \end{bmatrix}_{k+1} = \begin{bmatrix} \Phi & \Gamma & 0 \\ 0 & I & 0 \\ \Delta t H_p & 0 & I \end{bmatrix} \begin{bmatrix} \Delta\underline{x} \\ \Delta\underline{u} \\ \Delta\underline{\xi} \end{bmatrix}_k + \begin{bmatrix} 0 \\ I \\ 0 \end{bmatrix} \Delta\underline{v}_k + \begin{bmatrix} 0 \\ 0 \\ -I \end{bmatrix} \Delta\underline{y}_{d_{k+1}} \tag{3.4-9}$$

The PIF control law is derived in Appendix B and has the total-value incremental form,

$$\underline{u}_k = \underline{u}_{k-1} + \Delta t\, \underline{v}_{k-1} \tag{3.4-10}$$

$$\underline{v}_{k-1} = (I - \Delta t\, C_4)\, \underline{v}_{k-2} - C_3(\underline{x}_{k-1} - \underline{x}_{k-2}) - \Delta t\, C_5(\underline{y}_{k-2} - \underline{y}_{d_{k-1}}) + E_1(\underline{y}_{d_k} - \underline{y}_{d_{k-1}})$$

Control rate weighting induces a low-pass filtering effect defined by the gain C_4, which is not present in PI.

The Type 1 structure is implemented in PIF by explicit integrator state weighting in the cost function. Figure 3.4-2 shows the feedback, feedforward, and low-pass structures in PIF.

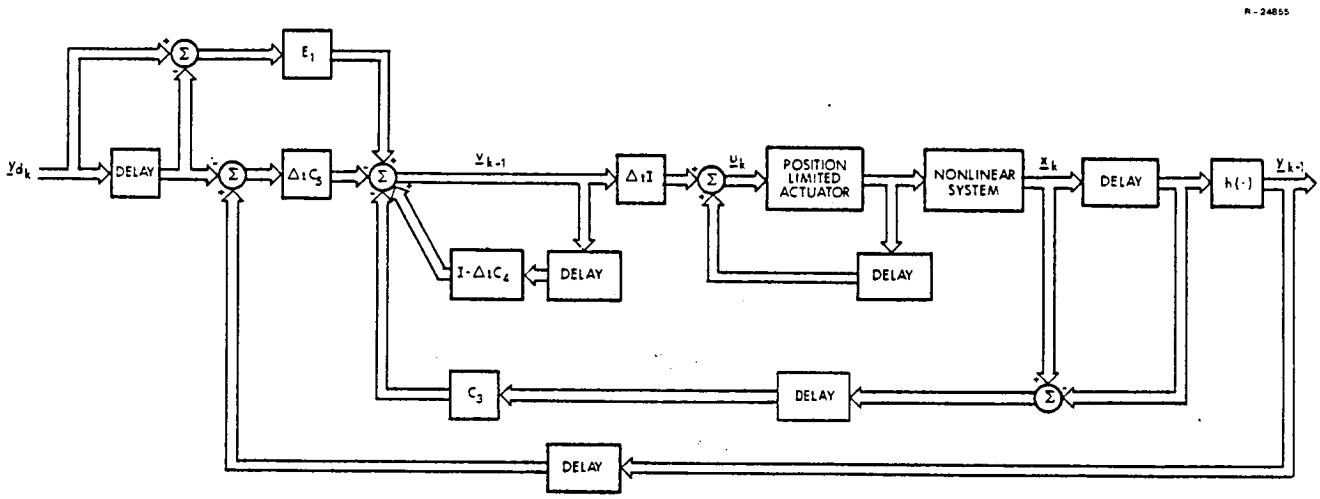

Figure 3.4-2 PIF Control Law in Incremental Form

PIF has a number of special properties which are useful in flight control applications,

- Depending on how $\underline{y}_{d_k}$ is obtained, (pilot or automatic guidance), almost all control calculations can be performed one sample period before the control command is needed because of the built-in state feedback delay.
- The break frequency of the PIF low-pass filter can be near system frequencies without significantly deteriorating performance because the feedback gains, C_3 and C_5 are optimally adjusted by the Riccati equation to compensate for phase lag. High frequency feedback effects

(rotor-fuselage coupling, body-bending modes, and sensor noise) are highly suppressed in PIF.

- The feedforward command of y_{d_k} optimally changes the control at index k through the feedforward matrix E_1, and is not low-pass filtered. E_1 greatly improves system rise-time and enables PIF to be the primary control design.

- PIF (and PI), in incremental form, does not require trim values for implementation.

- PIF (and PI) in incremental form does not have integrator wind-up if the control command is position limited to the natural limits of the actuator, as shown in Fig. 3.4-2.

- When the command vector changes from attitude to velocity guidance, only the H_p matrix changes in the design model. The PIF structure remains the same.

The control cost weighting factors for PIF use the same construction shown in Eqs. 3.4-6 and 3.4-7 with additional weights needed for Q_3. The values for Q and R, which are constant for the PIF attitude and PIF velocity designs, are shown in Table 3.4-3.

The resulting step responses at the 28 design flight conditions are given in Tables 3.4-4 and 3.4-5. For 336 separate requirements, 13 are not exactly satisfied for PIF attitude and 11 are not satisfied for PIF velocity. The yaw angle rise time requirement is increased to 1.8 sec for the PIF velocity design instead of using 1.5 sec as in PIF attitude. No yaw angle requirements were originally specified for PIF velocity. The slower yaw angle rise time complements the

TABLE 3.4-3
DESIGN PARAMETERS FOR THE PIF CONTROL LAWS

ALLOWABLE PERTURBATION	ATTITUDE COMMAND	VELOCITY COMMAND
Δu, m/s	-	4.88
Δv, m/s	-	5.49
Δw, m/s	2.13	1.83
Δp, deg/sec	7	10.00
Δq, deg/sec	15	10.00
Δr, deg/sec	7.5	10.00
$\Delta\phi$, deg/sec	3.3	6.5
$\Delta\theta$, deg	2.8	7.0
$\Delta\psi$, deg	3	3.5
$\Delta\xi_1(\phi \text{or } V_x)$	4.4 deg-sec	3.05 m-sec
$\Delta\xi_2(\theta \text{or } V_y)$	3.4 deg-sec	3.66 m-sec
$\Delta\xi_3(\psi \text{or } V_z)$	3.8 deg-sec	1.07 m-sec
$\Delta\dot{\xi}_4(V_z \text{ or } \psi)$	0.975 m	2.5 deg-sec
$\Delta\dot{u}$, m/s^2	-	0.0610
$\Delta\dot{v}$, m/s^2	-	0.0610
$\Delta\dot{w}$, m/s^2	0.0610	0.0914
$\Delta\delta_B$, m	0.165	0.165
$\Delta\delta_C$, m	0.117	0.117
$\Delta\delta_S$, m	0.0914	0.0889
$\Delta\delta_R$, m	0.106	0.106
$\Delta\dot{\delta}$(all), m/s	0.0508	0.0508

TABLE 3.4-4
PIF ATTITUDE STEP RESPONSE CHARACTERISTICS

FLIGHT CONDITION			PITCH ANGLE			ROLL ANGLE			YAW ANGLE			VERTICAL VELOCITY		
1	2	3	4	5	6	4	5	6	4	5	6	4	5	6
0	0 (0)	0 (0)	1.2	17.7	3.0	1.3	8.8	2.9	1.48	13.6	3.4	1.3	10.1	3.5
0	10.3 (20)	0 (0)	1.2	18.2	3.2	1.3	8.9	2.9	1.45	13.7	3.4	1.3	10.2	3.3
0	20.6 (40)	0 (0)	1.3	10.0	3.1	1.3	9.1	3.0	1.5	13.8	3.5	1.3	10.4	3.1
0	30.9 (60)	0 (0)	1.45	3.7	1.65	1.3	8.9	2.9	1.5	13.9	3.5	1.1	12.2	2.7
0	41.2 (80)	0 (0)	1.7	4.0	2	1.3	8.9	2.9	1.5	13.6	3.5	1.1	13.9	2.9
0	61.8 (120)	0 (0)	1.8	4.0	2.2	1.3	9.0	3.0	1.5	13.6	3.5	1.1	15.2	4.4
0	82.4 (160)	0 (0)	1.9	5.0	5.0	1.3	8.9	2.9	1.5	12.8	3.5	1.1	16.5	4.6
0	10.3 (20)	2.54 (500)	1.2	22.0	3.3	1.3	8.9	3.0	1.5	13.7	3.5	1.3	5.2	3.3
0	20.6 (40)	-2.54 (-500)	1.3	9.5	2.9	1.3	9.1	3.0	1.5	11.4	3.4	1.2	10.4	3.1
0	30.9 (60)	2.54 (500)	1.5	4.4	1.6	1.3	9.1	3.0	1.5	11.4	3.5	1.2	11.2	2.9
0	30.9 (60)	-2.54 (-500)	1.5	3.9	1.6	1.3	9.1	3.0	1.5	13.8	3.5	1.2	11.4	2.9
0	41.2 (80)	5.08 (1000)	1.6	3.9	1.8	1.3	9.1	3.0	1.5	14.0	3.5	1.1	12.5	2.8
0.05	30.9 (60)	0 (0)	1.5	4.0	1.6	1.3	11.7	3.3	1.5	13.7	3.5	1.2	11.3	2.9
0.05	51.5 (100)	0 (0)	1.7	4.1	2.0	1.3	13.7	3.8	1.5	12.7	3.5	1.2	14.0	4.0
0.05	20.6 (40)	2.54 (500)	1.3	11.5	3.3	1.3	10.3	3.2	1.5	13.9	3.4	1.2	10.3	3.1
0.05	30.9 (60)	2.54 (500)	1.45	4.2	1.55	1.25	12.1	3.3	1.5	13.8	3.4	1.2	11.2	2.9
0.05	41.2 (80)	2.54 (500)	1.6	3.7	1.9	1.3	13.6	3.4	1.52	13.4	3.5	1.1	7.7	2.7
0.05	30.9 (60)	-2.54 (-500)	1.5	3.8	1.6	1.25	11.2	3.2	1.5	13.7	3.5	1.2	11.5	2.9
-0.05	30.9 (60)	0 (0)	1.5	3.9	1.6	1.25	11.2	3.3	1.5	13.6	3.5	1.2	11.4	2.9
-0.05	51.5 (100)	0 (0)	1.7	4.0	2.0	1.25	13.9	3.5	1.6	12.6	3.5	1.1	14.4	4.2
-0.05	20.6 (40)	2.54 (500)	1.3	11.3	3.3	1.3	10.4	3.2	1.5	13.8	3.5	1.3	10.4	3.1
-0.05	30.9 (60)	2.54 (500)	1.5	4.2	1.6	1.3	12.2	3.3	1.5	13.7	3.5	1.2	11.2	2.9
-0.05	41.2 (80)	2.54 (500)	1.6	3.6	1.9	1.3	13.6	3.5	1.6	13.3	3.6	1.1	7.7	2.7
-0.05	30.9 (60)	-2.54 (-500)	1.5	3.7	1.6	1.3	11.5	3.3	1.5	13.6	3.5	1.2	11.4	2.9
0.1	20.6 (40)	2.54 (500)	1.3	12.2	3.3	1.3	11.4	3.4	1.5	13.8	3.5	1.3	10.3	3.1
0.1	30.9 (60)	2.54 (500)	1.5	4.1	1.7	1.1	23.5	4.0	1.6	13.1	3.6	1.2	11.3	2.9
-0.1	20.6 (40)	2.54 (500)	1.3	11.4	3.3	1.2	14.3	3.5	1.5	13.7	3.5	1.3	10.4	3.2
-0.1	30.9 (60)	2.54 (500)	1.5	4.0	1.6	1.1	23	4.2	1.6	13.0	3.6	1.2	11.4	2.9

1) Turn Rate, rad/sec 2) Forward Velocity m/s (kt) 3) Vertical Velocity m/s (fpm)
4) Rise Time, sec 5) Over-Shoot, Percent 6) Settling Time, sec

TABLE 3.4-5
PIF VELOCITY STEP RESPONSE CHARACTERISTICS

FLIGHT CONDITION			FORWARD VELOCITY			LATERAL VELOCITY			VERTICAL VELOCITY			YAW ANGLE		
TR[1]	FV	VV	RT	O	ST	RT	O	ST	RT	O	ST	RT	O	ST
0	0 (0)	0 (0)	3.8	(10.1)	*	3.6	(11.6)	*	1.2	(11.1)	3.3	1.4	(18.0)	3.3
0	10.3 (20)	0 (0)	3.3	(10.0)	*	3.0	(13.0)	*	1.2	8.7	3.2	1.4	(17.0)	3.2
0	20.6 (40)	0 (0)	3.0	11.6	*	3.0	12.5	*	1.3	7.1	3.0	Not Simulated		
0	30.9 (60)	0 (0)	3.3	12.4	*	2.7	13.1	*	1.2	8.9	2.8	Not Simulated		
0	41.2 (80)	0 (0)	3.9	12.5	*	3.1	13.3	*	1.2	10.5	4.6	1.8	8.0	4.3
0	61.8 (20)	0 (0)	4.4	14	*	3.6	11.4	*	1.1	10.1	2.6	(2.0)	6.0	5.0
0	82.4 (160)	0 (0)	4.7	*	*	3.0	13.9	*	1.3	8.1	2.8	(2.2)	6.0	(5.8)
0	10.3 (20)	2.54 (500)	3.3	9.5	*	3.3	12.0	*	1.4	7.7	3.1	1.4	(16.5)	3.2
0	20.6 (40)	2.54 (-500)	3.3	11.3	*	3.2	11.8	*	1.4	7.3	3.1	1.5	11.3	3.5
0	30.9 (60)	2.54 (500)	3.5	10.7	*	3.4	11.6	*	1.3	8.8	2.9	1.6	10.4	3.9
0	30.9 (60)	-2.54 (-500)	3.5	11.0	*	3.3	11.8	*	1.3	8.2	2.7	1.6	9.0	4.0
0	41.2 (80)	5.08 (1000)	3.9	9.0	*	3.3	11.6	*	1.2	12.1	2.8	1.7	8.0	4.2
0.05	30.9 (60)	0 (0)	3.6	10.8	*	3.3	10.9	*	1.3	8.1	2.9	1.6	10.0	4.0
0.05	51.5 (100)	0 (0)	4.2	10.1	*	3.1	10.8	*	1.3	7.1	2.7	(2.0)	7.0	4.8
0.05	20.6 (40)	2.54 (500)	3.3	11.6	*	3.4	10.9	*	1.5	6.4	2.9	1.5	13.2	3.5
0.05	30.9 (60)	2.54 (500)	3.6	10.8	*	3.3	10.7	*	1.3	8.6	2.9	1.6	10.1	3.9
0.05	41.2 (80)	2.54 (500)	3.9	9.8	*	3.2	10.7	*	1.3	9.4	2.8	1.8	8.2	4.3
0.05	30.9 (60)	-2.54 (-500)	3.6	10.7	*	3.2	11.2	*	1.3	7.8	2.8	1.6	9.9	4.0
-0.05	30.9 (60)	0 (0)	3.6	10.5	*	3.3	10.9	*	1.3	8.6	2.8	1.6	10.1	4.0
-0.05	51.5 (100)	0 (0)	4.3	10.2	*	3.4	8.8	*	1.2	9.9	2.6	(1.9)	8.2	4.8
-0.05	20.6 (40)	2.54 (500)	3.3	11.5	*	3.3	11.1	*	1.4	6.5	2.9	1.5	13.4	3.5
-0.05	30.9 (60)	2.54 (500)	3.3	10.4	*	3.4	10.9	*	1.3	9.4	2.9	1.6	10.3	3.9
-0.05	41.2 (80)	2.54 (500)	4.0	9.2	*	3.4	10.0	*	1.2	11.4	2.8	1.8	8.4	4.3
-0.05	30.9 (60)	-2.54 (-500)	3.6	10.6	*	3.2	11.2	*	1.3	8.1	2.8	1.6	10.1	4.0
0.1	20.6 (40)	2.54 (500)	3.4	9.1	*	3.3	11.5	*	1.4	8.1	2.9	1.4	(16.6)	3.4
0.1	30.9 (60)	2.54 (500)	3.6	10.9	*	3.4	9.3	*	1.4	7.7	2.9	1.6	10.4	4.0
-0.1	20.6 (40)	2.54 (500)	3.7	10.2	*	3.4	9.6	*	1.3	9.2	2.9	1.6	10.8	4.0
-0.1	30.9 (60)	2.54 (500)	4.2	9.5	*	3.6	8.0	*	1.2	10.5	2.7	1.8	9.4	4.4

*Response criteria not specified.

1) Turn Rate, rad/sec 2) Forward Velocity m/s (kt) 3) Vertical Velocity m/s (fpm)
4) Rise Time, sec 5) Over-Shoot, Percent 6) Settling Time, sec

slower velocity guidance requirements. The yaw angle rise time increases with velocity but is always less than 2.2 sec (Table 3.4-5). None of the violated criteria are considered particularly adverse and the increase in rise times with velocity for θ and ψ could even be considered beneficial.

The PI and PIF control laws are synthesized using complete state feedback without actuator dynamics, computation delay effects, and actuator position and rate limits. The control law is evaluated in Chapter 4 without these simplifications. The next section presents the control and filter gain schedules to be used in the VALT DFCS computer.

3.5 GAIN SCHEDULING

The control laws are adapted to a particular flight condition by scheduling their gains as a function of TAS, w, and $\dot{\psi}$. These three variables span the flight conditions chosen for design. The gain schedules are developed in a 3-step process: 1) determination of means and standard deviations of all gains (summed over all flight conditions), 2) determination of correlation coefficeints between gains and flight conditions, and 3) curve fitting by regression analysis (Ref. 1). The objective of the first step is to determine which gains can be zeroed or held constant. The second step indicates which functional relationships are most appropriate for gain scheduling, and the last step provides the scheduling coefficients.

The PIF control law for the helicopter, described by Eqs. 3.4-10 and 3.4-11, contains 84 gains; however, 29 and 25 gains can be zeroed in the attitude-command and velocity-command controllers, respectively. The PI-attitude control

law has 52 gains of which 16 can be zeroed. The zeroed gains have mean values which are generally less than 5% of similar types of gains.

The remaining gains are scheduled in three sets, which take the following forms:

$$\text{Gain} = a_1 TAS + a_2 TAS^2 + a_3 w + a_4 \dot{\psi} + a_5 \qquad (3.5\text{-}1)$$

$$\text{Gain} = a_1 TAS + a_2 w + a_3 \dot{\psi} TAS^2 + a_4 TAS^2/[1+TAS/V_N)^2] + a_5 \qquad (3.5\text{-}2)$$

$$\text{Gain} = a_1 TAS + a_2 TAS^2 + a_3 \dot{\psi} w + a_4/[1+(TAS/V_N)^2] + a_5 \qquad (3.5\text{-}3)$$

where a_1 to a_4 are the regression coefficients and a_5 is the regression constant. In these scheduling equations, V_N is 27 m/s (53.4 kt) and is chosen so that at full throttle an attenuation of 0.1 is provided:

$$\frac{1}{1 + \left(\frac{V_{\text{FULL THROTTLE}}}{V_N}\right)^2} = 0.1 \qquad (3.5\text{-}4)$$

Four independent variables are chosen because together, they give good scheduling results. Several variations of TAS, w, and $\dot{\psi}$ were tried and the three forms in Eqs. 3.5-1 to 3.5-3 yielded the best results.

The optimal gains computed at 28 flight conditions generally have correlation coefficients greater than 0.8 with the scheduled gains. Appendix D lists the regression coefficients and the correlation coefficient for all control gains. An example of gain variations with forward airspeed is given in Fig. 3.4-3, which shown the pitch rate feedback gains, $-\Delta t\ C_3(4,5)$, $-\Delta t\ C_3(1,5)$, and $-\Delta t\ C_3(2,5)$ for the velocity command controller.

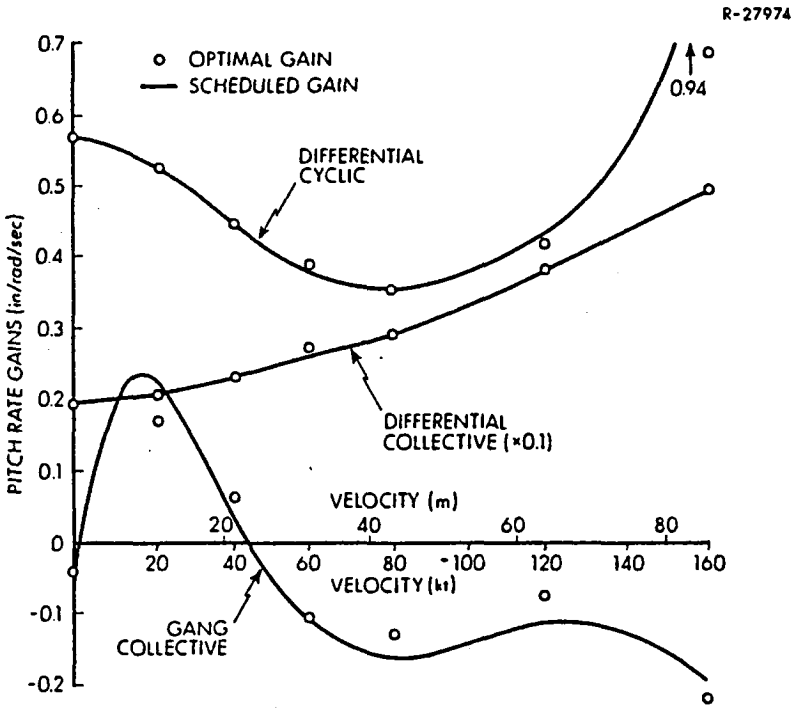

Figure 3.4-3 Optimal and Scheduled Pitch Rate Gains for PIF-Velocity

The scheduled and actual gains have correlation coefficients of 0.97, 0.99, and 0.96, respectively, and fit well, particularly in capturing the sign variation for $-\Delta tC_3(2,5)$. Other variables associated with trim are scheduled using the same functions as the control gains and are listed in Appendix D.

The velocity filters are adapted to a particular flight condition by scheduling their gains as functions of R_r, R_ε, z_E, and TAS. The TRI-ECF uses only functions of range to the center distance measuring equipment, R_r. The MLS-ECF uses only functions of range to the elevation equipment, R_ε. The enroute filter uses functions of height, z_E, and true airspeed, TAS. Range to measuring equipment is used in the filter gain scheduling for multilateration and MLS in order to make the filter insensitive to the touchdown point.

The TRI-ECF gains are partitioned into 3×3, 3×2 and 2×2 matrices as shown in Eq. 3.3-39. Only the diagonal elements in each partition are scheduled (the off diagonal terms tend to be insignificant and are set to zero). The TRI-ECF gains are scheduled using

$$\text{Gain} = a_1 / \left[1+R_r/R_{N1}\right] + a_2 \qquad (3.5\text{-}5)$$

$$\text{Gain} = a_1 / \left[1+(R_r/R_{N2})^2\right] + a_2 \qquad (3.5\text{-}6)$$

R_{N1} and R_{N2} are normalization variables and are 305 m (1000 ft) and 153 m (500 ft), respectively. The regression coefficients and correlation coefficients for TRI-ECF are shown in Table D-12. Figure 3.4-4 is an example of filter gain variations with range. The scheduled and actual gains for the figure have correlation coefficients of 0.99.

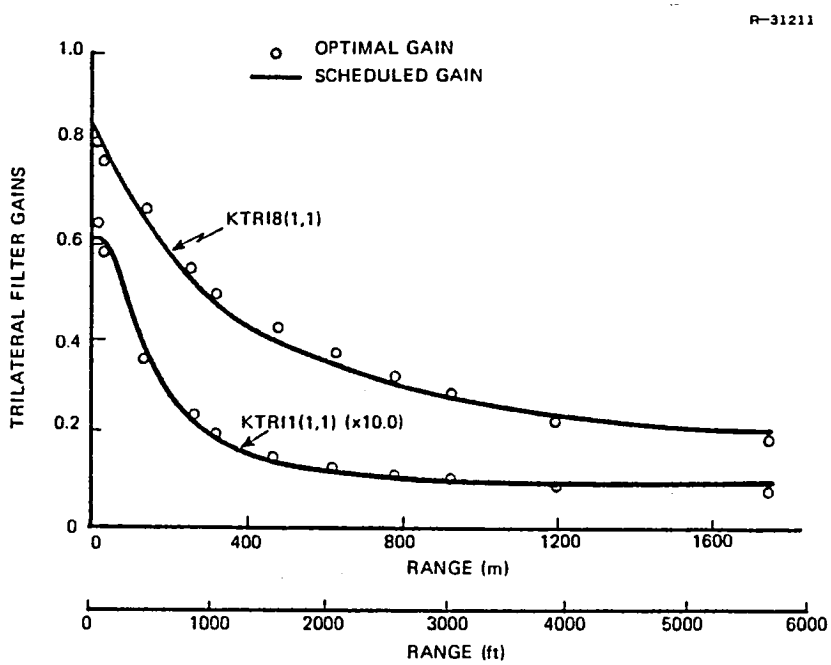

Figure 3.4-4 Examples of Optimal and Scheduled Gains for the Trilateration Filter.

Care must be taken in scheduling the filter gains, since the tails of the scheduling functions tend to cross the axis and change sign as the range increases (see Fig. 3.4-4), but the actual gains do not. Some regression coefficients are modified slightly to avoid the sign change in implementation.

The MLS gains are also partitioned into 3×3 and 2×2 matrices; however, unlike the TRI gains, some of the off-diagonal gains in the 3×3 and 2×2 matrices are scheduled as shown in Table D-13. The scheduling functions for MLS are

$$\text{Gain} = a_1 / \left[1 + (R_\varepsilon / R_{N3})^2\right] + a_2 \qquad (3.5\text{-}7)$$

and

$$\text{Gain} = a_1 / \left[1 + (R_\varepsilon / R_{N4})^2\right] + a_2 \qquad (3.5\text{-}8)$$

where R_{N3} and R_{N4} are 30480m (10^5 ft) and 1220 m (4000 ft), respectively.

The Enroute filter uses a combination of height and true airspeed for scheduling,

$$\text{Gain} = a_1 z_E + a_2 / \left[1 + (TAS/V_N)^2\right] + a_3 \qquad (3.5\text{-}9)$$

V_N has the same value as V_N in the control gain regressions and the coefficients are shown in Table D-11.

3.6 GUIDANCE ALGORITHMS

The guidance laws in the VALT DFCS are constructed to compare desired and actual position of the aircraft and issue commands to the control laws which will reduce these errors. The guidance command consists of a nominal command and a path-deviation-correcting perturbation command, both of which

are described below. Several alternative forms of guidance are discussed in this section, spiral guidance (Ref. 10) was simulated to produce results reported in Section 4.8.

3.6.1 Nominal Command Calculations

The nominal command geometry in the horizontal plane is illustrated in Fig. 3.6-1. The nominal guidance trajectory is composed of straight lines and circles, and it is updated as a function of range-to-go (for a straight segment) or heading-angle-to-go (for a circular segment). The nominal body yaw angle is calculated on-line so that the projection of the body x-axis lies along the air-relative velocity vector. This yaw angle is found by calculating the heading of the air-relative velocity vector as

$$\psi_o = \tan^{-1} ((V_y - W_y)/(V_x - W_x)) \qquad (3.6\text{-}1)$$

The earth-relative wind vector components in Eq. 3.6-1 are discussed in Appendix A (Eqs. A-48 and A-49 with a different sign convention), and the earth-relative vehicle velocity components were discussed in Section 3.1 (Eq. 3.1-3).

The nominal pitch Euler angle is used to initialize the pitch trim integrator,

$$\theta_o = 0.115 \left(1 - \frac{V_{DR}}{135 \text{ fps}} \right) \text{rad} \qquad (3.6\text{-}2)$$

Nominal roll angle is calculated so as to maintain the total specific aerodynamic vector in the helicopter x_B-z_B plane:

$$\phi_o = \tan^{-1} (V_x^2 + V_y^2)/(gR_{CT} \cos (\Delta\xi)) \qquad (3.6\text{-}3)$$

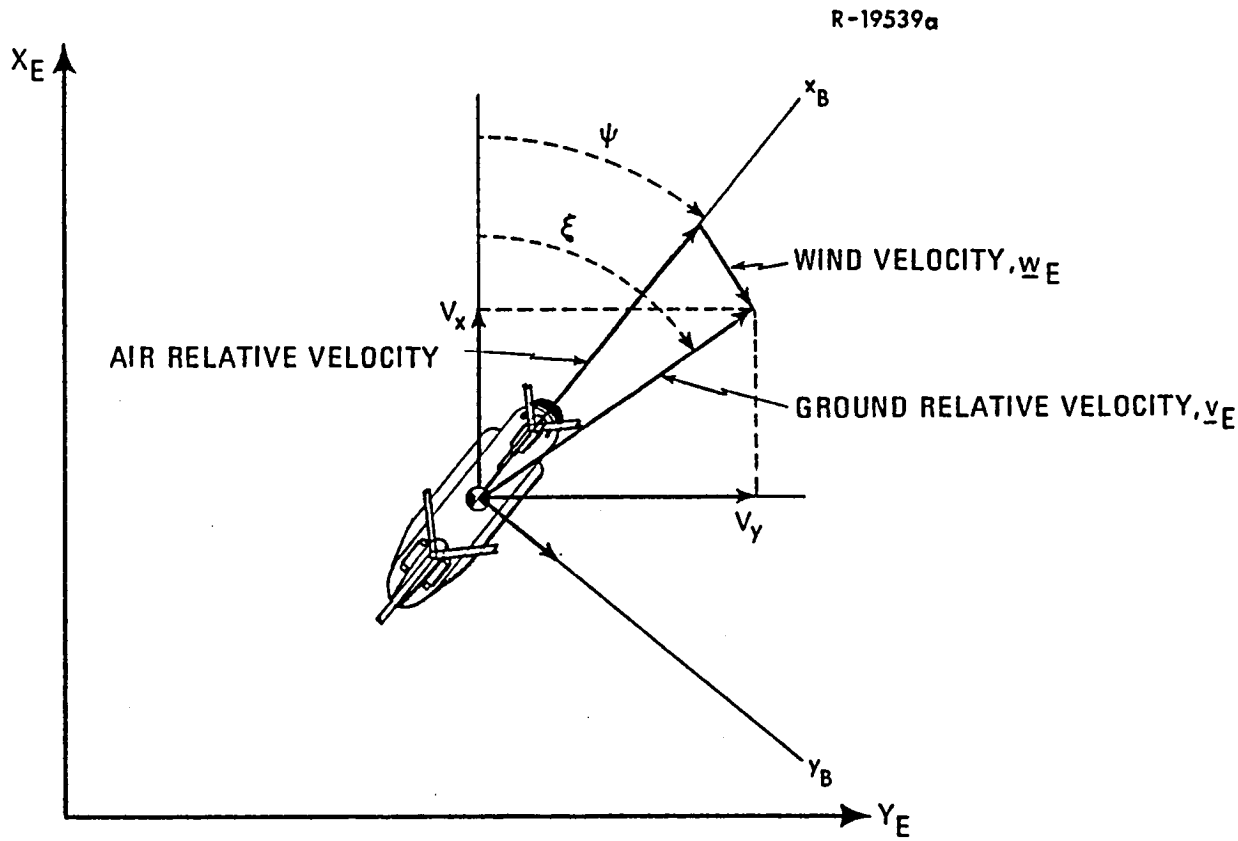

Figure 3.6-1 Horizontal Plane Guidance Command Geometry

where R_{CT} is the radius of turn and $\Delta\xi$ is the angle between the air-relative and ground-relative velocities. For straight flight,

$$\phi_o = 0 \qquad (3.6\text{-}4)$$

3.6.2 Perturbation Command Calculations

Vertical Channel Perturbation Guidance - The vertical channel involves either position error feedback (Ref. 9 and 10) or position, velocity, and acceleration error feedback (Ref. 33). The gain histories, shown in Ref. 9, indicate that the position feedback gain increases with horizontal velocity

by -0.013 s^{-1}/ms^{-1} (-0.004 s^{-1}/fps). An additional range-dependent factor near the hover point is implied. Another approach to guidance gain calculation is single channel optimization (Ref. 10). By assuming instantaneous controller/helicopter velocity response, the position gains are expressed as the ratio of a vertical velocity weighting factor to a vertical position weighting factor. Choosing 1.02 m/s (200 fpm) and 61 m (200 feet) for vertical velocity and position weighting factors, respectively, results in a position gain of -0.0333 sec^{-1}. Figure 3.6-2 illustrates the complete vertical velocity guidance command system, and Table 3.6-1 notes the position, velocity and acceleration feedback gains from Ref. 9, 10 and 33.

Horizontal Plane Velocity Command Perturbation Guidance - As illustrated in Fig. 3.6-3, downrange position error and nominal crossrange velocity can be defined to be zero by assuming that the helicopter's nominal position along the trajectory is defined by its actual position. Nominal and actual positions and velocities are available in earth-relative axes, and nominal heading (ξ_o) is used to transform these quantities to local-level guidance axes. Figure 3.6-4 illustrates the horizontal-plane velocity guidance algorithm, and Table 3.6-2 lists the guidance gains. The altitude to downrange gain, $K_{\dot{x}}$, is nonzero only during ascending or descending flight, and is 0.0013 m^{-1} (0.0004 ft^{-1}) times the vertical velocity. Hence, a 2.54 m/s (500 fpm) descent results in the gain value of 0.0033 sec^{-1}. The crossrange gain depends on forward velocity, and takes the value -0.00135 m^{-1} (-0.00041 ft^{-1}) times the downrange velocity. Note that a variant of the horizontal guidance reported in Ref. 33 calculates nominal position along the trajectory from a nominal trajectory time history. Thus, the 4-D modification in Ref. 33 would feedback the resulting non-zero Δx_{DR}.

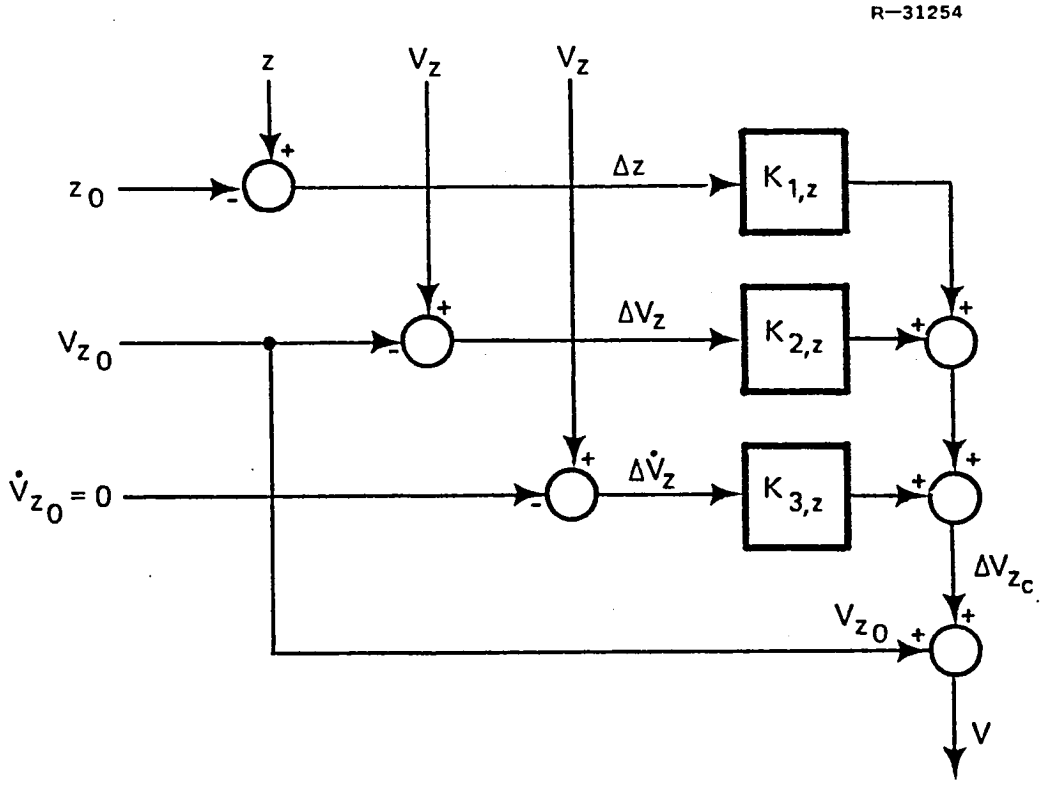

Figure 3.6-2 Vertical Guidance Flowchart

TABLE 3.6-1
VERTICAL GUIDANCE PERTURBATION GAINS

GAIN	REF. 9	REF. 33	REF. 10
$K_{1,z}$	$-0.0406\ sec^{-1}$ (60 kt, 31 m/s)	$-0.052\ sec^{-1}$	$-0.0333\ sec^{-1}$
$K_{2,z}$	0	$-0.207\ ms^{-1}/ms^{-1}$	0
$K_{3,z}$	0	-0.144 sec	0

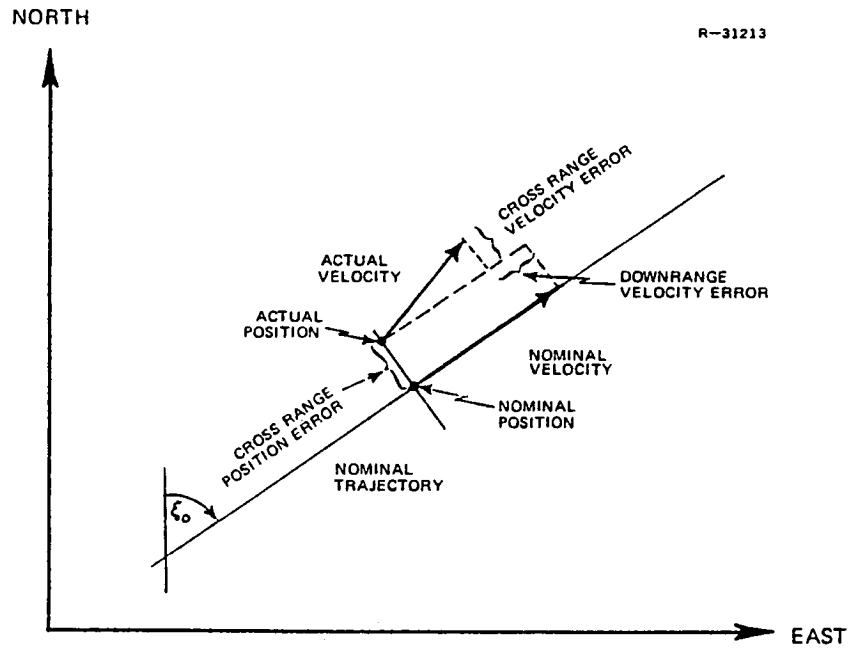

Figure 3.6-3 Horizontal Plane Position and Velocity Error Geometry

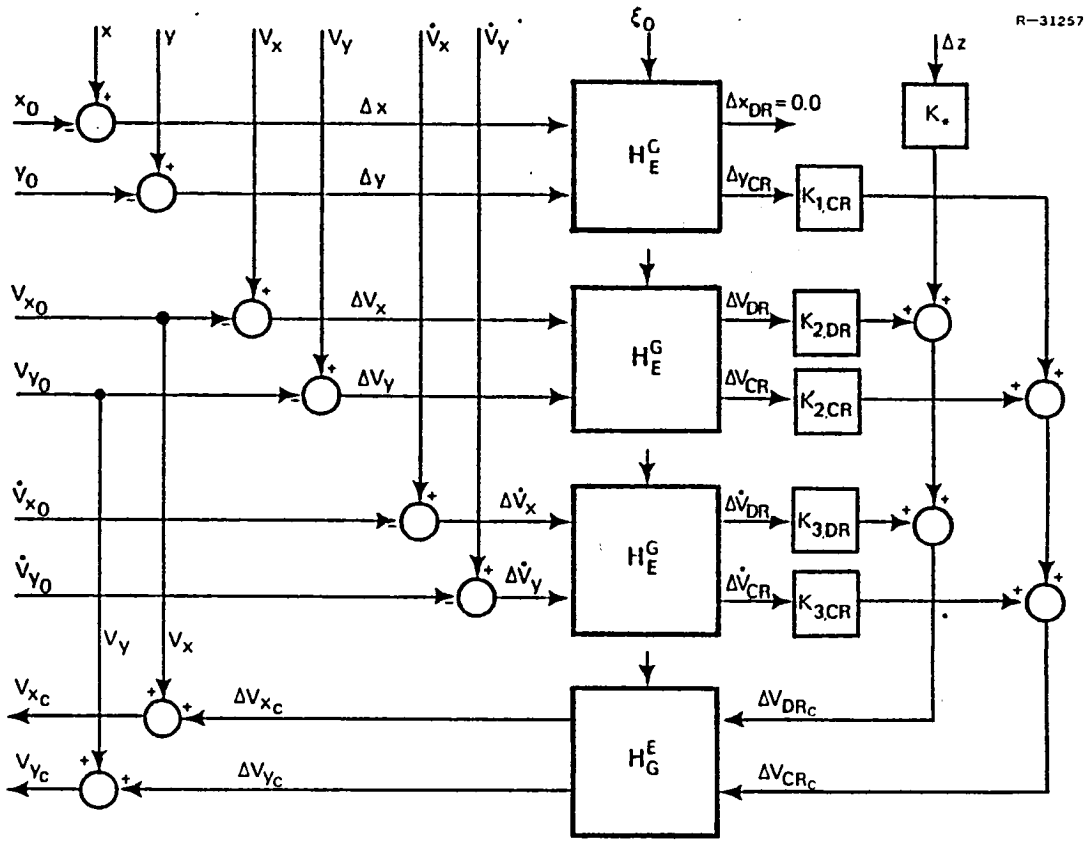

Figure 3.6-4 Horizontal Plane Velocity Guidance Flowchart

TABLE 3.6-2
HORIZONTAL PLANE PERTURBATION GUIDANCE GAINS

GAIN	REF. 9	REF. 33
K*	0.0 to 0.0033 sec^{-1}	0
$K_{2,DR}$	0	-2.05
$K_{3,DR}$	0	-2.32 sec
$K_{1,CR}$	-0.0416 sec^{-1} (60 kt, 31 m/s)	-0.0584 sec^{-1}
$K_{2,CR}$	0	-0.392
$K_{3,CR}$	0	9.5 sec

Horizontal Plane Attitude Command Perturbation Guidance - The pitch and roll Euler angle commands can be formed from perturbation local-level body axis velocity commands by the attitude autopilot given in Ref. 9 and shown in Fig. 3.6-5, where ΔV_{LAT} and ΔV_{LON} are the downrange and crossrange velocity errors, respectively. Table 3.6-2 gives the autopilot gains. The local level body axis velocity perturbation guidance algorithm shown in Fig. 3.6-6 is based on the velocity command algorithm discussed above and the gains (Table 3.6-4) are similar.

As defined in Ref. 10, the spiral guidance command vector consists of a longitudinal specific force command, a_c, a roll angle command, ϕ_c, and a vertical velocity command, V_{z_c}. By appending a yaw angle command and converting the a_c command to a θ_c command, it is possible to put the spiral command vector into the attitude form. The conversion from longitudinal specific force, a_c, to pitch command occurs by noting that a pitch attitude change tilts the lift vector forward, creating a longitudinal component of approximately $-g\Delta\theta$. The spiral perturbation guidance system is shown in Fig. 3.6-7. The gain values (Table 3.6-5) are derived from

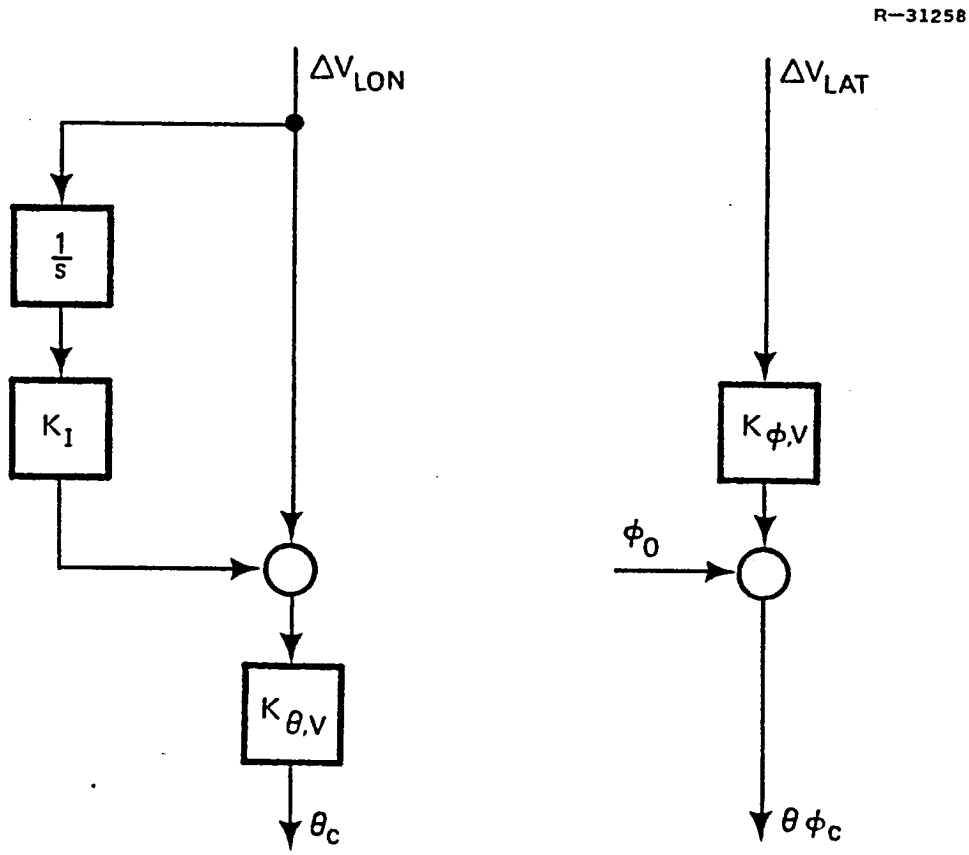

Figure 3.6-5 Attitude Autopilot Flowchart

TABLE 3.6-3
ATTITUDE AUTOPILOT GAINS

GAINS	VALUE
K_I	0.1 sec^{-1}
$K_{\theta,v}$	-0.01 rad/fps = -0.033 rad/m/s
$K_{\phi,v}$	-0.04 rad/fps = -0.13 rad/m/s

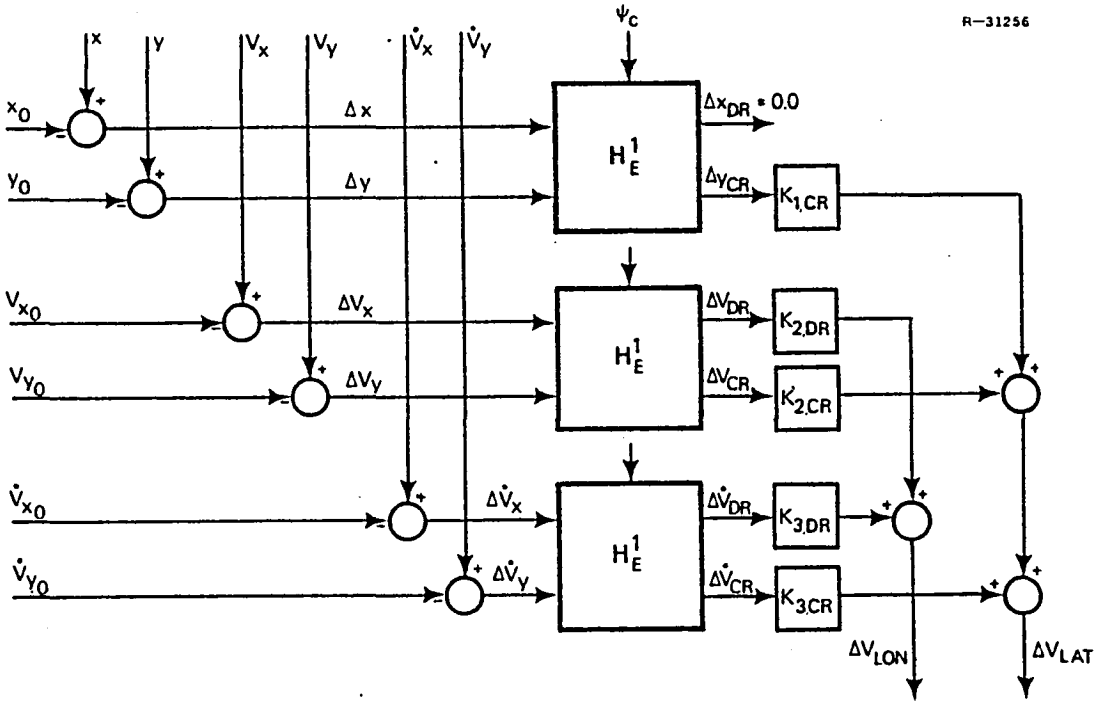

Figure 3.6-6 Local-Level Body Axis Velocity Perturbation Flowchart

TABLE 3.6-4

LOCAL-LEVEL-BODY VELOCITY PERTURBATION GAINS

GAINS	REF. 9	REF. 33
$K_{2,DR}$	-1.0	$-2.05\ ms^{-1}/ms^{-1}$
$K_{3,DR}$	0	-2.32 sec
$K_{1,CR}$	$-0.0416\ sec^{-1}$ (60 kt, 31 m/s)	$-0.0584\ sec^{-1}$
$K_{2,CR}$	-1.0	$-0.392\ ms^{-1}/ms^{-1}$
$K_{3,CR}$	0	-0.5 sec

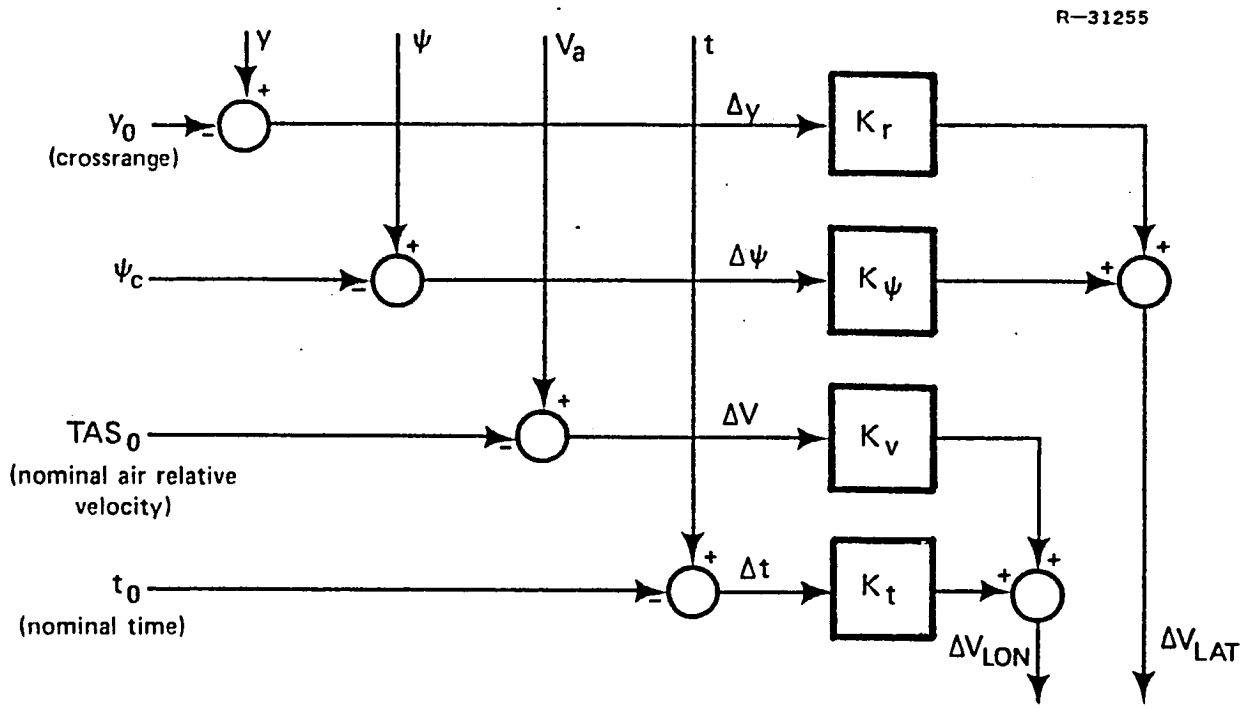

Figure 3.6-7 Spiral Guidance Perturbation Flowchart

TABLE 3.6-5
SPIRAL GUIDANCE GAINS

GAINS	REF. 10	
K_r	-0.125 sec^{-1}	$(C_{r_{REF.10}}/K_{\phi,v})$
K_ψ	13.5 m/s rad (44.25 fps/rad)	$(c_{\psi_{REF.10}}/K_{\phi,v})$
K_v	-0.466	$(-K_{v_{REF.10}}/(g\ K_{\theta,v}))$
K_t	0.95 m/s^2	$(-K_{t_{REF.10}}/(g\ K_{\theta,v}))$

the suggested gains in Ref. 10, as described by the formulae, which allow the use of the attitude autopilot in Fig. 3.6-5.

The longitudinal feedback loops merit some discussion. By flying a constant air-relative velocity (TAS) spiral, the aerodynamics remain constant as heading changes in the presence of wind, and the acceleration, although variable, is entirely lateral. The ground speed varies, which affects the time duration of the maneuver; hence, a time-error channel is given in Fig. 3.6-7. If time constraints are not necessary, this channel should be disabled (K_t=0) since it will introduce unwanted longitudinal acceleration.

3.7 FLIGHT COMPUTER SOFTWARE SPECIFICATIONS

The Kalman filter and control logic needed for real-time implementation of the VALT DFCS on board the VALT navigation, guidance and control (NGC) computer is presented in this section. The NGC computer provides a versatile autopilot structure while maintaining simplified communications with other programs, sensors, and control actuators by the use of an executive routine/functional subroutine format. The flight computer software outlined here reads all external variables at a single point, copying them into its dedicated storage, and forces the major support subroutines to be synchronous with the autopilot cycle. As a result, within each cycle the VALT DFCS is largely independent of other programs in the navigation, guidance, and control (NGC) computer because no additional information is needed by the VALT DFCS until the beginning of the next cycle.

The sequence of DFCS subroutines is arranged to minimize computation lag, i.e., the time interval between receiving a measurement in the NGC computer and transmitting

commands to the control actuators. As a consequence, the state estimation and control calculations are divided into two parts. State measurements are incorporated in the estimator (or filter) update in the early portion of the DFCS cycle, but the remaining state propagation does not occur until the DFCS commands have been written in the control actuator channels. Similarly, control calculations are broken down into components that must be performed to obtain a control command and components that can be performed while waiting for the next measurement cycle.

The sequence for a single DFCS frame is illustrated in the functional flow diagram of Fig. 3.7-1. The DFCS program is called on a periodic basis, at a single fixed rate of 10 frames per second. Initialization branches are asynchronous, occurring only when the flight control mode changes or when there is a computer restart. Control and filter gains are currently updated every second while all other branches in the program are synchronous with the DFCS sampling rate.

The basic subroutines of the VALT DFCS are the following

- Sequence and Input/Output Initialization Subroutine - This subroutine establishes the address of a list of subroutine addresses, according to the flight mode and initializes all indices.
- Read Subroutine - This subroutine copies required inputs to the program into dedicated temporary storage.
- Controller, Filter, and Guidance Initialization Subroutine - These subroutines initialize command values, state estimates, and gains either at predetermined values or at the appropriate values read in as required by restart or flight mode.

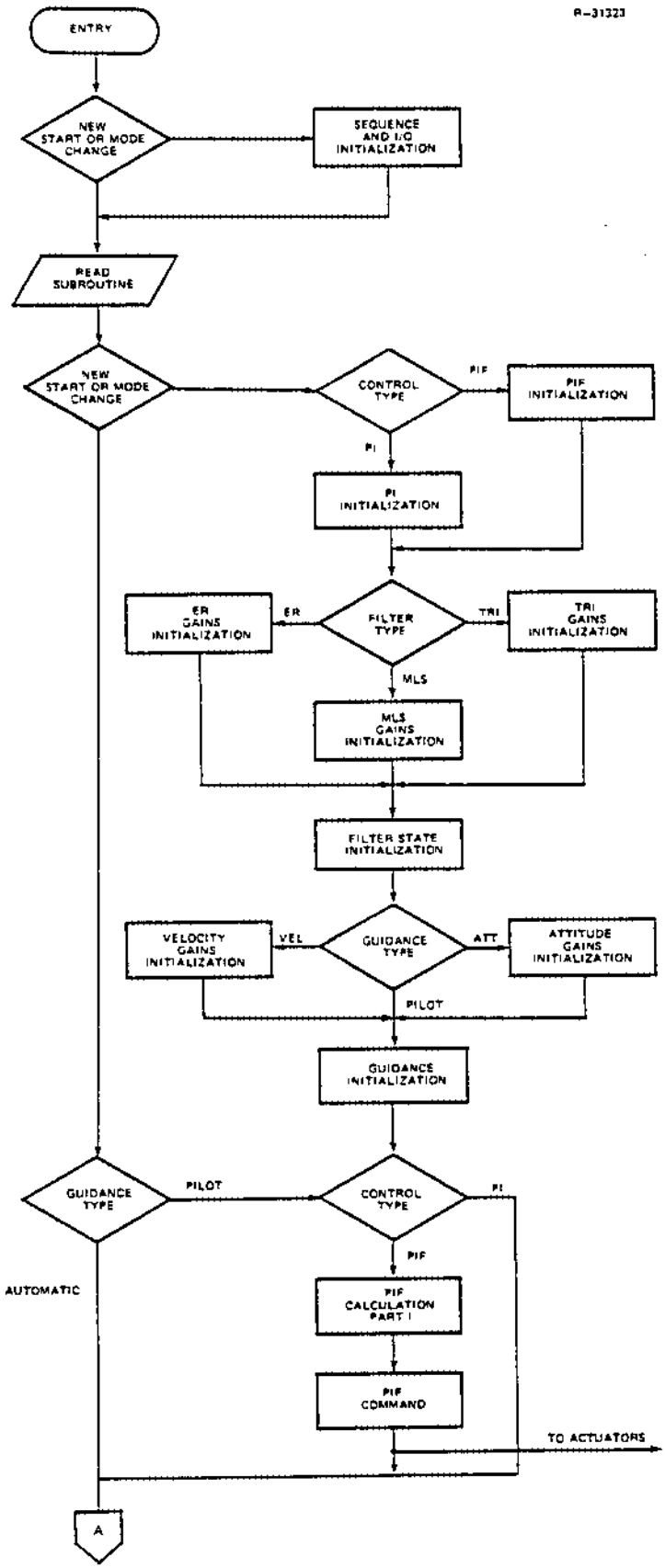

Figure 3.7-1 Functional Flow Diagrams for the DFCS

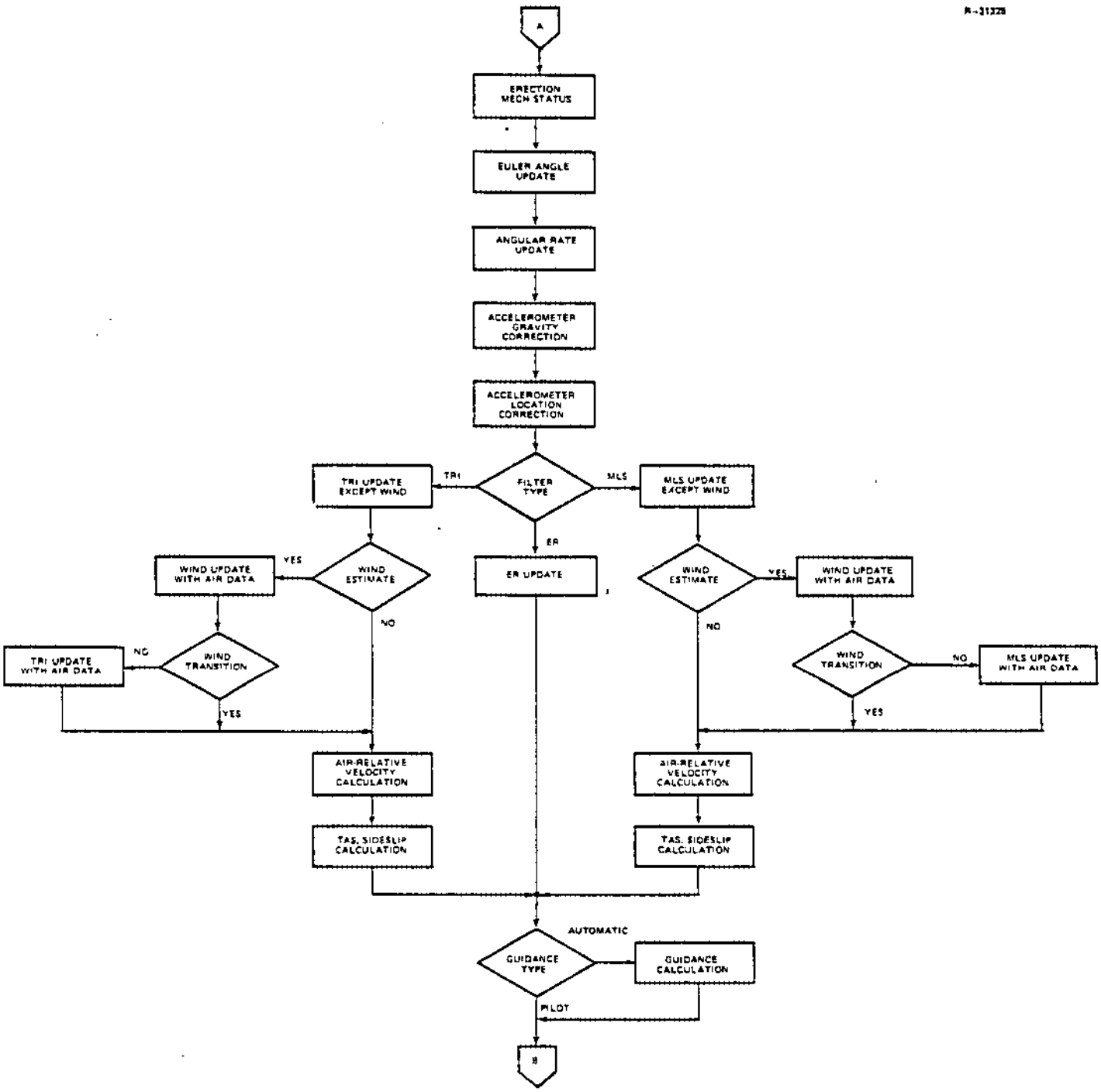

Figure 3.7-1 Functional Flow Diagrams for the DFCS (Continued)

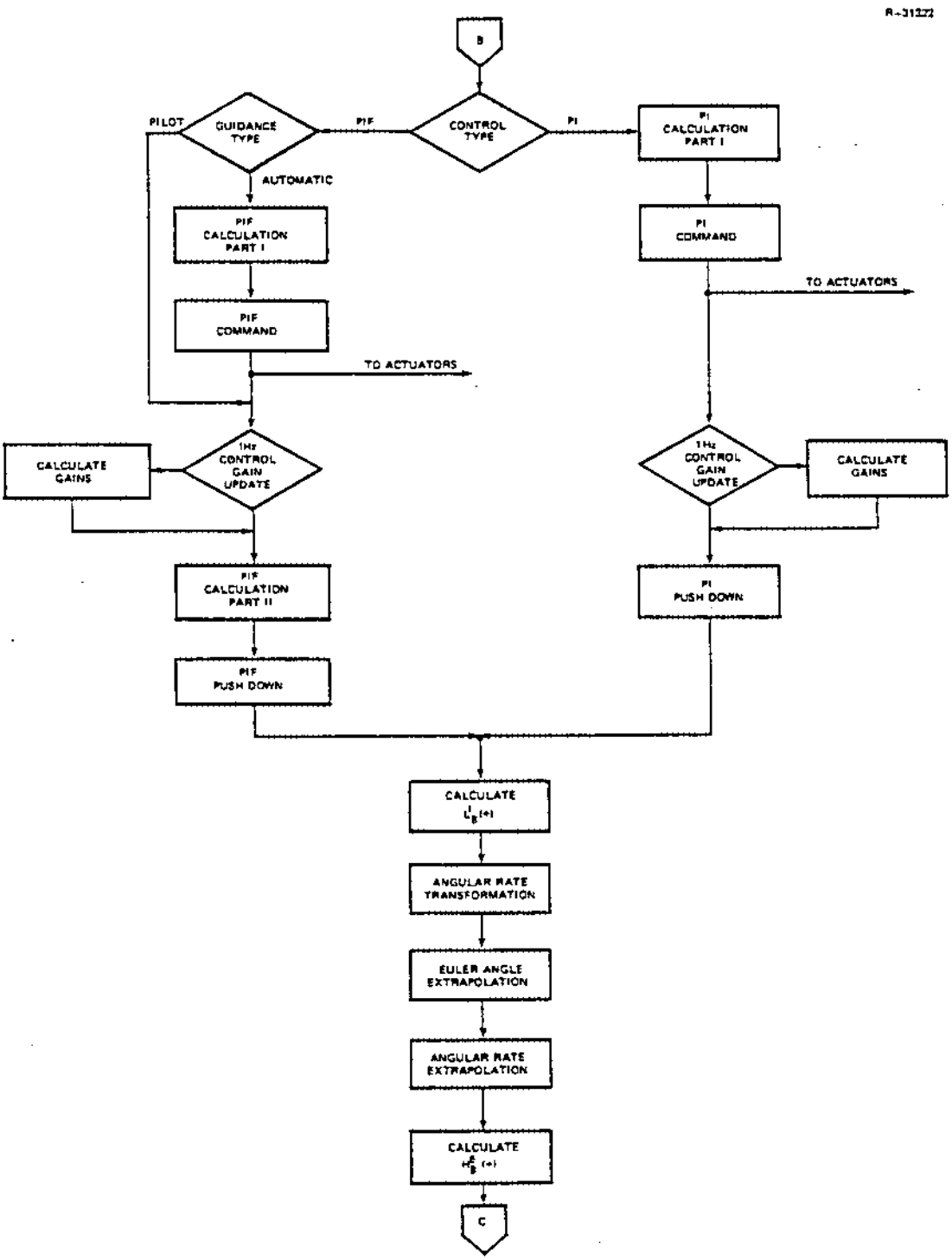

Figure 3.7-1 Functional Flow Diagrams for the DFCS (Continued)

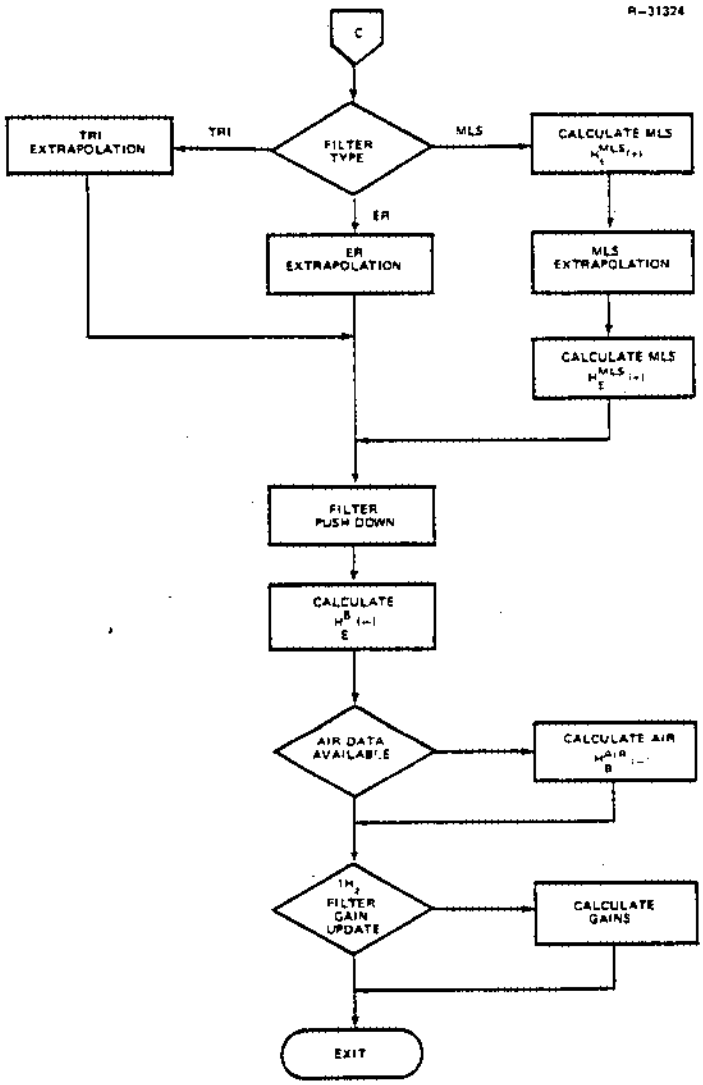

Figure 3.7-1 Functional Flow Diagrams for the DFCS (Continued)

- State Estimation Subroutines (Part I) - Measurements are processed in the update part of the filters.

- Guidance Subroutines - The state estimates are used to form the guidance commands.

- Control Subroutine (Part I) - This subroutine uses the outputs of the estimation subroutine and the guidance commands to derive control actuator commands.

- Control Subroutine (Part II) - This subroutine computes the controller gains from the gain schedules and prepares the controller for the next DFCS frame. For the incremental control laws, this consists of "pushing-down" the controller variables, i.e., storing the k^{th} value in the $(k-1)^{st}$ location, etc.

- State Estimation Subroutines (Part II) - The calculations performed here prepare the estimator for the incorporation of measurements on the next DFCS frame. For the state-space estimators, the state is propagated to the next sampling instant. The transformation matrices and the filter gains are updated as required.

Characteristics of the VALT software include: 1) considerable logic is required in the velocity filters to determine if the air-data sensors are in a valid operational region and 2) under pilot commands only a small portion of the PIF calculations need be performed before it is required to transfer the control command to the actuator channels. More detailed DFCS software logic can be found in TVHIS documentation (Ref. 4).

4. VALT DFCS EVALUATION

The performance of the VALT DFCS is evaluated in the following sections using straightforward linear systems techniques and a complex differential-difference equation helicopter simulation. These evaluations illustrate acceptable DFCS performance and lay the groundwork for actual flight test of the state estimators and control laws developed in earlier chapters of this report.

The eigenvalue-eigenvector analysis of the continuous-time helicopter model with a discrete-time controller is described in Section 4.1. Equivalent continuous-time eigenvalues and eigenvectors of the helicopter-controller system are derived, and they indicate desirable closed-loop helicopter response characteristics. An interesting facet of this analysis is that the dynamic controllers not only improve the classical aircraft mode characteristics but add new response modes associated with the controller integrators and filters.

The command response of the controller is examined in Section 4.2 along straight, steady trajectory segments. These results indicate that the response requirements are essentially met with scheduled controller gains and state estimators operating. The effects of rotor and actuator dynamics, examined in Section 4.3, are to increase response overshoot without large changes in response time. The advantages of an integrator compensator in the controller are evident, because the controller senses the response lag caused by the rotor and actuator lags and speeds up the response to compensate for them. Computation time delay is a major concern in digital

control system design, and Section 4.4 examines this problem. Stability is retained, even when the delay approaches an entire sampling period, but overshoot does increase somewhat as the controller attempts to compensate for the delay through the guidance error integration.

The effects of sensor errors and measurement noise are examined in Section 4.5, and the quality of the sensor suite is seen to have major impacts on controller structure, command vector specification and estimator design. Velocity command systems require careful inner-loop (angular rate) design and good sensors, and the extra filtering available in PIF (as compared to PI) is beneficial in the case of sub-optimal state estimators. The choice between multilateration and range-azimuth-elevation radio navigation aids is a trade-off between range and terminal-area accuracy. The effects of wind on controller-estimator performance are illustrated in Section 4.6.

The simulation of time-varying systems is discussed in Section 4.7, and an example is given in Section 4.8 which illustrates the performance of spiral guidance, controller and estimator in a spiral descent entry. Cross-axis effects are seen to be important, and there are indications that the roll guidance channel could be improved. These simulations provide the basis for the use of the VALT DFCS in actual flight tests.

4.1 EIGENVALUE/EIGENVECTOR ANALYSIS

The stability characteristics of a linear-time-invariant system are described by the eigenvalues of its fundamental matrix (or roots of its characteristic equation). The degree of involvement of each state variable in each mode of motion

is identified by the corresponding eigenvectors (Ref. 12). The variation in stability can be traced by the root locus plot, i.e., a complex-plane graph of the locations of the roots as parameters of the system vary. For continuous-time systems (e.g., helicopters with analog controllers), root locations in the "left-half plane" indicate stability, and the magnitude and phase angle of each root are direct indicators of the time constant (or natural frequency and damping ratio) of the corresponding mode of motion. For discrete-time systems (e.g., helicopters with digital controllers), root locations within the "unit circle" indicate stability, but there is no easy definition of system dynamics from the root locations -- in fact, closely spaced roots may represent markedly different characteristics. Consequently, it is common practice to "map" the discrete-time roots into an equivalent continuous-time representation for evaluation of the digital controller (Ref. 34).

The equivalent continuous-time eigenvalues and eigenvectors of the VALT Research Aircraft with digital control loops closed are computed by such a mapping. "Closing the loop" with the PIF controller in position form (Eqs. B-49 to B-52), the sampled-data version of the helicopter design model (Eq. 3.4-9) is

$$\begin{bmatrix} \Delta\underline{x} \\ \Delta\underline{u} \\ \Delta\underline{\xi} \end{bmatrix}_{k+1} = \begin{bmatrix} \Phi & \Gamma & 0 \\ -\Delta t C_3 & (I-\Delta t C_4) & -\Delta t C_5 \\ \Delta t H_p & 0 & I \end{bmatrix} \begin{bmatrix} \Delta\underline{x} \\ \Delta\underline{u} \\ \Delta\underline{\xi} \end{bmatrix}_k + \begin{bmatrix} 0 \\ \Delta t E_1 \\ -\Delta t I \end{bmatrix} \Delta\underline{y}_{d_{k+1}} \tag{4.1-1}$$

Similarly, using the PI controller in position form, the closed-loop system is described by

$$\begin{bmatrix}\Delta\underline{x}\\ \Delta\underline{\xi}\end{bmatrix}_{k+1} = \begin{bmatrix}\Phi-\Gamma C_1 & -\Gamma C_2\\ \Delta t H_p & I\end{bmatrix}\begin{bmatrix}\Delta\underline{x}\\ \Delta\underline{\xi}\end{bmatrix}_k + \begin{bmatrix}0\\ -\Delta t I\end{bmatrix}\Delta\underline{y}_{d_{k+1}} \tag{4.1-2}$$

Defining the closed-loop state vector $\Delta\underline{x}_{CL} = \left[\Delta\underline{x}^T\ \Delta\underline{u}^T\ \Delta\underline{\xi}^T\right]$ for PIF and $\Delta\underline{x}_{CL} = \left[\Delta\underline{x}^T\ \Delta\underline{\xi}^T\right]$ for PI enables either closed-loop system to be written as

$$\Delta\underline{x}_{CL_{k+1}} = \Phi_{CL}\ \Delta\underline{x}_{CL_k} + \Gamma_{CL}\Delta\underline{y}_{d_{k+1}} \tag{4.1-3}$$

where the closed-loop dynamics are described by Φ_{CL}. The continuous-time equivalent of Φ_{CL} is

$$F_{CL} = \frac{1}{\Delta t}\ \ln\Phi_{CL} \tag{4.1-4}$$

$$= \frac{1}{\Delta t}\ \left[(\Phi_{CL}-I) - \frac{1}{2}(\Phi_{CL}-I)^2 + \frac{1}{3}(\Phi_{CL}-I)^3 - \ldots\right] \tag{4.1-5}$$

and its eigenvalues are the roots of the characteristic equation specified by the determinant

$$\left|\lambda I - F_{CL}\right| = 0 \tag{4.1-6}$$

The eigenvector, $\underline{x}_i$, for the eigenvalue λ_i is the nonzero solution vector of the equation,

$$F_{CL}\underline{x}_i = \lambda_i\underline{x}_i \tag{4.1-7}$$

A comparison of scheduled and optimal root loci for PIF velocity is given in Ref. 2. Tables 4.1-1 and 4.1-2 present a comparison of the open-loop, optimal closed-loop, and scheduled closed-loop eigenvalues for TAS = 41.2 m/s (80 kt) straight and level flight, a primary design point. In addition to the classical aircraft modes, PI and PIF introduce new modes associated with control system integrators, and PIF introduces new modes associated with the low-pass filters.

Although closed-loop eigenvalue locations are not used as an indicator in controller design, they exhibit good control characteristics. Short period and Dutch roll complex pairs fall well within the requirements of military specifications MIL-F-8330 (Ref. 11) as does the roll mode time constant. All other complex pairs have damping ratios greater than 0.5. Noteworthy observations are 1) the attitude systems have slow velocity modes (real phugoid (speed) and closed-loop "spiral") in order to meet the angle command steady-state requirements, 2) the low-pass filter natural frequency locations are in close proximity to open-loop natural frequencies, and 3) the scheduled eigenvalues remain near their optimal counterparts, but with increased damping, in most cases.

Further comparisons of the short period, Dutch roll and phugoid modes for the optimal and scheduled designs over a number of flight conditions are in Tables 4.1-3 to 4.1-6. PIF increases the natural frequency of the complex pairs with velocity and decreases the low-pass filter bandwidths. Eigenvalues for PI remain fairly constant over the operating range. The gain schedule causes some of the PIF phugoid mode 2 damping ratios in Table 4.1-6 to decrease below 0.5 indicating possible problems with vertical height oscillations.

TABLE 4.1-1

COMPARISON OF OPTIMAL EIGENVALUES AT 41.2 m/s (80 kt) STRAIGHT AND LEVEL FLIGHT

DYNAMIC MODE	OPEN LOOP			PI ATTITUDE			PIF ATTITUDE			PIF VELOCITY		
	ω_n rad/sec	ζ, -	τ, sec	ω_n, rad/sec	ζ, -	τ, sec	ω_n, rad/sec	ζ, -	τ, sec	ω_n, rad/sec	ζ, -	τ, sec
SHORT PERIOD	0.359	-1.77	-	2.83	0.597	-	4.31	0.875	-	3.95	0.861	-
PHUGOID(1)*	0.256	0.342	-	-	-	40.2	-	-	40.4	0.445	0.668	-
(2)	-	-	-	1.60	0.760	-	2.05	0.563	-	1.93	0.575	-
DUTCH ROLL	0.394	-0.190	-	2.61	0.585	-	2.75	0.634	-	2.97	0.694	-
ROLL	-	-	0.899	-	-	0.288	-	-	0.551	-	-	0.642
SPIRAL	-	-	25.77	-	-	13.68	-	-	13.60	0.548	0.701	-
HEADING	-	-	∞	2.28	0.547	-	2.09	0.589	-	2.28	0.687	-
$\Delta\xi_\theta$ OR $\Delta\xi_{V_x}$	NONE			-	-	0.470	-	-	1.23	0.445	0.668	-
ξ_ϕ OR $\Delta\xi_{V_y}$				-	-	0.430	-	-	1.18	0.548	0.701	-
$\Delta\xi_\psi$				2.28	0.547	-	2.09	0.589	-	2.28	0.687	-
$\Delta\xi_{V_z}$				1.60	760	-	2.05	0.563	-	1.93	0.575	-
$\Delta\delta_B$	NONE			NONE			-	-	0.746	-	-	1.18
$\Delta\delta_C$							-	-	0.609	-	-	0.669
$\Delta\delta_S$							0.872	0.967	-	1.08	0.767	-
$\Delta\delta_R$							0.872	0.967	-	1.08	0.767	-

*Phugoid in closed-loop splits and each component either recombines with another mode to form a complex pair or the component becomes a real mode.

TABLE 4.1-2

COMPARISON OF SCHEDULED EIGENVALUES AT 41.2 m/s (80 kt) STRAIGHT AND LEVEL FLIGHT

DYNAMIC MODE	PI ATTITUDE			PIF ATTITUDE			PIF VELOCITY		
	ω_n rad/sec	ζ, -	τ, sec	ω_n rad/sec	ζ, -	τ, sec	ω_n rad/sec	ζ, -	τ, sec
SHORT PERIOD	2.92	0.630	-	4.05	0.892	-	3.73	0.875	-
PHUGOID(1)*	-	-	40.6	-	-	41.7	0.405	0.681	-
(2)	1.63	0.754	-	2.10	0.592	-	1.99	0.590	-
DUTCH ROLL	2.60	0.595	-	2.81	0.635	-	3.06	0.665	-
ROLL	-	-	0.322	-	-	0.630	-	-	0.685
SPIRAL	-	-	13.6	-	-	13.77	0.524	0.757	-
HEADING	2.26	0.563	-	2.27	0.594	-	2.35	0.661	-
$\Delta\xi_\theta$ OR $\Delta\xi_{V_x}$	-	-	0.462	-	-	1.41	0.405	0.681	-
$\Delta\xi_\phi$ OR $\Delta\xi_{V_y}$	-	-	0.423	-	-	1.18	0.524	0.757	-
$\Delta\xi_\psi$	2.26	0.563	-	2.27	0.594	-	2.35	0.661	-
$\Delta\xi_{V_z}$	1.63	0.754	-	2.10	0.592	-	1.99	0.590	-
$\Delta\delta_B$	NONE			1.32	0.961	-	1.29	0.979	-
$\Delta\delta_C$				1.32	0.961	-	1.29	0.979	-
$\Delta\delta_S$				1.12	0.948	-	1.00	0.775	-
$\Delta\delta_R$				1.12	0.948	-	1.00	0.775	-

*Phugoid in closed-loop splits and each component either recombines with another mode to form a complex pair or the component becomes a real mode.

TABLE 4.1-3

OPTIMAL SHORT PERIOD AND DUTCH ROLL EIGENVALUE VARIATION WITH FLIGHT CONDITION

FLIGHT CONDITION	OPEN LOOP				PI ATTITUDE				PIF ATTITUDE				PIF VELOCITY			
	SHORT PERIOD		DUTCH ROLL		SHORT PERIOD		DUTCH ROLL		SHORT PERIOD		DUTCH ROLL		SHORT PERIOD		DUTCH ROLL	
	ω_n, rps	ζ -	ω_n, rps	ζ -	ω_n, rps	ζ -	ω_n, rps	ζ -	ω_n, rps	ζ -	ω_n, rps	ζ -	ω_n, rps	ζ -	ω_n, rps	ζ -
HOVER	0.711	3.37*	0.466	-0.168	2.71	0.534	2.65	0.580	2.79	0.630	2.38	0.546	2.28	0.631	1.99	0.514
V=60 kt	0.391,	-1.93*	0.418	-0.161	2.79	0.587	2.61	0.584	3.56	0.903	2.76	0.634	3.32	0.880	2.60	0.652
V=120 kt	0.317,	-1.44*	0.380	-0.307	2.87	0.614	2.61	0.583	5.59	0.843	2.75	0.634	5.09	0.835	3.71	0.709
V=80 kt $\dot{z}$=1000 fpm	0.349,	-1.54*	0.328	-0.059	2.84	0.603	2.59	0.585	4.35	0.871	2.73	0.635	4.02	0.857	3.05	0.670
V=80 kt $\dot{z}$=500 fpm $\dot{\psi}$=0.05 rps	0.357,	-1.79*	0.361	-0.186	2.75	0.603	2.58	0.584	4.33	0.872	2.73	0.633	3.97	0.860	2.98	0.687

*Two Real Roots.

TABLE 4.1-4

SCHEDULED SHORT PERIOD AND DUTCH ROLL EIGENVALUE VARIATION WITH FLIGHT CONDITION

FLIGHT CONDITION	PI ATTITUDE				PIF ATTITUDE				PIF VELOCITY			
	SHORT	PERIOD	DUTCH	ROLL	SHORT	PERIOD	DUTCH	ROLL	SHORT	PERIOD	DUTCH	ROLL
	ω_n, rps	ζ -	ω_n, rps	ζ -	ω_n, rps	ζ -	ω_n, rps	ζ -	ω_n, rps	ζ -	ω_n, rps	ζ -
HOVER	2.66	0.551	2.64	0.579	2.81	0.634	2.45	0.514	2.34	0.658	2.09	0.581
V=60 kt	2.65	0.587	2.62	0.576	3.70	0.908	2.81	0.634	3.45	0.878	2.79	0.647
V=120 kt	3.49	0.725	2.62	0.590	5.06	0.803	2.76	0.630	4.54	0.794	3.64	0.703
V=80 kt $\dot{z}$=1000 fpm	3.13	0.650	2.56	0.599	3.89	0.911	2.81	0.630	3.76	0.883	3.01	0.671
V=80 kt $\dot{z}$=500 fpm $\dot{\psi}$=0.05 rps	3.14	0.648	2.59	0.582	4.09	0.912	3.08	0.662	3.72	0.884	2.97	0.706

TABLE 4.1-5

OPTIMAL PHUGOID EIGENVALUE VARIATION WITH FLIGHT CONDITION

FLIGHT CONDITION	PI ATTITUDE			PIF ATTITUDE			PIF VELOCITY			
	PHUGOID 1		PHUGOID 2	PHUGOID 1		PHUGOID 2	PHUGOID 1		PHUGOID 2	
	ω_n, rps	ζ -	τ, sec	ω_n, rps	ζ -	τ, sec	ω_n, rps	ζ -	ω_n, rps	ζ -
HOVER	1.64	0.728	45.2	2.38	0.546	46.0	0.507	0.715	1.99	0.514
V=60 kt	1.57	0.752	47.2	2.10	0.591	42.6	0.511	0.668	1.94	0.607
V=120 kt	1.64	0.781	28.6	2.12	0.558	28.3	0.361	0.682	2.03	0.554
V=80 kt $\dot{z}$=1000 fpm	1.57	0.758	43.1	2.03	0.563	43.4	0.447	0.666	1.91	0.582
V=80 kt $\dot{z}$=500 fpm $\dot{\psi}$=0.05 rps	1.58	0.762	42.8	2.1	0.562	43.1	0.442	0.645	1.92	0.580

TABLE 4.1-6

SCHEDULED PHUGOID EIGENVALUE VARIATION WITH FLIGHT CONDITION

FLIGHT CONDITION	PI ATTITUDE			PIF ATTITUDE			PIF VELOCITY			
	PHUGOID 1		PHUGOID 2	PHUGOID 1		PHUGOID 2	PHUGOID 1		PHUGOID 2	
	ω_n, rps	ζ -	τ, sec	ω_n, rps	ζ -	τ, sec	ω_n, rps	ζ -	ω_n, rps	ζ -
HOVER	1.64	0.745	45.2	1.98	0.532	46.9	0.569	0.715	1.95	0.423
V=60 kt	1.57	0.737	47.7	2.06	0.572	47.4	0.493	0.654	1.82	0.581
V=120 kt	1.64	0.761	29.3	2.14	0.654	29.2	0.319	0.664	2.10	0.608
V=80 kt $\dot{z}$=1000 fpm	1.62	0.755	43.5	2.13	0.590	44.5	0.375	0.655	1.99	0.582
V=80 kt $\dot{z}$=500 fpm $\dot{\psi}$=0.05 rps	1.85	0.794	44.2	1.79	0.374	44.5	0.398	0.673	2.07	0.540

Eigenvector magnitudes associated with symmetric, descending forward flight ($\dot{z}$ = 5.08 m/s (1000 fpm), $\dot{x}$ = 41.2 m/s (80 kt)) and asymmetric turning flight ($\dot{z}$ = 0 m/s, TAS = 30.9 m/s (60 kt), $\dot{\psi}$ = 0.05 rad/sec) are shown in Tables 4.1-5 and 4.1-6, respectively. Lateral and longitudinal dynamics are essentially uncoupled in symmetric flight but have significant interaction in asymmetric flight. The Dutch roll mode (typically a rolling-yawing motion) contains more pitch rate than roll rate in Table 4.1-6, and the short period mode (a pitch rate, Δw velocity oscillation) is felt in Δv, Δp, and Δr responses. This illustrates why coupled control laws, with feed-forward compensation (such as the VALT DFCS), are valuable in meeting precise control requirements. Cross-axis effects are significant in asymmetric fight even if the dynamic modes are well-damped.

4.2 COMMAND RESPONSE OF LINEAR, TIME-INVARIANT SYSTEM MODELS

The command response of the scheduled-gain DFCS, with and without operational filters in the feedback loop, is presented in this section. Simulations with the filters off (i.e., perfect measurements) are generated using the discrete-time linear perturbation helicopter design models shown in Eq. B-17 for PI and Eq. B-35 for PIF. The perfect measurement or DIGADAPT program (Ref. 14) simulations begin at the origin of the perturbation system with the vehicle heading north (ψ=0). Simulations with the operational velocity, angular rate, and angular position filters use total values and are produced with the program TVHIS. Aircraft perturbation dynamics in TVHIS are obtained by integrating the continuous-time linear time-invariant model shown in the first row of Eq. 3.1-1 and the result is added to the trim states to produce the total state. Two points in the approach trajectory are used to

TABLE 4.1-7

MAGNITUDES OF DUTCH ROLL AND SHORT PERIOD EIGENVECTOR COMPONENTS IN FORWARD FLIGHT

R-31262

SYSTEM	DUTCH ROLL	SHORT PERIOD*
OPEN LOOP		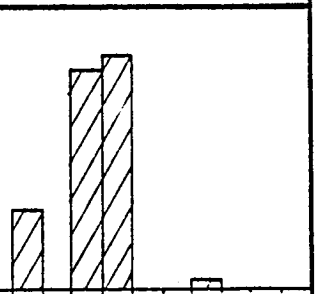
PI ATTITUDE	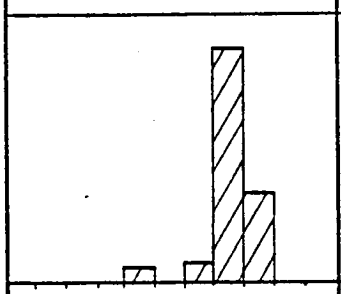	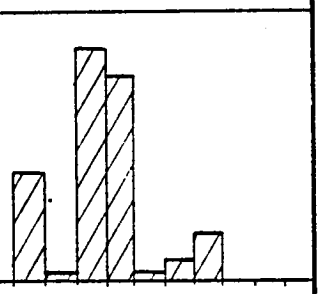
PIF ATTITUDE	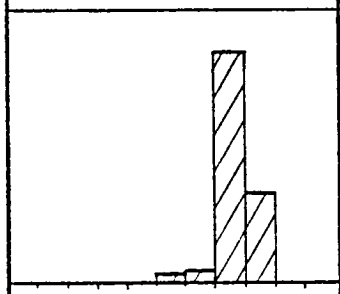	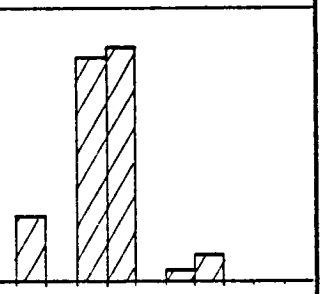
PIF VELOCITY	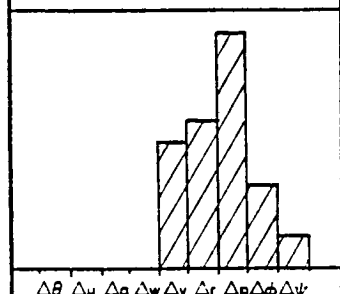	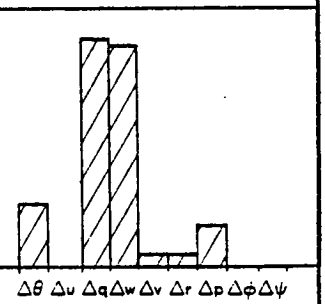

*REAL ROOT

TABLE 4.1-8

MAGNITUDES OF DUTCH ROLL AND SHORT PERIOD EIGENVECTOR COMPONENTS IN TURNING FLIGHT

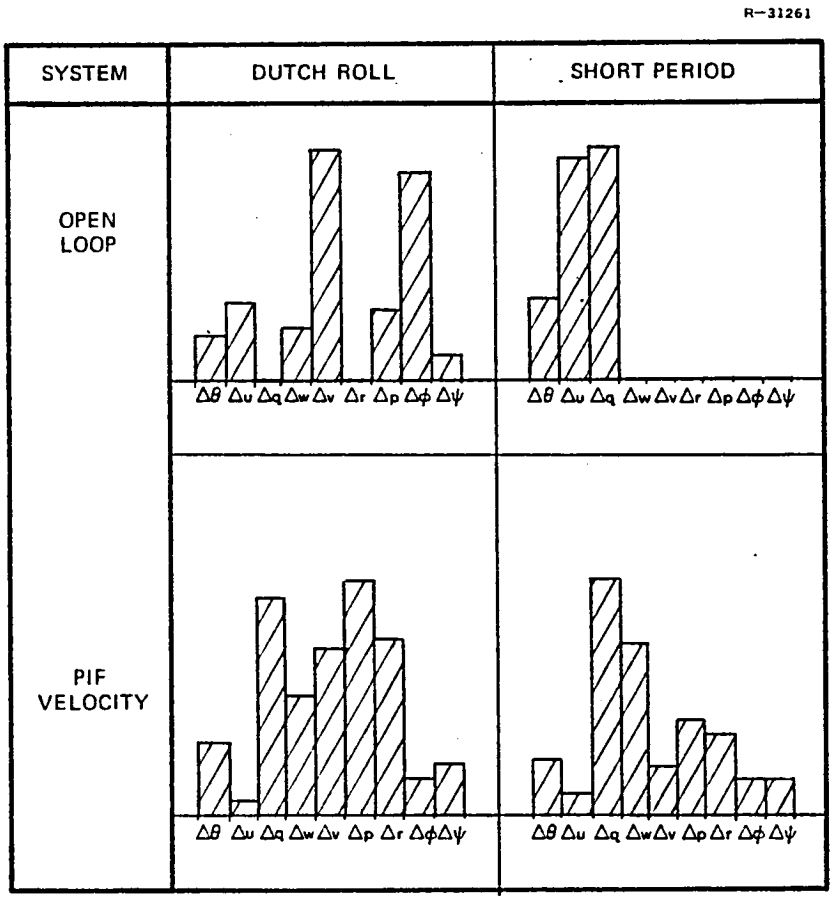

generate TVHIS results; hover and the initial starting point in Fig. 3.1-2 (TAS = 34 m/s (65 kt) straight and level, ψ = 135 deg). DIGADAPT results are developed (assuming perfect measurements) using hover, TAS = 30.9 m/s (60 kt) straight and level flight with ψ = 0 deg, and ascending flight, TAS = 30.9 m/s (60 kt), $\dot{z}$ = 2.54 m/s (500 fpm) with ψ = 0 deg.

Figure 4.2-1 illustrates response of the PI attitude-command law to a 3.28 m/s (10 fps) step command in vertical velocity at hover using the TRI-ECF filter, MLS-ECF filter and perfect measurements. The velocity filter gains are

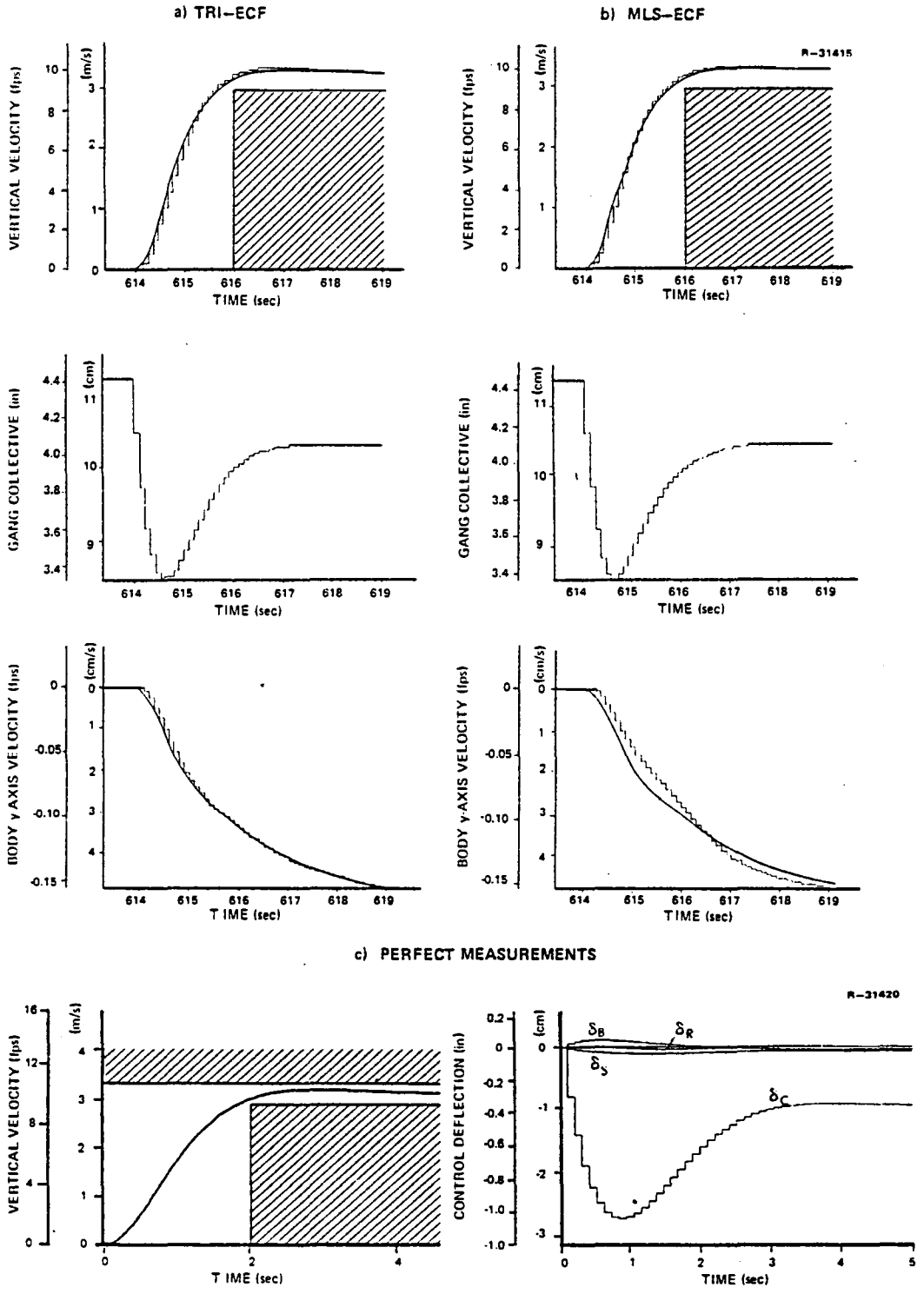

Figure 4.2-1 PI-Attitude Vertical Velocity Command Response at Hover

large at the touchdown point, and the V_z response in the three cases are almost identical, meeting the step response criteria. The difference in the filters are evident in the v response, where the TRI-ECF filter tracks better because of velocity measurements. As a whole, PI attitude step responses are good and meet the step response criteria in most cases (See Table 3.4-2).

The PIF attitude command responses to 0.1-radian step commands in pitch, yaw and roll are shown in Figs. 4.2-2 to 4.2-4. The design criteria are superimposed on the θ, ψ, and ϕ responses and are all satisfied except for the pitch response using perfect measurements (see Table 3.4-4). The "staircased" control inputs, which are smoothed by the actuators before reaching the rotors in DFCS simulations in Section 4.4, are well shaped and there is a small amount of coupled control action to minimize cross-axis response. Each of the three attitude simulations employ a different velocity filter. The flight condition is actually outside the range of the multilateration system, but the gain schedule gives adequate results.

The PIF velocity command responses for a 3.28 m/s (10 fps) lateral command and a 0.1 rad (large) yaw command are shown in Figs. 4.2-5 and 4.2-6, respectively. Neither command is accompanied by appropriate turn coordination subcommands; hence, the craft is held at a sideslip angle by gang cyclic (δ_s) deflection. All the commands satisfy the response criteria except for yaw angle which has a slight excessive overshoot using filtered measurements. The effects of the ER-ECF can be observed in Fig. 4.2-6 for the estimate of V_x. Errors near 0.3 to 1 m/s (1 to 3 fps) can be expected in noise-free transients because of inherent filter lag in both the angle and velocity filters. In the climbing forward flight condition

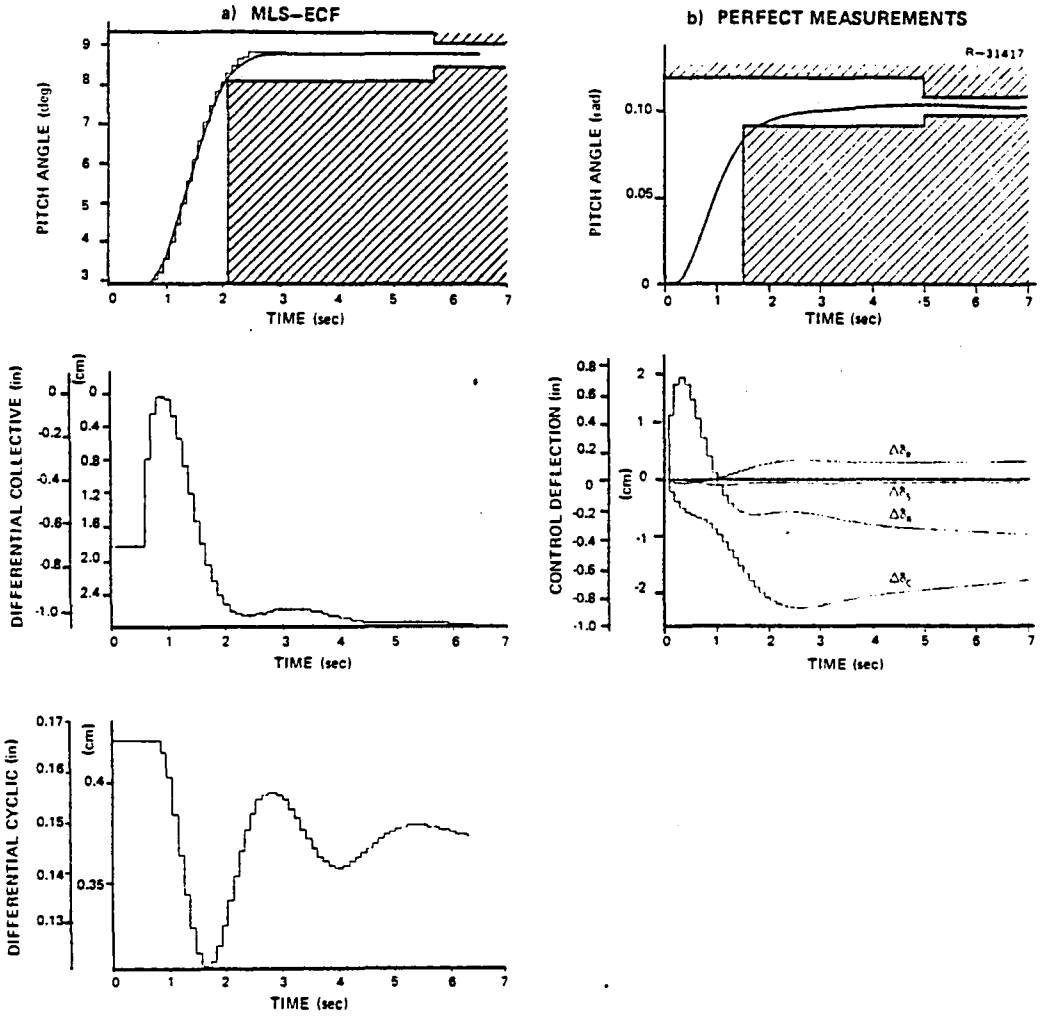

Figure 4.2-2 PIF Attitude Pitch Angle Response (TAS = 34 m/s (65 kt) for MLS-ECF and 30.9 m/s (65 ft) for Perfect Measurements, S&L Flight)

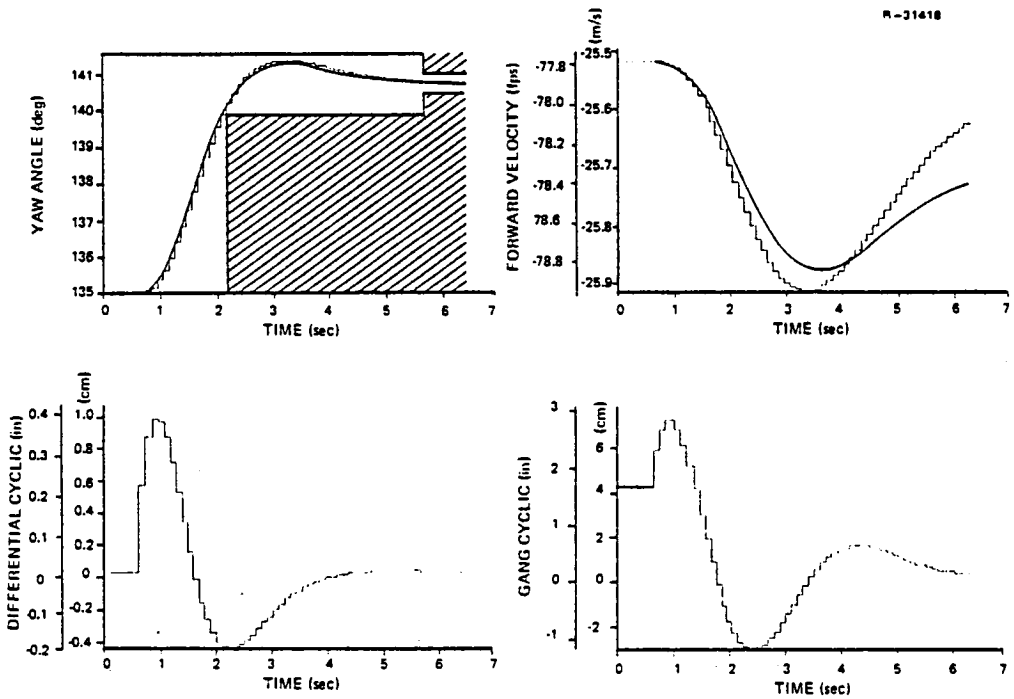

Figure 4.2-3 PIF Attitude Yaw Angle Response (TAS = 34 m/s (65 kt), S&L Flight)

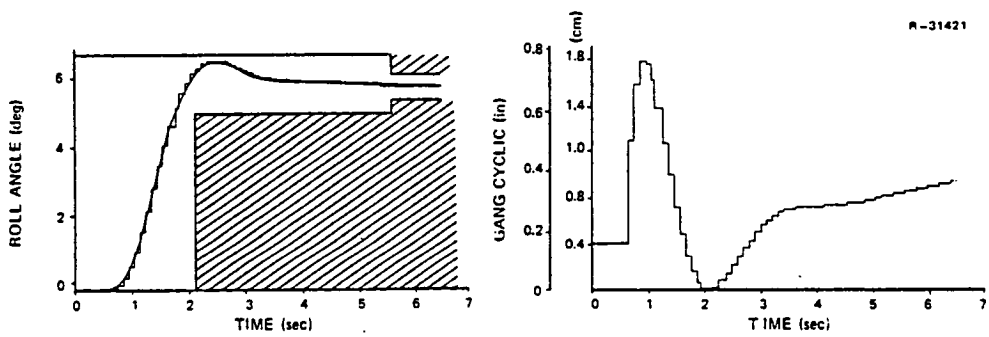

Figure 4.2-4 PIF Attitude Roll Response With the TRI-ECF (TAS = 34 m/s (65 kt) S&L Flight)

previously mentioned, the forward and vertical velocty step responses in Fig. 4.2-7 are within specifications with perfect measurements. Additional PIF velocity responses with operational filters are shown in Figs. 4.5-3 and 4.6-1.

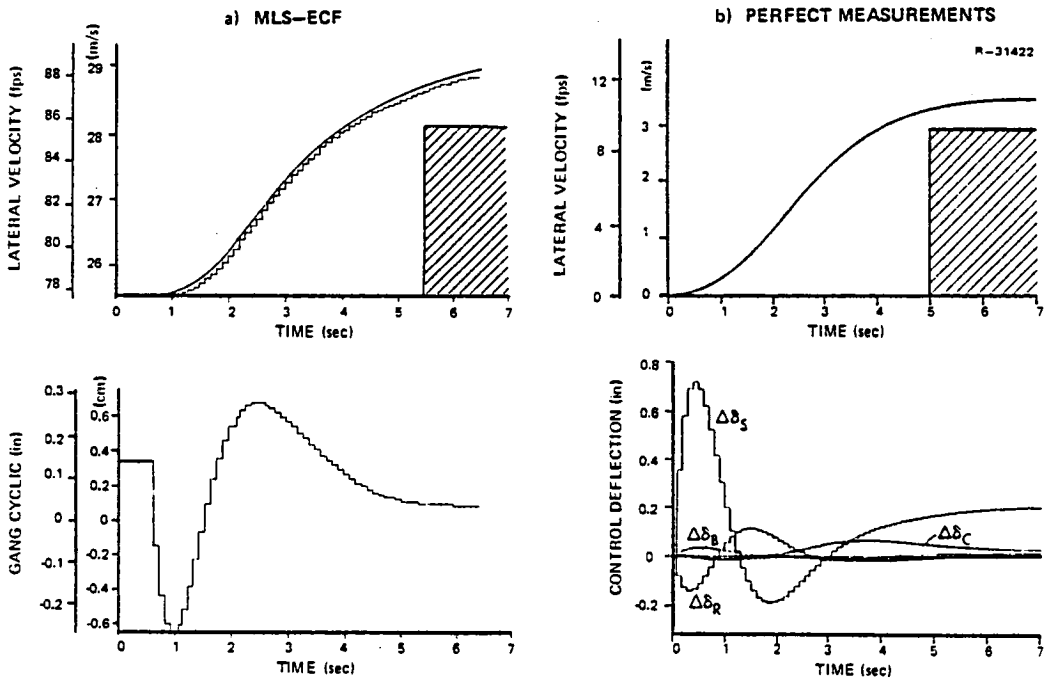

Figure 4.2-5 PIF Velocity Lateral Velocity Response (TAS = 34 m/s (65 kt) for MLS-ECF and 30.9 m/s (60 kt) for Perfect Measurements, S&L Flight)

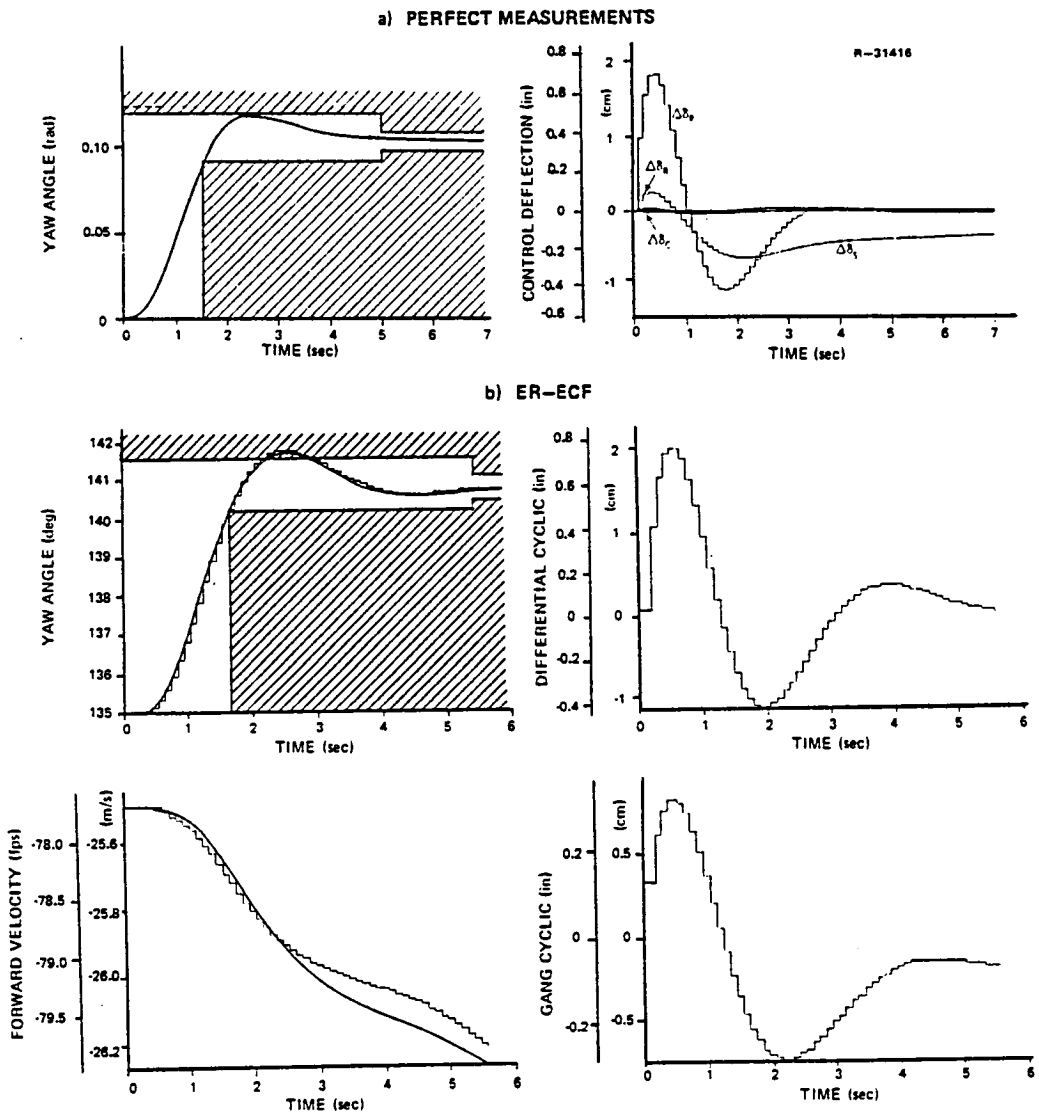

Figure 4.2-6 PIF Velocity Yaw Angle Response With the ER-ECF (TAS = 34 m/s (65 kt) for ER-ECF and 30.9 m/s (60 kt) for Perfect Measurements, S&L Flight)

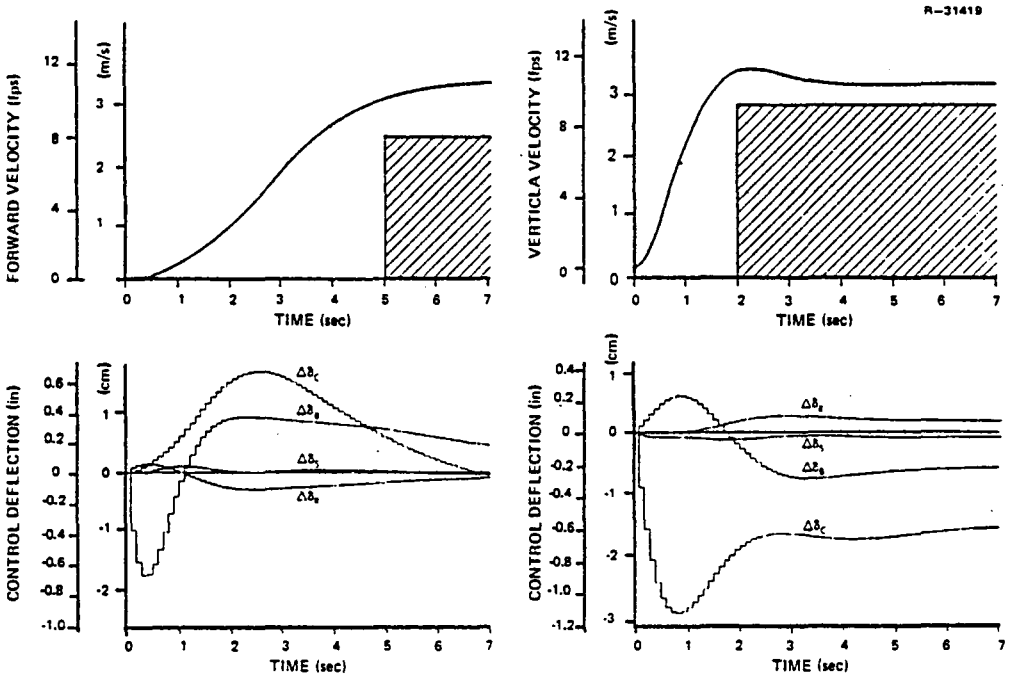

Figure 4.2-7 PIF Velocity Forward and Vertical Velocity Responses with Perfect Measurements (TAS = 30.9 m/s (60 kt) Descending at 2.54 m/s (500 fpm))

4.3 ACTUATOR DYNAMIC EFFECTS

The actuator and rotor dynamics translate the flight computer output into control forces and moments acting on the aircraft. These dynamics, modeled separately for each control channel, are illustrated in Fig. 3.2-5. The TAGS actuator model includes first-order dynamics, and the rate and displacement limits are discussed in Section 3.2. The rotor model is a second-order linear system.

The linear rotor and actuator dynamics filter the flight computer control commands, and, in extreme cases, the rate and displacement limits prevent excessive control

movements. The actuator time constant is one-eighth the length of the flight computer sample period, whereas the effective rotor time constant ($1/(\zeta\omega_n)$) is almost 0.7 of a sample period. The result is a significant lag, primarily due to the rotor dynamics, between the flight computer control command and the actual control displacement.

The pitch response of the PIF attitude control law with the rotor and actuator dynamics included is shown in Fig. 4.3-1. The response requirements are also illustrated, as is the vehicle response without actuator and rotor models. The control deflection lags the control command for differential collective, as illustrated in Fig. 4.3-4. The figure shows that the presence of actuator and rotor dynamics increases the overshoot without significant rise time variation.

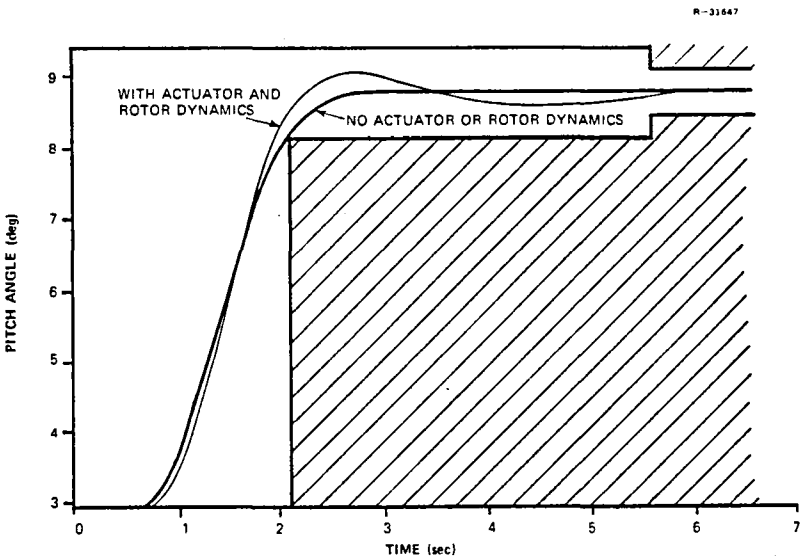

Figure 4.3-1 Pitch Command Response as Affected by Actuator and Rotor Dynamics

Very large velocity commands result in rapid and large control commands, which cause the actuator to run against its rate and displacement stops. The PIF control

laws incorporate an "anti-windup" feature to enable them to recover from a displacement limited actuator as quickly as possible. When $\underline{u}_k$ is calculated in Eq. 3.4-10, the resulting values are compared to the position limits of the actuator. If any element in $\underline{u}_k$ exceeds the limit, it is reset to the limit before the command is sent to the actuators. The modified $\underline{u}_k$ is also used in the next control cycle to generate $\underline{u}_{k+1}$. This anti-windup procedure is evaluated by commanding a vertical velocity of 4200 fpm, which is a very severe maneuver. (Engine torque limiting is not included in the simulation). The collective command that results causes the collective actuator to rate limit up to its position limit, as shown by Fig. 4.3-3. The rotor is rate-saturated during the initial transient, and at the position limit the control command is reset by the anti-windup compensation so that the actuator comes off the displacement stop quickly and settles smoothly to its steady-state value. The resulting command response shown in Fig. 4.3-4, is within the specification for V_z; the rise time is 1.8 sec, the overshoot is 4.3%, and the settling time is 2.0 sec.

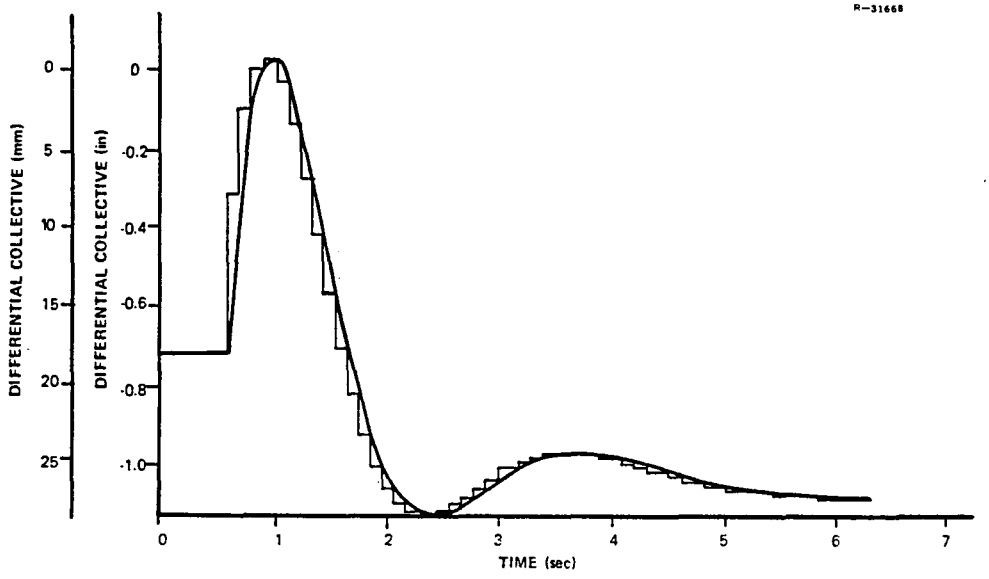

Figure 4.3-2 Differential Collective Command and Actuator/Rotor Output

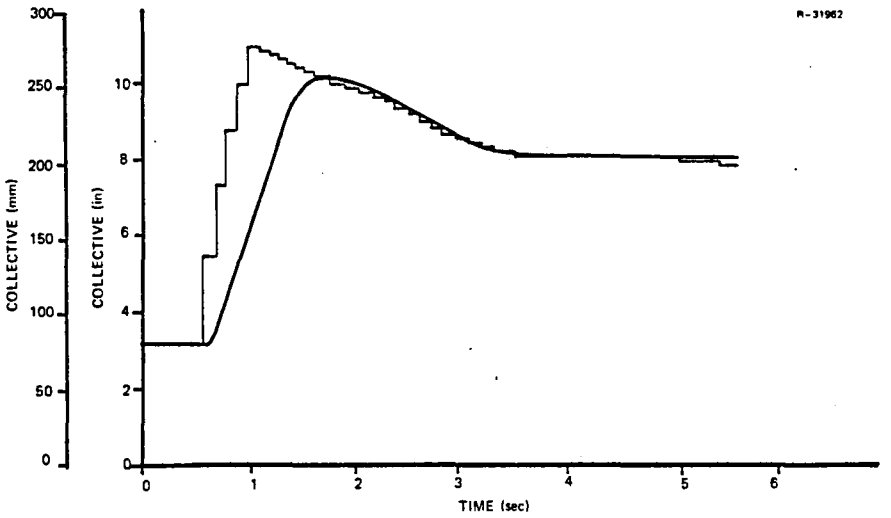

Figure 4.3-3 Collective Rate and Position Saturation Under Severe Vertical Command

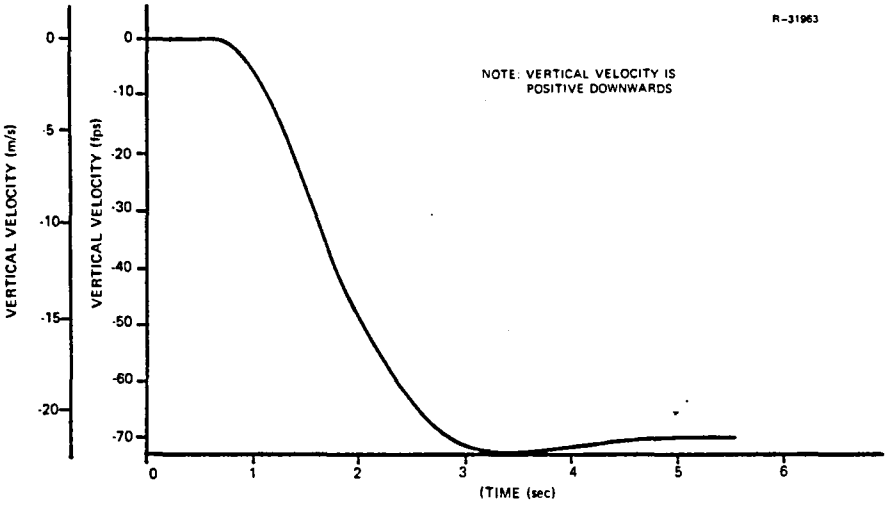

Figure 4.3-4 Vertical Velocity Response Under Collective Saturation

The differential collective actuator contacts neither the rate nor displacement limit stops. The differences between the rotor position and its commanded value are due to the actuator and rotor dynamics.

The lateral-longitudinal coupling of the helicopter dynamics leads to a lateral-directional response when the collective actuator reaches its limit. The roll rate which results is shown in Fig. 4.3-5, and the maximum roll angle magnitude is 1.7 deg. The pitch rate which is necessary to enter this climb is -5.0 deg/sec, and the pitch attitude goes to -3.2 deg before returning to its trim value of about -0.2 deg.

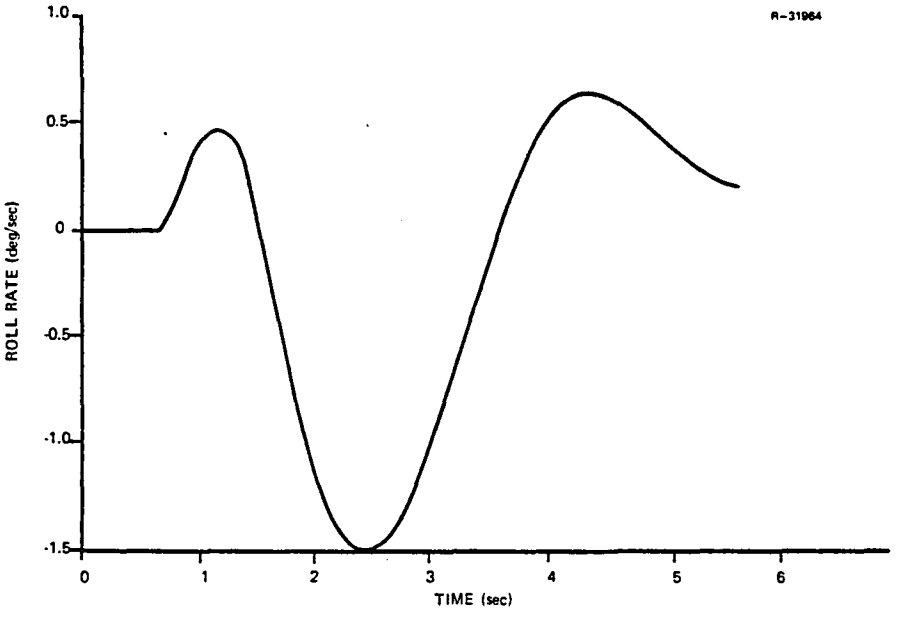

Figure 4.3-5 Roll Rate Response Due to Collective Saturation

4.4 COMPUTATION DELAY EFFECTS

Theoretical analysis of a sampled-data control system assumes the flight computer operates "instantaneously", i.e., that there is no delay between data input to the computer and

the computer control command. In this section the effects of computational delays that are significant fractions of the computer sample period are demonstrated. This is achieved by delaying the flight computer control command up to 90% of a computer sample period.

Figure 4.4-1 illustrates the effects on vertical velocity PIF command response of time delays of 0.0, 0.05 and 0.09 sec. The time delay results in a less well damped response (overshoot increases from 11.1% for no delay to 17.3% for a 0.09 sec delay). The rise time to 90% is identical at 1.18 sec in all three cases, even though the initial vehicle response occurs later in the presence of a time delay.

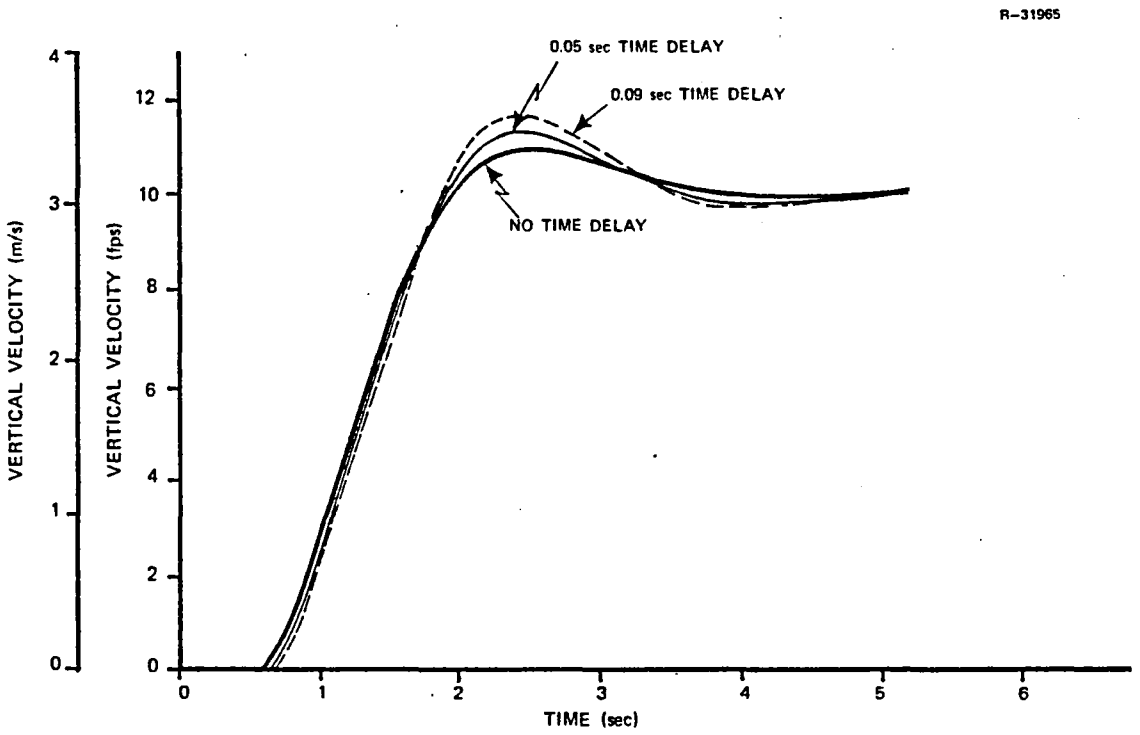

Figure 4.4-1 Vertical Velocity Command Response as Affected by Time Delay

The corresponding maximum vehicle pitch rates increase from 1.2 deg/sec (no time delay) to 1.7 deg/sec (0.09 sec time delay), illustrating the less-well-damped nature of the system in the presence of the time delay. Increased pitch response magnitude also occurs as time-delay increases. The time delay results in an aircraft response that is less-well-damped, but with unchanged response rise time.

The PI attitude control system also satisfies the response criteria in the presence of time delays. In the following simulation, the actuator and rotor lags are also modeled. Pitch angle response is shown in Fig. 4.4-2. It can be seen that the control system easily satisfies the response requirements even in the presence of actuator/rotor dynamics and a time delay. The differential collective command and response are shown in Fig. 4.4-3, and the lags shown in this plot account for the less-well damped nature of the responses with computational time delay. The presence of

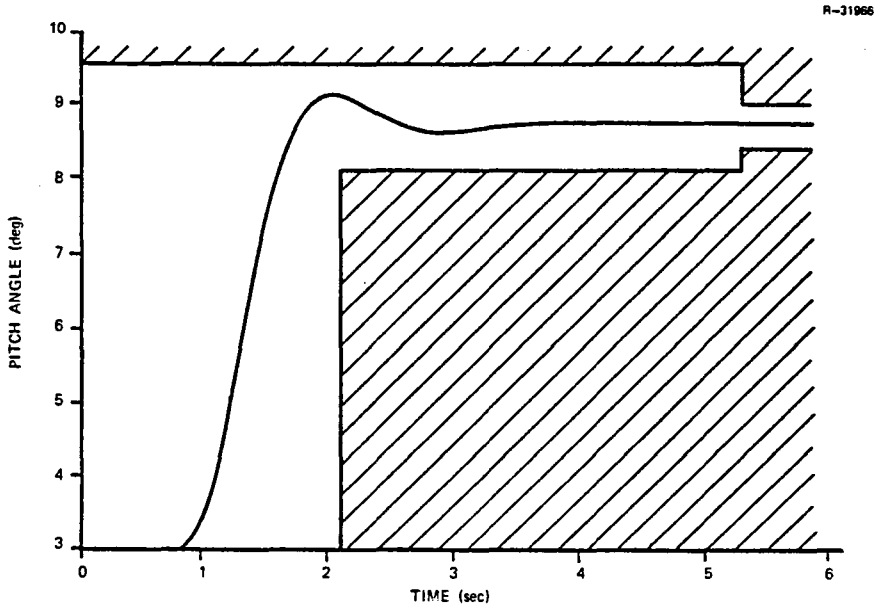

Figure 4.4-2 Pitch Response with Actuator and Rotor Dynamics and 0.09 sec Time Delay for PI Attitude Controller

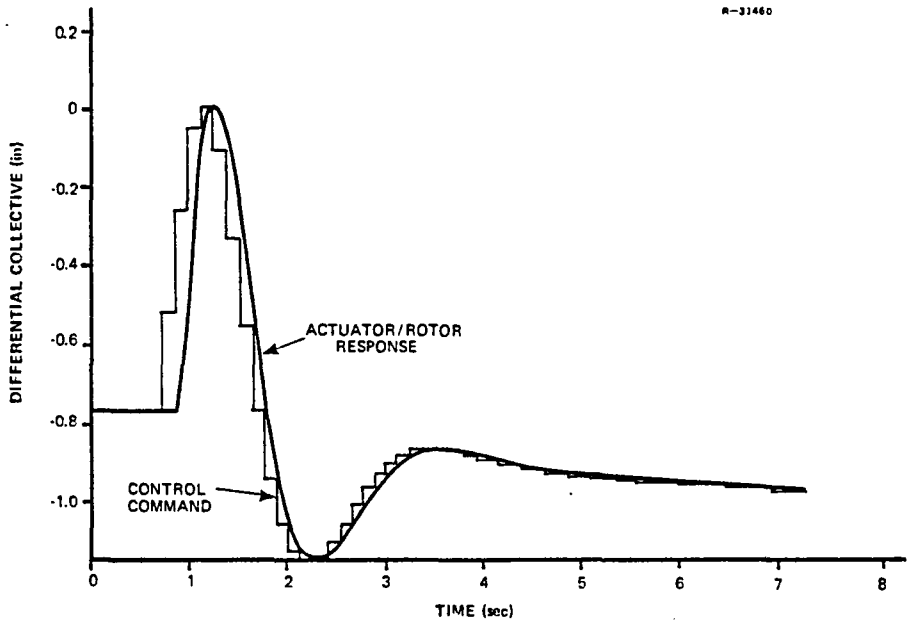

Figure 4.4-3 Differential Collective Command and Response with Actuator/Rotor Dynamics and Time Delay

a command error "integrator" in the control law results in responses which exhibit short rise times and rapid settling in the presence of these delays and lags.

4.5 MEASUREMENT NOISE EFFECTS

The effects of sensor noise and random errors are examined in this section with regard to the control law structure, command vector and radio navigation aids. Both PI and PIF control laws are implemented, and the command vector can include either earth-relative velocity or vehicle attitudes. The MLS system is based on either range-azimuth-elevation or multilateration signals. This section examines the performance of these systems in the presence of realistic sensor noise and errors.

The velocity and attitude command vectors are repeated in Eqs. 4.5-1 and 4.5-2, respectively.

$$\underline{y}_d = (V_x, V_y, V_z, \psi)^T \qquad (4.5\text{-}1)$$

$$\underline{y}_d = (\phi, \theta, \psi, V_z)^T \qquad (4.5\text{-}2)$$

These command vectors differ in the way the vehicle's horizontal plane motion is commanded, with actual north and east velocities used in the velocity command vector and body roll and pitch Euler angles used in the attitude command vector.

The velocity command vector achieves body-axis velocity control similar to or better than the attitude command vector. Table 4.5-1 shows this effect for two simulations; other simulations show similar velocity accuracies. The body attitudes, however, are more accurately controlled by an attitude command vector. Table 4.5-2 details the observed deviations, and the roll angle deviation is seen to be significantly different. Figures 4.5-1 (for PIF velocity) and 4.5-2 (for PIF attitude) show the roll angle time histories for these cases to illustrate the tighter roll angle control of the attitude system.

TABLE 4.5-1

BODY-AXIS VELOCITY STANDARD DEVIATIONS
DUE TO SENSOR NOISE - 33.4 m/s (65 KT)
STRAIGHT AND LEVEL FLIGHT COMMANDED

VELOCITY COMPONENT	PIF VELOCITY	PIF ATTITUDE
u	0.04 m/s (0.12 fps)	0.04 m/s (0.23 fps)
v	0.3 m/s (1.0 fps)	0.7 m/s (2.3 fps)
w	1.2 m/s (4.0 fps)	1.3 m/s (4.1 fps)

TABLE 4.5-2

BODY ATTITUDE STANDARD DEVIATIONS DUE TO SENSOR NOISE - 33.4 m/s (65 KT) STRAIGHT FLIGHT COMMANDED

ATTITUDE ANGLE	PIF VELOCITY	PIF ATTITUDE
ϕ	1.3 deg	0.15 deg
θ	0.5 deg	0.4 deg
ψ	1.1 deg	1.0 deg

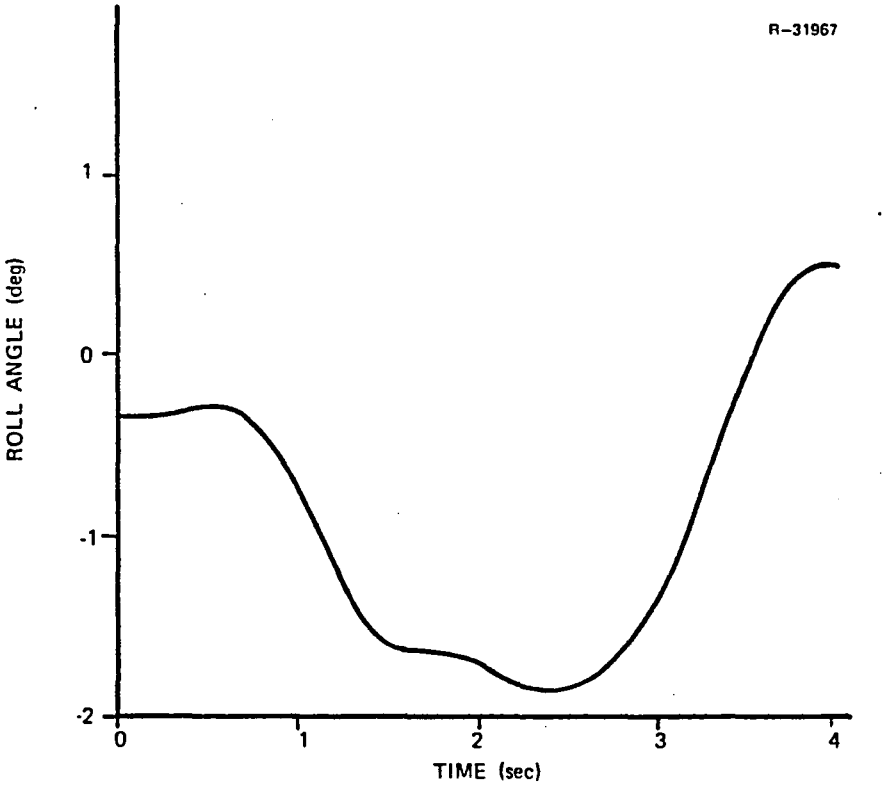

Figure 4.5-1 Roll Angle Response Due to Sensor Noise - PIF VElocity-33.4 m/s (65 KT) Straight Flight Commanded

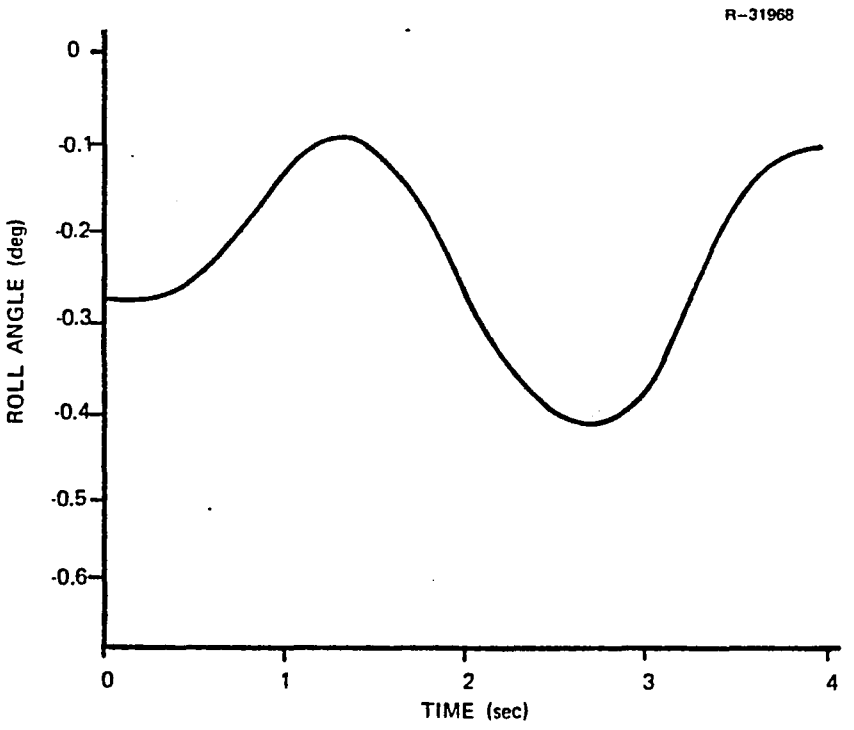

Figure 4.5-2 Roll Angle Response Due to Sensor Noise - PIF Attitude - 33.4 m/s (65 KT) Straight Flight Commanded

The earth-relative velocity is expressed as a transformation of body-axis velocity through the body attitude angles into earth-relative axes. Therefore, the body-axis velocity deviations and body attitude deviations result in earth-relative velocity deviations as listed in Table 4.5-3. Under sensor errors discussed in Section 3.2, the attitude command system achieves more accurate velocity control than the velocity command system. The easterly velocity histories for the two command systems are shown in Figs. 4.5-3 and 4.5-4. The northerly and easterly velocity errors are correlated such that almost all of the PIF velocity control system's horizontal earth-relative velocity error is normal to the nominal flight path. This is a consequence of the poor roll attitude control of the velocity command system.

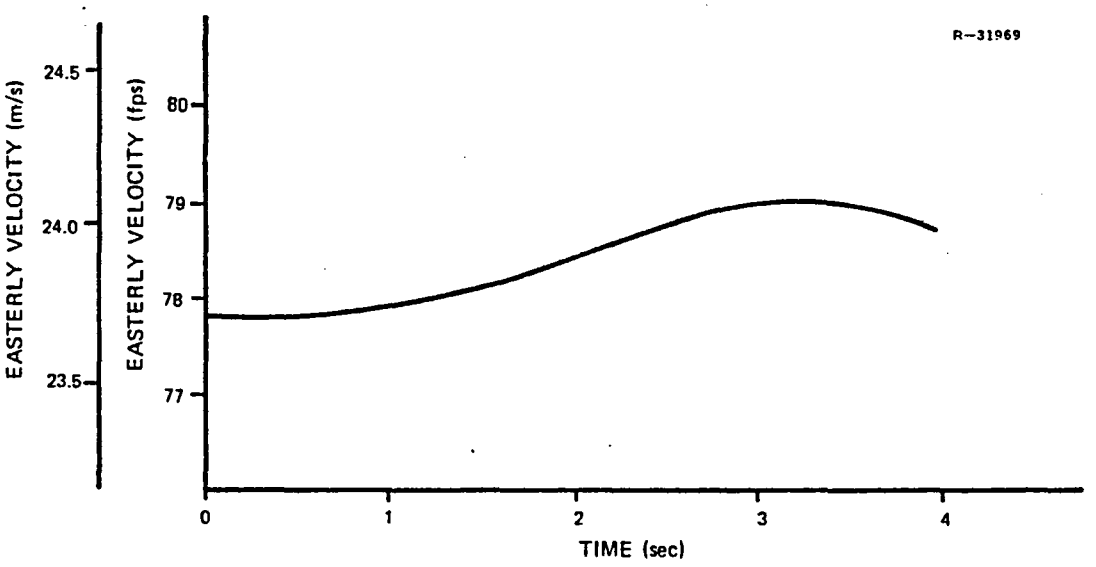

Figure 4.5-3 Easterly Velocity Response Due to Sensor Errors - PIF Velocity - 33.4 m/s (65 KT) Straight Flight at 135 Deg Heading

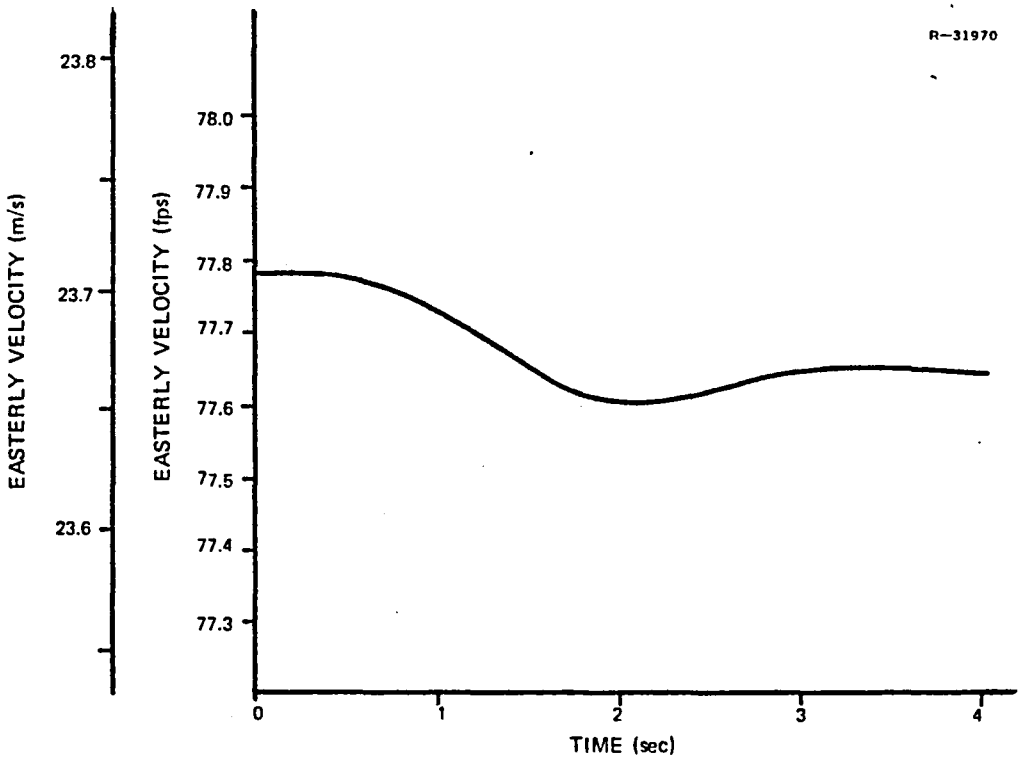

Figure 4.5-4 Easterly Velocity Response Due to Sensor Errors - PIF Attitude - 33.4 m/s (65 KT) Straight Flight at 135 Deg Heading

TABLE 4.5-3

EARTH-RELATIVE VELOCITY STANDARD DEVIATIONS - 33.4 m/s (65 KT) STRAIGHT FLIGHT

VELOCITY COMPONENT	PIF VELOCITY	PIF ATTITUDE
V_x	0.3 m/s (1.0 fps)	0.12 m/s (0.4 fps)
V_y	0.3 m/s (1.0 fps)	0.05 m/s (0.15 fps)
V_z	1.2 m/s (4.0 fps)	1.2 m/s (4.0 fps)

The controller structure plays a significant role in determining the vehicle response quality. The PIF controller, which includes low-pass filtering in the controller output channels, can be expected to be somewhat less sensitive to noisy state estimates than the PI controller, but may exhibit slower command response. The differential lateral cyclic control is shown for the PIF attitude controller in Fig. 4.5-5. The large control excursion between 4.1 and 5.5 sec is due to the step command of a 5.73 deg increase in yaw angle. Yaw rate follows the differential cyclic input, and the resulting yaw angle is shown in Fig. 4.5-6. In this particular simulation, the rise time is 0.15 sec longer than the specification value, probably due to the negative yaw rate at the time the positive yaw angle command is issued. For this step command, a settling requirement of ±5% is much tighter than the steady state yaw angle standard deviation of about 1.0 deg.

The PI controller, with direct state feedback to control command, results in differential cyclic control motion given noisy sensor output as shown in Fig. 4.5-7. The deviation of the control signal from its trim value is about three times as large as the deviation caused by the PIF controller.

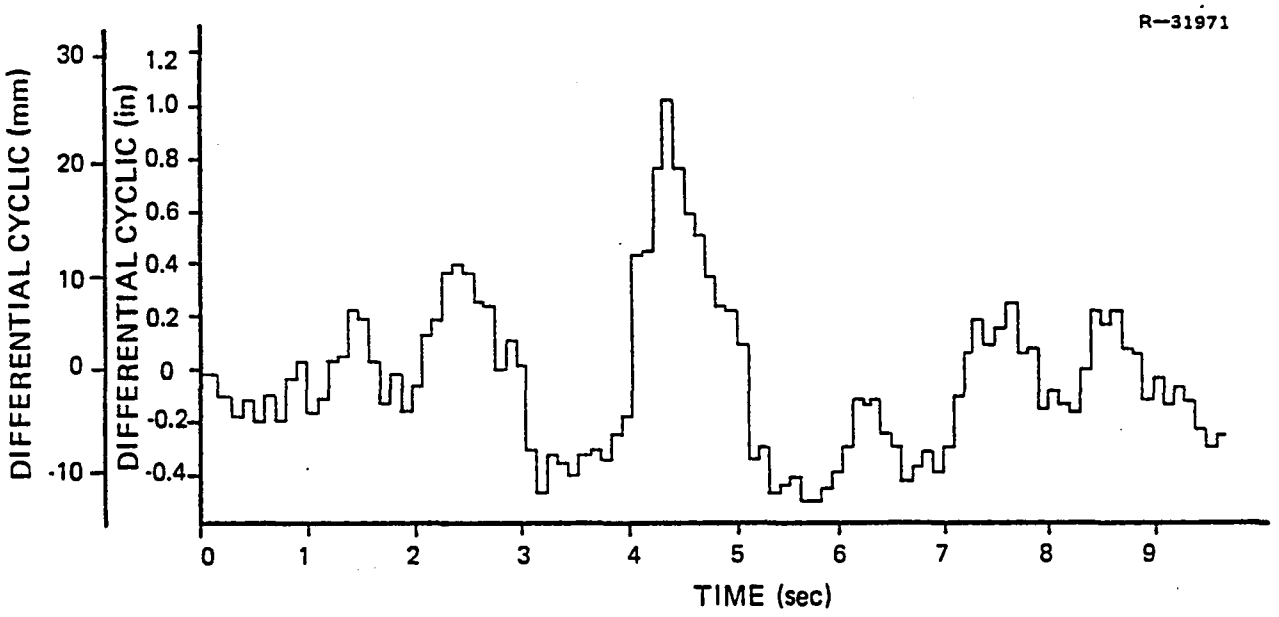

Figure 4.5-5 Differential Lateral Cyclic Control From PIF Attitude Controller - Step Command $\Delta\psi_c$=5.73 Deg at t=4.1 sec - 33.4 m/s (65 KT) Straight Flight at 135 Deg Heading

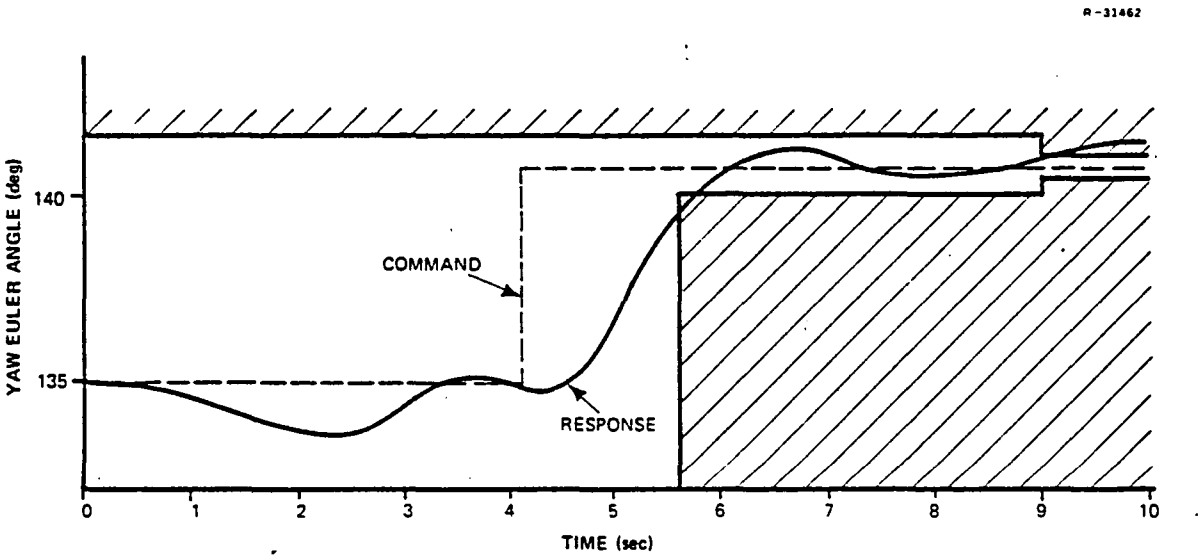

Figure 4.5-6 Yaw Angle Response Due to PIF Attitude Controller: Step Command $\Delta\psi_c$=5.73 Deg at t=4.1 sec - 33.4 m/s (65 KT) Straight Flight at 135 Deg Heading

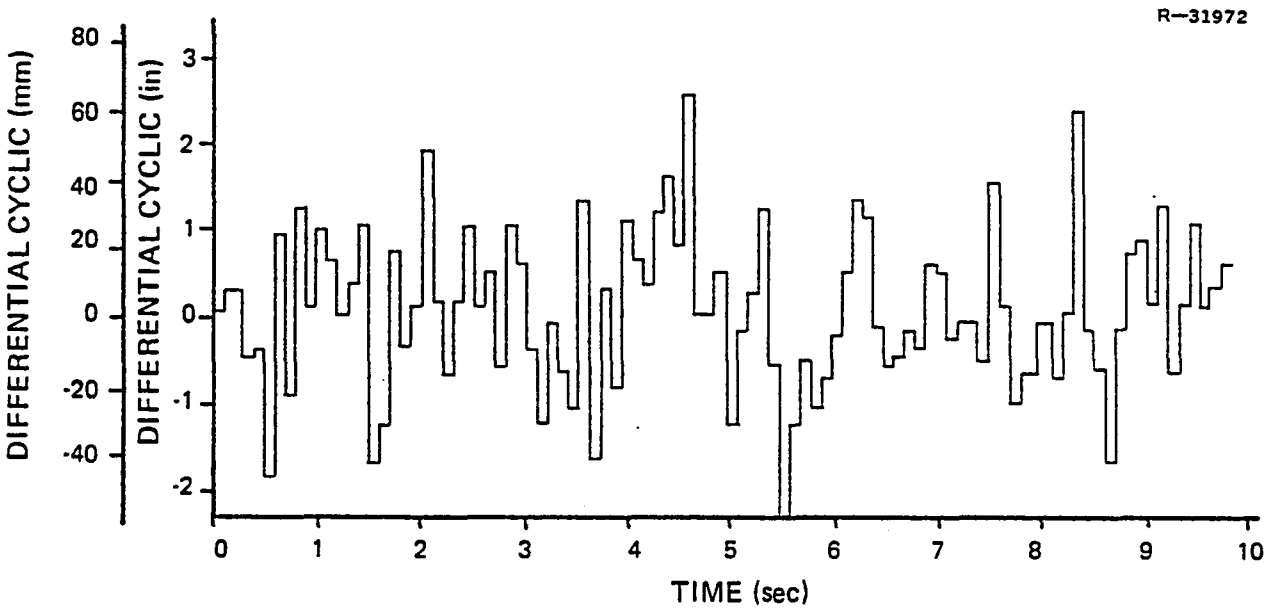

Figure 4.5-7 Differential Lateral Cyclic Control From PI Attitude Controller: Step Command $\Delta\psi_c$=5.73 Deg at t=4.1 sec - 33.4 m/s (65 KT) Straight Flight at 135 Deg Heading

The frequency is higher, however, so the resulting yaw rate standard deviation of PI is less than twice that of the PIF controller. The PI controller's yaw response is shown in Fig. 4.5-8. The rise time requirement is satisfied by about 0.2 sec, and the yaw angle deviations are comparable to the PIF controller results. In summary, PIF and PI produce comparable outer loop responses, although the PI angular rates and control deflections are much larger than those from the PIF controller.

The sensor suite and estimator performance also have a significant effect on the vehicle responses. The estimators are partitioned into two sets, one for angular motion and one for translation quantities. The angular rate and pitch and roll attitude sensors are fairly accurate, and Fig. 4.5-5 shows the actual yaw rate plotted with its estimate.

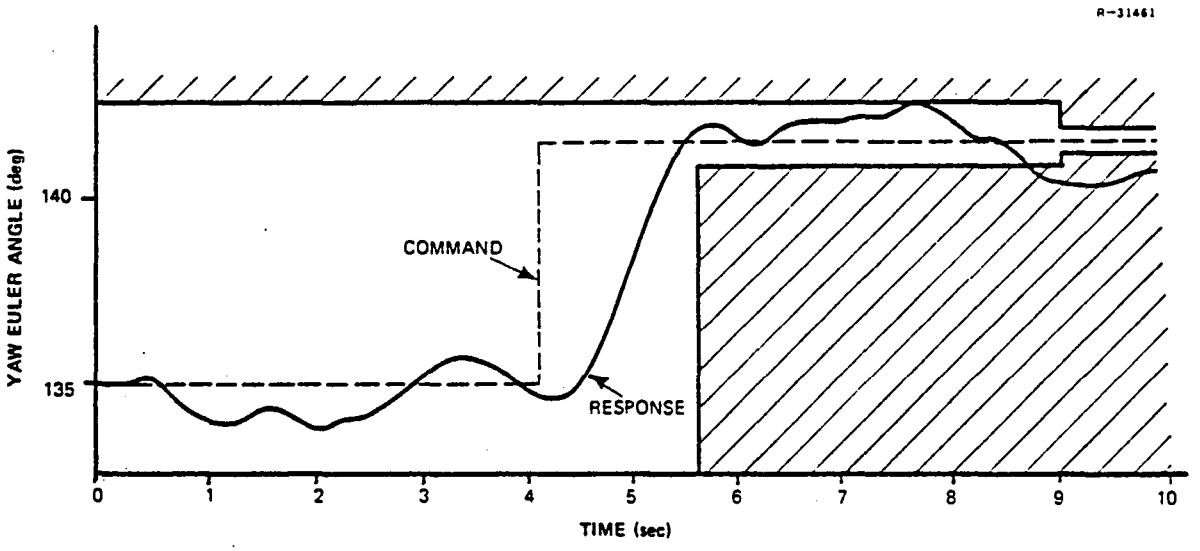

Figure 4.5-8 Yaw Angle Response Due to PI Attitude Controllers - Step Command $\Delta\psi_c$=5.73 Deg at t=4.1 sec - 33.4 m/s (65 KT) Straight Flight at 135 Deg Heading

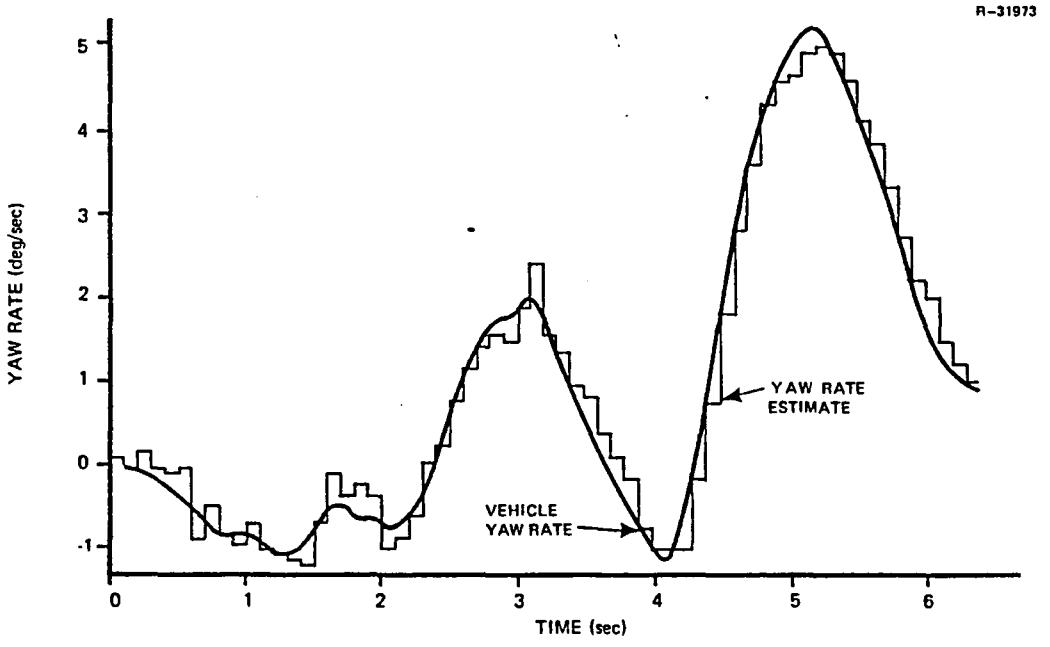

Figure 4.5-9 Yaw Rate Estimate and Response Due to PIF Attitude Controllers - Step Command $\Delta\psi_c$=5.73 Deg at t=4.1 sec - 33.4 m/s (65 KT) Straight Flight at 135 Deg Heading

The gyromagnetic heading sensor is less accurate and is a major yaw error source.

The on-board translational sensors consist of body-mounted accelerometers, true airspeed and sideslip sensors, and a baroaltimeter. The terminal area radio navigation system can consist of either a range-azimuth-elevation microwave landing system (MLS) or a multilateration system (TRI), which derives vehicle position and velocity on the ground and relays it to the aircraft. Due to geometry considerations, the multilateration scheme gives poor performance when the range is over two miles, especially in the vertical channel.

Body-axis velocity estimation errors are listed in Table 4.5-4 for three situations. The fourth possibility, MLS at short range, can be expected to perform almost as well as TRI at close range. The true airspeed and sideslip sensors provide significant information in the long-range cases, as can be seen in the w channel, where no angle of attack sensor is available. Short range velocity estimates by the TRI estimator are considered good.

The poor long range w channel estimate translates to errors in vertical velocity of a similar magnitude. These errors result in altitude estimation errors as listed in Table 4.5-5. At the long range, the TRI system produces its altitude estimate primarily from the relatively inaccurate baroaltimeter. Note that this range is somewhat longer than the TRI designed maximum range of 4 km (2 nm). In summary, the MLS system performs better at ranges beyond about 4 km (2 nm), but the TRI system, with its all aspect capability and excellent close range position and velocity estimates, may be desirable for actual landing zone navigation. A radar altimeter could improve the long-range TRI vertical channel,

TABLE 4.5-4

BODY AXIS VELOCITY ESTIMATION ERROR STANDARD DEVIATIONS AS A FUNCTION OF RADIO NAVIGATION AID

VELOCITY COMPONENT	TRI SHORT RANGE (1 km, 1/2 nm)	TRI LONG RANGE (5 km, 2.5 nm)	MLS LONG RANGE (5 km, 2.5 nm)
u	0.1 m/s (0.4 fps)	0.2 m/s (0.7 fps)	0.3 m/s (1.0 fps)
v	0.24 m/s (0.8 fps)	0.46 m/s (1.5 fps)	0.3 m/s (1.0 fps)
w	0.15 m/s (0.5 fps)	1.5 m/s (5.0 fps)	0.9 m/s (3.0 fps)

TABLE 4.5-5

ALTITUDE ESTIMATION ERROR STANDARD DEVIATIONS AS A FUNCTION OF RADIO NAVIGATION AID

TRI SHORT RANGE (1 km, 1/2 nm)	TRI LONG RANGE (5 km, 2.5 nm)	MLS LONG RANGE (5 km, 2.5 nm)
0.4 m (1.4 ft)	>15 m (>50 ft)	2.4 m (8 ft)

altimeter could improve the long-range TRI vertical channel, as well as being useful to an MLS system at close range. Thus, only one radio navigation system may then be necessary.

The choice of command vector and sensor suite are closely linked. A velocity command vector appears to require more accurate state measurement than the sensor suite used in this simulation series provides, except possibly at short range with multilateration. However, if this accuracy can be

achieved, the velocity command structure seems ideally suited to precision position and velocity control, especially at low speeds. The attitude command vector is more oriented to on-board angular sensors, and seems ideal for enroute control, and is probably a desirable command vector for pilot control of the vehicle.

For both command vectors, the PIF structure provides smoother response with much less control motion than the PI controller. The low-pass filter dynamics in PIF assist in filtering out residual noise in the state estimates. It appears that more sophisticated filters with less noise in the state estimates could operate well with a PI controller structure. The proper trade-off between filter and controller complexity is certainly an area of further research.

One possible vehicle system configuration would include an enroute portion consisting of a PIF attitude control law, with TACAN-Area Navigation providing trim updates. In the terminal area, a multilateration system would provide precise position and velocity information to a terminal guidance law driving a PIF velocity controller. The transition method from enroute to terminal control and the precise sensor suite desired would be a subject of further study.

4.6 WIND EFFECTS

Movement of the atmosphere relative to the earth (wind) has a significant impact on the aerodynamic forces on the aircraft. The controller operates on earth-relative quantities, and hence senses wind effects as they disturb the helicopter flight path. The controller then corrects for these disturbances. The wind estimate is used explicitly by the guidance laws and the wind estimate allows the use of true airspeed and sideslip sensors in the velocity filters.

To examine the controller effects, two simulations are run with "perfect" earth-relative velocity estimates. Figure 4.6-1 shows the PIF velocity controller's downrange (northerly) earth-relative velocity response to sudden wind changes at t=1 sec (3.05 m/s-10 fps headwind begins) and at t=6 sec (headwind stops, 3.05 m/s-10 fps wind from east begins). The response is due to the decelerating effect of the headwind on the aircraft, and earth-relative speed drops by 0.05 m/s (0.15 fps). The end of the head-wind produces a 0.10 m/s (0.32 fps) increase in velocity due to the excess thrust which is counteracting the wind. Figure 4.6-2 shows the vertical velocity variation caused by cross-axis effects; these errors are less than 0.06 m/s (0.2 fps). In both axes, the velocity response is not very highly damped.

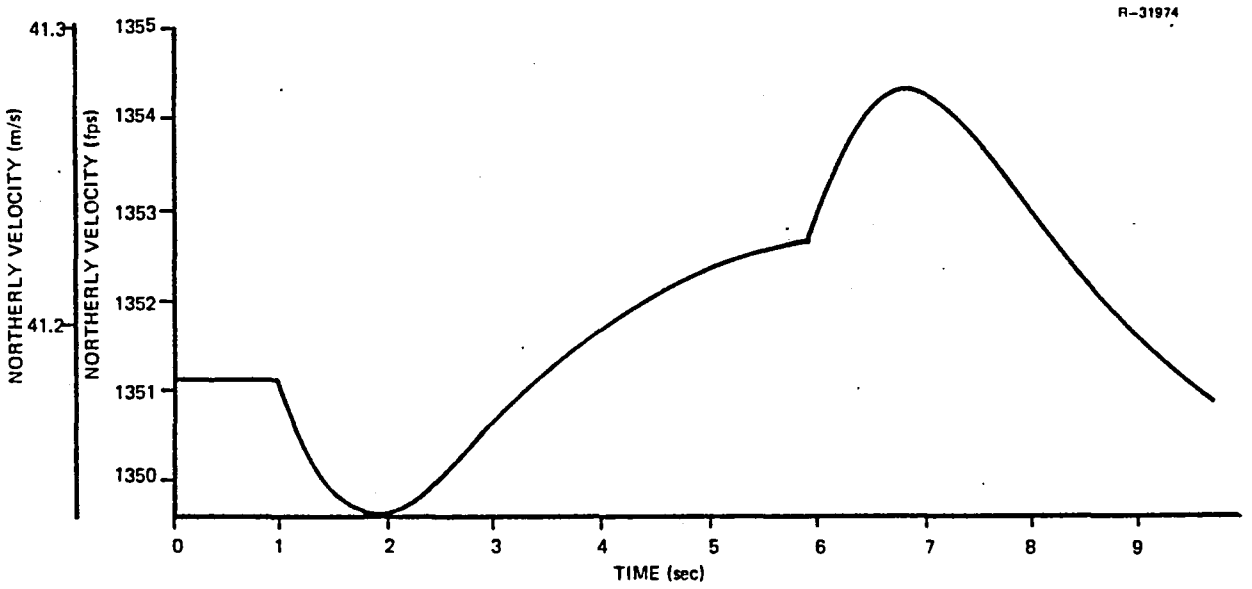

Figure 4.6-1 Northerly Earth-Relative Velocity Wind Response - PIF Velocity Controller - 41 m/s (80 kt) North - 3.05 m/s (10 fps) Headwind at t=1 sec, 3.05 (10 fps) Wind from East at t=6 sec

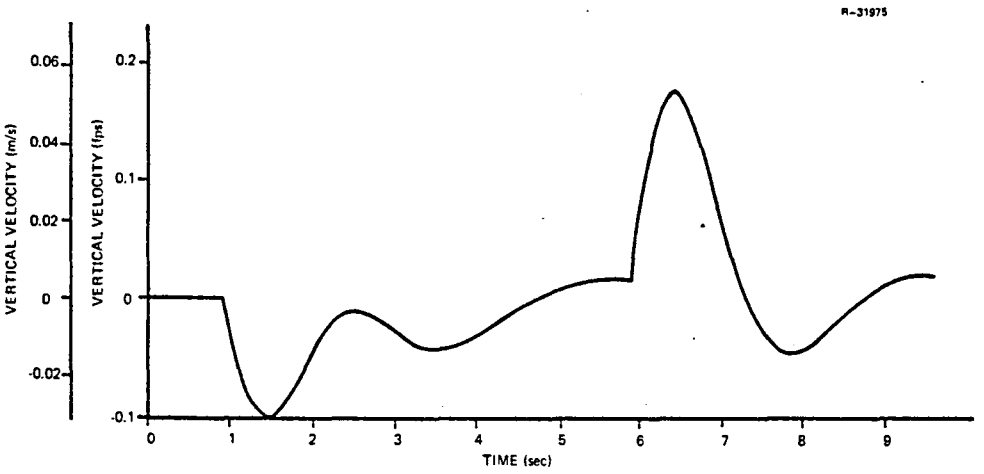

Figure 4.6-2 Vertical Velocity Wind Response - PIF Velocity Controller - 41 m/s (80 kt) North - 3.05 m/s (10 fps) Headwind at t=1 sec, 3.05 m/s (10 fps) from East at t=6 sec

The PI attitude controller reacts much differently to the same helicopter-relative wind profile. The pitch attitude response is shown in Fig. 4.6-3, and the rapid, well-damped return to the commanded pitch angle is apparent. The transients are smaller than 0.15 deg in magnitude. The northerly velocity response that accompanies this wind disturbance is shown in Fig. 4.6-4. This velocity is negative because the initial helicopter heading is 135 deg (south east), and both the headwind and the wind from the starboard side of the vehicle produce northerly accelerations. Because this is an attitude controller, it does not counteract the earth-relative velocity change. The vertical velocity disturbances are shown in Fig. 4.6-5, and are less than 0.08 m/s (0.25 fps) in magnitude. The more rapid PI response is apparent from a comparison of Figs. 4.6-2 and 4.6-5.

The accuracy and speed of the wind estimator is shown in a simulation in which an earth-relative speed increase is commanded, followed by a 3.05 m/s (10 fps) tailwind.

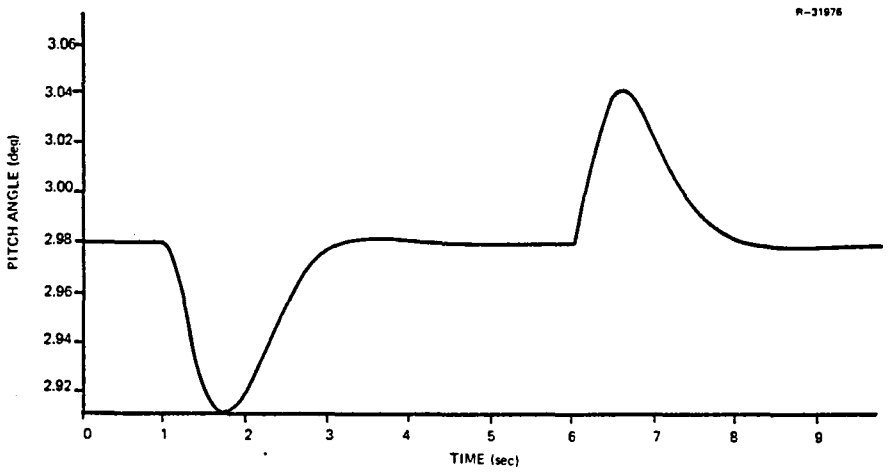

Figure 4.6-3 Pitch Response to Wind - PI Attitude Controller - 33.4 m/s (65 kt) SE - 3.05 m/s (10 fps) Headwind at t=1 sec, 3.05 m/s (10 fps) Wind from SW at t=6 sec

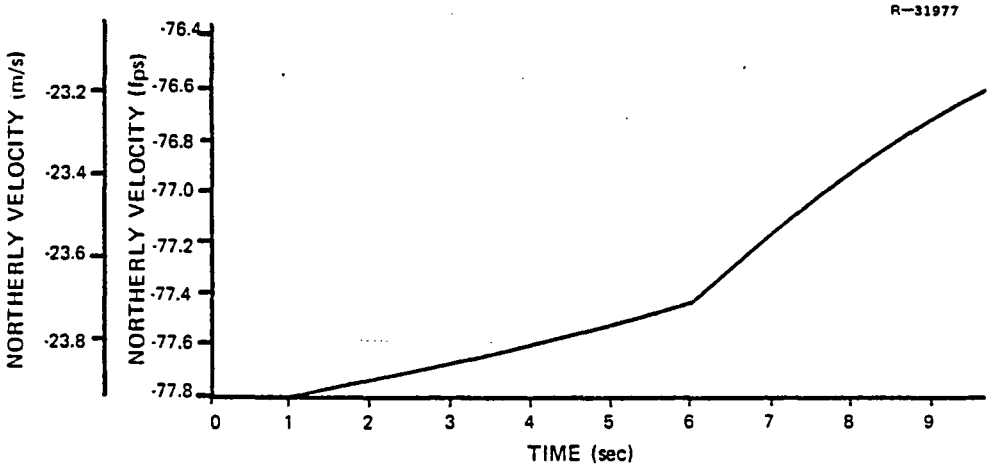

Figure 4.6-4 Northerly Velocity Wind Response - PI Attitude Controller - 33.4 m/s (65 kt) SE - 3.05 m/s (10 fps) Headwind at t=1 sec, 3.05 m/s (10 fps) Wind from SW at t=6 sec

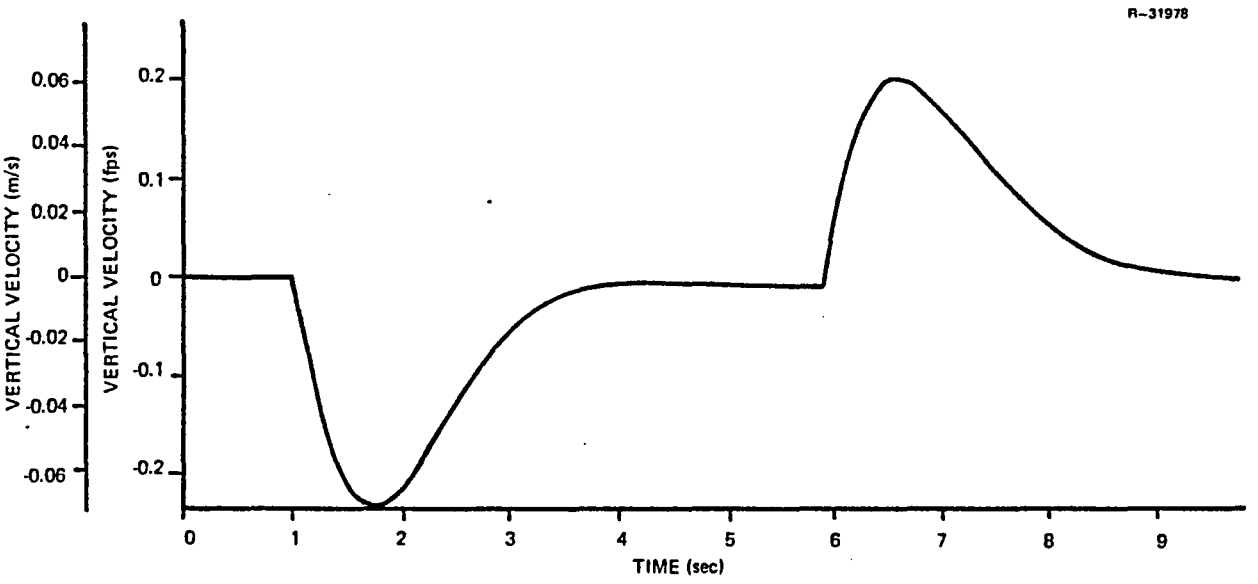

Figure 4.6-5 Vertical Velocity Wind Response - PI Attitude Controller - 33.4 m/s (65 kt) SE - 3.05 m/s (10 fps) Headwind at t=1 sec, 3.05 m/s (10 fps) from SW at t=6 sec

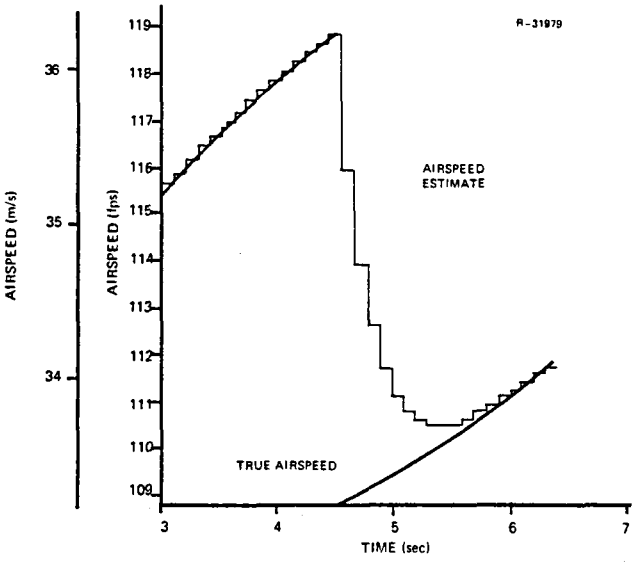

Figure 4.6-6 True Airspeed and Its Estimate - 3.05 m/s (10 fps) Tailwind at t=4.5 - 36.5 m/s (119.7 fps) Forward Velocity Command at t=0.6

The heading is 135 deg (southeast). The true airspeed is shown in Fig. 4.6-6 along with its estimated value. The estimate responds quickly to the appearance of the tailwind. The estimate of the easterly wind component is shown in Fig. 4.6-7, and it also tracks the actual wind. The easterly earth-relative velocity and its estimate are shown in Fig. 4.6-8. The estimator initially interprets the jump in the true airspeed sensor output as partially due to an earth-relative velocity change. As the airspeed change is finally estimated to be due to wind velocity, the easterly earth-relative velocity estimate again approaches the true value. The maximum velocity error is 0.4 m/s (1.3 fps).

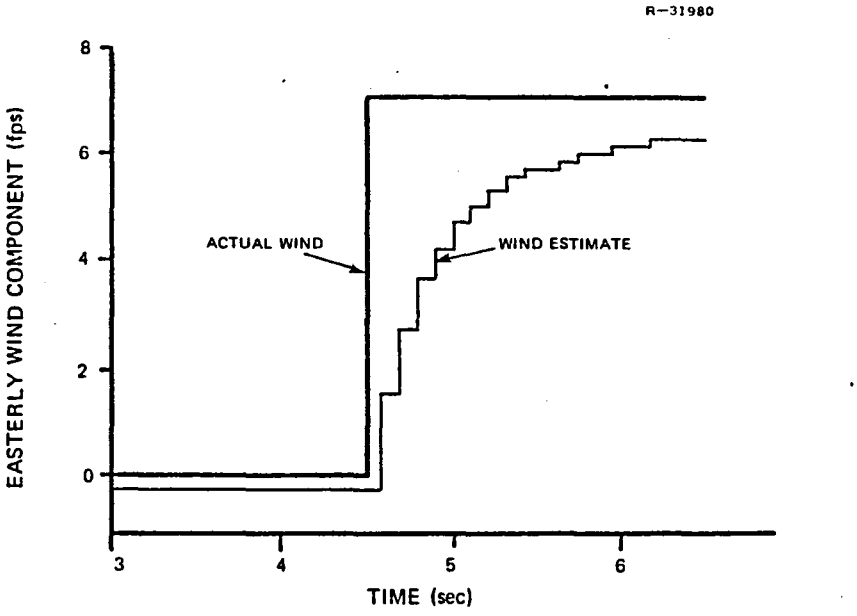

Figure 4.6-7 Easterly Wind Component and its Estimate - 3.05 m/s (10 fps) Tailwind at t=4.5 sec

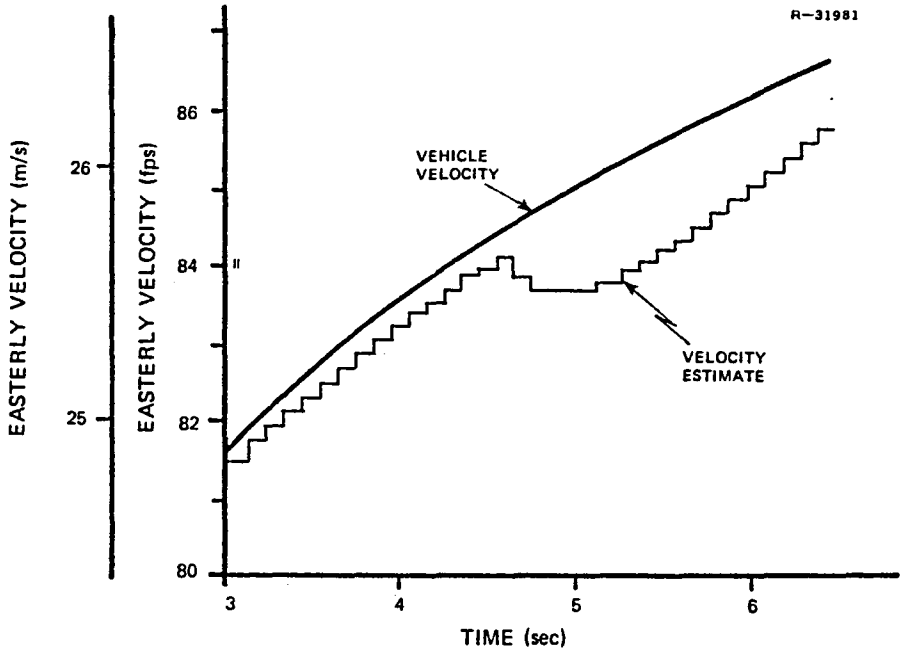

Figure 4.6-8 Easterly Earth-Relative Velocity and Its Estimate - 3.05 m/s (10 fps) Tailwind at t=4.5 sec

The wind changes examined in this section can be estimated by the DFCS estimator algorithms and both the PI and PIF control laws counteract wind disturbances in their commanded quantities. Velocity command laws return the vehicle to its commanded earth-relative velocity and attitude command laws return the vehicle to its commanded attitude, which results in earth-relative velocity variations due to wind.

4.7 SIMULATION OF A TIME-VARYING DYNAMIC MODEL

The simulation procedure used to test the vehicle state estimators and control laws is a total-valued state and control simulation based on a linear-time-varying vehicle model. The linear dynamics are represented by Eq. 4.7-1 and the total values of state and control vectors are defined in Eqs. 4.7-2 and 4.7-3. Note that the nominal values are time-varying.

$$\Delta\dot{\underline{x}}(t) = F(t)\Delta\underline{x}(t) + G(t)\Delta\underline{u}(t) + G_t(t)\Delta\underline{w}(t) \qquad (4.7\text{-}1)$$

$$\underline{x}(t) = \underline{x}_o(t) + \Delta\underline{x}(t) \qquad (4.7\text{-}2)$$

$$\underline{u}(t) = \underline{u}_o(t) + \Delta\underline{u}(t) \qquad (4.7\text{-}3)$$

The nominal trajectory is made up of segments of four types, as described in Table 4.7-1. The six translational and rotational velocities (u,v,w,p,q, and r) are constant along the first two types of trajectories, as are the roll and pitch attitude angles. This results in non-time-varying perturbation equations for these 8 states along straight and steady-spiral trajectory segments. One of the latter two time-varying nominal trajectory segment types shown in Table 4.7-1 must always separate two different non-time-varying nominal trajectory segments. For example, a linear acceleration segment must serve as the transition between two straight flight segments at different velocities. The time-varying nominal trajectory is constructed so that the total-value, linear-time-varying system responds to total-value control commands, $\underline{u}(t)$, much as a nonlinear simulation would. Hence, as the nominal trajectory moves from one segment to another, the total system state should <u>not respond</u> if a constant control command, $\underline{u}(t)$, is applied. Figure 4.7-1 illustrates the implications of this requirement. Assuming the different nominal segments between t_1 and after t_2 are non-time-varying, the segment between t_1 and t_2 is a time-varying segment. The differences in the nominal state up to t_1 and after t_2 imply a nominal state rate from t_1 to t_2 of $\dot{\underline{x}}_0$. For $\underline{x}_T$ to remain constant (as it should in the face of constant u_T), the perturbation state rate must exactly cancel the nominal state rate ($\Delta\dot{\underline{x}}=-\dot{\underline{x}}_0$). However, to induce this six-element perturbation state rate, discontinuities in a six-element nominal "control" vector must be allowed. The six-elements are

TABLE 4.7-1
NOMINAL TRAJECTORY SEGMENT TYPES

	V_H, V_Z	$\dot{V}_H$, $\dot{V}_Z$	ξ	$\dot{\xi}$	$\ddot{\xi}$
Straight	Constant	0	Constant	0	0
Steady Spiral	Constant	0	LTV	Constant	0
Turn Entry	Constant	0	QTV	LTV	Constant
Linear Acceleration	LTV	Constant	Constant	0	0

Note: LTV = Linear with time
QTV = Quadratic with time
V_H: Horizontal velocity
ξ: Velocity heading

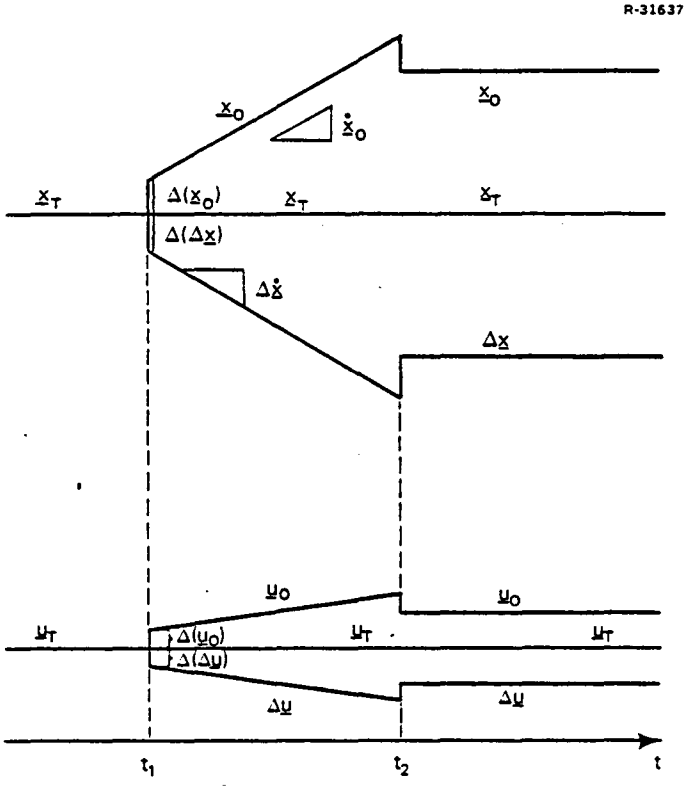

Figure 4.7-1 System Response Along an Accelerated Nominal Trajectory for Constant Total States and Controls

formed from the four controls (δ_B, δ_C, δ_S, δ_R) and the pitch and roll Euler angles (ϕ,θ). The resulting dynamic trim problem can then be stated as

$$\begin{bmatrix} \Delta(\Delta u) \\ \Delta(\Delta v') \end{bmatrix} = \begin{bmatrix} G' & F_{xv} \end{bmatrix}^{-1} \begin{bmatrix} \dot{x}_2^* - F_2 \Delta(x_2^*) \end{bmatrix} \qquad (4.7\text{-}4)$$

where $\Delta v'$ contains the two Euler angles, F_2(6x6) defines the effects of the dynamic states on their own state rates, x_2^* are the three velocity and three angular rate trim states, and F_{xv}(6x2) defines the effect of the roll and pitch Euler angles on the dynamic state rates. G_v is the 6x4 control input matrix describing the control effects on the six dynamic states. Implementation of these nominal state and control discontinuities ($\Delta(x_o)$, $\Delta(\Delta u)$, and $\Delta(\Delta v')$) results in a total-value linear-time-varying helicopter simulation which responds as a nonlinear simulation would, but which can be implemented using linear system models. This simulation method is used in the following section.

4.8 PATH FOLLOWING DURING THE SPIRAL DESCENT

The spiral descent enables a VTOL vehicle to descend rapidly while remaining within a limited area, where the trajectory involves the combination of a 2 minute turn with a 4.7 degree descending flight path angle. A view of the descent plan is shown in Fig. 4.8-1. The descent nominally starts at 19.75 sec into the trajectory. The guidance law used in the simulation is derived specifically for spiral descents (Ref. 10), and is described in Section 3.7.

For the initial 7.5 sec of the spiral descent, vertical velocity, which contains the important entry transient,

is shown in Fig. 4.8-2. The filters are implemented, but without sensor errors. The rise time requirement is satisfied, but overshoot is 35% instead of the desired 20% and settling time is about 5.7 sec instead of the desired 5.0 sec. The altitude error is steady at about 13 feet; the vehicle is above the nominal trajectory.

The vertical velocity response exceedances are due to the cross-axis effects that result when both roll angle and vertical velocity are commanded. The roll angle response is shown in Fig. 4.8-3, and its oscillation is seen to be the same frequency and damping as the oscillation in vertical velocity. This oscillation is, at least partially, a response commanded by the guidance system due to cross-range and yaw angle error oscillations. The lateral position response of the vehicle is illustrated in Fig. 4.8-4, which shows the east position time history as the vehicle heading goes through 180 deg. The cross range error at that point is 3.0 feet, and is caused by the filter and controller lags. The vehicle yaw response is relatively smooth and results in a steady-state yaw angle error of about 2.8 deg. (The control system is Type 1, which results in a non-zero steady-state yaw angle error to a constant yaw rate command.) The maximum magnitude sideslip during turn entry is -5.5 deg, which then decreases to match the yaw angle error as the vehicle velocity becomes tangent to the circle.

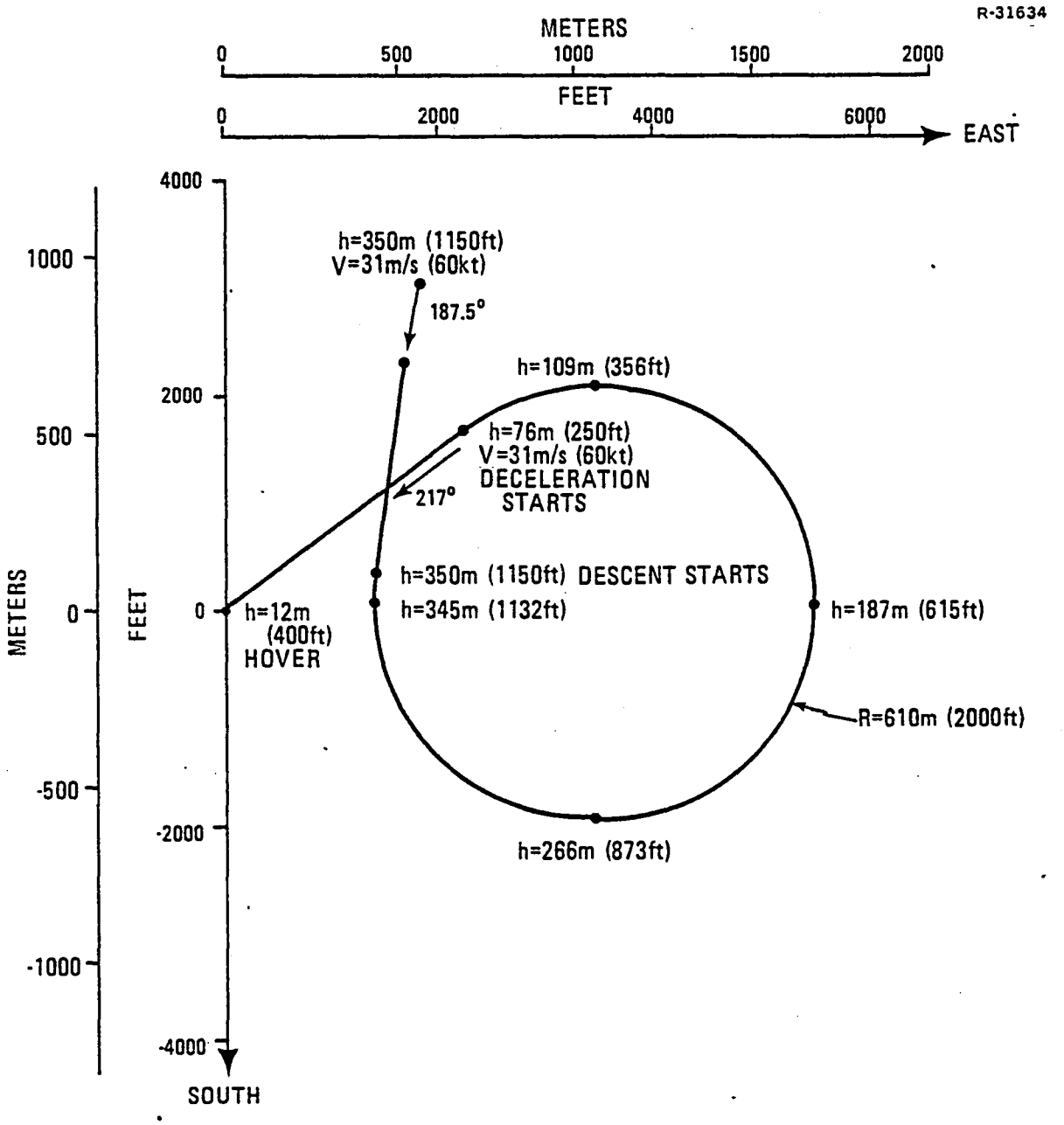

Figure 4.8-1 Spiral Descent Trajectory

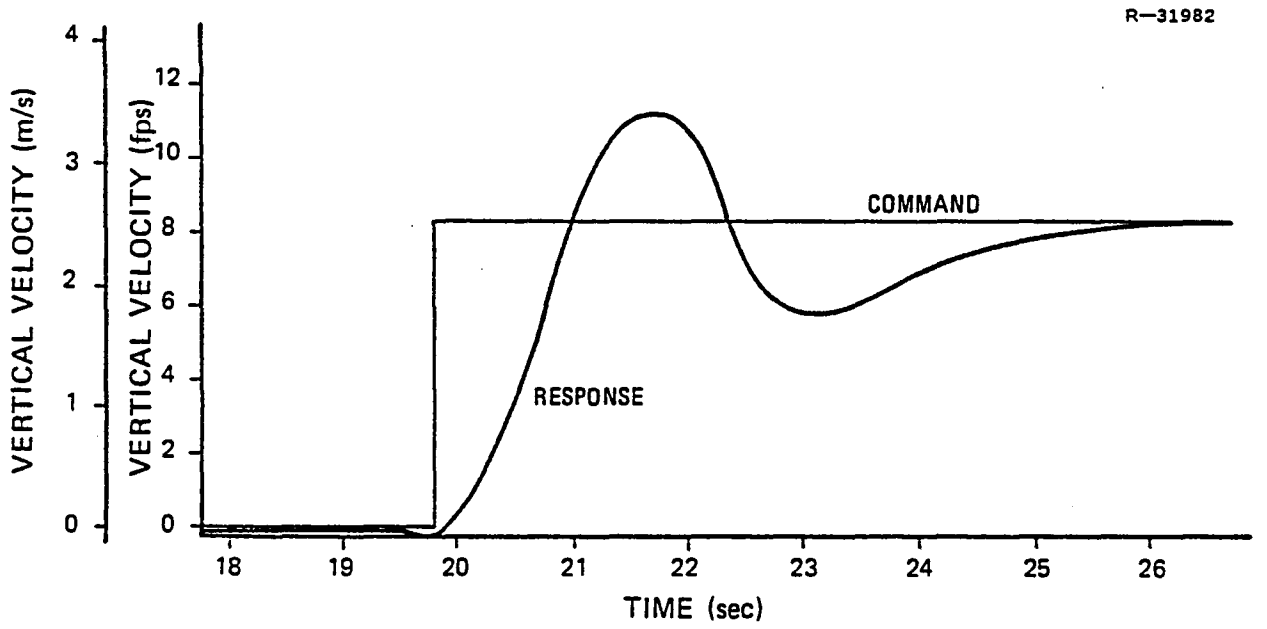

Figure 4.8-2 Vertical Velocity Response on Spiral Descent Entry - PI Attitude Controller - MLS-ECF with no Sensor Noise

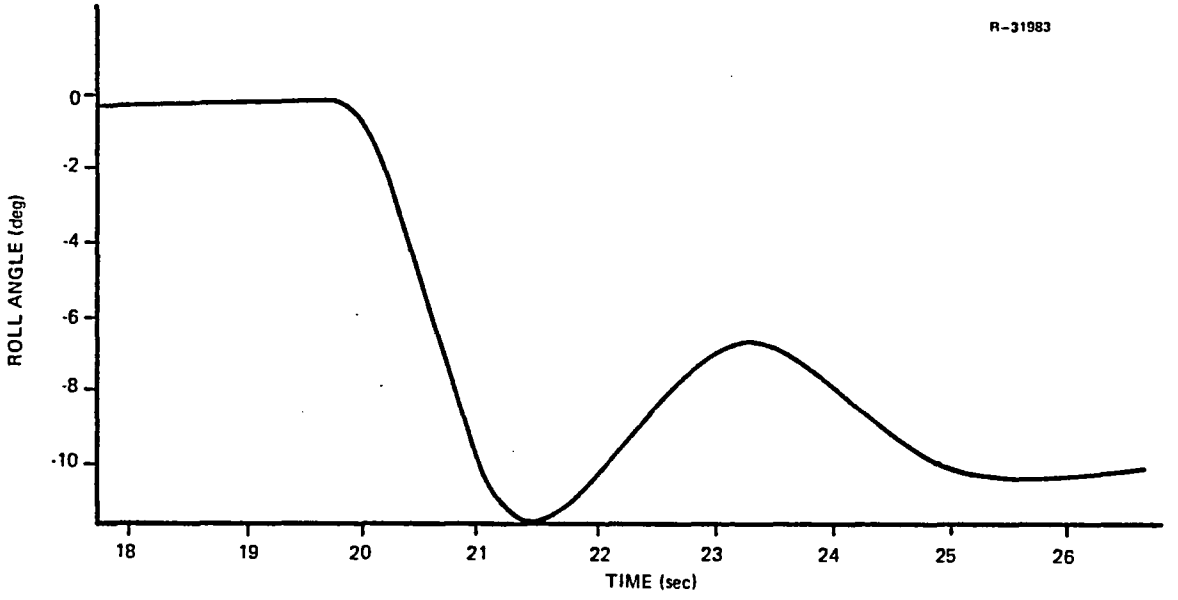

Figure 4.8-3 Roll Response in the Spiral Descent Turn Entry - PI Attitude Controller - MLS-ECF wth no Sensor Noise

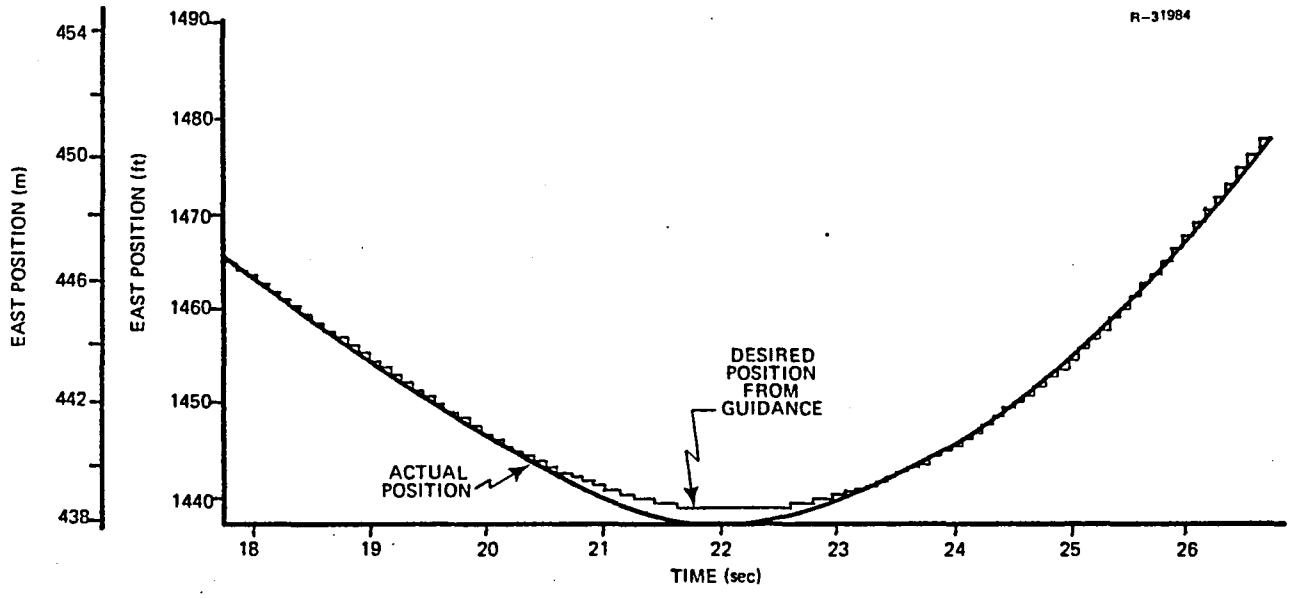

Figure 4.8-4 East Position Response in the Spiral Descent - PI Attitude Controller - MLS-ECF with no Sensor Noise

The aircraft horizontal speed is nominally constant, although the turn entry requires some pitch attitude adjustment to achieve this. Figure 4.8-5 illustrates both the pitch angle command and the vehicle pitch response. The large pitch transient is part of the cross-axis response noted previously. The guidance-controller pitch loop appears to operate more smoothly than the roll loop, probably due to the pitch trim integrator in the spiral guidance logic. These cross-axis effects can be significantly reduced by an integrated guidance-control design. A more extensive simulation effort would be necessary, however, to fully evaluate the helicopter-controller response to spiral guidance commands.

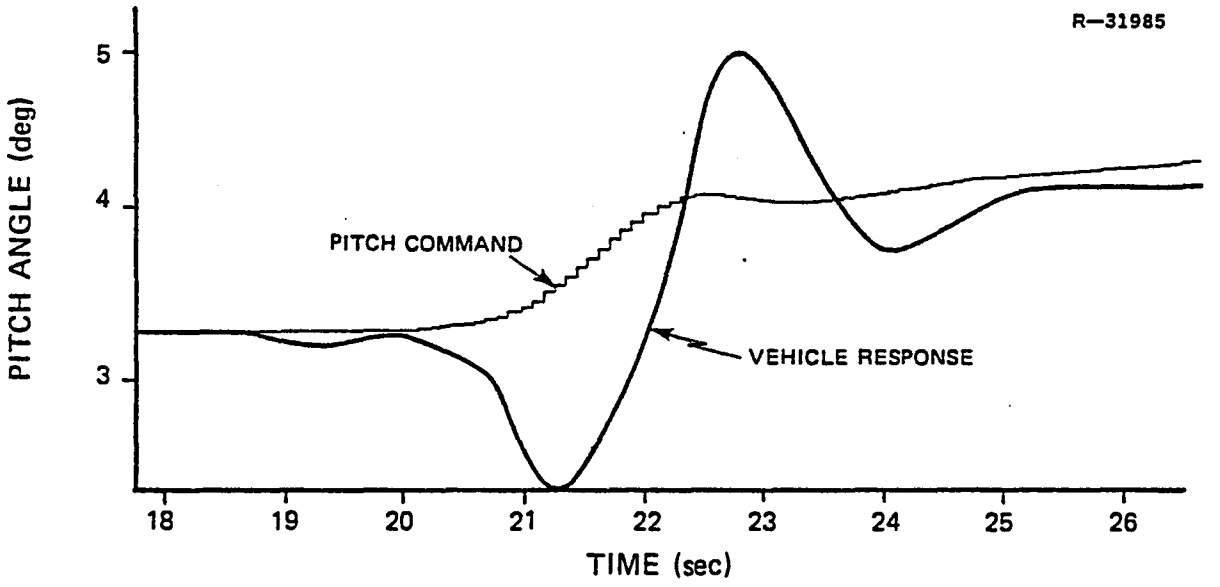

Figure 4.8-5 Pitch Angle Response in the Spiral Descent Entry - PI Attitude Controller - MLS-ECF with no Sensor Noise

5. CONCLUSIONS AND RECOMMENDATIONS

This report supported the development of novel tools in construction of the overall design. These tools include: 1) multivariable Type 1 digital control techniques, 2) techniques for designing controllers using the incremental form and state estimators using the extended complementary filter which in both cases do not require trim stages, 3) the Proportional-Integral-Filter (PIF) control law, 4) a mapping from discrete to continuous forms which enables discrete time closed loop eigenvalues and eigenvectors to be evaluated based on continuous time criteria, 5) a technique for estimating wind in the extended Kalman and complementary filters, 6) scheduling techniques and functions for optimal control and Kalman filter gains, which proved very successful and 7) a computer program for linear, time-varying helicopter simulations.

NASA Langley successfully coded the PIF velocity controller, with the MLS-CF, in the on-board flight computer. Subsequent testing of PIF/MLS-CF as part of a time-varying digital/analog simulation produced favorable results.

New methodologies and results for the design of a digital flight control system have been presented from which the following conclusions and recommendations can be drawn.

5.1 CONCLUSIONS

- Gain Scheduling - It is possible to schedule optimal control gains and Kalman Filter

gains with a high degree of precision. A number of gains in both the optimal controller and Kalman filter can be zeroed without significantly changing performance of the VTOL aircraft. Feedback paths that are the most significant tend to have the highest correlated scheduled and actual gains. In our work, most scheduled gains have correlation coefficients of 0.8 or better. The scheduled and actual gains must be carefully compared to assure that gain sign variation with flight condition is preserved.

- Design Criteria - We have demonstrated that step response criteria can result in an adequate design. Matching the step response criteria results in reasonably placed closed-loop eigenvalues. Fixing a well-chosen set of cost function weighting matrices for a flight condition design sweep is considered to produce a better overall controller than continually trying to match design criteria at every flight condition. The weighting matrices we used meet their response requirements in most cases when fed by accurate state estimates.

- Control Laws - The PIF controller is considered better than PI for the VTOL application. The PIF controller provides much smaller control and angular rate motions with noisy sensors even though attitude excursions are comparable with the PI design. High roll-off afforded by the low-pass filter designed concurrently with state feedback in PIF is concluded to be a good approach in modern control theory applications. In all of our time varying simulations and in analog/digital simulations at NASA Langley, the incremental form for PIF has performed well and exceeded expectations. The introduction of a computation delay, state estimators, and actuator dynamics in the feedback loop did not significantly change the rise time but did result in increased overshoot. Specific combinations of these lags (delays) result in overshoot larger than desired by the response specifications. Short

period, Dutch roll, and roll mode eigenvalues determined for the discrete control law using the natural logarithm for mapping eigenvalues fall within the requirements of MIL-F-8330 for both PIF and PI.

- State Estimators - The extended complementary filter concept worked well when simulated. The significant variation in filter gains suggest the ECF should perform better than the constant gain CF, although this has not been tested. The air data sensors are useful with accurate radio navigation aids, reducing velocity estimation error, and are important without radio navigation aids if the aircraft is expected to fly automatically. The estimate of wind performed reasonably and the wind estimates have a significant contribution to improving guidance performance.

- Commands - Attitude command laws result in better velocity control than velocity command laws and, of course, result in better attitude control because of the tighter inner loop control. Velocity control laws are superior only if very good velocity estimates are available (such as from multilateration or an INS system).

- Guidance - Spiral guidance and velocity guidance have comparable performance in the limited simulations run. The technique we used to implement the guidance laws in which the output of the filter is fed directly to perturbation guidance is, in retrospect, <u>not</u> considered to be a good approach.

5.2 RECOMMENDATIONS

- Gain Scheduling - The scheduling functions are found, at present, by searching many combinations of independent variables for good fits. The functions can be improved upon with more careful searching, using a goodness of fit criteria, like the F-test (Ref. 35). The function $\dot{\psi}TAS^2$ should be

changed to either $\dot{\psi}_c TAS^2$ or replaced. Noisy ψ measurements can make unnecessary significant gain variations at high speeds.

Even though we zeroed a number of gains, probably many more can be zeroed as comparing the DFCS with TAGS could demonstrate. Theory should be developed and applied during the cost function design which can selectively zero chosen gain paths without eliminating a state feedback path altogether (Ref. 36).

- Design Criteria - More design criteria should be used instead of just the step response of the commanded variable. Other time history criteria could include, limits on peak cross-axis effects (such as the V_x-V_z coupling), limits on maximum travel of states not commanded (such as roll in PIF velocity), step response criteria for coincident commands (such as θ-V_z). More frequency domain criteria (the roll off criteria in particular, Ref. 37) should be specified or at least checked during the design. The fixed control gains determined at a particular flight condition should stabilize the vehicle over a significant number of flight conditions. Later tests of PIF velocity indicated it does not have this property. The weighting matrices in PIF velocity should be changed to tighten the inner loop control.

  A new set of cost function weighting matrices should be chosen using the above recommendations. With the few flight conditions that have design difficulties identified in the report, we believe one set of Q and R matrices can meet at least the step response criteria at all design flight conditions. The current set of design flight conditions is considered adequate although more can be added if desired.

- Control Laws - The symbiosis of non-optimal filter and controller algorithms should be better understood. We recommend that the control law <u>not</u> be highly tuned to a

particular state estimator during the design process. The estimator design could change when improved sensor data is made available (this situation happened to us) and the controller may have to interact with estimators of varying accuracy (in our case, there are six different velocity estimators of varying capabilities).

The alternate PIF design approach of weighting control rate and control acceleration and then transforming either low-pass structure or both structures to a Type 1 form should be attempted as in PI. This alternate PIF approach eliminates the integrator state in the cost function and gives a better feel in choosing weighting elements.

- Frequency Folding Effects - We recommend that power spectral densities be computed for the rate sensor outputs to understand this effect. At least three actions can be taken to reduce folding effects,

  Increase the sensor and state estimator sampling rates particularly in the inner loops. Digital notch filters could be implemented to suppress rotor, vibration, and structural noise.

  Perform the above recommendation and also increase the control law sampling rates. Experience with the sampled-data regulator indicates that once a continuous time Q and R have been chosen, mapped closed-loop eigenvalues and step response criteria remain relatively unchanged for different small sampling times. This means that the control law continuous time weighting matrices do not have to be redesigned if Δt is decreased.

  Use analog prefilters or, alternatively, sample the sensors at a fast rate, prefilter the sampled signal with a bilinear transformed analog prefilter, then send the signal to

the DFCS at the required rate. Data compression (discussed in Ref. 38 could also be used.

More research should be undertaken to compare the impulse-invariant-like Kalman filter and the bilinear transform filter used in many flight control applications.

- State Estimators - It is not clear that a considerable savings in computation time is achieved in using the ECF over the EKF. We recommend an investigation in this area. The addition of an angle of attack sensor and the use of low velocity air data sensors should be investigated to improve the wind estimate. Other areas we did not address include: lack of sideslip sensor, transition below 25.7 m/s (50 kt), transition between estimators such as ER-ECF to MLS-ECF, improved wind models, wind shear effects, alternate procedures for computation of transformation matrices such as

$$H_B^E,\ H_E^{MLS} \text{ and } H_B^A,$$

and estimator simulation for long periods of time. More simulations should be performed to determined if TRI-ECF is better than MLS-ECF close to touchdown. TRI-ECF could perform better far out if the barometric altimeter sensor bias is estimated in the filter. An investigation should be made into eliminating the sideslip sensor by feeding back lateral acceleration. Because of the way the ECF gains are determined, it is possible to use the scheduled ECF gains shown in Table D-25 directly in the CF implementation. We recommend an investigation to determine if this will improve CF performance.

- Commands - Alternate command sets should be investigated. In particular yaw angle, ψ, should be replaced with $\dot{\psi}$. We recommend that PIF attitude be used far from touchdown with the MLS-ECF or ER-ECF as they become available, while PIF velocity can be used near touchdown with the TRI-ECF.

- Guidance - Guidance laws should be designed concurrently with control laws. In this way it may be possible to raise the lateral performance to match the smooth longitudinal performance shown in Section 4.8. New theory for simultaneous design has recently been developed by expanding on results shown in Ref. 39. The PIF control law can accommodate the noisy output of the state estimators but guidance has difficulties. Guidance operates with long time constants (~30 sec) and at low frequencies. Some form of additional low-pass filtering of velocity and position state estimator output (the bilinear transform approach is recommended here) should be used before the information is sent to guidance.

APPENDIX A

DIGITAL FILTERS FOR AIRCRAFT STATE ESTIMATION

A.1 INTRODUCTION

The Kalman filter is the result of a procedure for designing linear filters which minimizes the mean-square of the estimation error, given system models and corruptive noise statistics. This appendix provides the background, mathematical models, and notational conventions needed for understanding the Kalman filter algorithms developed for this study. The Kalman filter is designed independent of the optimal control law and provides a unified approach for combining the output of different aircraft sensors. Additional details can be found in Refs. 16 and 40 to 42.

The first part of this appendix describes the discrete linear Kalman filter with correlated disturbance and observation noise. A complementary filter design example using Kalman filter logic is shown. The basics of the extended Kalman filter are then presented for solving linear filtering problems which involve significant nonlinearities, e.g., the VTOL aircraft state estimation.

The appendix concludes with the construction of the extended complementary filter, which is used to design the microwave landing system filter.

A.2 DISCRETE-TIME KALMAN FILTER FOR A SAMPLED-DATA SYSTEM

A sampled-data system is one in which measurements of the states of a continuous-time system are available as a sequence of values $\ldots\Delta z_{k-2}$, Δz_{k-1}, Δz_k, where

$$\Delta \underline{z}(t) = H\Delta \underline{x}(t) + \Delta \underline{v}(t) \qquad \text{(A-1)}$$

$$\Delta \underline{z}_k = \Delta \underline{z}(t_k) \qquad \text{(A-2)}$$

$$\Delta t = t_k - t_{k-1} \qquad \text{(A-3)}$$

The quantity, Δt, is the sampling interval, and it is assumed constant. The continuous-time measurement vector, $\Delta \underline{z}(t)$, is composed of ℓ observations of the n-dimensional system state vector, $\Delta \underline{x}(t)$. The measurement is corrupted by a disturbance process represented as the ℓ-vector, $\Delta \underline{v}(t)$. The discrete measurement, $\Delta \underline{z}_k$, is a sample of the continuous observation at time t_k. H is the constant $\ell \times n$ observation matrix.

A discrete model of the sampled-data observation process is

$$\Delta \underline{z}_k = H\Delta \underline{x}_k + \Delta \underline{v}_k \qquad \text{(A-4)}$$

where $\Delta \underline{x}_k$ is the state of the discrete model representation of the continuous-time system, and $\Delta \underline{v}_k$ is assumed to be discrete, zero-mean, white Gaussian noise with covariance

$$E\left\{\Delta \underline{v}_k \, \Delta \underline{v}_j^T\right\} = \Upsilon \delta_{kj} \qquad \text{(A-5)}$$

For a physical system, $\Delta \underline{v}(t)$ is a bandlimited disturbance. An example of the frequency spectrum for a typical helicopter

sensor signal is shown in Fig. 3.4-3. After sampling, the real frequency exists up to the nyquist frequency where high frequency folding, from sampling, evenly distributes (whitens) the disburbance noise, so that Eq. A-5 becomes a reasonable assumption.

The continuous-time system treated here is assumed to be modeled by the linear-time-invariant representation

$$\Delta\dot{\underline{x}}(t) = F\Delta\underline{x}(t) + G\Delta\underline{w}(t) \qquad \text{(A-6)}$$

where F is a constant (n×n) fundamental matrix, G is a constant (n×m) disturbance effect matrix and $\Delta\underline{w}(t)$ is the state noise vector which contains zero-mean, white Gaussian noise, with covariance

$$E\left\{\Delta\underline{w}(t)\ \Delta\underline{w}^T(t)\right\} = W\delta(t-\tau) \qquad \text{(A-7)}$$

The discrete system model representation of Eq. A-6 for measurements every Δt seconds is given by

$$\Delta\underline{x}_{k+1} = \Phi\ \Delta\underline{x}_k + \Gamma\Delta\underline{w}_k \qquad \text{(A-8)}$$

where

$$\Phi = e^{F\Delta t} \qquad \text{(A-9)}$$

$$\Gamma\Delta\underline{w}_k = \int_{t_k}^{t_{k+1}} e^{F(t_{k+1}-\tau)} G\Delta\underline{w}(\tau)\, d\tau \qquad \text{(A-10)}$$

The covariance, χ, of the discrete process noise is then

$$E\left\{\Gamma\Delta\underline{w}_k\ \Delta\underline{w}_k^T\Gamma^T\right\} = \chi = \int_0^{\Delta t} e^{Ft}\ GWG^T e^{Ft^T} dt \qquad \text{(A-11)}$$

The discrete disturbance noise and discrete observation noise are assumed correlated, i.e.,

$$E\left\{\Gamma\Delta\underline{w}_k\ \Delta\underline{v}_j^T\right\} = \Xi\ \delta_{kj} \qquad \text{(A-12)}$$

where Ξ is the $n\times\ell$ cross correlation matrix.

The Kalman filter for the problem posed above can be found in Ref. 40. An unspecified $(n\times\ell)$ matrix, D, is employed to adjoin the measurement equation with the system dynamics as

$$\Delta\underline{x}_{k+1} = \Phi\Delta\underline{x}_k + \Gamma\Delta\underline{w}_k + D\ \ \Delta\underline{z}_k - H\Delta\underline{x}_k - \Delta\underline{v}_k \qquad \text{(A-13)}$$

The matrix, D, is chosen to uncorrelate the disturbance noise (Eq. A-13) and the observation noise (Eq. A-4)

$$E\ \ (\Gamma\Delta\underline{w}_k - D\Delta\underline{v}_k)(\Delta\underline{v}_j)^T = (\Xi - D\Upsilon)\delta_{kj} \qquad \text{(A-14)}$$

where D is chosen to be,

$$D = \Xi\ \Upsilon^{-1} \qquad \text{(A-15)}$$

With this choice of D, the estimation problem (Eqs. A-13 and A-4) is in the standard form for application of discrete Kalman filter theory, i.e.,

$$\Delta\underline{\hat{x}}_k(+) = \Delta\underline{\hat{x}}_k(-) + K\left[\Delta\underline{z}_k - H\Delta\underline{\hat{x}}_k(-)\right] \tag{A-16}$$

$$\Delta\underline{\hat{x}}_{k+1}(-) = \Phi\Delta\underline{\hat{x}}_k(+) + D\left[\Delta\underline{z}_k - H\Delta\underline{\hat{x}}_k(+)\right] \tag{A-17}$$

$$P(-) = (\Phi-DH)\,P(+)\,(\Phi-DH)^T + \chi - \Xi\Upsilon^{-1}\Xi^T \tag{A-18}$$

$$P(+) = [I-KH]P(-) \tag{A-19}$$

$$K = P(-)H^T\left[HP(-)H^T + \Upsilon\right]^{-1} \tag{A-20}$$

The measurements are assumed to have started in the distant past, so that the filter gain matrix, K, has reached steady state. $\Delta\underline{\hat{x}}_k(+)$ is the filter estimate, $\Delta\underline{\hat{x}}_{k+1}(-)$ is the one-step predicted estimate, P(+) is the steady-state error covariance matrix of the filter estimate,

$$E\left\{(\Delta\underline{x}_k - \Delta\underline{\hat{x}}_k(+))(\Delta\underline{x}_k - \Delta\underline{\hat{x}}_k(+))^T\right\} = P(+) \tag{A-21}$$

and P(-) is the steady-state error covariance matrix of the one-step predicted estimate,

$$E\left\{(\Delta\underline{x}_k - \Delta\underline{\hat{x}}_k(-))(\Delta\underline{x}_k - \Delta\underline{\hat{x}}_k(-))^T\right\} = P(-) \tag{A-22}$$

Substituting Eq. A-17 into Eq. A-16 produces the Kalman filter

$$\Delta\underline{\hat{x}}_k(+) = \Phi\Delta\underline{\hat{x}}_{k-1}(+) + K\left[\Delta\underline{z}_k - H\Phi\Delta\underline{\hat{x}}_{k-1}(+)\right] + (D-KHD)\left[\Delta\underline{z}_{k-1} - H\Delta\underline{\hat{x}}_{k-1}(+)\right] \tag{A-23}$$

The constant Kalman gain can be determined by eliminating P(+) from Eq. A-18 and solving for P(-) with the resulting algebraic discrete Riccati equation. A block diagram of the Kalman filter is shown in Fig. A-1.

When D is zero, the Kalman filter is analogous to the discrete impulse-invariant filter (Ref. 43) and when D is non-zero the Kalman filter resembles the bilinear transform filter (Refs. 43 to 45). Alternate techniques for relating the bi-linear transform filter and the Kalman filter are possible.

A unique feature of the Kalman filter is that the performance analysis is inherent in the Kalman gain computation; the computation of the second-order error statistics of the estimate must be computed on line when the state equation is time-varying.

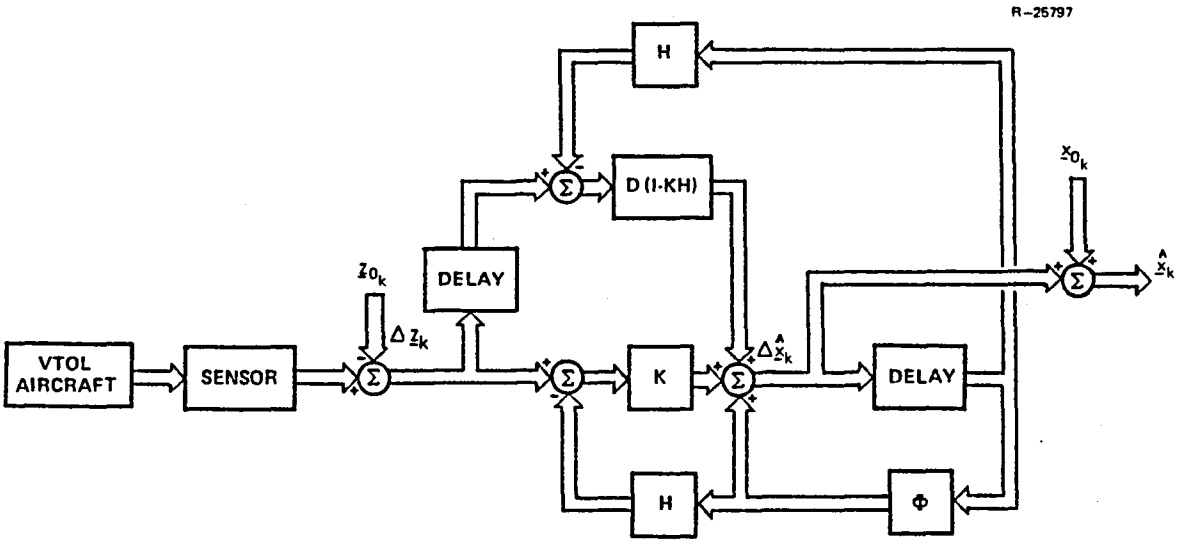

Figure A-1 Discrete-Time Kalman Filter

A.3 COMPLEMENTARY FILTER

A complementary filter combines noisy measurements to produce an estimate of a signal. A typical application of a complementary filter is where position and acceleration

measurements, from different sensors, combine to estimate velocity. Derivations of complementary filters using Kalman filter theory are discussed in Ref. 42 for the continuous-time case.

In discrete-time, many complementary filter problems of interest for aircraft state estimation can be reduced to the following: given the system model presented in Eq. A-8 and that measurements are functions of state and state rates, i.e.,

$$\Delta\underline{z}_k = \begin{bmatrix} H_1\Delta\underline{x}_k \\ H_2\Delta\dot{\underline{x}}_k \end{bmatrix} + \begin{bmatrix} \Delta\underline{v}_{1_k} \\ \Delta\underline{v}_{2_k} \end{bmatrix} = \begin{bmatrix} H_1\Delta\underline{x}_{m_k} \\ H_2\Delta\dot{\underline{x}}_{m_k} \end{bmatrix} \tag{A-24}$$

Replacing $\Delta\dot{\underline{x}}_k$ in the measurement model by

$$\Delta\dot{\underline{x}}_k \cong \frac{\Delta\underline{x}_{k+1} - \Delta\underline{x}_k}{\Delta t} = \frac{(\Phi-I)}{\Delta t}\Delta\underline{x}_k + \frac{\Gamma\Delta\underline{w}_k}{\Delta t} \tag{A-25}$$

the measurement model becomes,

$$\Delta\underline{z}_k = \begin{bmatrix} H_1\Delta\underline{x}_k \\ \dfrac{H_2(\Phi-I)}{\Delta t}\Delta\underline{x}_k \end{bmatrix} + \begin{bmatrix} \Delta\underline{v}_{1_k} \\ \dfrac{H_2\Gamma\Delta\underline{w}_k}{\Delta t} + \Delta\underline{v}_{2_k} \end{bmatrix} \tag{A-26}$$

The disturbance noise and measurement noise are correlated with covariance,

$$\Xi = \begin{bmatrix} 0 & \dfrac{\chi H_2^T}{\Delta t} \end{bmatrix} \tag{A-27}$$

where $\Delta\underline{v}_{1_k}$, $\Delta\underline{v}_{2_k}$ and $\Gamma\Delta\underline{w}_k$ are assumed uncorrelated with covariances Υ_1, Υ_2, and χ, respectively.

Using Eqs. A-16 and A-17, the discrete-time complementary filter for this model becomes

$$\Delta\hat{\underline{x}}_k(+) = \Delta\hat{\underline{x}}_k(-) + K_1 \left[H_1 \Delta\underline{x}_{m_k} - H_1 \Delta\hat{\underline{x}}_k(-) \right] \qquad \text{(A-28)}$$

$$\Delta\hat{\underline{x}}_{k+1}(-) = \Phi\Delta\hat{\underline{x}}_k(+) + \left[D_1 \quad H_2 \Delta\dot{\underline{x}}_{m_k} - H_2 \frac{(\Phi - I)}{\Delta t} \quad \Delta\hat{\underline{x}}_k(+) \right] \qquad \text{(A-29)}$$

If K_1 and D are chosen using Eqs. A-15 and A-20 as follows,

$$K = \begin{bmatrix} K_1 & 0 \end{bmatrix} \qquad \text{(A-30)}$$

$$D = \begin{bmatrix} 0 & D_1 \end{bmatrix} = \begin{bmatrix} 0 & \Delta t \chi H_2^T (H_2 \chi H_2^T + \Delta t^2 \Upsilon_2)^{-1} \end{bmatrix} \qquad \text{(A-31)}$$

Eqs. A-28 and A-29 become a Kalman filter implementation of the complementary filter form. If K_1 and D_1 are chosen based on some other criteria, Eqs. A-28 and A-29 are simply a complementary filter.

An interesting feature of the complementary filter is that if we assume perfect derivative measurements (i.e., Υ_2=0) of all states, the Kalman gain, K_1, is zero and the filter reduces to discrete Euler integration. The complementary filter also gives insight into the implications of correlated disturbance and measurement noise. The correlation indicates the measurement contains information about the disturbance, which translates into information about the future state at index k+1. The measurement must be processed by the update equation, to extract state information, and also by the propagation equation, to extract disturbance noise information.

Another feature of the complementary filter is illustrated by solving for the filter gains when the system is a scalar random walk process with position and derivative measurements. The filter is

$$\Delta\hat{x}_k(+) = \Delta\hat{x}_k(-) + K_1 \left[\Delta x_{m_k} - \Delta\hat{x}_k(-)\right] \tag{A-32}$$

$$\Delta\hat{x}_{k+1}(-) = \Delta\hat{x}_k(+) + D_1 \, \Delta\dot{x}_{m_k} \tag{A-33}$$

where

$$K_1 = \frac{2}{1 + \left[1 + \frac{4}{\Delta t^2}\left(\frac{\chi+\Delta t^2\tau_2}{\chi}\right)\left(\frac{\tau_1}{\tau_2}\right)\right]^{1/2}} \tag{A-34}$$

$$D_1 = \Delta t \left(\frac{\chi}{\chi+\Delta t^2\tau_2}\right) \tag{A-35}$$

For this simple problem, we observe that the disturbance noise covariance primarily determines complementary filter bandwidth and, if sufficiently large, has little effect on the gains K_1 and D_1. Values of measurement noise covariance are readily obtained from sensor specifications, but accurate values for the disturbance noise covariance in simplified system models are difficult to specify. The simple filter indicates that if the process noise is sufficiently large, the actual covariance value is unimportant.

Another property of the complementary filter, shown by Eq. A-34 is that the filter gain, K_1, is determined from

the ratio of measurement noise covariances. The ratio feature implies that knowing the relative accuracy between two sensors is more important in this filter that having individual accurate sensor characteristics. These two properties show that the simple complementary filter can be an effective and a reasonable design even with significant mismatch between the true system dynamics and the random walk model.

A.4 EXTENDED KALMAN FILTER

The VTOL aircraft state estimation problem is naturally formulated as a nonlinear system with nonlinear observations. One nonlinear estimation technique for solving the problem is the extended Kalman filter (EKF). The EKF is a conventional Kalman filter design applied to a mathematical model of the system obtained by linearizing the system about the current state estimate. The EKF yields nearly optimal estimates if the linearization is accurate -- i.e., as long as the state estimate is "close to" the true system state.

A derivation of the EKF is found in Ref. 16 and the resultant mechanization equations are given in Table A-1, below.

TABLE A-1
SUMMARY OF THE EXTENDED KALMAN FILTER

System Model	$\dot{\underline{x}}(t) = \underline{f}[\underline{x}(t), t] + \Gamma(t)\underline{w}(t)$; $\underline{w}(t) \sim N[0, W(t)]$
Measurement Model	$\underline{z}_k = \underline{h}_k[\underline{x}(t_k)] + \underline{v}_k$; $k = 1,2,\ldots$; $\underline{v}_k \sim N(0, \Upsilon_k)$
Initial Conditions	$\underline{x}(0) \sim N(\hat{\underline{x}}_o, P_o)$
Other Assumptions	$E\left[\underline{w}(t)\underline{v}_k^T\right] = 0$ for all k and all t
State Estimate Propagation	$\dot{\hat{\underline{x}}}(t) = \underline{f}[\hat{\underline{x}}(t), t]$
Error Covariance Propagation	$\dot{P}(t) = F[\hat{\underline{x}}(t), t]P(t) + P(t)F[\hat{\underline{x}}(t), t]^T + \Gamma(t)W(t)\Gamma(t)^T$
State Estimate Update	$\hat{\underline{x}}_k(t) = \hat{\underline{x}}_k(-) + K_k\left\{\underline{z}_k - \underline{h}_k[\hat{\underline{x}}_k(-)]\right\}$
Error Covariance Update	$P_k(+) = \left\{I - K_k H_k[\hat{\underline{x}}_k(-)]\right\} P_k(-)$
Gain Matrix	$K_k = P_k(-)H_k[\hat{\underline{x}}_k(-)]^T \cdot \left\{H_k[\hat{\underline{x}}_k(-)]P_k(-)H_k[\hat{\underline{x}}_k(-)]^T + \Upsilon_k\right\}^{-1}$
Definitions	$F[\hat{\underline{x}}(t), t] = \left.\frac{\partial \underline{f}[\underline{x}(t), t]}{\partial \underline{x}(t)}\right\|_{\underline{x}(t)=\hat{\underline{x}}(t)}$ $H_k[\hat{\underline{x}}(-)] = \left.\frac{\partial \underline{h}_k[\underline{x}(t_k)]}{\partial \underline{x}(t_k)}\right\|_{\underline{x}(t_k)=\hat{\underline{x}}(-)}$

A difficulty with the EKF is that the gains, K_k, depend upon the estimate; i.e., K_k must be computed on-line. Calculating K_k every sampling instant places a large computational burden on the onboard computer: efforts at alleviating this burden are discussed in the next section.

A.5 MICROWAVE LANDING SYSTEM - EXTENDED COMPLEMENTARY FILTER -- AN EXAMPLE

The terminal area microwave landing system - extended complementary filter (MLS-ECF) velocity-position filter, with operating MLS and air-data measurements, is derived to demonstrate the ECF construction procedure. The objective here is to produce an implementable filter which accounts for system nonlinearities without computing the EKF gain on-line.

The MLS system model assumed here is characterized by

$$\begin{bmatrix} \dot{\underline{x}}_{MLS} \\ \dot{\underline{w}}_E \\ \dot{\underline{v}}_B \\ \dot{\underline{b}}_B \end{bmatrix} = \begin{bmatrix} 0 & 0 & H_E^{MLS} H_B^E & 0 \\ 0 & \frac{1}{\tau_w} I & 0 & 0 \\ 0 & 0 & 0 & 0 \\ 0 & 0 & 0 & \frac{1}{\tau_b} I \end{bmatrix} \begin{bmatrix} \underline{x}_{MLS} \\ \underline{w}_E \\ \underline{v}_B \\ \underline{b}_B \end{bmatrix} + \begin{bmatrix} 0 \\ \underline{w}_w \\ \underline{w}_v \\ \underline{w}_b \end{bmatrix} \tag{A-36}$$

with the discrete observations,

$$\underline{z}_k = \begin{bmatrix} \underline{x}_E \\ \underline{x}_{MLS} \\ \underline{v}_{AD} \\ \underline{a} + \tilde{\omega}_B^E \underline{v}_B + \underline{b}_B \end{bmatrix}_k + \begin{bmatrix} \underline{v}_E \\ \underline{v}_{MLS} \\ \underline{v}_{AD} \\ \underline{v}_a \end{bmatrix}_k = \begin{bmatrix} \underline{x}_{E_M} \\ \underline{x}_{MLS_M} \\ \underline{v}_{AD_M} \\ \underline{a}_M \end{bmatrix}_k \tag{A-37}$$

The (3x1) vector $\underline{x}_E$ is vehicle position in inertial space, $\underline{x}_{MLS}$ is a (3x1) vector of vehicle position in inertial space using MLS measurements, $\underline{v}_B$ is a (3x1) vector of vehicle translational rate in body axes, $\underline{w}_E$ is a (3x1) vector of wind in earth-relative coordinates, b_B is a (3x1) vector of accelerometer bias in body axes, $\underline{v}_{AD}$ is a (3x1) vector of the air data sensor outputs, and $\underline{a}$ is a (3x1) vector of vehicle inertial acceleration expressed in body axis. The vectors $\underline{v}_E$, $\underline{v}_{MLS}$, $\underline{v}_{AD}$, and $\underline{v}_a$ are discrete, zero-mean, white Gaussian observation noises. The vectors $\underline{w}_w$, $\underline{w}_v$, and $\underline{w}_b$ are discrete, zero-mean, white Gaussian disturbance noises. The matrices H_E^{MLS}, H_B^E, and $\tilde{\omega}_b^E$ are defined in Eqs. A-44, A-42, and A-57 respectively. The nonlinearities in the system and measurement are geometric, i.e., the states are in different coordinate systems and vary with the position of the vehicle. The individual states and their model assumptions are discussed in the following paragraphs.

There are two principle reference frames employed here, the inertial reference frame and the body reference frame. The inertial reference frame used in this report is assumed to be fixed with respect to a nonrotating, flat earth. The origin of the inertial reference frame is located on the surface of the earth with the inertial z-axis pointing down the gravitational acceleration vector. For the MLS system, the inertial reference frame origin is shown in Fig. 3.2-1 and is at the beginning of the runway. The body reference frame is fixed with respect to the vehicle body; its origin is located at the center of mass, the x-axis extends forward to the vehicle nose, the y-axis extends to the right, and the z-axis is orthogonal to the x and y axis extending downward (see Fig. 3.2-1).

Vehicle position, in inertial space, is represented by the measurement vector $\underline{x}_E$ where

$$\underline{x}_E = \begin{bmatrix} \underline{x}_E \\ y_E \\ z_E \end{bmatrix} \tag{A-38}$$

Vehicle position in inertial space, with MLS measurements, is represented by

$$\underline{x}_{MLS} = \begin{bmatrix} R \\ a \\ \varepsilon \end{bmatrix} \tag{A-39}$$

which consists of range, R, azimuth, a, and elevation, ε.

The MLS measurements are related to the cartesian coordinates of the vehicle as shown in Table 3.2-2. The MLS measurement angles are taken in the conical coordinate system as shown in Fig. 3.2-2.

The translational rate of the vehicle through inertial space expressed in body axes is

$$\underline{v}_B = \begin{bmatrix} u \\ v \\ w \end{bmatrix} \tag{A-40}$$

This vector may be transformed to nonrotating, flat earth coordinates by

$$\underline{v}_E = H_B^E \, \underline{v}_B \tag{A-41}$$

where H_B^E is the direction cosine matrix given by

$$H_B^{E^T} = \begin{bmatrix} \cos\theta\cos\psi & \cos\theta\sin\psi & -\sin\theta \\ \cos\psi\sin\theta\sin\phi - \sin\psi\cos\phi & \sin\psi\sin\theta\sin\phi + \cos\psi\cos\phi & \cos\theta\sin\phi \\ \cos\psi\sin\theta\cos\phi + \sin\psi\sin\phi & \sin\psi\sin\theta\cos\phi - \cos\psi\sin\phi & \cos\theta\cos\phi \end{bmatrix} \quad \text{(A-42)}$$

The dynamic model for vehicle velocity is an integrator driven by white Gaussian noise which becomes a discrete time random-walk process. The rate of change of the MLS variables is obtained by differentiating R, a, and ε.

$$\dot{\underline{x}}_{MLS} = H_E^{MLS}\, \underline{v}_E \quad \text{(A-43)}$$

and then substituting in Eq. A-41 for earth-relative velocity. The transformation matrix from earth-relative velocity to MLS coordinate rates reveals the following structure,

$$H_E^{MLS} = \begin{bmatrix} \frac{(x-x_a)}{R} & \frac{(y-y_a)}{R} & \frac{(z-z_a)}{R} \\ -\frac{(x-x_a)(y-y_a)}{R^2\, R_{xz}} & \frac{R_{xz}}{R^2} & \frac{-(z-z_a)(y-y_a)}{R^2\, R_{xz}} \\ \frac{(z-z_\varepsilon)(x-x_\varepsilon)}{r^2\, r_{xy}} & \frac{(z-z_\varepsilon)(y-y_\varepsilon)}{r^2\, r_{xy}} & \frac{-r_\varepsilon}{r^2} \end{bmatrix} \quad \text{(A-44)}$$

where

$$R_{xz} = \left((x-x_a)^2 + (z-z_a)^2 \right)^{1/2} \qquad \text{(A-45)}$$

$$r = \left((x-x_\varepsilon)^2 + (y-y_\varepsilon)^2 + (z-z_\varepsilon)^2 \right)^{1/2} \qquad \text{(A-46)}$$

$$r_{xy} = \left((x-x_\varepsilon)^2 + (y-y_\varepsilon)^2 \right)^{1/2} \qquad \text{(A-47)}$$

As the vehicle travels through the atmosphere it is assumed that it encounters slowly varying, high-magnitude wind modeled as the vector, $\underline{w}_E$, where

$$\underline{w}_E = \begin{bmatrix} W_x \\ W_y \\ W_z \end{bmatrix} \qquad \text{(A-48)}$$

in earth-relative coordinates. The components are assumed to be uncorrelated, stationary, stochastic processes each with exponential autocorrelation. The shaping filters which model the process are shown in Eq. 3.1-11, (Refs. 19 to 21). The velocity of the vehicle with respect to the air mass becomes,

$$\underline{v}_A = \begin{bmatrix} u_A \\ v_A \\ w_A \end{bmatrix} = \underline{v}_B + H_E^B \, \underline{w}_E \qquad \text{(A-49)}$$

The sign convention chosen in Eq. A-49 indicates the filter estimates the negative of the true wind.

The air-data sensor outputs,

$$\underline{v}_{AD} = \begin{bmatrix} TAS \\ \beta \\ \alpha \end{bmatrix} \tag{A-50}$$

consist of true air speed, TAS, sideslip, β, and angle of attack, α. The air data is related to $\underline{v}_A$ as follows,

$$TAS = (u_A^2 + v_A^2 + w_A^2)^{1/2} \tag{A-51}$$

$$\beta = \sin^{-1}(v_A/TAS) \tag{A-52}$$

$$\alpha = \tan^{-1}(w_A/u_A) \tag{A-53}$$

and is only valid above 25.7 m/s (50 kt). Modifications for sensor air data acquisition and elimination as the vehicle TAS crosses 25.7 m/s (50 kt) are discussed in Section 3.4.5.

The MLS-ECF measurement vector, $\underline{a}$, consists of the three components of inertial acceleration at the center of gravity, and is expressed in body axis as

$$\underline{a} = H_E^B \, \ddot{\underline{x}}_E \tag{A-54}$$

If the accelerometers are not located at the center of gravity, they must be corrected as shown in Ref. 1. As shown in Ref. 1, corrections, which are easily implementable, for the accelerometer output, $\underline{a}_o$, from an arbitrary location, $\Delta\underline{x}_B$, where

$$\Delta \underline{x}_B = \begin{bmatrix} x_S \\ y_S \\ z_S \end{bmatrix} \tag{A-55}$$

in the vehicle body reference frame are

$$\underline{a} = \underline{a}_o - \tilde{\underline{\omega}}_B^E \tilde{\underline{\omega}}_B^E \Delta \underline{x}_B - \dot{\tilde{\underline{\omega}}}_B^E \Delta \underline{x}_B + H_E^B \begin{bmatrix} 0 \\ 0 \\ g \end{bmatrix} \tag{A-56}$$

(the $\dot{\tilde{\underline{\omega}}}_B^E \Delta \underline{x}_B$ term is ≈ 0)

where

$$\tilde{\underline{\omega}}_B^E = \begin{bmatrix} 0 & -r & q \\ r & 0 & -p \\ -q & p & 0 \end{bmatrix} \tag{A-57}$$

The last term in Eq. A-56 is the correction for gravity. The angular accelerations are neglected in constructing $\underline{a}$ from the accelerometer output, $\underline{a}_o$, because they are not measured and are usually insignificant. The inertial acceleration of the vehicle in body axes can be determined by differentiating Eq. A-41,

$$\ddot{\underline{x}}_E = H_B^E \dot{\underline{v}}_B + H_B^E \tilde{\underline{\omega}}_B^E \underline{v}_B \tag{A-58}$$

and rearranging to produce

$$\dot{\underline{v}}_B = \begin{bmatrix} \dot{u} \\ \dot{v} \\ \dot{w} \end{bmatrix} = \underline{a} - \tilde{\underline{\omega}}_B \underline{v}_B \tag{A-59}$$

Similarly, the MLS variable accelerations are given by

$$\underline{\ddot{x}}_{MLS} = H_E^{MLS}\,\underline{\ddot{x}}_E + \dot{H}_E^{MLS}\,\underline{v}_E = H_E^{MLS} H_B^E \underline{a} + \dot{H}_E^{MLS}\,\underline{v}_E \qquad \text{(A-60)}$$

The accelerometer sensor output contains numerous error sources (e.g., scale factor, cross-axis acceleration components, hystersis, bias, etc.) of which only bias is included in the estimation model. Accelerometer bias, $\underline{b}_B$, is assumed to be slowly varying and is thus modeled by the shaping filters shown in Eq. 3.1-11.

To apply the EKF, the linearized observation matrix is needed and is given by

$$\Delta\underline{z}_k = \begin{bmatrix} H_{MLS}^E & 0 & 0 & 0 \\ I & 0 & 0 & 0 \\ 0 & H_B^A H_E^B & H_B^A & 0 \\ 0 & 0 & \tilde{\omega}_B^E & I \end{bmatrix}_k \begin{bmatrix} \Delta\underline{x}_{MLS} \\ \Delta\underline{w}_E \\ \Delta\underline{v}_B \\ \Delta\underline{b} \end{bmatrix}_k + \begin{bmatrix} \underline{v}_x \\ \underline{v}_{MLS} \\ \underline{v}_{AD} \\ \underline{v}_a + \underline{w}_v \end{bmatrix}_k \qquad \text{(A-61)}$$

where the perturbation transformation, H_B^A, from body air-relative velocity to the air data measurements is

$$H_B^A = \begin{bmatrix} \frac{u_A}{TAS} & \frac{v_A}{TAS} & \frac{w_A}{TAS} \\ \frac{-u_A v_A}{V_{uw} TAS^2} & \frac{V_{uw}}{TAS^2} & \frac{-w_A v_A}{V_{uw} TAS^2} \\ \frac{-w_A}{V_{uw}^2} & 0 & \frac{u_A}{V_{uw}^2} \end{bmatrix} \qquad \text{(A-62)}$$

$$V_{uw}^2 = u_A^2 + w_A^2 \qquad \text{(A-63)}$$

In order to obtain an implementable MLS-ECF within the constraints of limited computer calculations, simplifications are necessary. The MLS-ECF design model is rendered linear and time-invariant, the transformation matrices are factored out of the resulting steady-state Kalman filter gains, and the remaining filter gains, after factorization, are scheduled. These simplifications are discussed in the following paragraphs.

The design models for the MLS-ECF are determined from a set of design points along a typical trajectory (Table 3.1-1). The set consists of vehicle position and vehicle velocity with the rest of the parameters; wind, Euler angles and body angular rates, zero. The nonlinear, time-varying system has a linear time-invariant representation at each design point, with Eq. A-36 representing the system model and Eq. A-61 representing the perturbation observation model. A discrete system model with sampled-data observations is obtained by applying the results developed in Section A.2. The acceleration measurement enables the discrete system and measurement to be in the format required for application of

the complementary filter derived in Section A.3. The gains of the filter, at each design point, are obtained by propagating the filter to steady-state.

In order that transformation matrices can be factored out of the steady-state Kalman filter gains (See Eq. A-66), the unavailable measurements, x_E, y_E and α are included in the design with large observation noise covariances. Tests with and without the x_E, y_E and α measurements indicated the significant steady-state Kalman filter gains changed little because of the redundancy in the measurements. The steady-state Kalman filter gains for x_E, y_E and α are zeroed in the final filter design shown in Section 3.4.5. Similarly, when the vehicle air relative velocity drops below 25.7 m/s (50 kt), the observation noise covariances for true air speed and sideslip are also set at large values.

When angle-of-attack is not measured, each wind state can have a component that is not observable. The system remains detectable (Ref. 12), however, and the unobserved component decays to zero. As the aircraft changes orientation, H_E^B in Eq. A-49 changes the wind state contribution to $\underline{v}_A$ causing the observable and decaying unobservable part of each wind state to vary. Vertical wind, W_z, has the largest component that is unobservable for small pitch and roll angles. Vertical wind is normally of low magnitude and an estimated component near zero is not a significant discrepancy.

The cartesian position measurements account for the barometric altimeter measurement of z_E. The barometric altimeter measurement is redundant, but becomes important far from the MLS equipment where elevation measurement accuracy is degraded. Below 25.7 m/s (50 kt), all wind states become unobservable because TAS and β measurements are unavailable

and are dropped from the update equation. The wind states are always retained in the propagate equation as discussed in Section 3.3.4.

The resultant MLS filter, derived with the linear-time-invariant system, perturbaton observations, and acceleration measurements, is of the following form:

$$\begin{bmatrix} \hat{\underline{x}}_B(+) \\ \hat{\underline{w}}_B(+) \\ \hat{\underline{v}}_B(+) \\ \hat{\underline{b}}_B(+) \end{bmatrix}_k = \begin{bmatrix} \hat{\underline{x}}_{MLS}(-) \\ \hat{\underline{w}}_E(-) \\ \hat{\underline{v}}_B(-) \\ \hat{\underline{b}}_B(-) \end{bmatrix}_k + \begin{bmatrix} KMLS1' & KMLS2' & KMLS3' & KMLS13' \\ KMLS4' & KMLS5' & KMLS6' & KMLS14' \\ KMLS7' & KMLS8' & KMLS9' & KMLS15' \\ KMLS10' & KMLS11' & KMLS12' & KMLS16' \end{bmatrix}_k \begin{bmatrix} \underline{x}_{E_M} - \hat{\underline{x}}_E(-) \\ \underline{x}_{MLS_M} - \hat{\underline{x}}_{MLS}(-) \\ \underline{v}_{AD_M} - \hat{\underline{v}}_{AD}(-) \\ \underline{a}_M - \tilde{\underline{\omega}}_B(-)\underline{v}_B(-) - \hat{\underline{b}}_B(-) \end{bmatrix}_k$$

(A-64)

$$\begin{bmatrix} \hat{\underline{x}}_{MLS}(-) \\ \hat{\underline{w}}_E(-) \\ \hat{\underline{v}}_B(-) \\ \hat{\underline{b}}_B(-) \end{bmatrix}_{k+1} = \begin{bmatrix} I & 0 & \Delta t H_E^{MLS} H_B^E & 0 \\ 0 & \Phi_w & 0 & 0 \\ 0 & 0 & I & 0 \\ 0 & 0 & 0 & \Phi_b \end{bmatrix}_k \begin{bmatrix} \hat{\underline{x}}_{MLS}(+) \\ \hat{\underline{w}}_E(+) \\ \hat{\underline{v}}_B(+) \\ \hat{\underline{b}}_B(+) \end{bmatrix}_k + \begin{bmatrix} DMLS1 H_E^{MLS} H_B^E \left[\underline{a}_M - \underline{b}_B(+)\right] \\ 0 \\ DMLS2 \left[\underline{a}_M - \tilde{\underline{\omega}}_B(+)\underline{v}_B(+) - \underline{b}_B(+)\right] \\ 0 \end{bmatrix}_k$$

(A-65)

The time rate of change of H_E^{MLS} given in Eq. A-60 is neglected. At long ranges $\dot{H}_E^{MLS}$ is insignificant and at short range, the signal to noise ratio for $\underline{x}_{MLS_M}$ is higher, reducing $\Delta t^2 \ddot{\underline{x}}_{MLS}$ in the propagate equation for $\hat{\underline{x}}_{MLS}$.

The MLS gains 13' to 16', in the filter, are coefficients of the accelerometer measurement and are nonzero because accelerometer bias is estimated. State corrections caused by accelerometer bias estimation mismatch are insignificant and MLS gains 13' to 16' are neglected. The accelerometer measurements are not required in the update equation but are in the propagate equation.

In flight, changes in geometry are accounted for by modifying the Kalman gain matrix as follows:

$$\begin{bmatrix} KMLS1' & KMLS2' & KMLS3' \\ KMLS4' & KMLS5' & KMLS6' \\ KMLS7' & KMLS8' & KMLS9' \\ KMLS10' & KMLS11' & KMLS12' \end{bmatrix} = \begin{bmatrix} H_E^{MLS} KMLS1 & KMLS2 & H_E^{MLS} H_B^E H_A^B KMLS3 \\ KMLS4 & H_{MLS}^E KMLS5 & H_B^E H_A^B KMLS6 \\ H_E^B KMLS7 & H_E^B H_{MLS}^E KMLS8 & H_A^B KMLS9 \\ H_E^B KMLS10 & H_E^B H_{MLS}^E KMLS11 & H_A^B KMLS12 \end{bmatrix}$$

(A-66)

The unprimed MLS-ECF gains in Eq. A-66 are scheduled. In actual implementation, the perturbation estimation errors are filtered by the unprimed MLS gains, then transformed to update the filter states: the filter states are estimated in a reference frame most convenient for control rather than for navigation. The final version of the MLS filter is described in Section 3.3.4.

APPENDIX B

DISCRETE-TIME PROPORTIONAL-INTEGRAL CONTROL LAWS

B.1 INTRODUCTION

Discrete-time linear optimal servos, which are used in the DFCS controller designs in Chapter 3, are derived in this appendix by extending continuous-time command augmentation system design procedures for use in digital control logic. The derivations of the linear optimal servos are accomplished by combining quadratic synthesis with zero steady-state error requirements for tracking commands. The resulting control laws have the familiar proportional-integral or Type 1 control structure.

Previous work in continuous-time Type 1 linear-optimal multi-input, multi-output control laws can be found in Refs. 47 and 48. Discrete-time Type 1 control law designs using frequency domain techniques for single-input, single-output system can be found in Ref. 7. Efforts at extending discrete-time Type 1 conditions to multi-input, multi-output systems using quadratic synthesis commenced in Refs. 1, 32 and 46.

This effort continues here and concentrates on DFCS applications. New results including optimum feedforward gain calculations, optimum control initialization, and theoretical definitions of discrete Type 1 systems are described.

Steady-state analysis and the linear-optimal sampled-data regulator play a major role in DFCS design. Steady-state relationships are discussed in Section 2.6. Basically, if the linear time-invariant discrete system shown in Eq. 3.4-2 is in steady-state, for the command $\Delta\underline{y}_d$, the states and controls satisfy

$$\begin{bmatrix} (\Phi - I) & \Gamma \\ H_p & 0 \end{bmatrix} \begin{bmatrix} \Delta\underline{x}^* \\ \Delta\underline{u}^* \end{bmatrix} = \begin{bmatrix} 0 \\ I \end{bmatrix} \Delta\underline{y}_d \qquad \text{(B-1)}$$

If the composite matrix is invertible, we have

$$\Delta\underline{x}^* = S_{12}\, \Delta\underline{y}_d \qquad \text{(B-2)}$$

$$\Delta\underline{u}^* = S_{22}\, \Delta\underline{y}_d \qquad \text{(B-3)}$$

where

$$\begin{bmatrix} (\Phi - I) & \Gamma \\ H_p & 0 \end{bmatrix}^{-1} = \begin{bmatrix} S_{11} & S_{12} \\ S_{21} & S_{22} \end{bmatrix} \qquad \text{(B-4)}$$

The linear trim states shown in Eqs. B-2 and B-3 are intimately related to the nonlinear aircraft trim as shown in Eqs. 2.6-10 and 2.6-11.

If steady-state analysis is combined with standard sampled-data regulator theory, Refs. 49 and 1, it becomes possible to regulate the system about the trim point ($\Delta\underline{x}^*$, $\Delta\underline{u}^*$). The objective of the regulator is to minimize

$$J = \sum_{k=0}^{\infty} \begin{bmatrix} \Delta\tilde{\underline{x}}_k^T & \Delta\tilde{\underline{u}}_k^T \end{bmatrix} \begin{bmatrix} \hat{Q} & \hat{M} \\ \hat{M}^T & R \end{bmatrix} \begin{bmatrix} \Delta\tilde{\underline{x}}_k \\ \Delta\tilde{\underline{u}}_k \end{bmatrix} \tag{B-5}$$

where

$$\Delta\tilde{\underline{x}}_k = \Delta\underline{x}_k - \Delta\underline{x}^* \tag{B-6}$$

$$\Delta\tilde{\underline{u}}_k = \Delta\underline{u}_k - \Delta\underline{u}^* \tag{B-7}$$

subject to the linear system dynamics shown in Eq. 2.2-3. The corresponding control law is

$$\Delta\underline{u}_k = S_{22}\,\Delta\underline{y}_d - K\,\Delta\underline{x}_k - S_{12}\,\Delta\underline{y}_d \tag{B-8}$$

If we wish to design a control law which optimally transfers the system from one steady-state to another, the regulator design is inadequate by itself. The response to the command is open loop and no effort is taken in the regulator to insure that the difference between the command,

$$\Delta\underline{y}_d = H_p\Delta\underline{x}^* \tag{B-9}$$

and the system output

$$\Delta\underline{y}_k = H_p\Delta\underline{x}_k \tag{B-10}$$

goes to zero in steady state, i.e.,

$$\lim_{k\to\infty} (\Delta\underline{y}_k - \Delta\underline{y}_{d_k}) = 0 \tag{B-11}$$

The steady-state value of the output, $\Delta\underline{y}^*$, will, in general, not be equal to the command if there are modeling errors in forming S_{12} and S_{22} or if disturbances affect the system.

In the next section a PI control law is developed which drives the command error to zero by transfering the system between equilibria using modest control steps and integral compensation.

B.2 PROPORTIONAL-INTEGRAL (PI) CONTROL LAW WITH CONTROL DIFFERENCE WEIGHTING

This section illustrates how augmenting the system state to include the discrete-time equivalent of the derivative of the control, leads to a Type 1 control law. The derivation concludes with the form of the PI controller most easily implemented onboard an aircraft. Control-difference-weighting to obtain Type 1 discrete control laws is the analog of penalizing control rate in continuous-time systems to obtain Type 1 continuous-time control laws.

The continuous-time Type 1 PI controller, derived in Ref. 50, is represented as

$$\Delta \underline{u}(t) = -K_1 \, \Delta \underline{x}(t) - K_2 \int_0^t \left\{ H_p \Delta \underline{x}(\tau) - \Delta \underline{y}_d(\tau) \right\} d\tau - K_2 \, \Delta \underline{\xi}(0) \tag{B-12}$$

where the variable, $\Delta \underline{\xi}(0)$, is the integrator initial condition. The desired <u>form</u> of the <u>discrete</u> Type 1 PI controller can be deduced by using rectangular integration for the integral in Eq. B-12, i.e.,

$$\Delta \underline{u}_k = -K_1 \, \Delta \underline{x}_k - \Delta t K_2 \sum_{i=0}^{k} \left(H_p \Delta \underline{x}_i - \Delta \underline{y}_{d_i} \right) - K_2 \, \Delta \underline{\xi}_0 \tag{B-13}$$

Decreasing the summation by one, regrouping, and replacing the summation with an explicit integrator state, $\Delta\underline{\xi}_k$, produces the discrete position form of the PI controller,

$$\Delta\underline{u}_k = -(K_1+\Delta tK_2H_p)\Delta\underline{x}_k - K_2\,\Delta\underline{\xi}_k + \Delta tK_2\,\Delta\underline{y}_{d_k} \qquad \text{(B-14)}$$

$$\Delta\underline{\xi}_k = \Delta\underline{\xi}_{k-1} + \Delta t(H_p\Delta\underline{x}_{k-1} - \Delta\underline{y}_{d_{k-1}}) \qquad \text{(B-15)}$$

The discrete incremental form for PI is obtained by simply subtracting $\Delta\underline{u}_{k-1}$ from $\Delta\underline{u}_k$, in Eq. B-14 producing,

$$\Delta\underline{u}_k = \Delta\underline{u}_{k-1} - (K_1+\Delta tK_2H_p)(\Delta\underline{x}_k-\Delta\underline{x}_{k-1})-\Delta tK_2(H_p\Delta\underline{x}_{k-1}-\Delta\underline{y}_{d_k}) \qquad \text{(B-16)}$$

The incremental form, for reasons shown later, is the desired structure of the control law. The gains in Eq. B-16, however, are to be determined by minimizing a discrete cost function.

The procedure used here to specify the PI gains is to augment the discrete system as

$$\begin{bmatrix}\Delta\tilde{\underline{x}}_{k+1}\\ \Delta\tilde{\underline{u}}_{k+1}\end{bmatrix} = \begin{bmatrix}\Phi & \Gamma\\ 0 & I\end{bmatrix}\begin{bmatrix}\Delta\tilde{\underline{x}}_k\\ \Delta\tilde{\underline{u}}_k\end{bmatrix} + \begin{bmatrix}0\\ \Delta tI\end{bmatrix}\tilde{\Delta\underline{v}}_k \qquad \text{(B-17)}$$

where $\Delta t\ \tilde{\Delta\underline{v}}_k$ is the control difference. The cost function we wish to minimize is

$$J = \sum_{K=-1}^{\infty} \begin{bmatrix} \Delta\tilde{\underline{x}}_k & \Delta\tilde{\underline{u}}_k & \Delta\tilde{\underline{v}}_k \end{bmatrix}^T \begin{bmatrix} \hat{Q}_{xx} & \hat{Q}_{xu} & \hat{M}_{xv} \\ \hat{Q}_{xu}^T & \hat{Q}_{uu}^T & \hat{M}_{uv} \\ \hat{M}_{xv}^T & \hat{M}_{uv}^T & \hat{R} \end{bmatrix} \begin{bmatrix} \Delta\tilde{\underline{x}}_k \\ \Delta\tilde{\underline{u}}_k \\ \Delta\tilde{\underline{v}}_k \end{bmatrix} \tag{B-18}$$

The control difference,

$$\Delta\tilde{\underline{v}}_k = \Delta\underline{v}_k - 0 \tag{B-19}$$

is zero in steady state and the cost function starts at k=-1 since $\Delta\underline{v}_{-1}$ is unknown with $\Delta\underline{u}_0$ unspecified, i.e.,

$$\Delta\underline{u}_0 = \Delta\underline{u}_{-1} + \Delta t\ \Delta\underline{v}_{-1} \tag{B-20}$$

In minimizing the cost function, we assume the command is constant for k<0, with the value, $\Delta\underline{y}_{d_{-1}}$, which changes at k=0 to $\Delta\underline{y}_{d_0}$, and remains constant thereafter. All states and controls are assumed coordinate shifted with respect to the new steady-state conditions,

$$\Delta\tilde{\underline{x}}_k = \Delta\underline{x}_k - S_{12}\ \Delta\underline{y}_{d_0} \tag{B-21}$$

$$\Delta\tilde{\underline{u}}_k = \Delta\underline{u}_k - S_{22}\ \Delta\underline{y}_{d_0} \tag{B-22}$$

for all k.

The system, Eq. B-17, and cost function, Eq. B-18, are in the proper regulator problem format which yields the solution,

$$\Delta\tilde{\underline{v}}_k = -K_3\ \Delta\tilde{\underline{x}}_k - K_4\ \Delta\tilde{\underline{u}}_k \tag{B-23}$$

where K_3 and K_4 are found from the discrete algebraic Riccati equation solution associated with the linear-optimal regulator.

The control law can be rewritten as

$$\Delta\tilde{\underline{u}}_k = \Delta\tilde{\underline{u}}_{k-1} - \Delta t\, K_3\, \Delta\tilde{\underline{x}}_{k-1} - \Delta t\, K_4\, \Delta\tilde{\underline{u}}_{k-1} \qquad \text{(B-24)}$$

The problem now is to transform the control law in Eq. B-24, which is Type 0, to a Type 1 form. The Type 1 PI form considered here is given in Eq. B-16 and with shifted coordinates has the structure

$$\Delta\tilde{\underline{u}}_k = \Delta\tilde{\underline{u}}_{k-1} - C_1(\Delta\tilde{\underline{x}}_k - \Delta\tilde{\underline{x}}_{k-1}) - \Delta t\, C_2\, H_p \Delta\tilde{\underline{x}}_{k-1} \qquad \text{(B-25)}$$

Comparing Eq. B-25 with Eq. B-24, we have $m(n+\ell)$ unknowns in C_1 and C_2 and $m(n+m)$ knowns in K_3 and K_4. Since ℓ and m are equal, there are as many knowns as unknowns and the transformation between the Type 0 and Type 1 controller should have a unique solution.

Substituting the system dynamics,

$$\Delta\tilde{\underline{x}}_k - \Delta\tilde{\underline{x}}_{k-1} = (\Phi - I)\, \Delta\tilde{\underline{x}}_{k-1} + \Gamma\, \Delta\tilde{\underline{u}}_{k-1} \qquad \text{(B-26)}$$

into Eq. B-25 and regrouping produces

$$\Delta\tilde{\underline{u}}_k = \Delta\tilde{\underline{u}}_{k-1} - \begin{bmatrix} C_1 & \Delta t C_2 \end{bmatrix} \begin{bmatrix} (\Phi - I) & \Gamma \\ H_p & 0 \end{bmatrix} \begin{bmatrix} \Delta\tilde{\underline{x}}_{k-1} \\ \Delta\tilde{\underline{u}}_{k-1} \end{bmatrix} \qquad \text{(B-27)}$$

The two gain sets are equivalent if the following relationship holds

$$\begin{bmatrix} C_1 & \Delta t C_2 \end{bmatrix} \begin{bmatrix} (\Phi - I) & \Gamma \\ H_p & 0 \end{bmatrix} = \begin{bmatrix} \Delta t K_1 & \Delta t K_2 \end{bmatrix} \tag{B-28}$$

The composite matrix is presumed invertible in Eq. B-4 and provides the relationships,

$$C_1 = \Delta t K_1 \, S_{11} + \Delta t K_2 \, S_{21} \tag{B-29}$$

$$C_2 = K_1 \, S_{12} + K_2 \, S_{22} \tag{B-30}$$

The incremental PI derivation is complete.

In order to understand why the incremental form is preferred over the position form, we write out each form for PI using total values,

Incremental Total Value PI

$$\underline{u}_k = \underline{u}_{k-1} - C_1(\underline{x}_k - \underline{x}_{k-1}) - \Delta t C_2(\underline{y}_{k-1} - \underline{y}_{d_k}) \tag{B-31}$$

Position Total Value PI

$$\underline{u}_k = \underline{u}_k^* - C_1(\underline{x}_k - \underline{x}_k^*) - C_2(\underline{\xi}_k - \underline{\xi}_k^*) \tag{B-32}$$

$$\underline{\xi}_k = \underline{\xi}_{k-1} + \Delta t(\underline{y}_{k-1} - \underline{y}_{d_k}) \tag{B-33}$$

$$\underline{\xi}_k^* = \underline{\xi}_{k-1}^* + C_2^{-1}\left[\underline{u}_{k-1}^* - \underline{u}_k^* + C_1(\underline{x}_{k-1}^* - \underline{x}_k^*)\right] \tag{B-34}$$

The total value forms are obtained by using the relationship between trim and linear system steady-state as shown in Eqs. 2.6-10 and 2.6-11 and noting that the assumption, given by Eqs. B-21 and B-22, causes all trim values to cancel out of the incremental form. The integrator trim equation can be deduced from Eq. B-14 at k=0. Comparing the two total value forms, the incremental form is easier to implement because of the smaller number of computations needed to determine $\underline{u}_k$. Experience in Ref. 6 with incremental forms has confirmed their utility. In the event of a temporary computer malfunction, the incremental form always holds the last command and, hence, may prevent temporary instabilities. A block diagram of the incremental total value PI control law is shown in Fig. 3.4-1.

The mechanism used to force the control difference weighted regulator solution into a Type 1 structure eliminates the low-pass filter effect of the gain K_4. Under ideal conditions the two forms have identical step response but markedly different responses to nonideal conditions such as measurement noise. The loss of the low-pass filtering effect is undesirable and leads to further development; i.e., the PIF control law.

B.3 PROPORTIONAL-INTEGRAL-FILTER (PIF) CONTROL LAW

In this section, an alternative Type 1 control law, PIF, is developed. The PIF control law is derived using a performance index with both integrator state and control difference weighting. The low-pass filter effect is not eliminated by manipulating the system dynamics.

The system model is augmented as follows,

$$\begin{bmatrix} \Delta\tilde{\underline{x}}_{k+1} \\ \Delta\tilde{\underline{u}}_{k+1} \\ \Delta\tilde{\underline{\xi}}_{k+1} \end{bmatrix} = \begin{bmatrix} \Phi & \Gamma & 0 \\ 0 & I & 0 \\ \Delta t H_p & 0 & I \end{bmatrix} \begin{bmatrix} \Delta\tilde{\underline{x}}_k \\ \Delta\tilde{\underline{u}}_k \\ \Delta\tilde{\underline{\xi}}_k \end{bmatrix} + \begin{bmatrix} 0 \\ \Delta t I \\ 0 \end{bmatrix} \Delta\tilde{\underline{v}}_k \tag{B-35}$$

The output $\Delta\underline{y}_k$ is to be transferred from the steady-state conditions for $\Delta\underline{y}_{d_{-1}}$ $(k<0)$ to the new steady-state conditions for the command $\Delta\underline{y}_{d_0}$ initiated at k=0, while minimizing the following cost function

$$J = \sum_{k=-1}^{\infty} \begin{bmatrix} \Delta\tilde{\underline{x}}_k^T & \Delta\tilde{\underline{u}}_k^T & \Delta\tilde{\underline{\xi}}_k^T & \Delta\tilde{\underline{v}}_k^T \end{bmatrix} \begin{bmatrix} \hat{Q}_{xx} & \hat{Q}_{xu} & \hat{Q}_{x\xi} & \hat{M}_{xv} \\ \hat{Q}_{xu}^T & \hat{Q}_{uu} & \hat{Q}_{u\xi} & \hat{M}_{uv} \\ \hat{Q}_{x\xi}^T & \hat{Q}_{u\xi}^T & \hat{Q}_{\xi\xi} & \hat{M}_{\xi v} \\ \hat{M}_{xv}^T & \hat{M}_{uv}^T & \hat{M}_{\xi v}^T & R \end{bmatrix} \begin{bmatrix} \Delta\tilde{\underline{x}}_k \\ \Delta\tilde{\underline{u}}_k \\ \Delta\tilde{\underline{\xi}}_k \\ \Delta\tilde{\underline{v}}_k \end{bmatrix} \tag{B-36}$$

The cost function begins at k=-1 for the reasons discussed in the previous section. The shifted integrator state is given by

$$\Delta\tilde{\underline{\xi}}_k = \Delta\underline{\xi}_k - \Delta\underline{\xi}_0^* \tag{B-37}$$

where the steady-state value of the integrator state, $\Delta\underline{\xi}_0^*$, is to be optimally specified.

Equations B-35 and B-36 are in the proper regulator format and yield the solution,

$$\frac{1}{\Delta t}\left(\Delta\tilde{\underline{u}}_k - \Delta\tilde{\underline{u}}_{k-1}\right) = \Delta\tilde{\underline{v}}_{k-1} = -C_3\,\Delta\tilde{\underline{x}}_{k-1} - C_4\,\Delta\tilde{\underline{u}}_{k-1} - C_5\,\Delta\tilde{\underline{\xi}}_{k-1} \tag{B-38}$$

where the gains C_3, C_4, and C_5 are determined from the algebraic Riccati equation solution associated with the optimal regulator.

It is well known that the minimum cost for the optimal regulator is

$$\min J = \Delta\underline{x}_0^T\, P\Delta\underline{x}_0 \tag{B-39}$$

where P is the steady-state solution to the discrete algebraic Riccati equation. It follows that the minimum value of the performance index, shown in Eq. B-36, is (for fixed $\Delta\underline{\xi}_0^*$)

$$\min J = \left[\Delta\tilde{\underline{x}}_{-1}^T \Delta\tilde{\underline{u}}_{-1}^T \Delta\tilde{\underline{\xi}}_{-1}^T\right] \begin{bmatrix} P_{xx} & P_{xu} & P_{x\xi} \\ P_{xu}^T & P_{uu} & P_{u\xi} \\ P_{x\xi}^T & P_{u\xi}^T & P_{\xi\xi} \end{bmatrix} \begin{bmatrix} \Delta\tilde{\underline{x}}_{-1}^T \\ \Delta\tilde{\underline{u}}_{-1}^T \\ \Delta\tilde{\underline{\xi}}_{-1}^T \end{bmatrix} \tag{B-40}$$

Further minimizing J with respect to $\Delta\tilde{\underline{\xi}}_{-1}$, because $\Delta\underline{\xi}_0^*$ is unspecified produces

$$\Delta\tilde{\underline{\xi}}_{-1} = \Delta\underline{\xi}_{-1} - \underline{\xi}_o^* = -P_{\xi\xi}^{-1}\left[P_{u\xi}^T(\Delta\underline{u}_{-1} - \Delta\underline{u}_0^*) + P_{x\xi}^T(\Delta\underline{x}_{-1} - \Delta\underline{x}_0^*)\right] \tag{B-41}$$

Since the system is assumed to be in steady state prior to k=0 we have,

$$\Delta\underline{\xi}_0^* = \Delta\underline{\xi}_{-1}^* + P_{\xi\xi}^{-1}\left[P_{u\xi}^T S_{22} + P_{x\xi}^T S_{12}\right]\left[\Delta\underline{y}_{d_{-1}} - \Delta\underline{y}_{d_0}\right] \tag{B-42}$$

which is the incremental version of

$$\Delta\underline{\xi}_0^* = -P_{\xi\xi}^{-1}\left[P_{u\xi}^T S_{22} + P_{x\xi}^T S_{12}\right]\Delta\underline{y}_{d_0} \tag{B-43}$$

In the coordinates of the original system, the PIF feedback law becomes,

$$\Delta\underline{u}_k = \Delta\underline{u}_{k-1} - \Delta t C_3\,\Delta\underline{x}_{k-1} - \Delta t C_4\Delta\underline{u}_{k-1} - \Delta t C_5\Delta\underline{\xi}_{k-1} + \Delta t E_1\,\Delta\underline{y}_{d_0} \tag{B-44}$$

$$\Delta\underline{\xi}_k = \Delta\underline{\xi}_{k-1} + \Delta t(H_p\Delta\underline{x}_{k-1} - \Delta\underline{y}_{d_0}) \tag{B-45}$$

where

$$E_1 = C_3 S_{12} + C_4 S_{22} - C_5 P_{\xi\xi}^{-1}(P_{x\xi}^T S_{12} + P_{x\xi}^T S_{22}) \tag{B-46}$$

and is a position form.

The total value PIF control law is similarly available in position and incremental forms as follows,

Incremental Total Value PIF

$$\underline{u}_k = \underline{u}_{k-1} + \Delta t\, \underline{v}_{k-1} \tag{B-47}$$

$$\underline{v}_{k-1} = (I-\Delta t C_4)\underline{v}_{k-2} - C_3(\underline{x}_{k-1} - \underline{x}_{k-2}) - \Delta t C_5(\underline{y}_{k-2} - \underline{y}_{d_{k-1}}) + E_1(\underline{y}_{d_k} - \underline{y}_{d_{k-1}}) \tag{B-48}$$

Position Total Value PIF

$$\underline{u}_k = \underline{u}_{k-1} + \Delta t\, \underline{v}_{k-1} \tag{B-49}$$

$$\underline{v}_{k-1} = -C_3(\underline{x}_{k-1} - \underline{x}^*_k) - C_4(\underline{u}_{k-1} - \underline{u}^*_k) - C_5(\underline{\xi}_{k-1} - \underline{\xi}^*_k) \tag{B-50}$$

$$\underline{\xi}_k = \underline{\xi}_{k-1} + \Delta t(\underline{y}_{k-1} - \underline{y}_{d_k}) \tag{B-51}$$

$$\underline{\xi}^*_k = \underline{\xi}^*_{k-1} - P^{-1}_{\xi\xi} P^T_{u\xi}(\underline{u}^*_k - \underline{u}^*_{k-1}) - P^{-1}_{\xi\xi} P^T_{x\xi}(\underline{x}^*_k - \underline{x}^*_{k-1}) \tag{B-52}$$

The simplicity of the incremental over the position total value PIF control law is readily apparent and discussed in the previous section. A block diagram of the incremental total value PIF control law is shown in Fig. 3.4-2.

B.4 SUFFICIENT CONDITONS FOR DISCRETE-TIME TYPE 1 CONTROL

This section demonstrates that the PIF control law satisfies sufficient conditions for discrete-time multi-input, multi-output, Type 1 control. The sufficient conditions are

obtained from the discrete analog of results presented in Ref. 48. The discrete-time results are obtained using the z-transform.

Heuristicly, it is clear PIF forces $\underline{y}_k$ to $\underline{y}_d$ under very general conditions. Assume PIF asymptotically stabilizes an unknown system which is driven by unknown constant disturbances and there are unknown constant biases on the state measurements but no biases on the commanded output measurements. In steady state PIF, in the incremental form, produces

$$0 = \underline{u}^* - \underline{u}^* = \Delta t\, \underline{v}^* \tag{B-53}$$

$$0 = \underline{v}^* = (I-\Delta t C_4)\underline{v}^* - C_3(\underline{x}^*-\underline{x}^*) - \Delta t C_5(\underline{y}^*-\underline{y}_d) + E_1(\underline{y}_d-\underline{y}_d) \tag{B-54}$$

which reduces to

$$0 = C_5(\underline{y}^* - \underline{y}_d) \tag{B-55}$$

If

$$\det\left[C_5\right] \neq 0, \tag{B-56}$$

then multiplying Eq. B-55 by C_5^{-1} demonstrates that $\underline{y}^*$ has been forced to $\underline{y}_d$.

We will demonstrate this property mathematically using two definitions which are discrete analogies to definitions in Ref. 48.

Definition 1: An m×m discrete-time transfer function matrix, G(z), is said to have non-singular d.c. gain if

$$\lim_{z \to 1} (\Delta(z) \det[G(z)]) \neq 0 \qquad \text{(B-57)}$$

where $\Delta(z)$ is the characteristic polynomial of G(z).

Definition 2: An m-input discrete-time control law as shown in Fig. B-1 is Type 1 if the return ratio matrix, G(z), can be written in the form

$$G(z) = \frac{1}{z-1} G'(z) \qquad \text{(B-58)}$$

where G'(z) has non-singular d.c. gain.

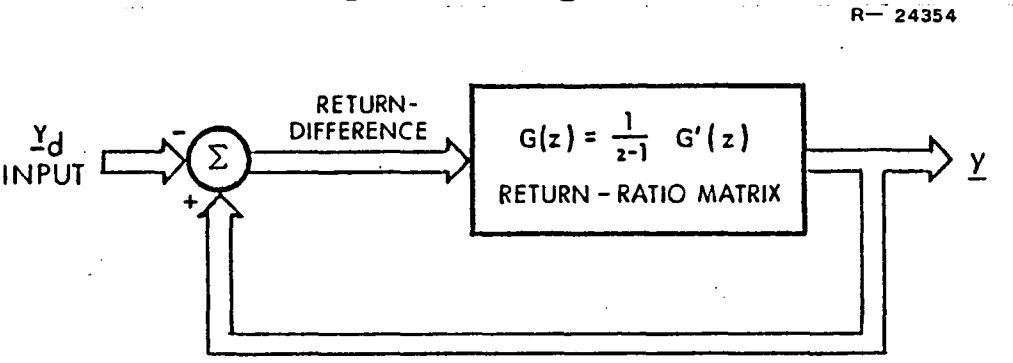

Figure B-1 Discrete-Time Type 1 Feedback Loop

Recall that the characteristic polynominal for a transfer function

$$G(z) = H(zI-\Phi)^{-1}\Gamma \qquad \text{(B-59)}$$

is (Ref. 51)

$$\Delta(z) = \det(zI-\Phi) \qquad \text{(B-60)}$$

if (Φ,Γ,H) is a minimal realization of $G(z)$.

The z-transform of the PIF control law is

$$\Delta\underline{u}(z) = \left[zI + (\Delta tC_4 - I)\right]^{-1} \left[-\Delta tC_3\ \Delta\underline{x}(z) - \frac{z^{-1}}{1-z^{-1}}\Delta t^2 C_5(H\Delta\underline{x}(z) - \Delta\underline{y}_d(z)) + (\Delta tE_1 z + \Delta t^2 C_5)\Delta\underline{y}_d(z)\right] \quad \text{(B-61)}$$

The return-ratio matrix in Fig. B-1 can be obtained for PIF by taking the open loop system dynamics

$$(zI-\Phi)\ \Delta\underline{x}(z) = \Gamma\ \Delta\underline{u}(z), \quad \text{(B-62)}$$

substituting in the PIF expression for $\Delta\underline{u}(z)$, and multiplying by H, producing

$$\Delta\underline{y}(z) = H(zI-\Phi+\Gamma\left[zI+(\Delta tC_4-I)\right]^{-1}\Delta tC_3)^{-1} \left\{\Gamma\left[zI+(\Delta tC_4-I)\right]^{-1}\left(\frac{z^{-1}}{1-z^{-1}}\Delta t^2 C_5(H\Delta\underline{x}(z) - \Delta\underline{y}_d(z)) + (\Delta tE_1 z + \Delta t^2 C_5)\Delta\underline{y}_d(z)\right\} \quad \text{(B-63)}$$

The transfer function of interest is the one between the command error, $H\Delta\underline{x}(z) - \Delta\underline{y}_d(z)$, and the system output, $\Delta\underline{y}(z)$, and is given by

$$G(z) = H(zI-\Phi-\Gamma\left[zI-A\right]^{-1}B)^{-1}\left\{\Gamma\left[zI-A\right]^{-1}\frac{1}{z-1}D\right\} \quad \text{(B-64)}$$

From definition 2, G(z) has the Type 1 property if

$$G'(z) = H(zI-\Phi-\Gamma\ [zI-A]^{-1}B)^{-1}\left\{\Gamma[zI-A]^{-1}D\right\} \qquad \text{(B-65)}$$

has non-singular d.c. gain where

$$A = I - \Delta t C_4 \qquad \text{(B-66)}$$

$$B = -\Delta t C_3 \qquad \text{(B-67)}$$

$$D = -\Delta t^2 C_5 \qquad \text{(B-68)}$$

To show G'(z) has non-singular d.c. gain we use the following identities,

$$\begin{bmatrix} Iz-\Phi & -\Gamma \\ -B & Iz-A \end{bmatrix} \begin{bmatrix} \Delta\underline{x}(z) \\ \Delta u(z) \end{bmatrix} = \begin{bmatrix} 0 \\ D \end{bmatrix} (H\Delta\underline{x}(z)-\Delta\underline{y}_d(z)) \qquad \text{(B-69)}$$

$$\underline{y}(z) = \begin{bmatrix} H & 0 \end{bmatrix} \begin{bmatrix} \Delta\underline{x}(z) \\ \Delta\underline{u}(z) \end{bmatrix} \qquad \text{(B-70}$$

and rewrite the transfer function as

$$G'(z) = \begin{bmatrix} H & 0 \end{bmatrix} \begin{bmatrix} Iz-\Phi & -\Gamma \\ -B & Iz-A \end{bmatrix}^{-1} \begin{bmatrix} 0 \\ I \end{bmatrix} D \qquad \text{(B-71)}$$

Since $\left(\begin{bmatrix} \Phi & \Gamma \\ B & A \end{bmatrix}, \begin{bmatrix} 0 \\ I \end{bmatrix}, \begin{bmatrix} H & 0 \end{bmatrix}\right)$ is a minimal realization of G'(z), the characteristic polynomial of G'(z) is

$$\Delta(z) = \det \begin{bmatrix} Iz-\Phi & -\Gamma \\ -B & Iz-A \end{bmatrix} \qquad \text{(B-72)}$$

Forming the expression $\Delta(z)\ \det[G'(z)]$ we have,

$$\Delta(z)\ \det\ G'(z) \;=\; \det\begin{bmatrix} Iz-\Phi & -\Gamma \\ -B & Iz-A \end{bmatrix} \det\ \begin{bmatrix} H & 0 \end{bmatrix} \begin{bmatrix} Iz-\Phi & -\Gamma \\ -B & Iz-A \end{bmatrix}^{-1} \begin{bmatrix} 0 \\ D \end{bmatrix} \tag{B-73}$$

Using the matrix identity (Ref. 51),

$$\det\begin{bmatrix} T & U \\ -V & W \end{bmatrix} = (\det[T])(\det[VT^{-1}U+W]) \tag{B-74}$$

Eq. B-73 can be rewritten as

$$\Delta(z)\ \det[G'(z)] = \det\ \begin{bmatrix} Iz-\Phi & -\Gamma & 0 \\ -B & Iz-A & D \\ -H & 0 & 0 \end{bmatrix} \tag{B-75}$$

Since interchanging rows or columns does not change the determinant of a matrix,

$$\lim_{z\to 1} \Delta(z)\ \det[G'(z)] = \det\ \begin{bmatrix} I-\Phi & -\Gamma & 0 \\ -H & 0 & 0 \\ -B & I-A & D \end{bmatrix} \tag{B-76}$$

Applying the matrix identity, Eq. B-74 to Eq. B-76 we obtain,

$$\lim_{z\to 1} \Delta(z)\ \det\ [G'(z)] = -\left(\det\ \begin{bmatrix} \Phi-I & \Gamma \\ H & 0 \end{bmatrix}\right)(\det[D]) \tag{B-77}$$

It follows that PIF satisfies the Type 1 definition because: 1) the composite matrix is assumed invertible in Eq. B-4 in order for $\Delta\underline{x}^*$ and $\Delta\underline{u}^*$ to exist and 2)

$$\det[D] = \det[-\Delta t^2 C_5] \neq 0 \qquad \text{(B-78)}$$

because the linear-optimal regulator for a completely observable and controllable system produces an asymptotically stabilizing, hence invertible, gain (Appendix C in Ref. 48). The scheduled integrator gains for PIF can be tested for invertibility to insure Eq. B-78 is satisfied. Equation B-78 is the same as the heuristic result shown in Eq. B-57.

APPENDIX C
SIMULATION OF CONTINUOUS-DISCRETE DYNAMIC MODELS

The VALT DFCS is evaluated using a digital simulation of the helicopter and on-board sensors. This simulation is implemented using a variable time-step Runge-Kutta integration routine which is driven by subroutines describing the continuous-time helicopter models, the discrete-time sensor models, and flight computer (DFCS) coding. Figure C-1 illustrates the simulation structure. The helicopter model which is implemented in the evaluation simulation is outlined in Fig. C-2, and the details of this model are discussed in the next paragraphs.

The rigid-body dynamics of the helicopter are simulated by implementing the linear time-varying system

$$\Delta\dot{\underline{x}}(t) = F(t)\ \underline{x}(t) + G(t)\ \underline{u}(t) + G_t(t)\ \underline{w}(t) \qquad \text{(C-1)}$$

where $\Delta\underline{x}$ contains the 12 rigid-body states, $\Delta\underline{u}$ is the 4-element control position vector and $\Delta\underline{w}$ is the 3-element wind and turbulence vector. The 12×12 F(t) matrix contains linearized dynamic equations. Helicopter stability derivatives are incorporated which result in a fully-coupled system even in straight-and-level flight. The construction of a linear time-varying model is discussed in Section 4.7.

The helicopter simulation contains identical models of the first-order actuator and second-order rotor dynamics in each of the four control channels, as discussed in Section 3.2. The computation time delay (which is restricted to be less than one flight computer sample period long) is simulated

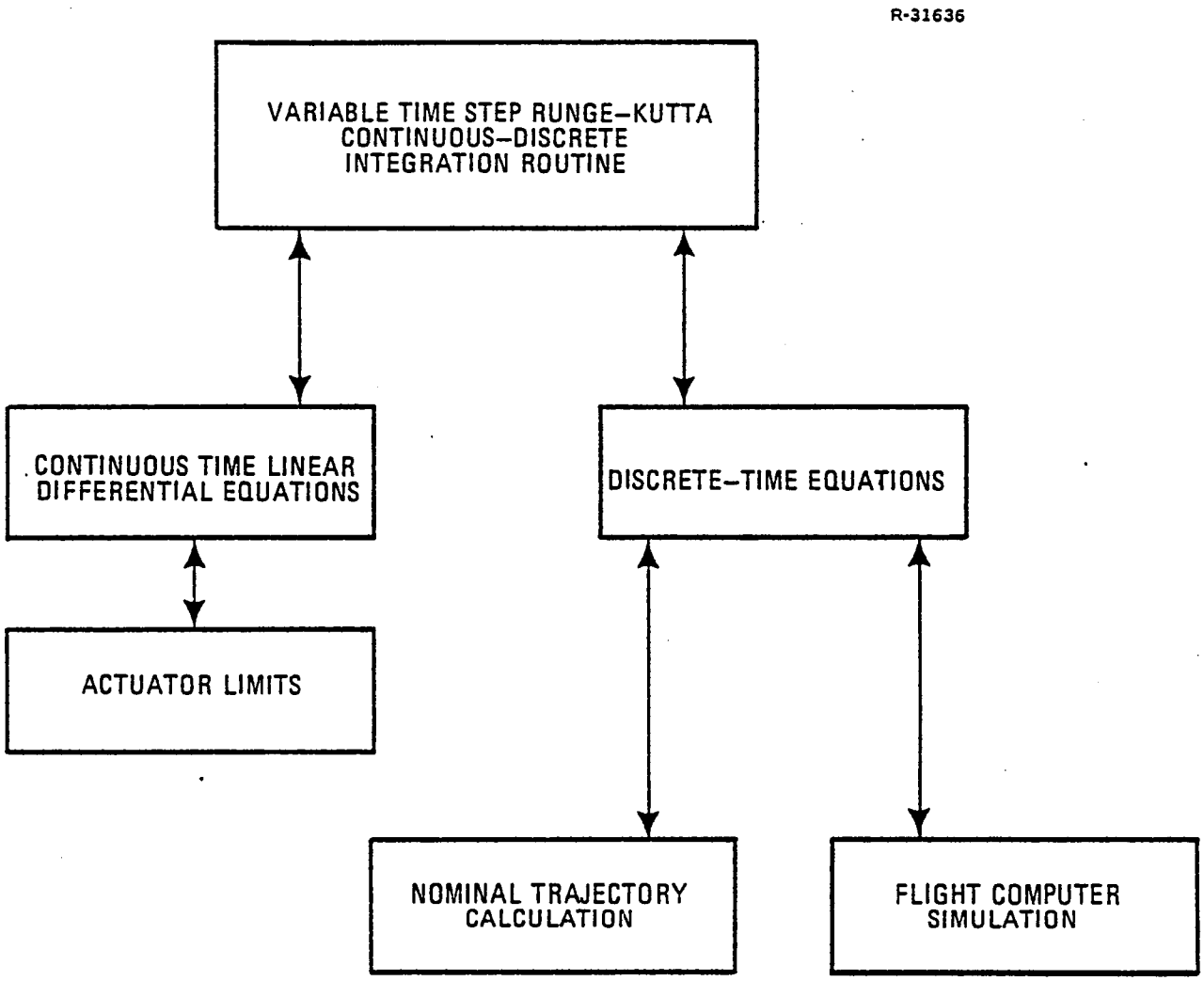

Figure C-1 DFCS Evaluation Simulation Structure

so that the sensitivity of the control laws to these delays can be tested. Some of the sensor transformations included in the evaluation model are nonlinear, as are some of the sensor errors (scale factor errors). Section 3.2 details the sensor suite and indicates which errors are included in these models.

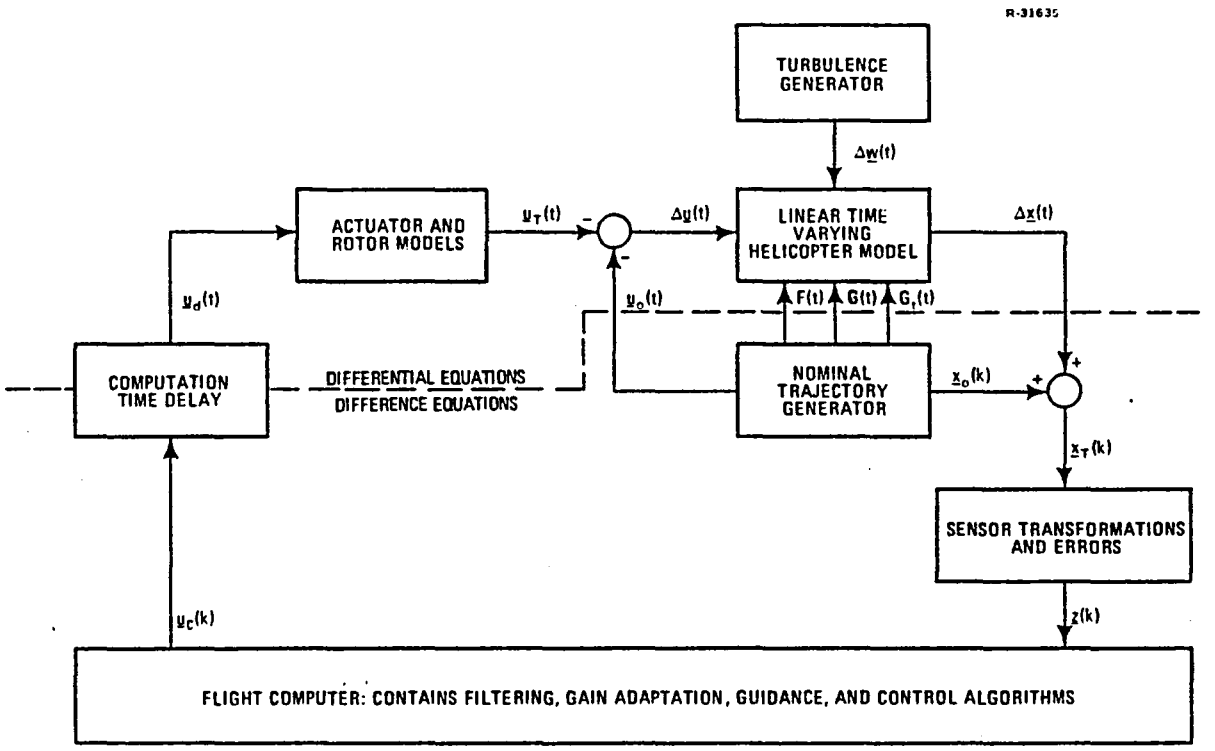

Figure C-2 Helicopter Model Structure

APPENDIX D
GAIN SCHEDULES

This appendix shows the scheduling functions and coefficients for the control laws, filters, and guidance laws. The scheduling methodology and techniques which produced the gain schedules are discussed in Section 3.6.

The control laws are adapted to flight conditions by scheduling their gains as function of TAS, w_E, and $\dot{\psi}$. Using these three variables, three groups of four functions (shown in Table 3.6-2) are used in the gain regression analysis. Table D-1 shows the correlation coefficients for each of the control law gain schedules. The optimal control law gains are all nonzero, although some are insignificant. Those gains which are insignificant and zeroed for implementation are indicated with an asterisk.

The PI-Attitude, PIF-Attitude, and PIF-Velocity regression coefficients and constants for the three scheduling groups are shown in Tables D-2 to D-10. There are 16 gains for PI-Attitude, 29 gains for PIF-Attitude, and 25 gains for PIF-Velocity that can be zeroed for implementation. Of those gain that must be scheduled, 83 percent for PI-Attitude, 85 percent for PIF-Attitude, and 85 percent for PIF-Velocity have regression coefficients greater than 0.8.

Note - The order of the states for feedback and guidance has θ and ϕ switched from the order shown in Eqs. 2.1-2 and 2.1-6 in all the tables in this appendix.

TABLE D-1

CORRELATION COEFFICIENTS, ρ, FOR VALT DFCS GAIN SCHEDULES

T-1443

GAIN	PI ATTITUDE		PIF ATTITUDE		PIF VELOCITY	
$-\Delta tC_3$ or $-C_1$	ρ	GROUP	ρ	GROUP	ρ	GROUP
(1,1)	0.92	3	0.89	2	0.91	3
(2,1)	0.96	3	0.97	2	0.97	3
(3,1)	0.41*	2	0.91*	3	0.99	2
(4,1)	0.92*	3	0.88*	3	0.98*	2
(1,2)	0.86*	2	0.88*	1	0.92	1
(2,2)	0.95*	2	0.96	2	0.97*	2
(3,2)	0.52	1	0.96	1	0.66	1
(4,2)	0.88*	3	0.84*	3	0.94	3
(1,3)	0.81	1	0.62	2	0.76	1
(2,3)	0.99	2	0.97	3	0.98	2
(3,3)	0.92*	2	0.97*	3	0.94*	3
(4,3)	0.77*	2	0.94*	2	0.89*	2
(1,4)	0.68*	3	0.88	3	0.86*	3
(2,4)	0.94	2	0.94*	1	0.91	3
(3,4)	0.40	2	0.96	2	0.80	2
(4,4)	0.40	2	0.97	3	0.98	2
(1,5)	0.97	2	0.99	1	0.99	3
(2,5)	0.98	3	0.91	3	0.96	3
(3,5)	0.90*	3	0.92*	3	0.70*	1
(4,5)	0.99	2	0.96	2	0.97	2
(1,6)	0.94	3	0.94	1	0.92	2
(2,6)	0.89*	2	0.99*	2	0.98*	2
(3,6)	0.83	2	0.98	3	0.99	1
(4,6)	0.83	2	0.78	1	0.99	1
(1,7)	0.98	3	0.96	2	0.97	1
(2,7)	0.99	3	0.99	3	0.99	2
(3,7)	0.81*	3	0.91*	3	0.92*	3
(4,7)	0.92	2	0.93	2	0.95	2
(1,8)	0.70*	1	0.78*	3	0.88*	2
(2,8)	0.87	3	0.96	2	0.96	1
(3,8)	0.87	2	0.93	1	0.98	1
(4,8)	0.83	1	0.93	3	0.98	1
(1,9)	0.96	2	0.98	2	0.83	2
(2,9)	0.98	2	0.99	2	0.87*	2
(3,9)	0.74	1	0.92	2	0.99	3
(4,9)	0.84	2	0.95	1	0.96	3

*Gain can be zeroed.

TABLE D-1

CORRELATION COEFFICIENTS, ρ, FOR VALT DFCS GAIN SCHEDULES (Continued)

T-1443

GAIN	PI ATTITUDE		PIF ATTITUDE		PIF VELOCITY	
$-\Delta t^2 C_5$ or $-\Delta t C_2$	ρ	GROUP	ρ	GROUP	ρ	GROUP
(1,1)	0.87	3	0.78	1	0.80	2
(2,1)	0.88	3	0.92	3	0.92	3
(3,1)	0.64*	3	0.85*	2	0.99*	2
(4,1)	0.95	2	0.98	2	0.99	2
(1,2)	0.84*	2	0.85*	2	0.99*	2
(2,2)	0.92	2	0.96*	1	0.98	2
(3,2)	0.77	1	0.76	2	0.25	1
(4,2)	0.95	3	0.95	3	0.73	1
(1,3)	0.93	2	0.95	2	0.81	3
(2,3)	0.96*	2	0.99*	2	0.76	2
(3,3)	0.92	2	0.91	2	0.96	2
(4,3)	0.95	1	0.67	3	0.97*	2
(1,4)	0.95	3	0.86	3	0.98	2
(2,4)	0.99	2	0.49	3	0.98*	2
(3,4)	0.95*	3	0.98*	3	0.95	2
(4,4)	0.93	2	0.98*	2	0.98	3
$\Delta t\ E_1$						
(1,1)			0.97	3	0.91	2
(2,1)			0.97	3	0.84*	3
(3,1)			0.92*	1	0.99*	2
(4,1)			0.93	2	0.99	2
(1,2)			0.98	2	0.87	3
(2,2)			0.95*	2	0.83*	3
(3,2)			0.50	2	0.45	2
(4,2)			0.80	2	0.92	2
(1,3)			0.92	1	0.58	2
(2,3)			0.99*	2	0.91	3
(3,3)			0.79	2	0.98	2
(4,3)			0.81	1	0.98*	2
(1,4)			0.85	3	0.95	2
(2,4)			0.95	1	0.86*	2
(3,4)			0.98*	1	0.86	2
(4,4)			0.98*	2	0.99	1
$(I-\Delta t C_4)$						
(1,1)			0.99	3	0.99	3
(2,1)			0.97	3	0.98	3
(3,1)			0.86*	3	0.86*	1
(4,1)			0.86*	3	0.94*	2
(1,2)			0.98	3	0.99	3
(2,2)			0.70	2	0.77	1
(3,2)			0.97*	3	0.94*	3
(4,2)			0.99	2	0.94	2

*Gain can be zeroed.

TABLE D-1

CORRELATION COEFFICIENTS, ρ, FOR VALT DFCS GAIN SCHEDULES (Continued)

T-1443

GAIN	PI ATTITUDE		PIF ATTITUDE		PIF VELOCITY	
$I - \Delta tC_4$	ρ	GROUP	ρ	GROUP	ρ	GROUP
(1,3)			0.88*	3	0.85*	1
(2,3)			0.96*	3	0.93*	3
(3,3)			0.99	2	0.91	2
(4,3)			0.83	3	0.99	2
(1,4)			0.90*	2	0.92	2
(2,4)			0.99	2	0.96*	2
(3,4)			0.88*	3	0.99	2
(4,4)			0.97	1	0.99	3

*Gain can be zeroed.

TABLE D-2

PI-ATTITUDE REGRESSION COEFFICIENTS - GROUP I

T-0783

	TAS fps	w fps	TAS^2 $(fps)^2$	$\dot{\psi}$ rps	REGRESSION CONSTANT
$-\Delta tC_2(3,2)$	-0.39088E-03	-0.23462E-02	0.14309E-05	-0.12149E 00	-0.29125E 01
$-\Delta tC_2(4,3)$	-0.19882E-03	-0.63172E-03	0.12771E-05	0.99948E-01	-0.44927E 01
$-C_1(3,2)$	0.19118E-04	0.24482E-03	0.94976E-08	0.50597E-01	0.18045E-01
$-C_1(1,3)$	-0.80402E-03	-0.48834E-03	0.26095E-05	-0.88248E-01	-0.32898E-01
$-C_1(1,8)$*	-0.86763E-02	-0.22560E-02	0.29525E-04	-0.11658E 01	0.21119E 00
$-C_1(4,8)$	0.40865E-02	0.49029E-02	-0.12777E-04	0.88295E 00	0.42094E 01
$-C_1(3,9)$	-0.10399E-01	0.21362E-01	0.42234E-05	0.36771E 01	-0.43914E 01

*Gain can be zeroed

TABLE D-3

PI-ATTITUDE REGRESSION COEFFICIENTS - GROUP II

T-0782

	TAS fps	$\dot{w}_E$ fps	$\dot{\psi}TAS^2$ $(rps)(fps)^2$	$\frac{TAS^2}{1 + 0.000123TAS^2}$ fps^2/fps^2	REGRESSION CONSTANT
$-\Delta tC_2(4,1)$	0.50212E-03	-0.64926E-02	0.89286E-04	-0.63655E-04	0.52076E 00
$-\Delta tC_2(1,2)$*	0.75057E-03	-0.67867E-03	0.32951E-04	-0.25464E-04	-0.63017E-02
$-\Delta tC_2(2,2)$	-0.83798E-03	-0.13447E-02	-0.10177E-03	0.14627E-04	0.89215E-01
$-\Delta tC_2(1,3)$	-0.33345E-03	0.51287E-02	-0.16361E-03	0.40564E-04	-0.40380E 00
$-\Delta tC_2(2,3)$*	0.91664E-03	0.18515E-02	0.30452E-03	-0.15270E-04	-0.47177E-01
$-\Delta tC_2(3,3)$	-0.49361E-04	-0.71879E-03	0.74965E-05	-0.21240E-04	-0.53533E 00
$-\Delta tC_2(2,4)$	-0.23850E-04	0.40281E-05	-0.31225E-07	-0.58203E-06	0.30010E-01
$-\Delta tC_2(4,4)$	-0.48978E-06	0.41078E-05	0.12881E-05	0.91169E-07	-0.31825E-03
$-C_1(3,1)$*	-0.39812E-04	-0.14144E-03	-0.30739E-05	0.19963E-05	-0.68444E-02
$-C_1(1,2)$*	-0.29165E-04	0.11664E-03	-0.16029E-04	0.37913E-06	0.20817E-02
$-C_1(2,2)$*	0.57874E-04	0.32711E-03	0.62224E-04	-0.16787E-05	-0.11001E-02
$-C_1(2,3)$	-0.45024E-04	0.99828E-04	0.15809E-05	-0.14575E-04	0.26115E 00
$-C_1(3,3)$*	-0.70132E-04	-0.53687E-04	-0.70186E-06	0.94453E-06	0.81251E-02
$-C_1(4,3)$*	0.41046E-04	0.37092E-04	0.68101E-05	-0.13493E-06	0.48457E-02
$-C_1(2,4)$	-0.15481E-02	0.18181E-02	-0.59506E-04	0.24171E-04	0.21766E 00
$-C_1(3,4)$	0.43500E-03	0.41581E-02	0.45071E-04	-0.18084E-04	-0.93561E 01
$-C_1(4,4)$	-0.21299E-03	-0.13350E-03	-0.15111E-04	0.99135E-05	0.19481E 01
$-C_1(1,5)$	-0.13604E-01	0.94529E-02	-0.10013E-04	0.79419E-03	-0.12412E 02
$-C_1(4,5)$	0.43483E-02	-0.42469E-01	0.39943E-04	-0.36664E-03	0.28012E 01
$-C_1(2,6)$*	-0.28766E-03	0.78872E-03	-0.46756E-03	0.36849E-04	-0.13436E 00
$-C_1(3,6)$	0.19544E-02	-0.12305E-01	0.30559E-04	-0.13387E-03	-0.26792E 01
$-C_1(4,6)$	0.54286E-02	-0.30152E-01	0.35399E-03	-0.31999E-03	-0.19855E 02
$-C_1(4,7)$	-0.69805E-02	-0.85095E-01	-0.51151E-03	-0.39884E-03	0.58520E 01
$-C_1(3,8)$	0.36859E-02	-0.32924E-01	0.65225E-04	-0.18106E-03	-0.28252E 02
$-C_1(1,9)$	-0.90393E-03	0.31222E-01	-0.38232E-02	0.27446E-03	-0.27488E 01
$-C_1(2,9)$	0.91502E-02	0.19684E-01	0.59958E-02	-0.16624E-03	-0.45009E 00
$-C_1(4,9)$	0.49539E-02	-0.39378E-01	0.47571E-03	-0.34580E-03	-0.46370E 02

*Gain can be zeroed

TABLE D-4

PI-ATTITUDE REGRESSION COEFFICIENTS - GROUP III

T-0784

	TAS fps	TAS^2 $(fps)^2$	$\frac{1}{1 + 0.000123TAS^2}$ $(fps)^{-2}$	$\dot{\psi}_{w_E}$ (rps)(fps)	REGRESSION CONSTANT
$-\Delta tC_2(1,1)$	-0.24433E-01	0.36613E-04	-0.46004E 01	0.2505E-01	-0.42296E 00
$-\Delta tC_2(2,1)$	0.27161E-01	-0.33825E-04	0.52469E 01	-0.88116E-01	-0.56765E 01
$-\Delta tC_2(3,1)$*	0.22025E-02	-0.58582E-05	0.15979E 00	0.32201E-01	-0.13377E 00
$-\Delta tC_2(4,2)$	0.76605E-04	0.10073E-07	-0.88391E-01	0.75585E-02	0.46200E 00
$-\Delta tC_2(1,4)$	0.23137E-03	-0.35127E-06	0.41808E-01	-0.41717E-03	-0.43976E-01
$-\Delta tC_2(3,4)$*	-0.12950E-04	0.14473E-07	-0.15727E-02	-0.21656E-03	0.25573E-02
$-C_1(1,1)$	-0.75709E-02	0.13085E-04	-0.12566E 01	0.11547E-01	0.11995E 01
$-C_1(2,1)$	-0.40758E-02	0.88715E-05	-0.59322E 00	-0.35551E-02	0.54722E 00
$-C_1(4,1)$*	0.72379E-03	-0.11909E-05	0.12559E 00	-0.16681E-02	-0.11919E 00
$-C_1(4,2)$*	-0.61669E-03	0.12634E-05	-0.87272E-01	-0.23251E-02	0.87344E-01
$-C_1(1,4)$*	0.18278E-02	-0.26036E-05	0.40282E 00	0.40057E-01	-0.44042E 00
$-C_1(2,5)$	0.71458E-01	-0.12898E-03	0.13299E 02	-0.71962E-01	-0.13791E 02
$-C_1(3,5)$*	0.18339E-01	-0.47335E-04	0.20688E 01	0.72220E-01	-0.18726E 01
$-C_1(1,6)$	-0.11864E-01	0.22386E-04	-0.23719E 01	-0.64317E 00	0.18384E 01
$-C_1(1,7)$	-0.25639E 00	0.45964E-03	-0.57295E 02	0.29874E-01	0.14976E 02
$-C_1(2,7)$	0.21053E-01	-0.16183E-03	0.47552E 02	-0.78583E 00	-0.51481E 02
$-C_1(3,7)$*	0.39466E-01	-0.76539E-04	0.56869E 01	0.38876E 00	-0.53537E 01
$-C_1(2,8)$	-0.59027E-02	-0.36129E-06	-0.92925E 00	-0.36419E 00	0.15765E 01

*Gain can be zeroed

TABLE D-5

PIF-ATTITUDE REGRESSION COEFFICIENTS - GROUP I

T-1444

	TAS fps	$\dot{w}_E$ fps	TAS^2 $(fps)^2$	$\dot{\psi}$ rps	REGRESSION CONSTANT
$\Delta tE_1(3,1)$*	-0.11123E-02	0.72740E-03	0.45605E-05	0.55695E 01	-0.51249E-01
$\Delta tE_1(1,3)$	-0.20714E-02	-0.33433E-02	0.36289E-05	0.23154E 01	0.33286E 00
$\Delta tE_1(4,3)$	0.10561E-03	0.71511E-03	-0.85877E-06	-0.15401E 00	0.37521E 01
$\Delta tE_1(2,4)$	0.48962E-04	-0.19985E-04	-0.16146E-07	-0.37819E-03	-0.45794E-01
$\Delta tE_1(3,4)$*	0.29196E-05	0.55606E-05	0.10547E-07	0.13619E-01	-0.12958E-02
$-\Delta t^2C_5(1,1)$	-0.10855E-03	-0.31810E-03	0.11225E-05	0.61061E-02	-0.24898E 00
$-\Delta t^2C_5(2,2)$*	0.11606E-05	-0.46449E-04	-0.84256E-07	-0.10191E 00	0.43085E-02
$(I-\Delta tC_4)(4,4)$	0.67495E-04	0.18953E-03	-0.43264E-06	-0.25464E-02	0.52389E 00
$-\Delta tC_3(1,2)$*	0.14118E-04	0.15585E-04	-0.10066E-06	0.95542E-01	-0.16421E-03
$-\Delta tC_3(3,2)$	-0.10633E-04	-0.72356E-04	0.78480E-07	0.46007E-03	0.72789E-02
$-\Delta tC_3(2,4)$*	-0.35369E-04	-0.54070E-03	-0.85476E-06	0.84712E 00	0.54948E-01
$-\Delta tC_3(1,5)$	-0.16157E-02	-0.14572E-02	-0.36720E-04	0.12045E 00	-0.26624E 01
$-\Delta tC_3(1,6)$	0.13457E-02	0.16657E-02	0.89514E-06	-0.39412E 01	-0.27104E 00
$-\Delta tC_3(4,6)$	-0.27166E-02	-0.51280E-02	0.47353E-05	0.77402E 00	-0.48241E 01
$-\Delta tC_3(3,8)$	-0.72458E-03	-0.31643E-02	0.28428E-05	0.60774E-01	-0.46557E 01
$-\Delta tC_3(4,9)$	-0.66482E-03	-0.19377E-02	0.25676E-05	0.35161E 00	-0.58154E 01

TABLE D-6

PIF-ATTITUDE REGRESSION COEFFICIENTS - GROUP II

T-1445

	TAS fps	w fps	$\dot{\psi}$ TAS^2 rps(fps)^2	$\frac{\text{TAS}^2}{1+0.000123\text{TAS}^2}$ (fps)^2/(fps)^2	REGRESSION CONSTANT
$\Delta tE_1(4,1)$	-0.59384E-03	0.43683E-02	-0.19929E-03	0.66031E-04	-0.45136E 00
$\Delta tE_1(1,2)$	-0.52846E-03	0.40932E-03	-0.47230E-03	0.20755E-04	0.58421E-02
$\Delta tE_1(2,2)$*	0.56595E-03	0.65871E-03	0.23714E-03	-0.82739E-05	-0.78437E-01
$\Delta tE_1(3,2)$	-0.17513E-02	0.10014E-01	0.42819E-05	0.79494E-04	0.31263E 01
$\Delta tE_1(4,2)$	-0.26514E-04	-0.87250E-03	0.11159E-05	-0.23130E-04	-0.35738E 00
$\Delta tE_1(2,3)$*	-0.39738E-03	-0.97316E-03	-0.57559E-03	0.43299E-05	0.35981E-01
$\Delta tE_1(3,3)$	-0.99308E-04	0.13815E-02	-0.82213E-05	0.43721E-04	0.34507E 00
$\Delta tE_1(4,4)$*	-0.53172E-05	-0.19294E-04	-0.40917E-05	0.64393E-07	0.68224E-03
$-\Delta t^2C_5(3,1)$*	-0.55531E-04	0.22614E-04	-0.39693E-5	0.15949E-05	0.46938E-02
$-\Delta t^2C_5(4,1)$	-0.19012E-04	-0.26322E-03	0.16965E-04	-0.24306E-05	0.25294E-01
$-\Delta t^2C_5(1,2)$*	0.41519E-04	-0.35646E-04	0.38973E-05	-0.13973E-05	-0.45965E-03
$-\Delta t^2C_5(3,2)$	0.90553E-05	-0.98259E-04	-0.11079E-06	-0.27031E-06	-0.19744E 00
$-\Delta t^2C_5(1,3)$	0.77999E-05	0.22845E-03	-0.11997E-04	0.22825E-05	-0.21830E-01
$-\Delta t^2C_5(2,3)$*	0.23711E-04	0.55587E-04	0.31950E-04	-0.25016E-06	-0.20477E-02
$-\Delta t^2C_5(3,3)$	-0.94879E-05	-0.26455E-04	0.27700E-06	-0.14131E-05	-0.24476E-01
$-\Delta t^2C_5(4,4)$*	0.58099E-06	0.18294E-05	0.53780E-06	-0.64967E-08	-0.79658E-04
$(I-\Delta tC_4)(2,2)$	-0.95570E-04	0.24696E-03	-0.22960E-06	-0.16197E-06	0.61057E 00
$(I-\Delta tC_4)(4,2)$	0.11037E-04	0.61665E-05	-0.17568E-04	-0.56880E-08	-0.23332E-02
$(I-\Delta tC_4)(3,3)$	-0.17151E-03	0.87445E-03	-0.35676E-06	0.69408E-05	0.46472E 00
$(I-\Delta tC_4)(1,4)$*	0.47953E-04	0.75213E-04	-0.22163E-05	0.68758E-06	-0.12347E-01
$(I-\Delta tC_4)(2,4)$	0.21437E-04	0.14536E-04	-0.22019E-04	-0.28137E-06	-0.16316E-02
$-\Delta tC_3(1,1)$	-0.13598E-03	0.95214E-04	-0.51176E-07	0.63688E-05	-0.92735E-02
$-\Delta tC_3(2,2)$	-0.12949E-05	0.11410E-04	0.16144E-04	0.41955E-07	-0.41009E-03
$-\Delta tC_3(1,3)$	0.49981E-04	-0.29767E-03	0.27227E-06	-0.18246E-05	-0.12126E-01
$-\Delta tC_3(4,3)$*	0.29893E-04	0.39857E-04	0.54429E-05	-0.51626E-06	0.15767E-02
$-\Delta tC_3(3,4)$	-0.59260E-03	0.60731E-02	-0.19715E-05	0.29955E-04	-0.27879E 01
$-\Delta tC_3(4,5)$	0.18925E-02	-0.99040E-02	-0.10842E-04	-0.99175E-04	0.64285E 00
$-\Delta tC_3(2,6)$*	0.63859E-03	0.63748E-03	-0.54989E-03	-0.12545E-04	-0.29306E-02
$-\Delta tC_3(1,7)$	-0.22741E-01	0.13947E-01	-0.16309E-04	0,40046E-03	-0.56450E 01
$-\Delta tC_3(4,7)$	-0.31321E-02	-0.11809E-01	-0.62861E-03	0.17345E-04	0.69182E 00
$-\Delta tC_3(2,8)$	-0.87578E-03	-0.64844E-03	0.18296E-03	0.14473E-04	0.96107E-01
$-\Delta tC_3(1,9)$	0.26307E-03	0.46926E-02	-0.49679E-03	0.46876E-04	-0.45913E 00
$-\Delta tC_3(2,9)$	0.37344E-03	0.11097E-02	0.90567E-03	-0.10256E-05	-0.50603E-01
$-\Delta tC_3(3,9)$	-0.46827E-03	-0.71714E-03	0.14516E-04	-0.39449E-04	-0.54442E-00

*Gain can be zeroed.

TABLE D-7

PIF-ATTITUDE REGRESSION COEFFICIENTS - GROUP III

T-1446

	TAS fps	TAS^2 $(fps)^2$	$\frac{1}{1+0,000123TAS^2}$ $(fps)^{-2}$	$\dot{\psi}_{w_E}$ (rps)(fps)	REGRESSION CONSTANT
$\Delta tE_1(1,1)$	0.29339E-01	-0.26433E-04	0.48991E 01	0.91694E-02	-0.84312E 00
$\Delta tE_1(2,1)$	-0.33683E-01	0.42785E-04	-0.37770E 01	-0.58685E-02	0.41142E 01
$\Delta tE_1(1,4)$	-0.39679E-03	0.66474E-06	-0.53811E-01	-0.57944E-04	0.57189E-01
$-\Delta t^2C_5(2,1)$	0.18451E-02	-0.30254E-05	0.21720E 00	0.40487E-03	-0.23324E 00
$-\Delta t^2C_5(4,2)$	-0.10818E-04	0.65921E-07	-0.10004E-01	0.66688E-03	0.32217E-01
$-\Delta t^2C_5(4,3)$	-0.14592E-04	0.71377E-07	-0.29697E-02	0.50220E-03	-0.23257E 00
$-\Delta t^2C_5(1,4)$	0.46036E-04	-0.82285E-07	0.60455E-02	0.15560E-04	-0.63375E-02
$-\Delta t^2C_5(2,4)$	-0.61614E-05	0.72938E-08	-0.78701E-03	0.54000E-06	0.59543E-02
$-\Delta t^2C_5(3,4)$*	-0.14471E-05	0.13549E-08	-0.15019E-03	-0.84132E-04	0.28890E-03
$(I-\Delta tC_4)(1,1)$	0.14592E-04	-0.31249E-05	0.16421E 00	-0.38645E-03	0.40845E 00
$(I-\Delta tC_4)(2,1)$	0.24656E-02	-0.49357E-05	0.38979E 00	-0.46385E-03	-0.39175E 00
$(I-\Delta tC_4)(3,1)$*	-0.12149E-03	0.21006E-06	-0.16325E-01	0.31348E-02	0.12573E-01
$(I-\Delta tC_4)(4,1)$*	-0.47702E-04	0.15971E-06	-0.18959E-01	0.17708E-02	0.92224E-02
$(I-\Delta tC_4)(1,2)$	0.22958E-02	-0.52222E-05	0.42867E 00	-0.41222E-03	-0.42414E 00
$(I-\Delta tC_4)(3,2)$*	-0.25617E-04	-0.30103E-07	-0.25153E-02	0.55899E-02	0.99309E-02
$(I-\Delta tC_4)(1,3)$*	-0.15019E-03	0.31343E-06	-0.20681E-01	0.51752E-02	0.16831E-01
$(I-\Delta tC_4)(2,3)$*	-0.35343E-05	-0.58379E-07	0.10286E-02	0.62964E-02	0.54452E-02
$(I-\Delta tC_4)(4,3)$	-0.12402E-03	0.19920E-06	-0.23669E-01	-0.12080E-02	0.26184E-01
$(I-\Delta tC_4)(3,4)$*	-0.11413E-03	0.35675E-07	-0.20653E-01	-0.85205E-03	0.22319E-01
$-\Delta tC_3(2,1)$	-0.47383E-03	0.10955E-05	-0.71508E-01	-0.47815E-04	0.61921E-01
$-\Delta tC_3(3,1)$*	-0.19138E-04	0.43791E-07	-0.22860E-02	0.15945E-03	0.21561E-02
$-\Delta tC_3(4,1)$*	0.17252E-04	0.25672E-07	0.82722E-02	-0.34675E-03	-0.70504E-02
$-\Delta tC_3(4,2)$*	-0.23447E-03	0.46649E-06	-0.35402E-01	-0.13129E-02	0.35516E-01
$-\Delta tC_3(2,3)$	0.71704E-04	-0.17212E-06	0.41147E-01	0.16140E-03	0.25302E-01
$-\Delta tC_3(3,3)$*	-0.99288E-05	-0.11161E-08	0.48239E-04	-0.96477E-03	0.12114E-02
$-\Delta tC_3(1,4)$	-0.16182E-02	0.34368E-05	-0.20197E 00	0.58166E-01	0.18804E 00
$-\Delta tC_3(4,4)$	0.69795E-05	0.11516E-05	-0.58807E-01	-0.10999E-01	0.57487E 00
$-\Delta tC_3(2,5)$	0.28174E-01	-0.48856E-04	0.38716E 01	0.10068E-01	-0.39612E 01
$-\Delta tC_3(3,5)$*	0.42303E-02	-0.12235E-04	0.43050E 00	0.16734E-01	-0.39241E 00
$-\Delta tC_3(3,6)$	0.16915E-02	-0.75717E-05	0.41219E 00	-0.10444E-01	-0.11739E 01
$-\Delta tC_3(2,7)$	-0.10229E-01	-0.55771E-04	0.78188E 01	0.76332E-02	-0.84975E 01
$-\Delta tC_3(3,7)$*	0.44632E-02	-0.74285E-05	0.69199E 00	0.10693E 00	-0.65547E 00
$-\Delta tC_3(1,8)$*	-0.18660E-02	0.55828E-05	-0.88312E-01	0.25057E-01	0.11488E 00
$-\Delta tC_3(4,8)$	-0.23226E-02	0.49601E-05	-0.52626E 00	0.65575E-02	0.11089E 01

*Gain can be zeroed.

TABLE D-8

PIF-VELOCITY REGRESSION COEFFICIENTS - GROUP I

T-0785

	TAS fps	w_E fps	TAS^2 $(fps)^2$	$\dot{\psi}$ rps	REGRESSION CONSTANT
$\Delta t E_1(4,4)$	0.10090E-02	0.22799E-02	0.96354E-05	-0.58140E 00	0.37982E 01
$-\Delta t^2 C_5(3,2)$	-0.53838E-06	0.50384E-05	0.51227E-08	-0.15045E-03	-0.14110E-02
$-\Delta t^2 C_5(4,2)$	0.15521E-05	-0.14875E-05	-0.65710E-08	-0.27920E-04	0.19200E-03
$(I-\Delta t C_4)(3,1)^*$	0.24397E-04	0.94490E-04	-0.13816E-06	0.38839E-01	-0.71662E-02
$(I-\Delta t C_4)(2,2)$	-0.35004E-04	0.63489E-04	-0.32479E-06	-0.16621E-01	0.63279E 00
$(I-\Delta t C_4)(1,3)^*$	0.44439E-04	0.69766E-04	-0.17926E-06	0.63535E-01	-0.79729E-02
$-\Delta t C_3(1,2)$	0.42811E-04	-0.46437E-04	-0.19331E-06	0.11946E 00	-0.21352E-02
$-\Delta t C_3(3,2)$	-0.93849E-04	-0.40022E-04	0.51111E-06	0.26523E-02	-0.39262E-01
$-\Delta t C_3(1,3)$	-0.14552E-03	-0.12489E-03	0.33695E-06	0.47306E-02	0.15558E-02
$-\Delta t C_3(3,5)^*$	0.53336E-03	-0.15132E-02	-0.30792E-05	0.13796E 00	0.73706E-01
$-\Delta t C_3(3,6)$	-0.23001E-02	0.20830E-01	-0.11894E-04	-0.34283E 00	-0.82865E 00
$-\Delta t C_3(1,7)$	-0.11802E-01	0.78336E-01	0.63999E-05	0.14227E 00	-0.39697E 01
$-\Delta t C_3(2,8)$	0.77265E-03	-0.21165E-02	-0.38687E-05	0.24339E 01	0.62514E-02
$-\Delta t C_3(3,8)$	-0.24418E-02	0.47054E-01	0.13806E-04	0.13094E 00	-0.30124E 01

*Gain can be zeroed

TABLE D-9

PIF-VELOCITY REGRESSION COEFFICIENTS - GROUP II

T-07878

	TAS fps	w_E fps	$\dot{\psi}TAS^2$ rps(fps)^2	$\frac{TAS^2}{1+0.000123TAS^2}$ rps	REGRESSION CONSTANT
$\Delta tE_1(1,1)$	-0.20237E-04	0.87452E-04	-0.79836E-06	-0.98840E-06	-0.30848E-01
$\Delta tE_1(3,1)^*$	-0.76228E-05	-0.18925E-04	-0.87944E-05	0.21992E-06	0.81165E-03
$\Delta tE_1(4,1)$	0.95208E-05	-0.76142E-04	0.37048E-05	-0.50554E-06	0.40751E-02
$\Delta tE_1(3,2)$	0.21606E-05	-0.49992E-04	0.10280E-05	-0.56398E-06	0.30907E-01
$\Delta tE_1(4,2)$	0.34963E-04	0.17552E-04	0.21262E-06	-0.12279E-05	-0.42676E-02
$\Delta tE_1(1,3)$	-0.17409E-04	-0.50477E-04	0.18130E-05	0.64943E-06	0.28526E-02
$\Delta tE_1(3,3)$	0.28716E-04	0.48202E-04	0.11190E-04	-0.64132E-06	-0.13502E-02
$\Delta tE_1(4,3)^*$	-0.63986E-05	-0.15301E-04	-0.45878E-05	0.14049E-06	0.10042E-03
$\Delta tE_1(1,4)$	-0.10457E-02	-0.24157E-02	0.39518E-03	-0.37883E-04	0.54155E 00
$\Delta tE_1(3,4)$	-0.14592E-01	0.97721E-03	-0.16762E-03	0.36835E-03	0.43587E 00
$-\Delta t^2C_5(1,1)$	-0.15654E-05	-0.11939E-05	0.11553E-07	0.78379E-08	0.16926E-02
$-\Delta t^2C_5(3,1)^*$	0.11233E-06	0.24217E-06	0.26343E-06	-0.26874E-08	-0.41255E-04
$-\Delta t^2C_5(4,1)$	-0.26684E-06	0.28872E-05	-0.12733E-06	0.28782E-07	-0.21956E-03
$-\Delta t^2C_5(1,2)^*$	0.44655E-07	-0.26430E-06	0.21152E-06	-0.30097E-08	-0.44701E-06
$-\Delta t^2C_5(2,2)$	-0.34286E-06	-0.40041E-06	-0.18710E-06	0.79413E-08	0.19919E-04
$-\Delta t^2C_5(2,3)$	-0.98105E-06	-0.68666E-06	0.25765E-07	0.19904E-08	0.47433E-02
$-\Delta t^2C_5(3,3)$	-0.12422E-05	-0.98652E-06	-0.41467E-06	0.27312E-07	0.73731E-04
$-\Delta t^2C_5(4,3)^*$	0.31594E-06	0.23582E-05	0.38632E-06	-0.88719E-09	-0.85645E-04
$-\Delta t^2C_5(1,4)$	-0.59584E-04	0.55149E-03	-0.14607E-04	0.62071E-05	-0.46174E-01
$-\Delta t^2C_5(2,4)^*$	0.35341E-04	0.12944E-03	0.32390E-04	-0.50093E-06	-0.25824E-02
$-\Delta t^2C_5(3,4)$	0.47893E-03	-0.46447E-03	0.18537E-05	-0.15483E-04	-0.49082E-01
$(I-\Delta tC_4)(4,1)^*$	0.81947E-05	0.25361E-03	-0.66110E-06	0.16453E-05	-0.18480E-01

TABLE D-9 (Continued)

T-0787b

	TAS fps	w_E fps	$\dot{\psi}TAS^2$ rps(fps)^2	$\frac{TAS^2}{1+0.000123TAS^2}$ rps	REGRESSION CONSTANT
$(I-\Delta tC_4)(4,2)$	0.42318E-04	0.72099E-05	-0.12082E-04	-0.72227E-06	-0.23030E-02
$(I-\Delta tC_4)(3,3)$	-0.14497E-03	0.99726E-03	-0.12288E-05	0.57025E-05	0.54426E 00
$(I-\Delta tC_4)(4,3)$	-0.31003E-03	0.97578E-03	-0.17455E-05	0.58518E-05	-0.10812E-01
$(I-\Delta tC_4)(1,4)$	-0.13320E-04	0.29737E-03	-0.25173E-05	0.18921E-05	-0.19589E-01
$(I-\Delta tC_4)(2,4)^*$	0.50353E-04	0.19520E-04	-0.16822E-04	-0.91193E-06	-0.16082E-02
$(I-\Delta tC_4)(3,4)$	-0.36332E-03	0.10784E-02	-0.15451E-05	0.58912E-05	-0.12090E-01
$-\Delta tC_3(3,1)$	0.42918E-05	0.10611E-04	0.17596E-04	-0.20053E-06	-0.17751E-02
$-\Delta tC_3(4,1)^*$	0.14451E-04	0.13542E-03	-0.68562E-05	-0.91028E-07	-0.77707E-02
$-\Delta tC_3(2,2)^*$	-0.87237E-05	0.94588E-05	0.10503E-04	0.14331E-06	0.60123E-03
$-\Delta tC_3(2,3)$	0.83822E-05	0.11708E-04	0.68456E-06	-0.41534E-05	0.63824E-01
$-\Delta tC_3(4,3)^*$	0.37230E-04	0.35576E-04	0.31353E-05	-0.41724E-06	0.17147E-03
$-\Delta tC_3(3,4)$	-0.88422E-04	0.42234E-02	0.78439E-05	0.16906E-04	-0.18957E 01
$-\Delta tC_3(4,4)$	-0.28121E-03	0.73010E-02	-0.17322E-04	0.32880E-04	0.39070E 00
$-\Delta tC_3(4,5)$	0.32314E-02	-0.12291E-01	-0.40203E-05	-0.11615E-03	0.63059E 00
$-\Delta tC_3(1,6)$	-0.31289E-03	0.80392E-02	-0.30555E-03	0.32893E-04	-0.42261E 00
$-\Delta tC_3(2,6)^*$	0.12552E-02	0.12010E-02	-0.49182E-03	-0.25120E-04	-0.10866E-01
$-\Delta tC_4(2,7)$	-0.42950E-01	-0.10707E-01	-0.39849E-04	-0.40424E-03	-0.13882E 00
$-\Delta tC_3(4,7)$	-0.48634E-03	-0.18135E-01	-0.44328E-03	-0.17537E-04	0.64693E 00
$-\Delta tC_3(1,8)^*$	0.13568E-03	0.48117E-03	0.41485E-04	-0.93671E-05	0.18451E-01
$-\Delta tC_3(4,8)$	-0.18671E-02	-0.61442E-02	-0.10232E-04	0.10378E-03	0.48214E 00
$-\Delta tC_2(1,9)$	-0.21377E-02	0.97116E-02	0.12636E-03	0.11515E-03	-0.76025E 00
$-\Delta tC_3(2,9)^*$	-0.70874E-03	0.20510E-02	0.20346E-03	0.34436E-04	-0.26308E-01

*Gain can be zeroed

TABLE D-10
PIF-VELOCITY REGRESSION COEFFICIENTS - GROUP III

T-0786

	TAS fps	TAS^2 $(fps)^2$	$\frac{1}{1+0.000123TAS^2}$ $(fps)^{-2}$	$\dot{\psi}w_E$ (rps)(fps)	REGRESSION CONSTANT
$\Delta tE_1(2,1)^*$	0.33757E-03	-0.43970E-06	0.56106E-01	0.41543E-03	-0.5556E-01
$\Delta tE_1(1,2)$	-0.37956E-03	0.76644E-06	-0.52693E-01	-0.19132E-02	0.53717E-01
$\Delta tE_1(2,2)^*$	-0.39908E-03	0.84965E-06	-0.57912E-01	-0.12342E-02	0.57353E-01
$\Delta tE_1(2,3)$	0.33052E-03	-0.61299E-06	0.30802E-01	0.11408E-03	-0.76382E-01
$\Delta tE_1(2,4)^*$	0.96597E-02	-0.36994E-04	0.14240E 01	0.65374E-03	-0.12661E 01
$-\Delta t^2C_5(2,1)$	-0.13856E-04	0.24608E-07	-0.17413E-02	-0.55982E-05	0.18015E-02
$-\Delta t^2C_5(1,3)$	0.46891E-04	-0.89703E-07	0.61944E-02	-0.23981E-04	-0.63861E-02
$-\Delta t^2C_5(4,4)$	-0.48109E-04	0.36464E-06	-0.26110E-01	0.66454E-03	-0.32757E 00
$(I-\Delta tC_4)(1,1)$	-0.97526E-04	-0.27242E-05	0.15625E 00	0.10477E-02	0.47697E 00
$(I-\Delta tC_4)(2,1)$	0.19306E-02	-0.40615E-05	0.33521E 00	0.13165E-03	-0.33506E 00
$(I-\Delta tC_4)(1,2)$	0.16840E-02	-0.39539E-05	0.33920E 00	0.21472E-03	-0.33497E 00
$(I-\Delta tC_4)(3,2)^*$	-0.15766E-03	0.28385E-06	-0.19627E-01	0.62455E-02	0.25868E-01
$(I-\Delta tC_4)(2,3)^*$	-0.16376E-03	0.29952E-06	-0.20679E-01	0.71884E-02	0.26168E-01
$(I-\Delta tC_4)(4,4)$	0.15160E-03	-0.24939E-05	0.75385E-01	-0.26867E-02	0.44080E 00
$-\Delta tC_3(1,1)$	-0.28071E-03	0.35237E-06	-0.75275E-01	0.29557E-03	0.13106E 00
$-\Delta tC_3(2,1)$	-0.10089E-02	0.19889E-05	-0.13535E 00	-0.37629E-03	0.12858E 00
$-\Delta tC_3(4,2)$	-0.21774E-03	0.33282E-06	-0.42103E-01	-0.15049E-02	0.49184E-01
$-\Delta tC_3(3,3)^*$	-0.19366E-04	0.27194E-07	-0.18247E-02	-0.3840E-03	0.24070E-02
$-\Delta tC_3(1,4)^*$	-0.20252E-02	0.32650E-05	-0.30932E 00	0.55377E-01	0.29795E 00
$-\Delta tC_3(2,4)$	-0.76532E-03	0.11002E-05	-0.10289E 00	0.79432E-01	0.13096E 00
$-\Delta tC_3(1,5)$	-0.29085E-03	-0.33303E-04	0.47894E 00	0.19988E-01	-0.24624E 01
$-\Delta tC_3(2,5)$	0.24492E-01	-0.43279E-04	0.33938E 01	0.15252E-01	-0.34563E 01
$-\Delta tC_3(4,6)$	-0.58208E-03	-0.37283E-04	0.18176E 01	0.10333E 00	-0.68527E 01
$-\Delta tC_3(3,7)^*$	-0.18828E-02	0.10290E-04	-0.66230E-01	0.21962E 00	0.14067E 00
$-\Delta tC_3(3,9)$	-0.43547E-01	0.22714E-04	0.30365E 01	0.12235E-02	-0.38894E 01
$-\Delta tC_3(4,9)$	0.61003E-02	-0.20277E-04	-0.83920E 00	0.38772E-01	-0.60375E 01

*Gain can be zeroed

The regression coefficients for the ER-ECF, TRI-ECF, and MLS-ECF filters are shown in Tables D-11 to D-13. All of the ER schedules, 85 percent of the TRI-ECF schedules and 84 percent of the MLS-ECF schedules have correlation coefficients greater than 0.8. Only schedules of non-zero gains are shown in the Tables.

TABLE D-11
ENROUTE-ECF REGRESSION COEFFICIENTS

T-1447

	z_E ft	$\frac{1}{1+0.000123TAS^2}$ $(fps)^{-2}$	REGRESSION CONSTANT	CORRELATION COEFFICIENT ρ
KER1	0.14912E-05	-0.96219E-02	0.31774E-01	0.99
KER2(1,1)	-0.50738E-08	-0.19297E-02	0.94919E-01	0.95
KER2(2,2)	-0.35435E-07	-0.17317E-01	0.96816E-01	0.99
KER3	0.38229E-06	-0.18865E-02	0.49825E-02	0.99
KER4(1,1)	0.12026E-06	0.39365E-01	0.10033E-00	0.95
KER4(2,2)	0.72011E-07	0.34871E-00	0.62320E-01	0.99
KER5	-0.30126E-07	0.12598E-03	-0.31335E-03	0.99
KER6(1,1)	-0.19636E-07	-0.66174E-02	-0.14322E-01	0.95
KER6(2,2)	-0.12211E-06	-0.59000E-01	-0.78726E-02	0.99
DER1	0.00000E-00	0.00000E-00	0.49950E-02	----
DER2	0.00000E-00	0.00000E-00	0.99900E-01	----

In previous work, Ref. 1, on the VALT DFCS, a technique for determining the trim parameters of the aircraft is given. The aircraft states are divided into the trim parameter sets

$$\underline{x}_2^{*T} = [u, v, w, p, q, r]^* \qquad \text{(D-1)}$$

$$\underline{\mu}_o^{*T} = [\delta_B, \delta_C, \delta_S, \delta_R, \phi, \theta]^* \qquad \text{(D-2)}$$

The vector $\underline{\mu}_o^*$ is composed of the six independent control variables which, under trim equilibrium specify $\underline{x}_2^*$.

TABLE D-12
MULTILATERATION-ECF REGRESSION COEFFICIENTS

T-1448

	$\frac{1}{1+\left(\frac{R_r}{500}\right)^2}$ $(ft)^{-2}$	$\frac{1}{1+\left(\frac{R_r}{1000}\right)}$ $(ft)^{-1}$	REGRESSION CONSTANT	CORRELATION COEFFICIENTS
KTRI1(1,1)	0.55181E-01	0.00000E-00	0.87256E-02	0.99
KTRI1(2,2)	0.00000E-00	0.33055E-01	0.20945E-02	0.99
KTRI1(3,3)	-0.34960E-02	0.00000E-00	0.30686E-01	0.22
KTRI2(1,1)	0.00000E-00	-0.44178E-01	0.94916E-01	0.99
KTRI2(2,2)	0.00000E-00	-0.41878E-01	0.94613E-01	0.99
KTRI2(3,3)	0.87670E-01	0.00000E-00	0.28455E-02	0.99
KTRI3(1,1)*	0.00000E-00	-0.19599E-03	0.16976E-03	0.40
KTRI3(2,2)*	0.65251E-04	0.00000E-00	-0.56463E-04	0.33
KTRI4(1,1)‡	-0.74080E-04	0.00000E-00	-0.38234E-03	0.64
KTRI4(2,2)‡	0.00000E-00	0.19234E-03	-0.36252E-03	0.90
KTRI4(3,3)	0.00000E-00	-0.35047E-02	-0.23116E-02	0.45
KTRI5(1,1)	0.00000E-00	0.00000E-00	-0.28600E-02	----
KTRI5(2,2)	-0.72509E-01	0.00000E-00	-0.16556E-00	0.20
KTRI5(3,3)	0.00000E-00	0.00000E-00	-0.30000E-03	----
KTRI6(1,1)	0.00000E-00	0.00000E-00	0.73000E-00	----
KTRI6(2,2)	0.00000E-00	0.00000E-00	0.83000E-00	----
KTRI7(1,1)	0.17888E-03	0.00000E-00	0.38425E-03	0.98
KTRI7(2,2)	0.00000E-00	-0.23919E-03	0.37853E-03	0.99
KTRI7(3,3)	0.00000E-00	0.23444E-02	0.43861E-02	0.24
KTRI8(1,1)	0.00000E-00	0.82652E-00	0.76756E-01	0.99
KTRI8(2,2)	0.00000E-00	0.82647E-00	0.76743E-01	0.99
KTRI8(3,3)	0.13964E-00	0.00000E-00	0.10000E-03	0.98
KTRI9(1,1)	0.00000E-00	-0.39584E-02	0.39584E-02	0.88
KTRI9(2,2)	0.00000E-00	-0.46956E-02	0.46956E-02	0.86
KTRI10(1,1)	-0.45481E-04	0.00000E-00	-0.16274E-04	0.99
KTRI10(2,2)‡	0.00000E-00	0.12694E-05	-0.13491E-04	0.84
KTRI10(3,3)	0.00000E-00	-0.41808E-03	-0.23208E-03	0.36
KTRI11(1,1)	0.00000E-00	-0.14056E-00	-0.10234E-01	0.99
KTRI11(2,2)	0.00000E-00	-0.14056E-00	-0.10229E-01	0.99
KTRI11(3,3)	-0.19490E-01	0.00000E-00	0.10000E-04	----
KTRI12(1,1)	0.00000E-00	0.66239E-03	-0.66239E-03	0.88
KTRI12(2,2)	0.00000E-00	0.79216E-03	-0.79216E-03	0.86
DTRI1	0.00000E-00	0.00000E-00	0.49950E-02	----
DTRI2	0.00000E-00	0.00000E-00	0.99900E-01	-----

*Gain can be zeroed.

†R_r - Range from vehicle to center multilateration receiver.

‡Gain can be constant with the value of the regression constant.

TABLE D-13

MICROWAVE LANDING SYSTEM-ECF REGRESSION COEFFICIENTS

T-1449

	$\frac{1.0}{1.0 + \left(\frac{R_\varepsilon}{10^5}\right)^2}$ *	$\frac{1.0}{1.0 + \left(\frac{R_\varepsilon}{4000.0}\right)^2}$	REGRESSION CONSTANT	CORRELATION COEFFICIENT
KMLS1(3,3)	-0.29967E-01	0.00000E-00	0.29967E-01	0.97
KMLS2(1,1)	0.00000E-00	0.24187E-02	0.50483E-01	0.82
KMLS2(2,2)	0.00000E-00	0.92004E-01	0.84110E-01	0.93
KMLS2(3,3)	0.00000E-00	0.40720E-00	0.54753E-01	0.98
KMLS3(1,1)	0.00000E-00	-0.52387E-01	0.55476E-01	0.85
KMLS3(2,2)	-0.20393E-00	0.00000E-00	0.21183E-00	0.93
KMLS4(3,3)	0.1 830E-02	0.00000E-00	-0.12830E-02	0.93
KMLS5(1,1)	0.00000E-00	0.77826E-02	-0.13667E-01	0.83
KMLS5(2,2)	-0.20809E-00	0.00000E-00	0.14515E-00	0.60
KMLS5(3,3)	0.00000E-00	-0.13700E-01	-0.11400E-02	0.58
KMLS6(1,1)	0.00000E-00	-0.24156E-00	0.26239E-00	0.83
KMLS6(2,2)	0.00000E-00	-0.32034E-00	0.40207E-00	0.68
KMLS7(3,3)	-0.62502E-02	0.00000E-00	0.62502E-02	0.99
KMLS8(1,1)	0.00000E-00	0.13108E-02	0.13175E-01	0.82
KMLS8(1,2)	0.00000E-00	-0.14500E-01	0.00000E-00	0.77
KMLS8(2,2)	0.00000E-00	0.11095E-00	0.37412E-01	0.96
KMLS8(2,3)	0.00000E-00	-0.15930E-02	0.00000E-00	0.89
KMLS8(1,3)	0.00000E-00	-0.94016E 02	-0.50568E 01	0.82
KMLS8(2,3)	0.00000E-00	-0.16427E-02	0.00000E-00	0.90
KMLS9(3,3)	0.00000E-00	0.81765E-00	0.00000E-00	0.96
KMLS9(1,1)	0.00000E-00	-0.55174E-01	0.57857E-01	0.84
KMLS9(2,2)	0.00000E-00	-0.61397E-01	0.66158E-01	0.80
KMLS10(3,3)	0.48516E-03	0.00000E-00	-0.48516E-03	0.99
KMLS11(1,1)	0.00000E-00	-0.15274E-03	-0.11712E-02	0.83
KMLS11(1,2)	0.00000E-00	0.27304E-00	-0.11384E-02	0.76
KMLS11(2,2)	0.00000E-00	-0.15984E-01	-0.42761E-02	0.97
KMLS11(3,2)	0.00000E-00	0.24866E-03	0.00000E-00	0.90
KMLS11(1,3)	0.00000E-00	0.10587E-02	-0.34148E-01	0.82
KMLS11(2,3)	0.00000E-00	0.25607E-03	0.00000E-00	0.90
KMLS11(3,3)	0.00000E-00	-0.12598E-00	0.00000E-00	0.96
KMLS12(1,1)	0.00000E-00	0.78379E-02	-0.82047E-02	0.84
KMLS12(2,2)	0.00000E-00	0.93169E-02	-0.10233E-01	0.78
DMLS1	0.00000E-00	0.00000E-00	0.49950E-02	----
DMLS2	0.00000E-00	0.00000E-00	0.99900E-01	----

*R_ε - Range from vehicle to elevation equipment.

In control applications which must operate on perturbation state variables, the trim parameters are required in flight. As an example of how the trim variables could be obtained using velocity guidance, $\underline{\mu}_o^*$ is scheduled, u^*, v^*, and w^* are obtained from the command vector, and p^*, q^*, and r^* are determined in turning flight from

$$\begin{bmatrix} p^* \\ q^* \\ r^* \end{bmatrix} = \begin{bmatrix} 1 & 0 & -\sin\theta^* \\ 0 & \cos\phi^* & \sin\phi^*\cos\theta^* \\ 0 & -\sin\phi^* & \cos\phi^*\cos\theta^* \end{bmatrix} \begin{bmatrix} 0 \\ 0 \\ \dot{\psi}_c \end{bmatrix} \qquad \text{(D-3)}$$

Additional dynamic scheduling for $\underline{\mu}_o^*$ can be obtained, as shown in Ref. 1 and Eq. 4.7-4, by solving for $\underline{\mu}_o^*$ in

$$\underline{\mu}^* = G_u^{-1}\,\dot{\underline{x}}_2^* - G_u^{-1}\,F_2\,\underline{x}_2^* \qquad \text{(D-4)}$$

where

$$\underline{\mu}_T^* = \underline{\mu}_o^* + \underline{\mu}^* \qquad \text{(D-5)}$$

Back-differencing is used to provide the necessary derivatives.

The PI and PIF control laws in position form require trim settings and Eq. D-4 is one procedure for obtaining the trim values. Although the position form is not the current recommended implementation, the schedules for $\underline{\mu}_o^*$, G_u^{-1}, and $G_u^{-1}F_2$ were produced and are shown in Tables D-12 to D-20 for possible future use.

The constant filter gains and design covariances used in the angular rate and angular position filters are shown in Tables D-21 to D-22, respectively. The constant gains and design covariances for the complementary filter version of the enroute filter are shown in Tables D-23 and D-24. The constant

TABLE D-14
TRIM VECTOR $\underline{\mu}^*$, REGRESSION COEFFICIENTS

T-1450

	TAS fps	w_E fps	TAS^2 $(fps)^2$	$\dot{\psi}$ rps	REGRESSION CONSTANT
δ_B (in)	0.14135E-02	-0.21174E-01	0.17909E-04	0.29738E-01	-0.97651E-00
δ_C (in)	-0.18980E-01	-0.59813E-01	0.63147E-04	0.64339E-01	0.48169E 01
δ_S (in)	-0.87605E-03	-0.30081E-02	0.17026E-05	0.65433E-00	0.25504E-00
δ_R (in)	-0.58160E-03	0.64538E-02	-0.66739E-05	0.17029E-00	0.14387E-00
θ (deg)	-0.33214E-01	0.32910E-01	-0.11465E-04	-0.74552E-01	0.66541E 01
ϕ (deg)	0.26186E-02	0.69645E-02	-0.87524E-05	0.17532E 03	-0.49704E-00

TABLE D-15
G_u^{-1} REGRESSION COEFFICIENTS - GROUP I

T-1451

	TAS fps	w_E fps	TAS^2 $(fps)^2$	$\dot{\psi}$ rps	REGRESSION CONSTANT	MEAN VALUE	ρ
$G_u^{-1}(6,1)$*	0.18016E-06	0.39944E-07	-0.40944E-09	-0.59619E-02	-0.17895E-04	0.0	0.97
$G_u^{-1}(2,2)$	-0.66940E-05	-0.12501E-04	0.18540E-07	-0.32882E-00	0.10704E-02	0.00055	0.98
$G_u^{-1}(3,2)$*	-0.96222E-07	-0.69407E-05	-0.11824E-08	-0.99449E-02	0.29627E-04	-0.00004	0.98
$G_u^{-1}(4,2)$*	-0.30172E-06	0.18717E-05	0.19293E-08	-0.79186E-02	0.56318E-05	0.00001	0.91
$G_u^{-1}(5,2)$*	-0.18260E-06	-0.10248E-06	0.22047E-09	-0.41481E-02	0.24312E-04	0.00001	0.96
$G_u^{-1}(5,3)$*	-0.33838E-02	-0.14052E-04	-0.36978E-07	0.51735E-04	-0.33837E-02	-0.00137	0.99
$G_u^{-1}(6,3)$*	-0.27694E-05	-0.47946E-05	0.69959E-08	-0.79171E-03	0.44836E-03	0.00023	0.96
$G_u^{-1}(2,4)$	0.17724E-04	0.14712E-04	-0.45519E-07	0.98596E-00	-0.28326E-02	-0.00153	0.98
$G_u^{-1}(5,4)$*	0.52655E-06	0.37370E-06	-0.82259E-09	0.98933E-02	-0.65373E-04	-0.00002	0.97
$G_u^{-1}(2,5)$	0.11267E-02	0.14613E-02	-0.39802E-05	-0.32246E-01	0.33785E-01	0.105	0.85
$G_u^{-1}(5,5)$†	0.23605E-04	0.12079E-04	-0.12336E-06	-0.74880E-03	0.10476E-01	0.0113	0.95
$G_u^{-1}(6,5)$*	0.29500E-05	-0.14699E-04	0.60171E-07	0.38874E-02	-0.78569E-03	0.00023	0.98
$G_u^{-1}(2,6)$	0.46585E-05	-0.10605E-04	-0.15970E-07	0.56910E-00	-0.61681E-03	-0.00042	0.99
$G_u^{-1}(4,6)$†	0.40857E-02	0.89500E-02	-0.13426E-04	-0.84831E-00	0.47951E 01	5.09	0.86

*Gain can be zeroed.

†Gain can be constant at mean value.

TABLE D-16

G_u^{-1} REGRESSION COEFFICIENTS - GROUP II

T-1452

	TAS fps	w_E fps	$\dot{\psi}TAS^2$ rps(fps)^2	$\frac{TAS^2}{1+0.000123TAS^2}$ rps	REGRESSION CONSTANT	MEAN VALUE	ρ
$G_u^{-1}(1,1)$	0.46272E-04	-0.35049E-04	0.77291E-08	-0.11729E-05	-0.1458E-02	-0.00179	0.89
$G_u^{-1}(2,1)$	-0.47992E-04	0.77690E-04	-0.50326E-08	-0.79048E-06	0.14237E-01	0.00653	0.99
$G_u^{-1}(4,1)$*	-0.56192E-05	0.32616E-05	-0.35558E-08	0.14627E-06	0.54039E-04	0.0001	0.87
$G_u^{-1}(1,2)$	0.56776E-06	0.26753E-05	0.10339E-04	-0.39937E-07	-0.80454E-04	0.00017	0.95
$G_u^{-1}(6,2)$	-0.28951E-05	0.15355E-04	0.87123E-08	0.14283E-06	0.31120E-01	0.0315	0.41
$G_u^{-1}(1,3)$	-0.25324E-04	0.20286E-03	-0.11396E-07	0.12336E-04	0.73555E-02	0.0337	0.92
$G_u^{-1}(2,3)$	0.21814E-04	-0.19097E-03	-0.16464E-06	0.51675E-05	-0.12809	-0.105	0.97
$G_u^{-1}(1,4)$	-0.50189E-05	0.11723E-04	-0.19472E-04	0.17765E-06	0.26686E-03	0.00056	0.85
$G_u^{-1}(3,4)$†	-0.73986E-03	0.25663E-02	0.90634E-06	0.29276E-04	0.22547E-01	2.32	0.98
$G_u^{-1}(4,5)$	-0.76664E-03	0.10163E-01	0.58725E-05	0.91052E-04	-0.74554E-00	-0.379	0.99
$G_u^{-1}(3,6)$	-0.12694E-02	0.36820E-02	-0.33081E-05	0.53233E-04	0.59528E-00	0.709	0.84
$G_u^{-1}(5,6)$*	0.38647E-07	-0.89671E-07	-0.49307E-07	0.85378E-09	-0.12506E-04	-0.00001	0.62
$G_u^{-1}(6,6)$†	-0.16908E-04	0.45491E-04	-0.16022E-06	0.70156E-06	-0.17751E-01	-0.0163	0.81

TABLE D-17

G_u^{-1} REGRESSION COEFFICIENTS - GROUP III

T-1453

	TAS fps	TAS^2 $(fps)^2$	$\frac{1}{1+0.000123TAS^2}$ $(fps)^{-2}$	$\dot{w}_E$ (rps)(fps)	REGRESSION CONSTANT	MEAN VALUE	ρ
$G_u^{-1}(3,1)$*	-0.36258E-05	0.58306E-08	0.80761E-05	0.50092E-04	0.50753E-03	0.00022	0.97
$G_u^{-1}(5,1)$†	-0.34958E-05	0.84327E-08	-0.19003E-03	-0.26413E-06	-0.30677E-01	-0.0310	0.98
$G_u^{-1}(3,3)$*	0.20509E-04	0.16658E-07	0.20178E-02	-0.66490E-03	-0.64782E-02	-0.00316	0.97
$G_u^{-1}(4,3)$*	0.24119E-03	-0.48963E-06	0.32962E-01	0.71184E-04	-0.36425E-01	-0.00203	0.57
$G_u^{-1}(4,4)$†	-0.75927E-03	0.17215E-05	-0.89317E-01	0.67323E-03	-0.40107E-00	-0.500	0.29
$G_u^{-1}(6,4)$†	0.27901E-04	-0.62862E-07	0.34534E-02	-0.10079E-03	-0.85544E-01	-0.0818	0.16
$G_u^{-1}(1,5)$	0.34397E-02	-0.36401E-05	0.16963E 01	-0.11225E-01	0.14326E 01	2.56	0.97
$G_u^{-1}(3,5)$	-0.35550E-02	0.10158E-04	-0.34435E-00	0.38532E-02	0.27360E-00	-0.124	0.88
$G_u^{-1}(1,6)$	-0.56310E-04	0.32923E-06	0.17696E-02	0.16886E-00	-0.16276E-02	-0.00212	0.97

*Gain can be zeroed.

†Gain can be constant at mean value.

TABLE D-18
$G_u^{-1}F_2$ REGRESSION COEFFICIENTS - GROUP I

T-1454

		TAS fps	w_E fps	TAS $(fps)^2$	$\dot{\psi}$ rps	REGRESSION CONSTANT	MEAN VALUE	ρ
7	$G_u^{-1}F_2(1,2)$	-0.15308E-04	-0.75372E-05	0.13534E-06	-0.20931E-00	-0.30502E-03	0.00011	0.89
8	$G_u^{-1}F_2(2,2)$*	0.63334E-05	-0.40156E-05	-0.18059E-07	0.82159E-01	-0.81318E-03	-0.00043	0.96
9	$G_u^{-1}F_2(3,2)$	0.11483E-04	0.82949E-04	-0.13181E-06	0.10675E-01	-0.13528E-01	-0.0136	0.96
12	$G_u^{-1}F_2(6,2)$*	0.23668E-04	0.12049E-04	-0.10826E-06	-0.10279E-03	-0.33114E-02	-0.00225	0.87
19	$G_u^{-1}F_2(1,4)$	-0.19095E-02	0.35175E-02	0.74996E-05	-0.17967E-01	0.94268E-01	0.0214	0.75
20	$G_u^{-1}F_2(2,4)$	0.15916E-03	-0.43328E-03	-0.62535E-06	0.19009E-00	-0.10885E-01	-0.00572	0.56
24	$G_u^{-1}F_2(6,4)$	-0.84229E-04	0.31303E-01	0.28487E-06	-0.21538E-02	0.15050E-01	0.213	0.99
26	$G_u^{-1}F_2(2,5)$	-0.99117E-01	-0.14714E-01	0.69340E-04	-0.23997E-00	-0.10157E 01	-10.37	0.99
29	$G_u^{-1}F_2(5,5)$	-0.23279E-02	0.29838E-01	0.12620E-04	-0.19028E-02	-0.10525E-00	0.0179	0.99
33	$G_u^{-1}F_2(3,6)$	-0.46147E-03	-0.14025E-02	0.13559E-05	0.12069E 01	-0.18213E-00	-0.220	0.96
34	$G_u^{-1}F_2(4,6)$	0.43145E-03	0.25861E-03	-0.21992E-05	0.12074E-01	-0.206112-00	-0.189	0.94

*Gain can be zeroed.

TABLE D-19
$G_u^{-1}F_2$ REGRESSION COEFFICIENTS - GROUP II

T-1455

		TAS fps	w_E fps	$\dot{\psi}TAS^2$ $rps(fps)^2$	$\frac{TAS^2}{1+0.000123TAS^2}$ rps	REGRESSION CONSTANT	MEAN VALUE	ρ
1	$G_u^{-1}F_2(1,1)$	0.30135E-03	-0.14134E-03	0.79654E-07	-0.13293E-04	0.18616E-01	-0.00637	0.88
11	$G_u^{-1}F_2(5,2)$*	0.85256E-06	-0.72167E-06	0.88057E-07	-0.19792E-07	-0.96031E-05	-0.00001	0.82
14	$G_u^{-1}F_2(2,3)$	-0.12886E-03	-0.72069E-04	-.78282E-07	0.73718E-05	0.40067E-01	0.0569	0.98
15	$G_u^{-1}F_2(3,3)$*	0.22653E-02	-0.16021E-04	0.55294E-07	0.46816E-06	0.22653E-02	0.00276	0.82
17	$G_u^{-1}F_2(5,3)$*	-0.28176E-05	0.22851E-05	-0.25432E-08	-0.12339E-07	0.53661E-04	-0.00027	0.99
21	$G_u^{-1}F_2(3,4)$	0.24669E-02	-0-17942E-01	0.14171E-04	-0.12030E-03	-0.16216E 01	-1.98	0.99
30	$G_u^{-1}F_2(6,5)$*	0.33501E-03	-0.48280E-03	-0.12186E-06	-0.42103E-05	0.10529E-01	0.0244	0.94
31	$G_u^{-1}F_2(1,6)$	0.73266E-03	0.12743E-02	-0.14294E-02	-0.13186E-04	-0.14296E-01	0.0147	0.99
32	$G_u^{-1}F_2(2,6)$	-0.14604E-02	-0.12259E-02	0.32386E-02	0.37386E-04	-0.62753E-01	-0.0670	0.99
36	$G_u^{-1}F_2(6,6)$	-0.30081E-02	0.12712E-02	-0.91944E-06	-0.42377E-04	0.38394E-01	-3.22	0.99

*Gain can be zeroed.

TABLE D-20

$G_u^{-1}F_2$ REGRESSION COEFFICIENTS - GROUP III

T-1456

		TAS fps	TAS^2 $(fps)^2$	$\frac{1}{1+0.000123TAS^2}$ $(fps)^{-2}$	$\dot{\psi}w_E$ (rps)(fps)	REGRESSION CONSTANT	MEAN VALUE	ρ
2	$G_u^{-1}F_2(2,1)$	0.12390E-02	-0.26048E-05	0.16786E-00	0.45400E-04	-0.16737E-00	0.00737	0.92
3	$G_u^{-1}F_2(3,1)$*	0.49308E-04	-0.11782E-06	0.48155E-02	-0.81517E-04	-0.52197E-03	0.00363	0.87
4	$G_u^{-1}F_2(4,1)$*	0.37189E-05	-0.13827E-06	-0.12730E-01	-0.16471E-03	0.96246E-02	0.00191	0.87
5	$G_u^{-1}F_2(5,1)$*	-0.90750E-05	0.32439E-07	-0.10697E-02	0.14387E-05	0.17125E-02	0.00069	0.98
6	$G_u^{-1}F_2(6,1)$*	-0.32752E-05	0.70318E-08	-0.45551E-03	-0.15814E-04	0.44991E-03	-0.00002	0.76
10	$G_u^{-1}F_2(4,2)$*	0.53897E-03	-0.11115E-05	0.76459E-01	0.30091E-02	-0.77482E-01	0.00051	0.93
13	$G_u^{-1}F_2(1,3)$	0.15726E-02	-0.33920E-05	0.21014E-00	-0.21529E-03	-0.19665E-00	0.02257	0.70
16	$G_u^{-1}F_2(4,3)$*	-0.33975E-03	0.63487E-06	-0.42967E-01	-0.31282E-04	0.40669E-02	-0.00681	0.60
18	$G_u^{-1}F_2(6,3)$*	-0.21709E-06	0.13207E-08	0.51837E-04	0.21029E-04	0.21029E-04	-0.00013	0.94
22	$G_u^{-1}F_2(4,4)$	-0.37494E-03	-0.32638E-05	-0.10870E-00	0.46208E-01	0.13797E-00	0.00228	0.95
23	$G_u^{-1}F_2(5,4)$*	-0.32413E-05	0.63980E-08	-0.79551E-03	0.46116E-03	0.46857E-03	-0.00017	0.95
25	$G_u^{-1}F_2(1,5)$	-0.81531E-01	0.21941E-03	-0.17252E 02	0.20583E-02	0.13537E 02	-0.3628	0.99
27	$G_u^{-1}F_2(3,5)$	-0.59088E-00	0.10364E-04	0.61791E-00	-0.51705E-01	-0.59088E-00	-0.170	0.97
28	$G_u^{-1}F_2(4,5)$	0.29567E-01	-0.74622E-04	0.34296E 01	0.74618E-02	-0.37525E 01	-0.0322	0.71
35	$G_u^{-1}F_2(5,6)$*	0.23120E-04	-0.73389E-07	0.35558E-02	0.62960E-01	-0.17991E-02	0.00133	0.96

*Gain can be zeroed.

TABLE D-21

DISCRETE FILTER GAINS AND NOISE COVARIANCES FOR THE ANGULAR RATE FILTERS

T-1457

FILTER	PROCESS NOISE COVARIANCE, χ deg^2/sec^4	OBSERVATION NOISE COVARIANCE, T deg^2/sec^2	FILTER GAIN, K
Roll Rate	$(8.6)^2$	$(0.167)^2$	0.965
Pitch Rate	$(9.7)^2$	$(0.167)^2$	0.972
Yaw Rate	$(7.4)^2$	$(0.167)^2$	0.954

TABLE D-22

DISCRETE FILTER GAINS AND NOISE COVARIANCES FOR THE ANGULAR POSITION FILTERS

T-1458

FILTER	PROCESS NOISE COVARIANCE, χ deg^2/sec^2	ANGLE OBSERVATION NOISE COVARIANCE, T deg^2	ANGULAR RATE OBSERVATION NOISE COVARIANCE, T deg^2/sec^2	FILTER GAIN, K	WHITENING GAIN, D
Roll	$(5.33)^2$	$(0.167)^2$	$(0.527)^2$	0.270	0.09998
Pitch	$(4.64)^2$	$(0.167)^2$	$(0.527)^2$	0.270	0.09998
Yaw	$(4.27)^2$	$(0.167)^2$	$(0.527)^2$	0.051	0.09998

filter gains for the complementary filter version of the MLS and TRI filters are shown in Table D-25. The MLS-CF filter gains in Table D-25 are obtained by choosing constant variances for the process and observation noise sources. The TRI-CF filter gains are obtained by averaging the TRI-ECF filter gains whose schedule in shown in Table D-12.

TABLE D-23

CF-ENROUTE u_A (ROW 1) AND v_A (ROW 2) VELOCITY FILTER COVARIANCES AND GAINS

T1462

RANDOM WALK PROCESS NOISE COVARIANCE, χ_u ft^2/sec^3	BIAS PROCESS NOISE COVARIANCE, χ_b ft^2/sec^4	VELOCITY OBSERVATION NOISE COVARIANCE, τ_u ft^2/sec^2	ACCELERATION OBSERVATION NOISE COVARIANCE, τ_a ft^2/sec^4	BIAS TIME CONSTANT, τ_b sec	SAMPLING TIME, Δt sec
$(0.25g)^2$	0.005	3.5	4	100	0.1
$(0.25g)^2$	0.005	9	4	100	0.1
K_{uu}	K_{uu}	K_{bu}	K_{bu}	D_{uu}	
0.111	-0.000067	-0.123	0.0000836	0.0994	
0.0748	-0.00011	-0.0079	0.0000882	0.0994	

TABLE D-24

CF-ENROUTE w NOMINAL (ROW 1) AND ALTERNATIVE (ROWS 2 AND 3) VELOCITY - POSITION FILTER COVARIANCES AND GAINS

T-1463

RANDOM WALK PROCESS NOISE COVARIANCE, χ_v ft^2/sec^3	BIAS PROCESS NOISE COVARIANCE, χ_b ft^2/sec^4	BAROMETRIC ALTIMETER OBSERVATION NOISE COVARIANCE, T_z ft^2	ACCELERATION OBSERVATION NOISE COVARIANCE, T_n ft^2/sec^4	BIAS TIME CONSTANT, τ_b sec	SAMPLING TIME, Δt sec
$(0.25g)^2$	0.005	2900	4	100	0.1
$(0.25g)^2$	0.005	1500	4	100	0.1
$(0.25g)^2$	0.005	2900	9	100	0.1

K_{zz}	$K_{z\ddot{z}}$	$K_{\dot{z}z}$	$K_{\dot{z}\ddot{z}}$	K_{bz}	$K_{b\ddot{z}}$
0.0366	-0.00211	0.00683	-0.000779	-0.000473	0.00144
0.0415	-0.00150	0.00882	-0.000633	-0.000640	0.000134
0.0400	-0.00215	0.00816	-0.000870	-0.000484	0.000178

$D_{z\ddot{z}}$	$D_{\dot{z}\ddot{z}}$
0.00497	0.0994
0.00497	0.0994
0.00497	0.0986

TABLE D-25

MLS-CF AND TRI-CF NONZERO VELOCITY - POSITON FILTER GAINS

T1464

	MLS-CF FILTER GAIN	TRI-CF FILTER GAIN
$K_{xx}(1,1)$	0.0587	0.0213
$K_{xx}(2,2)$	0.0587	0.0150
$K_{xx}(3,3)$	0.0587	0.0299
$K_{vx}(1,1)$	0.0176	0.000425
$K_{vx}(2,2)$	0.0176	0.000293
$K_{vx}(3,3)$	0.0176	0.00534
$K_{bx}(1,1)$	-0.00149	-0.0000312
$K_{bx}(2,2)$	-0.00149	-0.0000130
$K_{bx}(3,3)$	-0.00149	-0.000392
$K_{xv}(1,1)$	-	0.0777
$K_{xv}(2,2)$	-	0.0783
$K_{xv}(3,3)$	-	0.0228
$K_{vv}(1,1)$	-	0.399
$K_{vv}(2,2)$	-	0.399
$K_{vv}(3,3)$	-	0.0257
$K_{bv}(1,1)$	-	-0.0650
$K_{bv}(2,2)$	-	-0.0650
$K_{bv}(3,3)$	-	-0.00371
$D_{x\dot{v}}$	0.00497	0.00497
$D_{v\dot{v}}$	0.0994	0.0994

REFERENCES

1. Stengel, R.F., Broussard, J.R., and Berry, P.W., "The Design of Digital Adaptive Controllers for VTOL Aircraft," NASA CR-144912 (TASC Report TR-640-1), March 1976.

2. Stengel, R.F., Broussard, J.R. and Berry, P.W., "Digital Flight Control Design for a Tandem-Rotor Helicopter," 33rd Annual National Forum of the American Helicopter Society, Washington, May 1977.

3. Stengel, R.F., Broussard, J.R. and Berry, P.W., "Digital Controllers for VTOL Aircraft," Proceedings of the 1976 IEEE Conference on Decision and Control, Clearwater, Florida, December 1976, pp. 1009-1016.

4. Burns, M.R., "Users Manual for Program TVHIS Linear Time Varying Helicopter Simulation," The Analytic Sciences Corporation, TR-804-2, November 1976.

5. Berry, P.W., Broussard, J.R. and Stengel, R.F., "Evaluation of Digital Flight Control Design for V/STOL Approach and Landing," AGARD Symposium on Guidance and Control Design Considerations for Low Altitude and Terminal Area Flight, Dayton, Ohio, October 1977.

6. Bristol, E.H., "Designing and Programming Control Algorithms for Direct Digital Control System," Control Engineering, January 1977, pp. 24 to 26.

7. Smith, C.L., Digital Computer Process Control, International Textbook Co., Pennsylvania, 1972.

8. Hartmann, G.L., Harvey, C.A. and Mueller, C.E., "Optimal Linear Control (Formulation to Meet Conventional Design Specs)," ONR-CR215-238-1, March 1976.

9. Hoffman, W.C., Zvara, J., Bryson, A.E., Jr. and Ham, N.D., "An Automatic Guidance Concept for VTOL Aircraft," AIAA Paper No. 70-1035, New York, August 1970.

10. Hoffman, W.C. and Hollister, W.M., "A Spiral Guidance Approach Concept for Commercial VTOL Operations," NASA CR-132651, Burlington, MA, May 1975.

REFERENCES (Continued)

11. Anon., "Flying Qualities of Piloted V/STOL Aircraft," MIL-F-83300, USAF/USN, December 1970.

12. Kwakernaak, H. and Sivan, R., Linear Optimal Control Systems, Wiley-Interscience, New York 1972.

13. Stengel, R.F. and Berry, P.W., "Stability and Control of Maneuvering High Performance Aircraft," NASA CR-2788 (TASC Report TR-587), April 1977.

14. Nalbandian, J., "Users Manual for Flight Control Design Programs," NASA CR-144913 (TASC Report TR-640-2), September 1975.

15. Berman, H. and Gran, R., "Design Principles for Digital Autopilot Synthesis," Journal of Aircraft, Vol. 11, No. 7, July 1974, pp. 414-422.

16. Gelb, A., Ed., Applied Optimal Estimation, MIT Press, Cambridge, Massachusetts, 1974.

17. Moen, G.C., "Simulation and Flight Studies of an Approach Profile Indicator for VTOL Aircraft," NASA TN D-8051, Washington, November 1975.

18. Moen, G.C., DiCarlo, D.J. and Yenni, K.R., "A Parametric Analysis of Visual Approaches for Helicopters," NASA TN D-8275, Washington, December 1976.

19. Jackson, C.T., et al, "Flight Evaluation of Advanced Navigation Techniques for General Aviation Using Frequency Scanning," AIAA Guidance and Control Conference, San Diego, August 16-18, Paper 76-1992.

20. Hemesath, N.B., "Optimal and Suboptimal Velocity Aiding for VOR/DME Systems," AIAA Guidance, Control, and Flight Mechanics Conference, Santa Barbara, California, August 1970, Paper No. 70-124.

21. Bryson, A.E. and Bobick, J.C., "Improved Navigation by Combining VOR/DME Information and Air Data," AIAA Guidance and Control Conference, 1971, Paper No. 71-928.

22. Kayron, M. and Fried, W.R., ed., Avionics Navigation Systems, John Wiley & Sons, Inc., New York, 1969.

23. Elliott, J.R., "Introductory Remarks on NASA's F-8 Program," 1976 IEEE Conference on Decision and Control, Clearwater, Florida, December 1976.

24. Personal Correspondence with NASA Langley Personnel, 1976-1977.

25. Jones, H.L. and Luders, G., "Space Shuttle Navigation Analysis," The Analytic Sciences Corporation, TR-548-1, Reading, Massachusetts, December 1975.

26. Frost, C.J., "Helicopter Air Data Measurement," AGARD-CP-176, Medium Accuracy Low Cost Navigation, September 1975.

27. Britt, Charles L., "An Investigation of Errors and Data Processing Techniques for an RF Multilateration System," RTI No. 43U-954, NASA CR-132609, February 1975.

28. Niessen, Frank R., "A Complementary Filter Technique for Deriving Aircraft Velocity and Position Information," NASA Langley Research Center, Hampton, Virginia, 1975.

29. Sorensen, J.A., Mohr R.L. and Cline, T.B., "Instrumentation Requirements for Aircraft Parameter Identification with Application to the Helicopter," NASA CR-132675, June 1975.

30. Anon., "Tactical Aircraft Guidance System Advanced Development Program Flight Test Phase Report," Vols. I and II, USAAMRDL TR-73-89A,B, Ft. Eustis, Virginia, (prepared by CAE Electronics Ltd., Boeing Vertol Co., and IBM Federal Systems Division), April 1974.

31. Isakson, D., "Linear and Angular Vibration Measurement of V/STOL Aircraft, Volume I," NASA Contract No. NAS12-2028, April 1970.

32. Lee, W.J., "Linear Tracking Systems," B.S. Thesis, Massachusetts Institute of Technology, June 1976.

33. Personal communication from Dr. David Downing, NASA LRC, June 1977.

34. Lindorff, D.P., Theory of Sampled Data Control Systems, J. Wiley & Sons, New York, 1965.

35. Astrom, K.J. and Eykhoff, P., "System Identification -A Survey," Automatica, Vol. 7, 1971, pp. 123-162.

36. Katzbera, J.D., "Structured Feedback Control of Discrete Linear Stochastic Systems with Quadratic Sosts," IEEE Transactions Automatic Control, Vol. AC-22, No. 2, April 1977, pp. 232-235.

37. Hartmann, G.L., Hauge, J.A., Hendrick, R.C., "F-8C Digital CCV Flight Control Laws," NASA CR-2629, February 1976.

38. Joglekar, A.N. and Powell, J.D., "Data Compression in Recursive Estimation with Applications to Navigation Systems," AIAA Guidance and Control Conference, Key Biscayne, Florida, Paper No. 73-901, August 1973.

39. Trankle, T.L. and Bryson, A.E., "Control Logic to Track the Outputs of a Command Generator or Randomly Forced Target," AIAA Guidance and Control Conference, Hollywood, Florida, Paper No. 77-1041, August 1977.

40. Sage, A.P. and Melsa, J.L., Estimation Theory with Applications to Communications and Control, New York, McGraw-Hill, 1970.

41. Farrell, J., Integrated Aircraft Navigation, Academic Press, New York, 1976.

42. Higgins, W.T., "A Comparison of Complementary and Kalman Filtering," IEEE Trans. Aerospace and Electronic Sy., Vol. AES-11, No. 3, May 1975, pp. 321 to 325.

43. Rabiner, L.R. and Gold, B., "Theory and Application of Digital Signal Processing," Prentice-Hall, Inc., New Jersey, 1975.

44. Kafer, G., Toles, R. and Golan, E., "Digital Control Laws for the Space Shuttle Orbiter ALT," Proceedings of the 1976 IEEE Decision and Control Conference, Clearwater, Florida, December 1976.

45. Konar, A.F., et al. "Digital Flight Control Systems for Tactical Fighters," AFFDL-TR-74-69, Wright-Patterson Air Force Base, Ohio, July 1974.

46. Lee, W.H., Athans, M., Castanon, D. and Bacchioloni, F., "Linear Tracking Systems with Applications to Aircraft Control System Design," M.I.T., ELS-R-720, January 1977.

47. Young, P.C. and Willems, J.C., "An Approach to the Linear Multivariate Servomechanism Problem," International Journal of Control, Vol. 15, No. 5, May 1972.

48. Sandell, N.R., "Optimal Linear Tracking Systems," M.I.T., ESL-R-156, September 1971.

49. Dorato, P. and Levis, A.H., "Optimal Linear Regulators: The Discrete-Time Case," IEEE Trans. Auto. Control, Vol. AC-16, No. 6, December 1971, pp. 613-620.

50. Stengel, R.F., Broussard, J.R., Berry, P.W., and Taylor, J.H., "Modern Methods of Aircraft Stability and Control Analysis," ONR-CR-215-237-2, May 1977.

51. Rosenbrock, H.H., State Space and Multivariable Theory, Wiley Interscience, New York, 1970.

NASA Contractor Report 159019
NASA Contractor Report 159020
Distribution List
NAST-14358

	No. Copies
NASA Langley Research Center Hampton, VA 23665 Attn: Report and Manuscript Control Office, Mail Stop 180A Dr. David R. Downing, Mail Stop 494	1 25
NASA Ames Research Center Moffett Field, CA 94035 Attn: Library, Mail Stop 202-3	1
NASA Dryden Flight Research Center P. O. Box 273 Edwards, CA 93523 Attn: Library	1
NASA Goddard Space Flight Center Greenbelt, MD 20771 Attn: Library	1
NASA Lyndon B. Johnson Space Center 2101 Webster Seabrook Road Houston, TX 77058 Attn: JM6/Library	1
NASA Marshall Space Flight Center Marshall Space Flight Center, AL 35812 Attn: Library, AS61L	1
Jet Propulsion Laboratory 4800 Oak Grove Drive Pasadena, CA 91103 Attn: Library, Mail 111-113	1
NASA Lewis Research Center 21000 Brookpark Road Cleveland, OH 44135 Attn: Library, Mail Stop 60-3	1
NASA John F. Kennedy Space Center Kennedy Space Center, FL 32899 Attn: Library, NWSI-D	1
National Aeronautics and Space Administration Washington, DC 20546 Attn: RE-4	1

	No. Copies
NASA Scientific and Technical Information Facility 6571 Elkridge Landing Road Linthicum Heights, MD 21090	30 plus original